Fracture mechanisms and failure criteria of adhesive joints and toughened epoxy adhesives

Xu, Botao

Queen Mary, University of London

School of Engineering and Materials Science

Fracture Mechanisms and Failure Criteria of Adhesive Joints and Toughened Epoxy Adhesives

By

Botao Xu

A thesis submitted to Queen Mary, University of London in partial fulfilment of the requirements for the degree of Doctor of Philosophy

Abstract

Adhesive bonded applications are used widely in industry because of significant advantages such as uniform stress distribution, and the ability to join different materials. However most epoxy structural adhesives are brittle at room temperature and it is required to improve their toughness. The objective of this work was to understand the fracture of adhesive joints, failure criteria and rubber toughening mechanisms via a series of experiments and FEA modelling.

Double lap joints (DLJ) bonded by commercial AV119 adhesive were studied. It was found that local strain and failure path were controlled by adhesive thickness. In order to model adhesive joints accurately and efficiently, systematic fracture tests were implemented to determine the fracture criteria. Mode-I, mode-II and mixed mode fracture energy release rates were obtained by Fixed Arm Peel, 4-point End Notched Flexure (ENF) and Mixed Mode Bending (MMB) tests. Numerical analysis was applied to determine the parameters of the Drucker-Prager material model and Cohesive Zone Model (CZM). The 3D FEA results showed good agreement with experimental results of DLJ and MMB. FEA results successfully demonstrated bonding strength, stress and strain distribution and plastic deformation; and further details were found using sub models.

The rubber toughening mechanism was studied by modelling different face-centred micromodels. The stress distributions ahead of the crack tip in global DLJ models were extracted and used as the loading condition for the micromodels, so that a relationship between macromodel and micromodel has been established. It is found that Von Mises and hydrostatic stress play very important roles in the toughening mechanisms and also predicted that rubber particles with multi-layer structure have more potential to toughen epoxy resin than simple rubber particles.

***Keywords*: adhesive; toughening; fracture; joint failure; finite element analysis; cohesive zone model; micro model**

Author's declaration

I declare that the work in this thesis entitled "Fracture Mechanisms and Failure Criteria of Adhesive Joints and Toughened Epoxy Adhesives" was carried out in accordance with the regulations of the University of London. This thesis and work presented in it are my own work and is submitted for the degree of Doctor of Philosophy in School of Engineering and Material Science in Queen Mary, University of London. The work is original except where are indicated and acknowledged by means of comprehensive list of references in the text. I further declare that no part of the thesis has been submitted by me at any anther university for any other degree.

I hereby declare that the above statements are true.

Botao Xu
May 2010

Acknowledgements

I would like to express my sincere gratitude to my supervisor, Prof. Felicity Guild, for her continued guidance and support of my study and research. Her immense instructions and knowledge enabled me to develop an understanding of the subject from the initial to the final level.

A number of people offered their help to my study in Queen Mary College. I am very grateful to Mr. John Caulfield for specimen cutting and apparatus manufactures. I would also like to thank Mr. Bill Godwin for his help with test instructions and problem resolving. Also I would like to thank Mr. Stephen Wicks and Mr. Raymond Lam for their IT supports which enabled my simulation work to proceed smoothly. Moreover, I offer my regards and appreciations to all of those who supported me in various respects during the completion of the study. Finally I would like to thank all those staff who offered me heartfelt help and advice.

In my time at Queen Mary, I have befriended with many research students who offered me endless discussions and helpful knowledge. It is my pleasure to thank those friends here.

It is an honour for me to express my gratitude to my parents and my brother's family due to their continuous encouragement and support throughout my study. Last but certainly not least, I thank my wife. Here I feel there is no word to express my gratitude to her because she have inspired and encouraged me for these years.

Table of Contents

List of Figures

List of Tables

Notation

Abbreviation

ASE	Artificial Strain Energy
CBT	Corrected Beam Theory
CC	Compliance Calibration
CDE	Creep Dissipation Energy
COD	Crack Tip Displacement
COTD	Crack Tip Opening Displacement
CZM	Cohesive Zone Model
DCB	Double Cantilever Beam
DLJ	Double Lap Joint
ENF	End Notched Flexure
EPFM	Elastic Plastic Fracture Mechanics
FPZ	Fracture Process Zone
IE	Total Energy
LEFM	Linear Elastic Fracture Mechanics
MMB	Mixed Mode Bending
MMF	Mixed Mode Flexure
PDE	Plastic Dissipation Energy
PEEQ	Equivalent Plastic Strain at Integration Points
PTFE	Polytetrafluoroethylene
SDEG	Scalar Stiffness Degradation at Integration Point
SE	Strain Energy
SJL	Single Lap Joint
TAST	Thick Adherend Lap Shear
VCCT	Virtual Crack Closure Technique

Alphabetical symbols

a	crack length
a_0	initial crack length
D	scalar stiffness degradation

E	Young's modulus
E_{1f}	bending stiffness of MMB specimen
E_{eff}	effective Young's modulus
$f(\sigma_{ij})$	yield function
G_C	fracture energy release rate
G_{IC}	mode-I fracture energy release rate
G_{IIC}	mode-II fracture energy release rate
G_{IIIC}	mode-III fracture energy release rate
$g(\sigma_{ij})$	plastic potential function
I_1, I_2, I_3	stress invariant
J_1, J_2, J_3	deviatoric stress invariant
K	bulk modulus
k	penalty stiffness
m	ratio of compressive yield stress to tensile yield stress
p	equivalent hydrostatic stress
q	von Mises effective stress
R_{tri}	stress triaxiality
S	deviatoric stress tensor
T_g	glass transition temperature
t	thickness
W	width

Greek symbols

α	power law parameter
β	friction angle
δ_t	crack tip opening displacement
ε_e	equivalent strain
ε_p	equivalent plastic strain
ε_p^e	Von Mises equivalent plastic strain
ε_{eng}	engineering strain
ε_{ture}	true strain
ζ	mixed mode ratio defined as $G_I/(G_I+G_{II})$
η	BK parameter

θ	contact angle in Young's equation
λ	bulk modulus ratio of rubber particle to epoxy matrix
μ	Poisson's ratio
ν	Poisson's ratio
ν_p	plastic Poisson's ratio
ν_e	effective Poisson's ratio
σ_e	von Mises equivalent stress
σ_{eng}	engineering stress
σ_{true}	true stress
σ_y	yield stress
σ_{yt}	tensile yield stress
σ_{yc}	compressive yield stress
σ_{ys}	shear yield stress
$\sigma_{n,0}$	maximum normal stress in cohesive zone model
τ_{oct}	octahedral shear stress
$\tau_{s,0}$	in-plane maximum shear stress in cohesive zone model
$\tau_{t,0}$	out-of-plane maximum shear stress in cohesive zone model
φ	dilation angle
χ	crack length correction term in MMB calculation
Γ_{SV}	surface free energy between substrate and vapour
Γ_{SL}	surface free energy between substrate and adhesive
Γ_{LV}	surface free energy between adhesive and adhesive

Chapter 1-Introduction

Epoxy resin is a thermosetting polymer which contains one or more epoxy functional groups and is cured to a cross-linked network for many applications. Compared with other thermosetting materials, epoxy resin has many chemical and physical advantages. It displays low shrinkage and few volatiles or by-products are created during curing. It can be cured at a wide range of temperatures resulting in different glass transition temperature. Its curing agents vary from amine to anhydride which can control the degree of cross-link. It is very stable when exposed to many chemical environments and cured epoxy has strong mechanical properties.

However, epoxy exhibits disadvantages such as brittleness and high internal stress due to a highly cross-link structure. Thus epoxy has to be modified to be suitable for industrial applications. The most important modification for epoxy is to improve its toughness and usually epoxy resin is toughened by rubber particles and used in many fields such as structural adhesives, composite materials and encapsulation (Kinloch, Shaw et al. 1983).

The rubber particles normally occupy a volume fraction of between 5 and 30%; the diameter of these particles ranges from 0.5 to 5 μm (Guild and Kinloch 1995). Because of the presence of rubber particles the toughness of epoxy polymer increases significantly, but other important properties of epoxy are not much affected. Therefore the mechanisms of rubber-modified epoxy are important and should be clarified. The implementation of Finite Element Analysis (FEA) modelling is powerful and able to demonstrate experimental observations and predict possible methods to improve epoxy toughness (Guild and Kinloch 1995).

In order to establish a predictive model for rubber toughened epoxy, understanding of the toughness mechanisms is required for more advanced studies. There are two main toughening mechanisms. One is shear yielding, or shear banding, that occurs between rubber particles at an angle of around ±45 º to the direction of the maximum principal tensile stress (Kinloch 1989; Guild and Kinloch 1995). The mechanism of shear

yielding leads to the irreversible hole-growth process in epoxy matrix which can dissipate energy and then contribute to the improved fracture toughness. The other is internal cavitation, or interfacial debonding (Jasiuk, Sheng et al. 1997; Lu, Cantwell et al. 1997), it means rubber particles release their elastic energy through the internal cavitation within particles and epoxy matrix during load, which leads to the local stress within material to change from plane strain to plane stress.

This work aims at developing the understanding of the mechanics of bonding and rubber toughening mechanism when applying epoxy resins as adhesive. Although much work has been implemented for decades regarding the above two fields, there are still too many areas to be resolved. In particular, the failure mode and criterion is still drawing a lot of attention from researchers, and new mechanisms and analysis methods need to be exploited to disclose the nature and properties of the toughened adhesive.

In this work, Double Lap Joints (DLJs) bonded by commercial rubber toughened epoxy (AV119) is investigated. Experiments have been implemented to study the influence of adhesive thickness upon the joints strength. Because this AV119 is a paste adhesive, and the proper bonding process is important and essential. Adhesive users need to understand fracture criteria. The important modes of fracture are mode-I and mode-II; mode-III is generally ignored. Thus the experiments of mode-I, mode-II and mixed mode failure were implemented. It should be appreciated that there are many mixed mode tests available; here Mixed Mode Bending (MMB) was applied to obtain the toughness of AV119 adhesive although MMB is considered as the most successful and efficient method for unidirectional fibre reinforced composite currently (Reeder and Crews 1990). Few researcher exploit MMB test to adhesive-bonded joints so far, thus this is a new area for adhesive users.

In the modern age, finite element analysis is important and essential to establish deep understanding of engineering problem in industry. It is helpful and powerful to obtain details which experiments cannot achieve. The FEA code ABAQUS is applied in this work. As it is well known, many failure criterions have been proposed for joints failure and choosing the most accurate criterion is desirable to every researcher. However, in order to simulate Double Lap Joint successfully and precisely in FEA, the first matter must be taken into account is the material model itself. Because most polymers

including epoxy adhesive are very sensitive to hydrostatic stress, the Drucker-Prager model was chosen to simulate the AV119 properties. Therefore obtaining the true model parameters is an important part of this work. Cohesive zone model (CZM) was chosen as criterion model which was proposed to resolve composite failure in the beginning and is drawing more attention for other applications now. Although CZM is powerful, there are still many unknown areas because of its complicated constitutive law, and currently few researchers use it for adhesively bonded joints directly. In this work, traction-separation law and BK criterion (mixed-mode criterion, see Section 7.2.5.3) of CZM was applied for 3D joint modelling; its six parameters were obtained from experimental test and theory analysis. A technique in FEA, the application of orphan model, was applied to simulate zero thickness cohesive zone layers which represent the real failure situation and crack paths were defined from observation of failure morphology of specimens. It is noted that cohesive zone with zero thickness is able to prevent penetration problem which results in solution problem in FEA package. The influences of CZM parameters and the effects of failure path position to modelling results are discussed as well. However, CZM is still an open area for many applications.

Although above 3D modelling achieved success in simulating the failure of Double Lap Joints, more details can be disclosed by 2D plain strain modelling and associated submodels which is much more accurate than its global models. 2D models with various crack lengths and crack positions were analysed; J-Integral approaches and stress distributions were used to compare the difference between various adhesive thickness joints. Furthermore the principal stress distributions from submodels were extracted to be the load conditions of rubber toughened micromodels.

As it is well known, the toughening mechanism is still an unresolved issue and debated topic; there is no single mechanism which is able to explain all phenomena from the experimental observations of the rubber-toughened epoxy. In this work, 3D micromodel with a certain particle volume fraction was studied; it is noted that the mechanical properties of micromodel is confirmed by the AV119 tensile property. The comparisons of Rubber model, Void model and core-shell model under various load condition were investigated. Specially, various core-shell (Onion) models with respect to different ratio of core radius to shell thickness gave interesting results. Uniquely, the

stress-strain condition and energy distribution of Void model were also disclosed; it should be appreciated that the load conditions of these Void models are derived from the stress field which is ahead of crack tip in submodel. Combined toughening mechanism was exploited through all micromodels. It was found rubber cavitation and shear yielding in matrix play important role to increase the system toughness. The mesh controls (i.e. the combination of sweep and structure mesh control) were used to all micromodels which were partially important for complex geometries, and energy approach was applied to validate the modelling results.

This objective of this work is to integrate experimental observations and finite element analysis using global joint models and rubber toughened micromodels. It aims to present systematic understanding of adhesively bonded joints and toughening mechanisms ahead of the crack tip. It also demonstrates a new analysis method and proposal to the adhesive bonding structure and rubber toughened system.

Chapter 2-Literature Review

2.1 Introduction

The advantages and conveniences of adhesive bonding are well known. Compared with other jointing technologies such as rivets or screws, the adhesive-bonded joints are able to alleviate stress concentrations and improve fatigue strength, distribute load to wider area and provide excellent corrosion resistance against various environments. Furthermore, different materials can be bonded together by adhesive and the mass of adhesive is very small compared to the whole structure. Among many kinds of adhesive, structural adhesives play a very important role in the world, and the epoxy-based adhesive is most popular in structural bonding applications.

Adhesive joints have been applied in many mechanical structures including vehicle manufacturing, and aerospace industry, etc. Although there is a range of chemically different structural adhesives used in many fields, adhesives based on epoxy resins have earned a good reputation due to their high load-bearing characteristics and ease of processing, thus these adhesives are regarded as mainstream products. To investigate the joints strength and stress distribution, finite element analysis (FEA) has been developed to study rubber-toughened epoxy and various adhesive bonded joints (Kinloch and Guild 1996a; Adams, Comyn et al. 1997). Finite element analysis originates from solving complex problems in civil, nuclear and aerospace industries. The high speed development of modern technology including computer science and other fundamental science has allowed FEA to become more powerful to analyse nonlinear and structural problems.

2.2 Adhesion theory and fracture criteria of adhesive-bonded joints

2.2.1 Adhesion theory

The theories of adhesion and wetting phenomena are presented in order to achieve a deep understanding of the experimental procedure. Four main adhesive theories have been proposed to account for the phenomenon of adhesion including a) mechanical

interlocking, b) electrostatic, c) diffusion and d) adsorption theory.

Mechanical interlocking, as its name implies, proposed that adhesion between an adhesive and substrate is primarily dependent on mechanical keying function of the adhesive embedding into substrates irregularly. However, this theory takes no account of the dominant factors which only exist on a molecular level. The electrostatic theory of adhesion is based on the existence of an electrical double layer which crosses the interface, but in most real adhesive examples, this theory does not make a significant contribution to adhesion. The diffusion theory proposes that the adhesion between two phases occurs as the result of intermixing of the two contact substrates at the molecular level. It is obvious that it requires molecules to have high molecular mobility and high degree of compatibility with each other, but in some examples of adhesion adhesive molecules have high molecular weights with low mobility. Thus this theory cannot explain the bonding information such as metals and composites with epoxy or other type of structural adhesive. So far, the adsorption theory is the only one which has achieved more general acceptability and can offer reasonable explanation of the bonding using epoxies. The basic idea of adsorption is that two different materials will adhere together because of surface force interactions between the atoms.

The most important factor likely to influence the strength of an adhesive joint is the ability of the adhesive to wet and spread spontaneously on the substrate surface which can be quantified by the contact angle and surface free energy by Young's equation. The equation of Young is shown as follows:

$$\Gamma_{SV} = \Gamma_{SL} + \Gamma_{LV} \cos\theta \qquad \textbf{(2- 1)}$$

Where Γ_{SV} is surface free energy between substrate and vapour, Γ_{SL} is surface free energy between substrate and adhesive and Γ_{LV} represents the surface free energy between adhesive and vapour. The angle θ means the contact angle between adhesive and substrate. Since a contact angle of zero describes complete wetting and if the interfacial free energy can be ignored, the above equation can be simplified to the follow form:

$$\Gamma_{SV} \geq \Gamma_{LV} \qquad \textbf{(2- 2)}$$

When the surface free energy of the substrate is greater than that of the intended adhesive, the adhesive is able to wet and spread over the surface of substrate

spontaneously and perfectly. Thus surface pre-treatment has to focus on the purpose to make the surface free energy of adherend higher and make the surface free energy of adhesive lower if possible.

Surfaces treatment can be divided into three broad areas which are solvent cleaning, mechanical abrasion and chemical treatment. Solvent cleaning is concerned with the removal of organic contaminates such as greases and oils from the surface because these contaminants will reduce surface free energy and thus result in poor adhesive wetting. The mechanical abrasion is regarded as a process incorporating both physical and mechanical methods without having significant impact on the chemistry of the surfaces. Chemical treatments are an important method specially when preparing aerospace materials such as aluminium and titanium alloys. Using chemical treatments can remove the existing weak and unstable oxide layer and generate a new stable and compatible oxide layer.

Since steel was chosen to use in this work, it is well know that the procedure including simple solvent cleaning and grit blasting is most suitable for the major non-stainless steels. However, it is important that solvent degreasing is prior to abrasive treatment in order to prevent transfer of organic contaminant to the abrasive medium.

2.2.2 Fracture criteria

The failure of materials under load can be yielding dominant or fracture dominant; adhesive joints focus on fracture dominant damage. The failure of adhesive joints usually occurs from cracks within the adhesive, the interface or cracks very close to the interface between bi-materials. The initial cause of failure may be defects in adhesive such as flaw, void, dirty particles and micro crack. There has been much research regarding failure criteria; more and more attention has been paid to this field because it is essential to predict the strength and service life of adhesive joints. In practice, the failure of adhesive joints is not only dependent on materials itself, but also the joint geometry and test condition such as load rate and temperature, thus the fracture of creep and fatigue has been another important field to be investigated for decades.

To resolve the fracture mechanisms of adhesive joints, the energy approach is the most

used which is derived from Griffith's theory; later many works have developed this to the current application to many mechanical problems. The basic proposal of Griffith's energy approach is that fracture occurs and propagates on the consumption of energy dissipation in order to create new fracture surface. This dissipation energy is usually produced by potential energy of load system. Thus the fracture mechanism is turned into assessing the strain energy release rate which is well known as G_c and is defined as follows:

$$\frac{1}{b}\frac{\partial(W_d - U)}{\partial a} \geq G_c \qquad \textbf{(2- 3)}$$

Where W_d is the work done by the external force, U is the elastic energy stored in specimen, ∂a is an increment of crack growth and b is thickness of specimen. G_c consists of any dissipated energy around of crack tip. It should be noted that Eq.2- 3 is based on the assumption of linear elastic fracture mechanics (LEFM), but it has been proved that the above equation is still valid to explain nonlinear and reversible elastic behaviour. Furthermore Kinloch has proposed that this equation is still applicable for hyperelastic rubbery material which has large number of energy dissipation rate inside and outside the region of crack tip (Kinloch 1987a).

The energy release rate is also related to load, then the Eq.2- 3 is expressed as follows:

$$\frac{F_C^2}{2b}\frac{\partial C}{\partial a} = G_C \qquad \textbf{(2- 4)}$$

Where Fc is the load when crack propagation occurs, C is the compliance of system and defined as the reciprocal of load-displacement curve. The important application for this equation is to calculate energy release rate from experiment. For example, combined with simple beam theory, energy release rate of mode-I and mode-II can be obtained from the test of Double Cantilever Beam (DCB) and End Notched Flexure (ENF), respectively. It should be noted that Eq.2- 4 is only valid in the linear deformation region when determining G_c from experiment. The energy approach supports a convenient and effective method to deduce the value of G_c. More importantly, this approach is independent of geometry and failure positions in bonded structure, i.e. this approach is valid whether the adhesive layer is thin or thick and whether the crack occurs cohesively or adhesively (Kinloch 1987a). Some researchers consider the critical energy release rate is one of the intrinsic property of materials and independent of geometry and external factors, but some researchers argue that G_c is combination of internal fracture

energy (G_i) and energy dissipation (G_e) caused by external works (Wake 1982), which is expressed as follows:

$$G_C = G_i + G_e \quad \textbf{(2- 5)}$$

Thus this internal fracture energy represents the intrinsic property of materials and external energy dissipation is due to the plastic and viscoelastic deformation around the crack tip. External fracture dissipation is the main cause of the critical energy dissipation and obviously is dependent on load rate and temperature. However, the behaviour of external energy dissipation should be related to the intrinsic energy release rate.

Another very useful and important fracture mechanism is stress intensity factor K. This parameter was introduced by Irwin (Irwin 1964). Irwin found that, in the case of sharp crack tip in linear-elastic material, stress around crack can be expressed by K which is measurement of the fracture toughness, and fracture occurs as the value of K exceed the critical value. In practice, a general adhesive failure is the combination of various modes, i.e. opening mode, in-plane shear mode and anti-plane (or transverse) shear mode, thus the stress intensity factor, K, normally has three forms to express the stress situation around of a sharp crack tip which is plotted in Figure 2. 1.

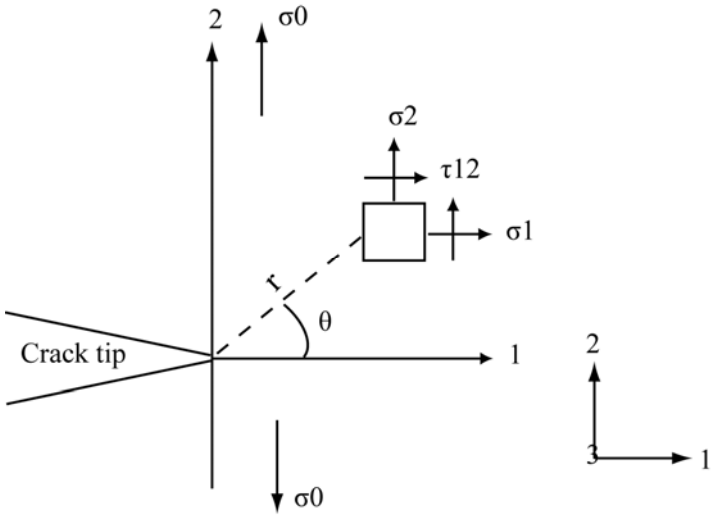

Figure 2. 1 Sharp crack in an infinite and homogenous specimen under uniform load

For the different mode failure, their expressions are demonstrated by Eq.2- 6, 2- 7 and 2- 8, respectively. It is known that failure of adhesive joints is mostly caused by opening force (mode-I) and the magnitude of K_{IC} is smaller than other two failure modes (Adams, Comyn et al. 1997), thus the value of K_{IC} is more useful than other two critical stress intensity factors and the fracture criterion is usually expressed that failure

of joints occurs when the stress intensity factor around crack tip exceeds the critical stress intensity factor in the case of mode-I. It should be noted that σ_{33} is equal to zero in plane stress condition and σ_{33} is equal to ν ($\sigma_{11}+\sigma_{22}$) in the plain strain condition when mode-I load occurs. Furthermore, the plane $\theta=0^{\circ}$ is the principal surface where shear stress is equal to zero. The thickness of the specimen affects the stress intensity factor via two ways, in the thin specimen (plain stress condition) the critical stress factor, K_C, is dependent on the specimen thickness and in thick specimen (plain strain condition) the critical stress factor, K_C, is close to K_{IC} which is a material property. Moreover, the outer surface of thick specimen is subject to the plain stress condition and the width of specimen also affects the K_C. It is also found that the value of K_{IC} varies from the specimen width because in the very thin specimen the stress state varies from plain stress to plain strain near the centre of plane (Kinloch 1987b).

$$\begin{Bmatrix}\sigma_{11}\\ \tau_{12}\\ \sigma_{22}\end{Bmatrix}=\frac{K_I}{(2\pi r)^{\frac{1}{2}}}\begin{Bmatrix}1+\sin\frac{\theta}{2}\sin\frac{3\theta}{2}\\ \sin\frac{\theta}{2}\cos\frac{3\theta}{2}\\ 1-\sin\frac{\theta}{2}\sin\frac{3\theta}{2}\end{Bmatrix} \qquad \textbf{(2- 6)}$$

$$\begin{Bmatrix}\sigma_{11}\\ \sigma_{22}\\ \sigma_{33}\end{Bmatrix}=\frac{K_{II}}{(2\pi r)^{\frac{1}{2}}}\begin{Bmatrix}-\sin\frac{\theta}{2}(2+\cos\frac{\theta}{2}\cos\frac{3\theta}{2})\\ \sin\frac{\theta}{2}\cos\frac{\theta}{2}\cos\frac{3\theta}{2}\\ \cos\frac{\theta}{2}(1-\sin\frac{\theta}{2}\sin\frac{3\theta}{2})\end{Bmatrix} \qquad \textbf{(2- 7)}$$

$$\begin{Bmatrix}\sigma_{13}\\ \sigma_{23}\end{Bmatrix}=\frac{K_{III}}{(2\pi r)^{\frac{1}{2}}}\begin{Bmatrix}-\sin\frac{\theta}{2}\\ \cos\frac{\theta}{2}\end{Bmatrix} \qquad \textbf{(2- 8)}$$

The stress intensity factor is based on the LEFM, but, in practice, there is an unavoidable plastic zone occurring in the vicinity of crack tip. If the plastic zone is small enough, the LEFM is still valid for the condition of small plastic deformation. On the base of LEFM, the energy released rate and stress intensity factor of homogeneous body with crack under plain strain has the following relationship (Kinloch 1987c):

$$G_C=G_{IC}+G_{IIC}+G_{IIIC}=\frac{(1-\nu^2)}{E}K_{IC}^2+\frac{(1-\nu^2)}{E}K_{IIC}^2+\frac{(1+\nu)}{E}K_{IIIC}^2 \qquad \textbf{(2- 9)}$$

For the case of adhesive joints with a crack growing inside the adhesive layer, the above equation is still valid, but if the crack occurs at the interface or very close to the interface, the relationship is very complicated and another theory is necessary to explain it.

The relationship between energy release rate and stress intensity factor is the basis of all LEFM applications, a suitable specimen can be chosen to determine the value of K. However LEFM, as its name implies, has a significant disadvantage that it can only cope with the limited plasticity around crack tip. This limited plastic zone must be small enough compared to the crack size and the general crack structure must be in an approximate elastic condition. In the case of high plasticity, Elastic-Plastic Fracture Mechanics (EPFM) is applied to deal with this problem instead of LEFM (Janssen, Zuidema et al. 2002d).

This first main EPFM concept was proposed by Wells (Wells 1963). He used a strain criterion, i.e. the crack opening displacement (COD) to replace the stress intensity criterion. Later he also proposed crack tip opening displacement (CTOD) as the fracture criterion since the geometry of crack tip is blunt not sharp under EPFM. Thus the critical crack opening displacement can be used to determine the onset of crack. It is found that COD is related to the specimen geometry and plastic constraint which implies it is a rate-dependent parameter. In 1966 Burdekin and Stone proposed the improved COTD using Dugdale strip yield model (Janssen, Zuidema et al. 2002a).

Rice proposed another important EPFM concept, J-Integral, which is based on energy approach for LEFM behaviour materials (Rice 1968). J-Integral can be calculated along any arbitrary path surrounding a crack tip as the specimen is subject to a monotonic load. Plastic behaviour can be considered by nonlinear elastic behaviour under certain constraint (the main constraint is that the load is monotonic and no unloading occurs in any part of body since plastic deformation is irreversible). The total energy of an elastic plate with crack is given as follows (Janssen, Zuidema et al. 2002b):

$$U = U_O + U_a + U_\gamma - F \qquad \textbf{(2- 10)}$$

Where U_o is the total energy before crack which is considered as elastic energy (a

constant), *Ua* is the change of elastic energy caused by crack, *Uγ* is the change of surface energy caused by crack, *F* is the external work during the introduction of crack. The potential energy *Up* is defined as follows:

$$U_p = U_O + U_a - F \quad \textbf{(2- 11)}$$

Then the J-integral is defined as the energy released by unit crack length as follows:

$$J = -\frac{dU_p}{da} = \frac{d(F - U_a)}{da} \quad \textbf{(2- 12)}$$

In the case of a two-dimensional cracked body and nonlinear elastic behaviour, the J-integral schematic is shown in Figure 2. 2.

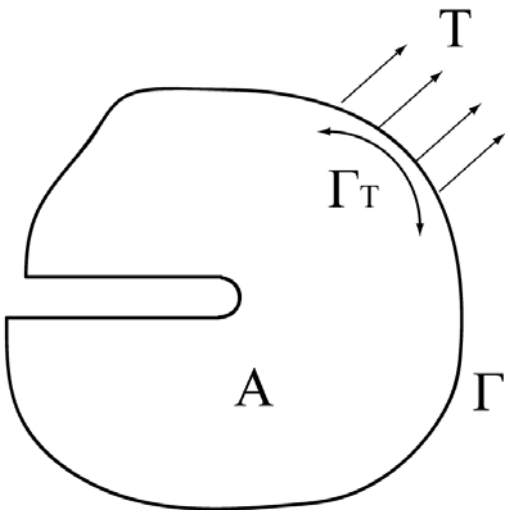

Figure 2. 2 The schematic of J-integral for nonlinear material

The body has surface *A* and perimeter Γ, it is noted that the cracked flank is traction free and is not a part of perimeter Γ, the traction force *T* performs along a part of Γ_T. Thus the released potential energy rate can be defined as follows:

$$J = -\frac{dU_p}{da} = \frac{d}{da}\left(\int_A W dA - \int_\Gamma T_i u_i ds\right) \quad \textbf{(2- 13)}$$

Where *W* is the strain energy density of body, *ds* is the increment along perimeter, T_i is the *i*-th component of the traction acting on the perimeter, u_i is the displacement along the part of perimeter Γ_T.

It is noted that J is equal to *G* defined in LEFM when the material is linear elastic. J-integral is proved to be a path-independent approach which allows the contour Γ to be chosen small enough to just cover the region of crack tip. It is noted that the stress intensity approach in LEFM suggests that the stress distribution around crack tip is the same, thus J-integral can be considered as the extension of stress intensity factor in

EPFM region. Like the critical energy release rate (G_c) in LEFM, J-approach proposes that there is a critical J value which determine the initial crack, thus J is an important fracture criterion in elastic-plastic fracture mechanics. It is known that J-approach is derived from two dimensional cases for simplified reason, thus J calculation varies with plain stress and plain strain. Furthermore, in practice, J-approach is still valid in three dimensional cases but J is not path-independent any more and highly localised and J value varies along the crack front. It should be noted that J-approach is based on two important assumptions that load is monotonic and material is nonlinear elastic and therefore deformation is reversible. However, in practice, plastic deformation is irreversible and unloading maybe cause plastic deformation, thus some restrictions must be applied to J to make it valid and meaningful.

In the 1970s, the relation between J and COTD (δ_t) was established; later simpler relation using the Dugdale strip yielding model was proposed as follows (Janssen, Zuidema et al. 2002c):

$$J = M\sigma_y\delta_t \qquad \textbf{(2- 14)}$$

Where M is a coefficient and a function of Young's modulus and yield stress (Tracey 1976), σ_y is the yield stress ahead of the crack tip and δ_t is the crack tip opening displacement. The above equation becomes Hutchinson's proposal when M is equal to 1. Because Dugdale model does not refer to the crack length a Eq.2- 14 is valid in both cases of LEFM and EPFM.

2.2.3 Cohesive zone model and its applications

Linear elastic fracture mechanics (LEFM) neglects plastic zone ahead of crack tip, but this plastic zone is notable in many ductile materials. Furthermore, LEFM predicts that stress ahead of crack tip is infinite. Thus Barenblatt proposed a cohesive zone ahead of the crack tip where the magnitude of stress is limited to physical level (Barenblatt 1959). Barenblatt also describes fracture as a material separation process along the interface and used it to predict the mode-I fracture. It has been proved that cohesive zone model is suitable for other mode fracture problems (Davila, Camanho et al. 2001; Li, Thouless et al. 2006).

The cohesive zone model was originally applied to concrete composites and interface

fracture. Later cohesive zone model is used to model the behaviour of interfaces of polymer-based composites, adhesively bonded joints and other similar conditions where strength and failure of interfaces is most of interest. This method is based on energy principle and Traction-Separation law generally. In the typical application, the cohesive zone represents a single layer which is an interface between two surfaces in isotropic materials. The cohesive zone thickness can be a limited thickness or zero thickness according to the real conditions. In the Traction-Separation law, there are five model parameters: penalty stiffness k, maximum stress σ_{max} and corresponding initial displacement δ_0, failure displacement δ_f and the fracture toughness *G* (see Figure 2. 3). When load starts, stresses increase along the path of OA which is defined by the penalty stiffness k. The crack initiates from the point A where stress reaches the maximum value, then softening occurs along the path AB, the descent from A to B can be different, but it was proved that it is of lower relevance (Tvergaard and Hutchinson 1993). Generally only three parameters including k, σ_{max} and *G* are required and used in the cohesive zone model.

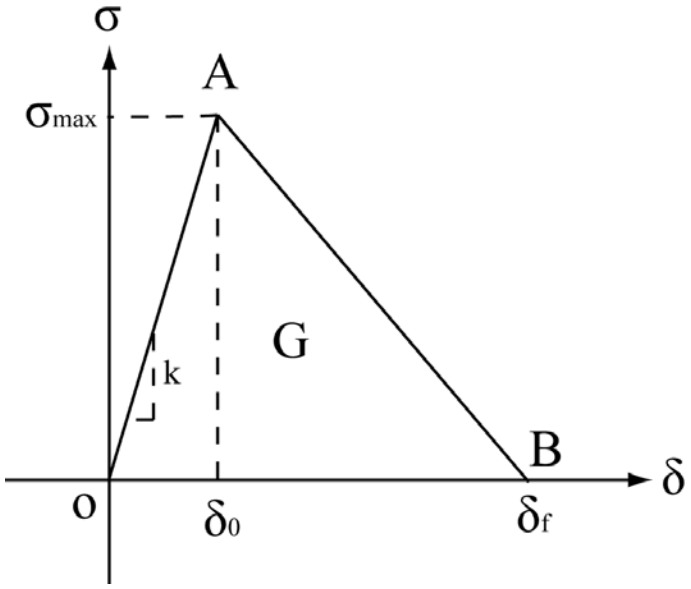

Figure 2. 3 The illustration of traction-separation law

In FEA, cohesive zone is represented by cohesive elements which connect top and bottom surfaces of adjoining materials. Generally this connection is achieved by interface constraint or sharing common nodes. During simulation, cohesive elements hold the surfaces together until the stress in any cohesive element reaches the critical maximum value to initiate the crack and then complete the failure (i.e. point B in Figure 2. 3).

Cohesive zone model is a powerful technology to simulate the initial crack and crack propagation along the interface between materials. Researchers determine cohesive zone parameters in several ways. In the beginning researchers assumed that the values of parameters depend on which value can produce the best results compared with the experimental results. Later some researchers, like Yang et al., determined these parameters via DCB or ENF experiments but needed to compare their results with tests of bulk materials (Yang, Thouless et al. 2001). This typical approach also was implemented by Andersson and Stigh later (Andersen and Stigh 2004). Lijedahl and his co-workers used the cohesive zone for their mixed-mode flexure (MMF) simulation via determination of the initial traction stress from the curve of load-displacement of MMF test and then determining the fracture energy by correlation of the predicted failure load with the experimental failure load (Liljedahl, Crocombe et al. 2006).

Many researchers assumed interfacial stiffness i.e. the penalty stiffness for cohesive layer on the base of experience (Blackman, Hadavinia et al. 2003; Diehl 2008). They argued that the stiffness should be strong enough to avoid any penetration occurring between interfaces which exhibit compliance of cohesive element before the onset of failure. Lately Turon et al. proposed a mechanical consideration about penalty stiffness and an equation between the properties of adjacent sub-laminate and the interfacial stiffness was established (Turon, Davila et al. 2005). They considered that cohesive interface should have adequate stiffness in order to connect two neighbouring layers strongly, however the stiffness of cohesive interface should not be too hard which would cause numerical problems such as spurious oscillation in the FEA solution.

The spurious oscillation problem was also investigated by Schellekens (Schellekens and de Borst 1993). Because the stiffness of cohesive zone is introduced into composite, it is obvious that cohesive interface definitely contributes its compliance to global property and this contribution should be small enough i.e. the interface has enough stiffness. Thus the approach of effective Young's modulus was applied to determine the appropriate stiffness of cohesive interface (see Section 7.2.5.1); in addition, the relationship between cohesive interface and the bulk materials was established too. However this relationship was derived from composite, and in Turon's works, cohesive zone is only assumed to be one layer which is located between two

sub-laminates whose properties including mechanical and geometrical characters are exactly the same. Thus, when cohesive zone model is applied in other geometry, the original equation from Turon's work has to be modified to be suitable for the new condition.

2.2.4 Adhesive joint tests

In practice, the users of adhesive-bonded joints are always interested in the strength, durability and failure mode of joints. Researchers also consider how various factors affect the joints, such as the surface treatment, joint geometry, material properties, load conditions and environmental impact. Thus many test methods have been developed in order to obtain information to instruct the design and manufacture of adhesive joints. Failure mode is another interesting field, since the failure mode could occur inside adhesive, close to interface or at the interface. In some cases failure may happen inside adherend when composite adherends are used. Adhesive users normally desire cohesive failure if the failure cannot be avoided since the interface failure is often very sudden; this failure is usually caused by stress concentration when load goes beyond the adhesive strength, and localised defect gives rise to cohesive failure. Adhesive failure may be caused by inadequate surface treatment since interface bonding is not strong enough to endure load.

Adhesive joints are tested under different load conditions, direct-tension, tensile-shear, torsion, cleavage for thick adhesive layer and peel for thin adhesive layer are the most common test methods. In practice, the adhesive joints generally are subject to mixed load in above conditions. Adhesive joints perform much better under the load of shear and compression than opening force such as peel and cleavage. Thus people do their best to avoid use of adhesive joints under opening load in order to obtain the maximum joint strength.

According to industrial applications, several geometries are chosen to obtain the strength and other information of joints. Single lap joint (SLJ) may be the easiest method because it is convenient to manufacture and test, but high stress concentration focus on the free ends of joints and peel stress is harmful to decrease the joint strength. Another similar shear test is Double Lap Joint (DLJ) whose geometry reduces the

bending moment and peel stress, but these stresses could be increased when thick adhesive is applied (see Figure 2. 4). Compared with Single Lap Joint, Double Lap Joint can be used in a wide range of applications. Both SLJ and DLJ have stress concentration at the free ends of joint, but fillets or a scarf can be introduced to reduce those effects. Butt joint is suitable for testing adhesive under torsion force which eliminates peel and bending stress. In order to obtain correct geometry, two butts have to be adhered to each other in the same axis, thus more care has to be paid to this joint in manufacture. Scarf joints can eliminate the peel and bending stress if correctly designed and has higher strength than SLJ and DLJ. It should be noted that adhesive has slightly different performance in the forms of joint specimen and bulk specimen. This is because the adhesive used in joint specimens is restricted by adherends, the shear strain cannot be developed freely, but both specimens should have the similar property under opening load since adherends do not confine adhesive in this direction. Furthermore, the joint strength is much different from bulk specimen when failure occurs at interface.

Fracture criterion has been developed for many years, the energy release rate is the most important approach to investigate adhesive joint. Many test methods has been proposed to determining G_c value under different failure mode or mixed failure mode. Some methods are already accepted as standard tests. Generally Double Cantilever Beam (DCB) test and peel test are the main approaches to determine mode-I energy release rate; End Notched Flexure (ENF) and 4-point End Notched Flexure (4p-ENF) are used to obtain mode-II energy release rate. Mode-III failure can be ignored since this failure is not important in practice. More importantly, adhesive failure combines mode-I and mode-II in most cases, thus this failure mode is the most complicated condition and many approaches have been proposed to obtain real mixed mode energy dissipation.

It is noted that energy release rate will vary with the geometry of the joint. The adhesive thickness is seen to control G_c. For a thin adhesive, the tensile stresses will increase and this will in turn increase the size of plastic zone. For thick adhesive the plastic zone size may be constrained, so optimised fracture energy G_c may not be found. However, if the adhesive thickness is very thin, the size which the plastic zone can achieve will be limited, and then G_c will decrease. It is known that G_{Ic} and K_{Ic} have their maximum values when the size of the plastic zone is equal to the thickness of the

glue line, and because of the constraining effect of the adherends these values can exceed those measured in the bulk adhesive (Dillard and Pocius 2002).

2.3 Finite element analysis of adhesive joints

2.3.1 The background of analysis of lap shear joints

Adhesive bonded joints have been used widely in many industries. The applications of adhesive cover aerospace industry, mechanical structures, architecture and wood industries etc. People have been interested in the stress analysis of the adhesive joint for more than a half century. Firstly, Goland and Reissner developed an analytical model for single-lap joint (Goland and Reissner 1944), so the stress distribution of the single-lap joint was formulated in line with the material properties and geometries of joints. As results, the joint edge moment was set up and transverse normal stress was found near the ends of the overlap.

Later the Goland and Reissner's analysis was developed by Hart-Smith (Hart-Smith 1973); in this model the adherend was considered as an elastic beam and the stress distribution can be calculated for both linear elastic and elastic-plastic adhesives. Oplinger considered the geometrical nonlinear effect to overlap range and developed a more realistic beam model (Oplinger 1991). Chen and Cheng first applied the variational principle of complementary energy to analyse the stress distribution in single-lap joint (Chen and Cheng 1983), and they found more realistic stress distributions because of further understanding of the stress distribution along the thickness of the adhesive and satisfied boundary conditions applied in the free ends. Barthelemy et al developed a two-dimensional finite element analysis using eight-node isoparametric element and proved this element is accurate compared with their experimental data (Barthelemy, Kamat et al. 1984). However, all those previous studies focus on perfectly bonded joints; the mechanism of imperfectly-bonded joints is still unclear. It is known that the aerospace industries must consider the safety and reliability of imperfectly-bonded joints. Firstly Baik and Thompson created a quasi-static spring model to study the interface of the imperfectly-bonded joints (Baik and Thompson 1984). Later Margetan et al developed this model to represent the ultrasonic reflectivity of an imperfectly-bonded interface in crack studies (Margetan, Thompson et al. 1988). Furthermore, this spring model is used to predict the

environmental degradation by Lavrentyev and Rokhlin (Lavrentyev and Rokhlin 1994). But all these works fail to predict the strength change when joints are debonding which is important for the safe use in some industries.

Due to the disadvantages of classical methods, finite element modelling of adhesives was developed to predict stress distribution in adhesive-bonded joints. The finite element analysis is able to simulate a wide range of complicated adhesive bonded joints. A typical geometry and model mesh of single and double joints are shown in Figure 2. 4. The parameter l_b represents the outer adherend length, $2C_b$ represents the overlap length, t is the thickness of the adhesive layer, and t_b is the thickness of the adherend. It is noted that fine mesh is applied in adhesive layer in order to obtain more accurate results because of the stress singularity.

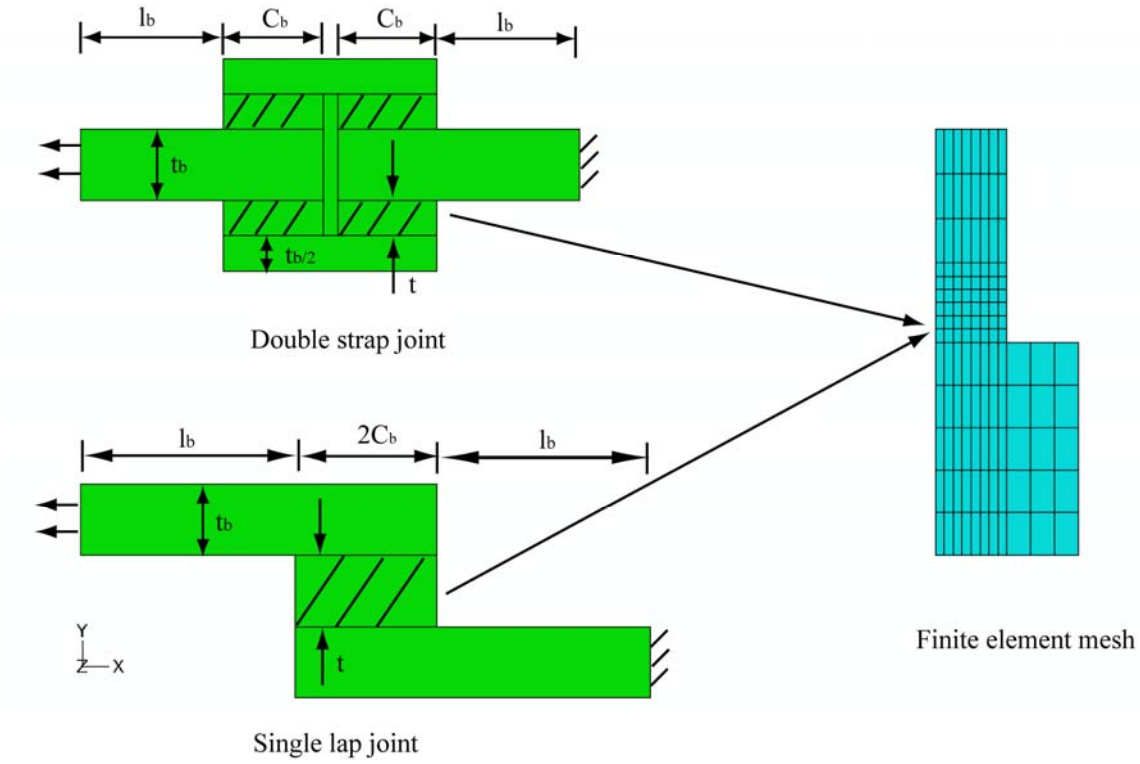

Figure 2. 4 The geometry and finite element mesh for Single Lap Joint and Double Strap Joint (Yen 2000)

Both single-lap joint and double-lap joint are used widely in many works. Single-lap joints are easy to manufacture and test, but significant moment force exist at overlap range. Double-lap shear joint overcome this disadvantage since the load eccentricity is eliminated and peel stress in the adhesive is reduced. Stress analysis for single-lap shear joint has been presented in a lot of studies; the double-lap shear joint is very useful in the study of normal deformation of adherend and adhesive plasticity.

2.3.2 Finite element analysis for adhesive bonded joints

2D finite element analysis is commonly used to study the stress distributions in Single Lap Joints. Figure 2. 5 shows the schematic of mesh refinement across the bonded area in different models.

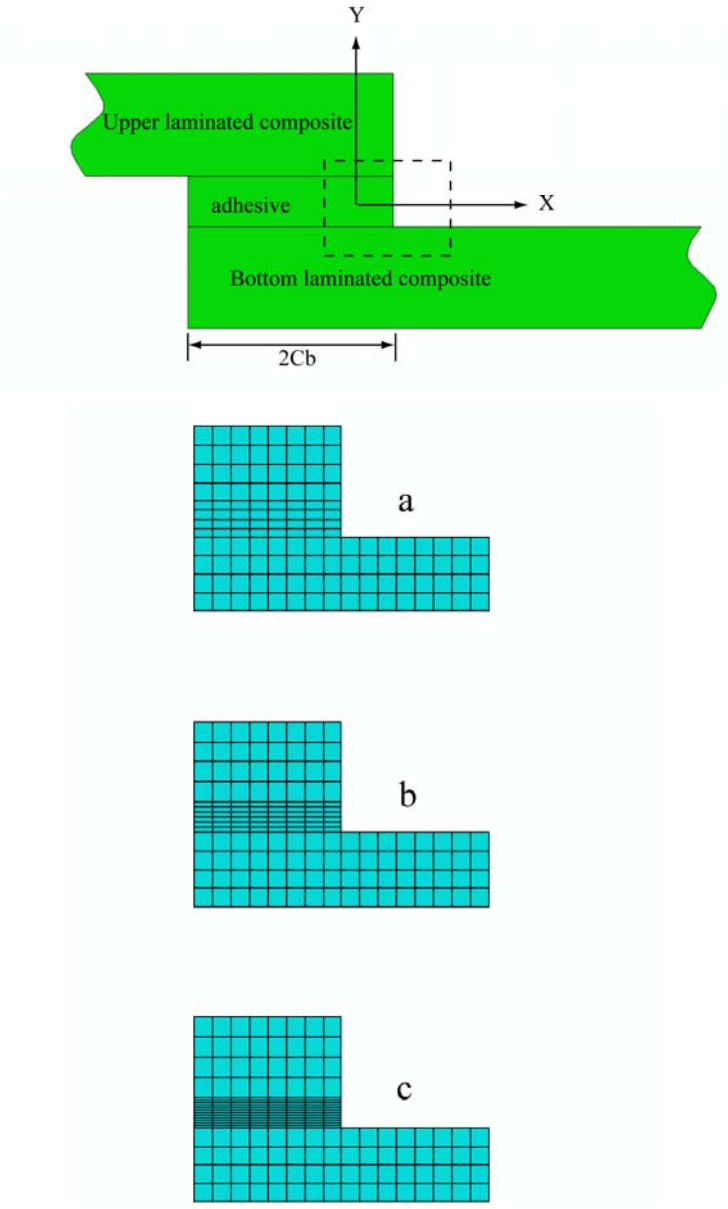

Figure 2. 5 Schematic of mesh refinement across the bond layer at the right overlap end (Li 1999)

Figure 2. 6 compares the stress distribution results of Single Lap Joint from linear finite element analysis with three classical methods. The linear finite element analysis does not take into account the change in shape under load. It is noted that all stresses are normalised by the uniform tensile load (P). It is clear that the transversal stresses decrease from the centre of the overlap to free edge for all three classical methods, but

sharply increase near the free edges of the overlap. It is known that the classical results cannot represent real stress distribution at end of overlap due to stress singularity and their one-dimensional approach. It is found that the classical results are close to the finite element result because all classical methods assumed the geometrical linearity which is similar to the finite element analysis. The finite element analysis shows both peel and shear stresses decreases sharply to near zero at the free edge.

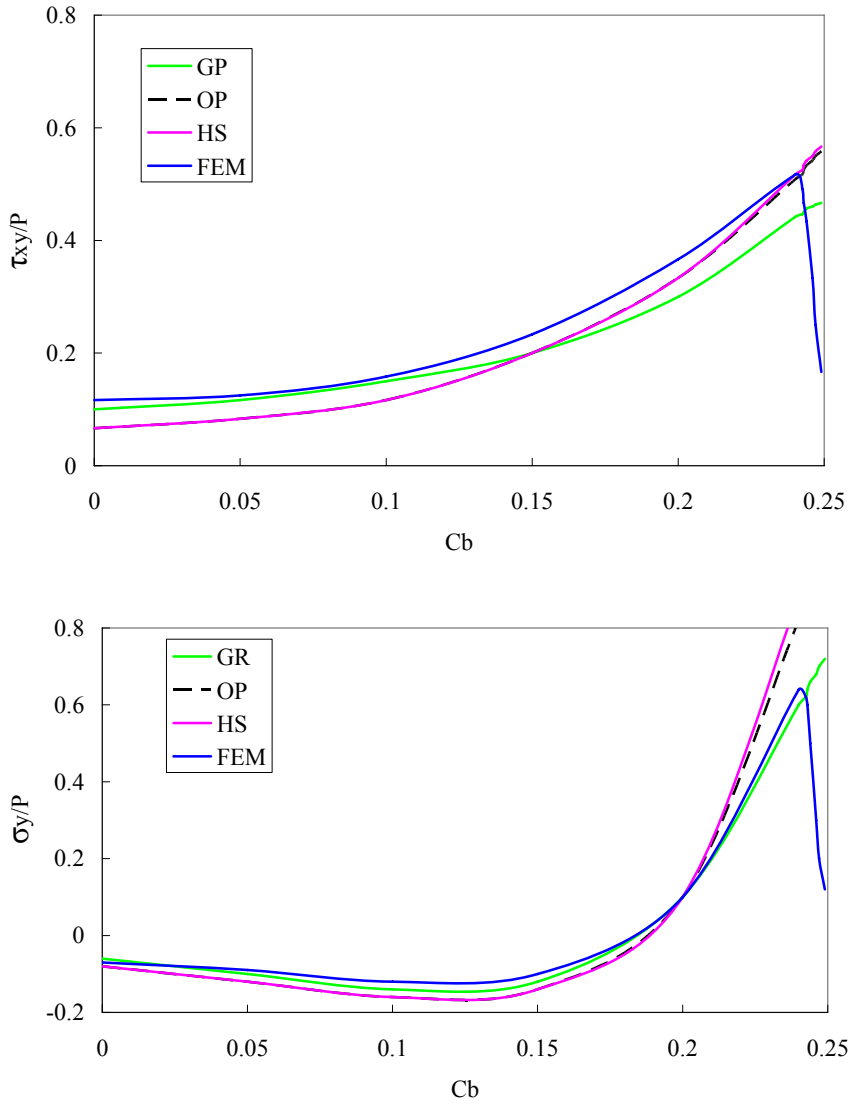

Figure 2. 6 Adhesive stress distributions obtained from the finite element analysis with linear geometry (uniform loads) (GR: Goland and Reissner; OP: Opliner; HS: Hart-Smith; FEM: Finite Element Analysis) (y=0) (Yen 2000)

It is known that another commonly used structure is Double Lap Joint which is applied especially in aerospace industry. In the FEA modelling of Double Lap Joint (DLJ), only a half adhesive joint is chosen to study because of the geometrical symmetry.

Adhesive joints are usually simulated as rigid joints, semi-rigid joints, spring joints, or other equivalent approaches. Yen compared the results of DLJ using finite element method with the results of classical methods (Yen 2000), it is found that the finite element results are close to the results of Oplinger's theoretical method as shown in Figure 2. 7. It should be noted that the mesh dependency is not clear in Yen's work.

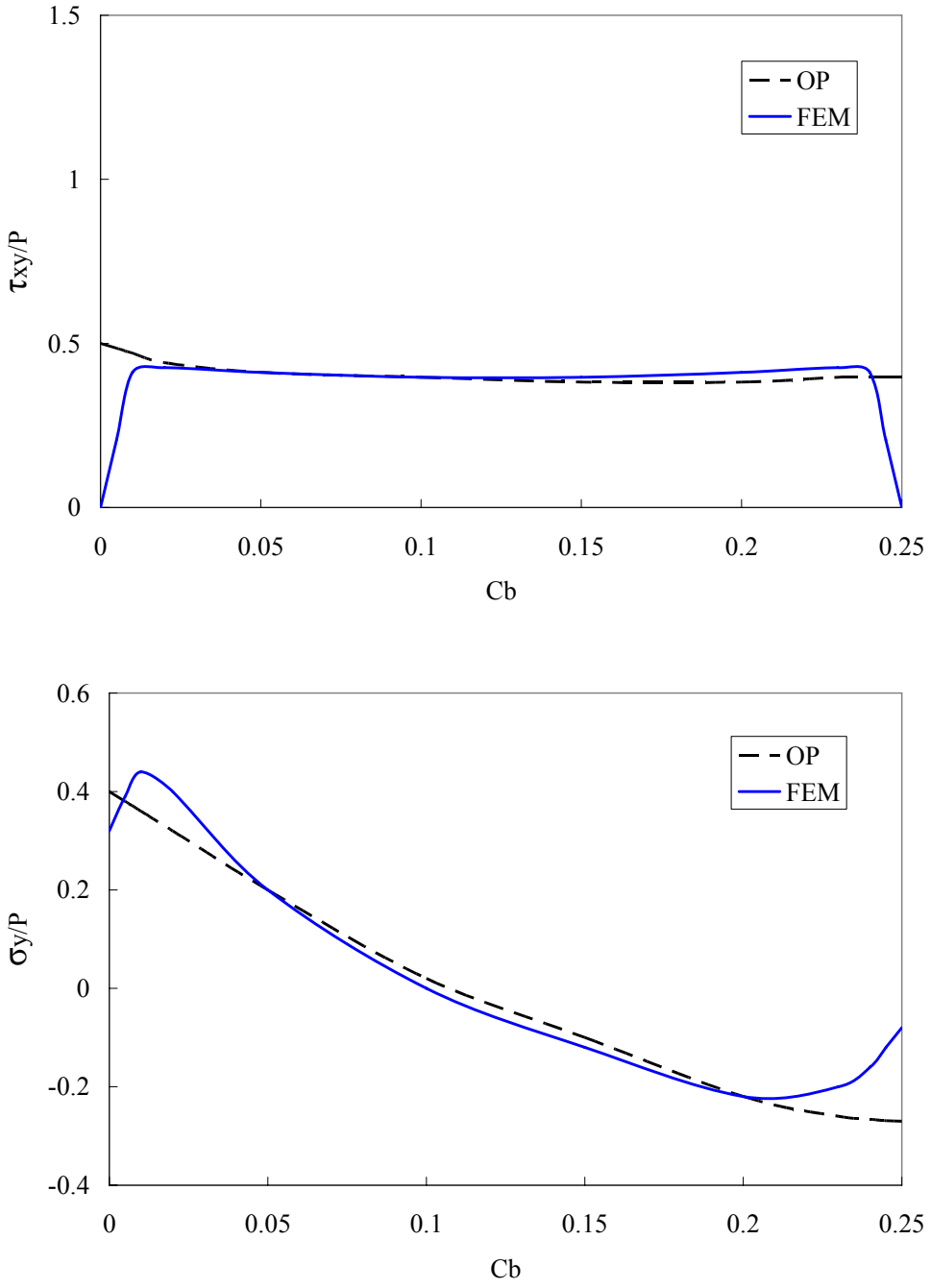

Figure 2. 7 Adhesive stress distributions obtained from the finite element analysis compared with TJOITNL program (OP: Opliner) (Yen 2000)

Wu and Crocombe simulated Double Lap Joints by using 2D continuum model,

simplified beam model and hybrid model.(Wu and Crocombe 1994). Beacsue of geometrical symmetry, only half Double Lap Joint was modelled. The DLJ scheme and models used by Wu and Crocombe are shown in Figure 2. 8. Both adhesive and adherend were simulated by 4-node isoparametric elements in 2D continuum model; adherends were simulated by beam elements and adhesive was simulated by 4-node isoparametric elements. They found both 2D continuum model and simplified beam model show very similar results except some areas with complex deformation such as the corner of joint. Thus they used hybrid model to obtain more accurate results. Using the hybrid model, adhesive was still simulated by 4-node isoparametric elements and most adherends were simulated by beam elements, but the corners of joint were simulated by quadrilateral elements.

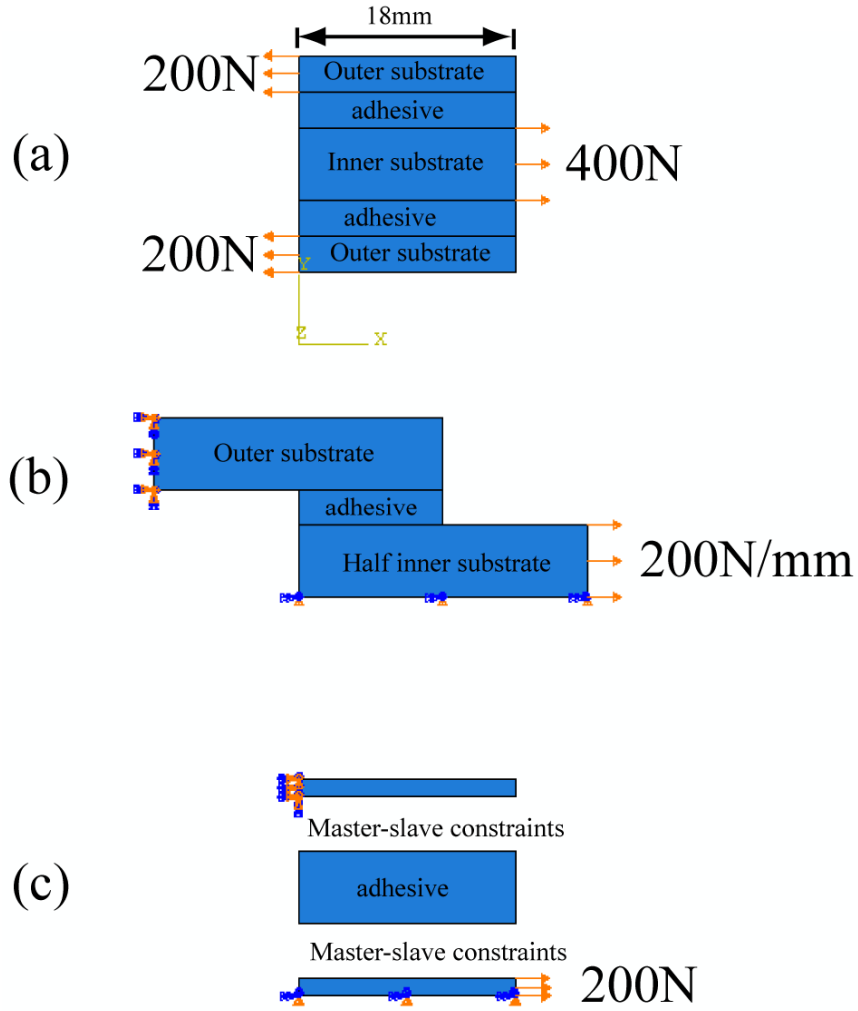

Figure 2. 8 Double Lap Joint and the boundary conditions used for different modelling schemes ((a) overlap area of Double Lap Joint, (b)two-dimensional continuum modelling, (c)simplified beam modelling)) (Wu and Crocombe 1994)

Later Sawa and Suga applied an elastic-plastic finite element method to predict the

stress distribution and strength of DLJs (Sawa and Suga 1996). More recently Xiao et al predicted the in-plane stiffness response in DLJ (Xiao, Foss et al. 2004). His method was first derived from a model which considered the shear deformation in adhesive layer and then was extended to other simplified models. They also analyzed the base finite element model using shell/solid element and then studied the simplified finite element model by tiebreak-contact model and line rigid model. These three models are shown in Figure 2. 9, Figure 2. 10 and Figure 2. 11, respectively.

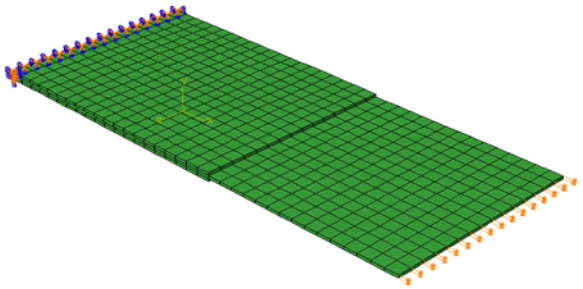

Figure 2. 9 Basal shell/solid finite element model for DLJ (shell elements are used for adherend and solid elements are used for adhesive) (Xiao, Foss et al. 2004)

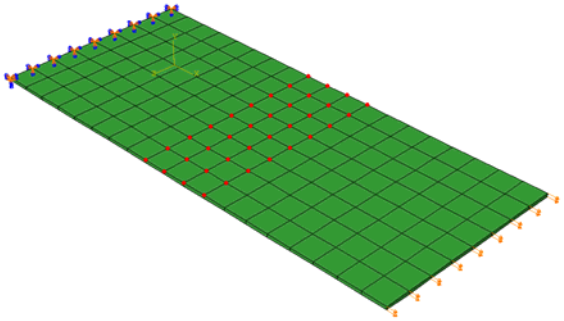

Figure 2. 10 Tiebreak-contact model for DLJ (adhesive bond is simulated by tied contact between nodes and surface) (Xiao, Foss et al. 2004)

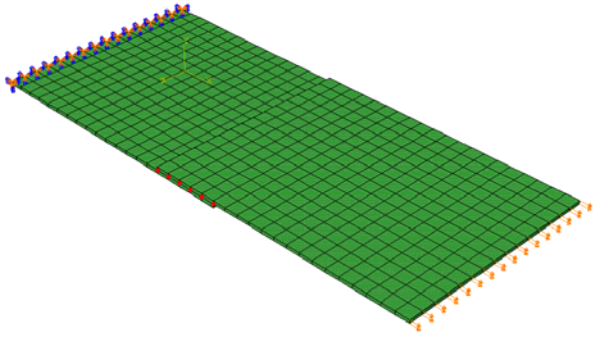

Figure 2. 11 The line-rigid model for DLJ (adhesive bond is modelled by a line of rigid links) (Xiao, Foss et al. 2004)

In FEA model, monitoring energy balance is a helpful tool to check the simulation results. In the term of energy balance of model, there is a relation between various

energies defined as follows:

$$IE = SE + PDE + CDE + ASE \quad \textbf{(2- 15)}$$

Where *IE* is the total internal energy, *SE* is the strain energy caused by elastic deformation, *PDE* is the plastic dissipation energy caused by plastic deformation, *CDE* is the creep dissipation energy caused by elastic-viscous or creep deformation and *ASE* is the artificial strain energy caused by the hourglassing force in reduced element or transversal shear deformation in beam and shell element. For example, when normal plain strain element is used for structural material, *ASE* and *CDE* should maintain zero. Thus only *SE* and *PDE* are contributing to the total internal energy.

2.4 Rubber toughened epoxy and its toughening mechanisms

2.4.1 Main toughening particles

There are three main particle toughened epoxy systems (Riew and Kinloch 1996). Liquid rubbers were the first and widely applied to epoxy resin; these rubber particles are easily mixed into resin and dispersed well, but the main disadvantage of liquid rubber is that toughened system has decreased thermal properties. Later solid rubbers and thermoplastic were applied to epoxy resins. The Tg (glass transition temperature) and thermal properties of toughened system are not decreased too much, but the distribution of particles to resins is more difficult than liquid rubbers to resins. Besides, undesired solvent is introduced into resin since solid particles need to be dispersed in solvent before use. Both rubber particle and thermoplastic particle usually have functional groups which are able to react with epoxy matrix, and the system enhances its toughness when the particles separate from matrix, i.e. phase separation process.

It has been found that the properties of separated phase depend on the competition between the phase separation rate and matrix reaction kinetics (Wise, Cook et al. 2000; Delides, Hayward et al. 2003). Thus the toughening effect is related to the curing process and particles' chemical properties. It is found that the strength of particle toughened epoxy and thermal properties decreased when particles do not separate from matrix. Currently, more attention has been paid to core-shell rubber (CSR). CSR is a kind of latex which consists of hard core and soft shell, the current technique is able to control the shell thickness and core size which allows fine control of particle chemical

and physical properties. These toughening particles do not reduce the thermal properties of epoxy resin and it is easy to control the particle morphology. For some special applications, polyorganic siloxane is chosen to modify epoxy resin. Siloxane has functional group to react with epoxy and has unique properties such as very low surface energy, thus epoxy resin toughened with siloxane has a hydrophobic surface which increases the anti-friction properties of toughened epoxy resin (Yorkgitis, Tran et al. 1984).

2.4.2 Main toughening mechanism

The toughness property of resin system can be increased by simple mixing rubber particles, thus the toughening mechanism has been studied for many years. The rubber toughening mechanisms mainly include particle cavitation (or cavitation resistance), void growth, yielding banding and crazing in matrix. J.N. Sultan and F.J. McGarry firstly used rubber particles to toughen epoxy and increased the toughness of epoxy resin significantly in 1970s (Sultan and McGarry 1973). They proposed that matrix shear yielding and crazing are the main toughening mechanism. Bascom et al. firstly observed the particle cavitation from rubber toughened epoxy (Bascom, Cottington et al. 1974). Kunz and Beaumont proposed that the increased toughness is due to the crack bridging (i.e. the tearing of elongated rubber particles which is behind the crack tip) by rubber particles (Kunz and Beaumont 1981). They suggested that the enhanced fracture is due to the extra energy required to break the rubber particles, but they did not take the matrix into account. It has been shown that the toughness depends on the matrix itself; lower cross-link matrix often has higher toughness. Evans et al. proposed microcracking mechanism which suggests microcracks cause tensile yielding and significant tensile deformation because of the presence of rubber particles (Evans, Ahmad et al. 1986). Then microcracks reduce the modulus around the crack tip thus reduce the stress intensity. However this mechanism cannot explain the plastic deformation.

Later Yee and Pearson developed the theory for the toughening mechanism which is applied currently for rubber toughened polymer (Yee and Pearson 1986a; Yee and Pearson 1986b). They found that rubber particle cavitation followed by void growth reduces the stress constraint around the crack tip then triggers more yield banding in

matrix; both processes cooperate to develop the toughness of material. Since rubber cavitation creates voids and the bond force between rubber particles and epoxy matrix is generally weak, some researchers doubt the role of rubber cavitation. Thus, Kinloch et al. proposed that rubber cavitation is not important (Kinloch, Shaw et al. 1983). Later Bagheri and Pearson found that rubber cavitation does not contribute to the epoxy toughness when they used micro-voids to toughen low crosslink epoxy (Bagheri and Pearson 1996); however the influence of rubber cavitation in high crosslink epoxy toughness is not clear.

At present, many researchers are still studying the toughening mechanism and propose new quantitative tools to predict the toughness. However, there is no unique mechanism which is able to account for all phenomena of a toughened system, each mechanism has its own advantages and disadvantages. Currently, the combined mechanism has to be applied to explain the results of rubber toughened system. There are several factors contributing to the toughness in a toughened system as described in Chapter 9.

2.5 Finite element analysis of microstructure model

In order to obtain deep understanding of toughened system and design new materials structure, researchers have been paying more attention to the microstructure morphology and relation between rubber particles and polymer matrix. A typical fracture surface of toughened resin is shown in Figure 2. 12. It is obvious that rubber spheres are separated inside matrix. Based on experimental observation, the finite element analysis has been successfully applied to study the toughening mechanics and stress distribution of rubber toughened polymer; so far, there are several main models which are based on different assumptions. These models mainly include axi-symmetric model, improved cylinder model, single spherical model, statistical spherical model and three-dimensional model.

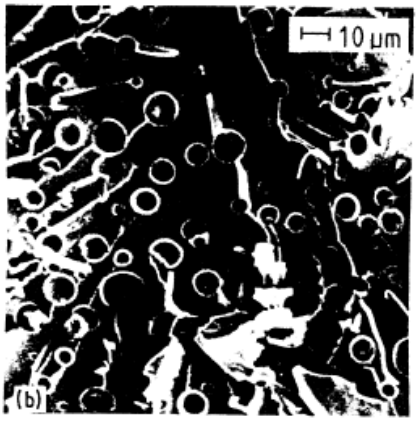

Figure 2. 12 Fracture surface of polymers modified with rubber spheres (Guild and Young 1989)

2.5.1 The axi-symmetric (cylinder) model of particle-filled material

The axi-symmetric model is simulated as an array of periodic cylinders (Guild and Young 1989; Steenbrink and Van der Giessen 1997); each cylinder consists of one rubber particle. The structure of axis symmetric model and the meshed model are shown in Figure 2. 13.

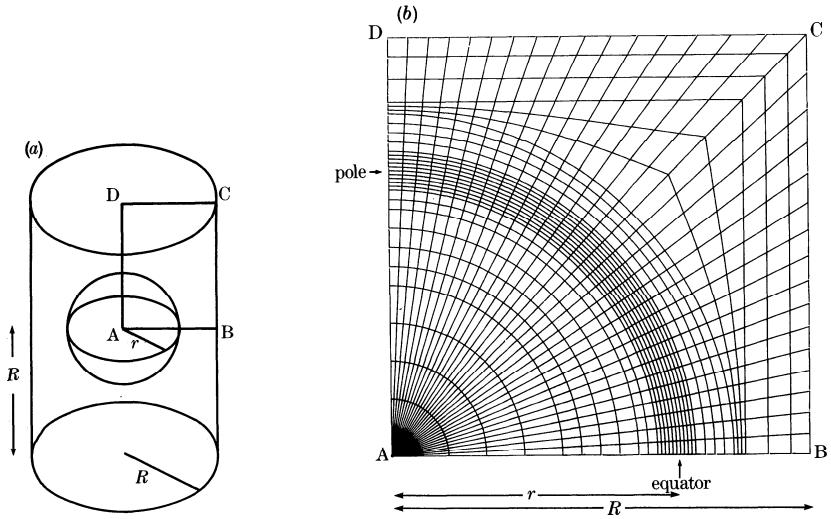

Figure 2. 13 Axis-symmetric model of rubber-toughened epoxy and its finite element mesh (Davy and Guild 1988)

In this model, each cylinder has equal height and diameter and can be represented by the plane ABCD using axis-symmetric element (Kinloch and Guild 1996b). It is noted that y axis is the axis of symmetry. When the displacement load is applied at the CD line, constraint equations are used to the line of BC to maintain it straight and parallel to its original shape; meantime, the lines of AB and AD are fixed by symmetrical

boundary conditions because they are the sides of the symmetry of the cylinder. 8-node axi-symmetric elements are applied in this model. This model predicts the Young's modulus for both hard and soft particles toughened system and has a good agreement with experimental results. However, the predicted values of Poisson's ratio from glass bead toughened epoxy is lower than experimental results from literature (Kinloch and Guild 1996b). This may arise from the assumptions used in the model.

2.5.2 The improved cylinder model

The typical cylinder model assumed that the array of particles in latitudinal direction is different from that in longitudinal direction; it means that the distance between neighbour particles from the same layer is different from distance between the neighbour particles from different layers. Thus the particles in the typical cylinder model are not uniformly distributed and this model cannot present the overall isotropic behaviour of material. Thus Wang and Lee proposed an improved cylinder model and determined the mechanical properties and stress concentration factors for the rubber-toughened system (Wang and Lee 1999).

The structure and distribution of improved cylinder model used by Wang and Lee is shown in Figure 2. 14. In this model, the position of next layer is changed such that the distance between the centres of neighbour particles is set to the value of 2b, so the height of each prism is set to 0.82b, and then each prism can be modelled as a cylinder. The advantage of this improved cylinder model is the distance between every neighbour particle is identical. In order to match the compatibility condition of displacement between all layers, the bottom and upper surfaces must be maintained as plane in the simulation.

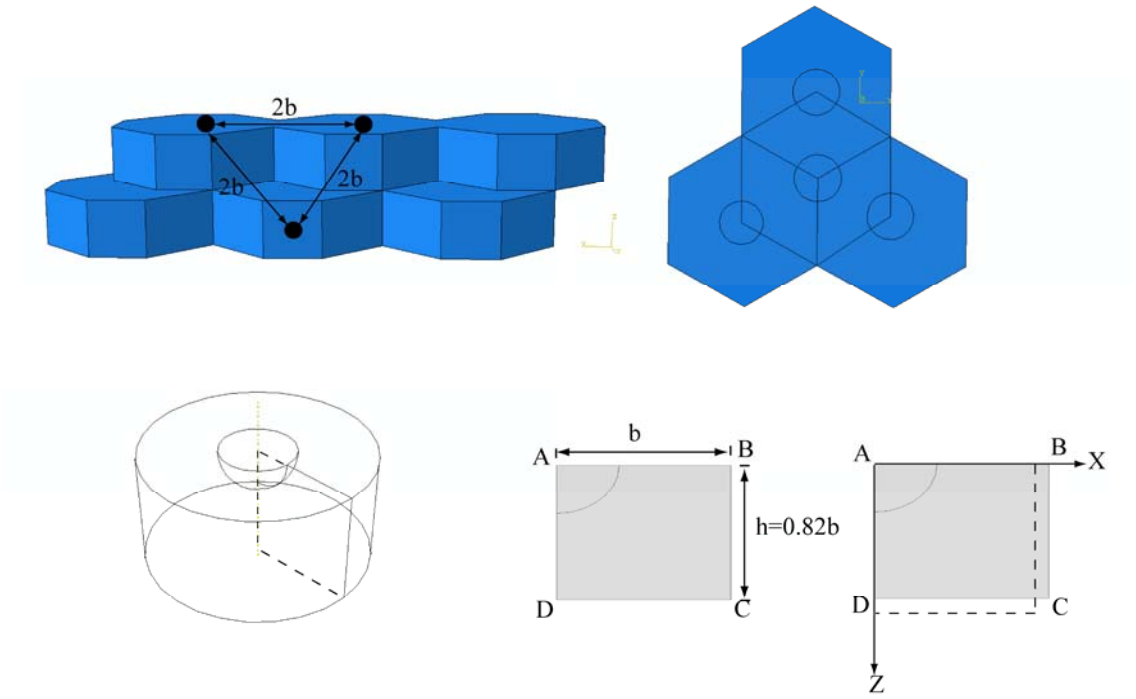

Figure 2. 14 The improved cylinder model (Wang and Lee 1999)

The comparison between improved cylinder model and experiment are shown in Figure 2. 15 and Figure 2. 16. It should be noted that V_f represents the volume fraction of rubber particles in matrix; Ee/E is normalized effective Young's modulus and ν_e/ν is normalized effective Poisson's ratio; Ee and ν_e can be calculated from effective stress (σ_e) and effective strain (ε_e) which are shown at following equations (Chen and Mai 1998b):

$$\sigma_e = \frac{1}{V_\Omega}\int_{V_\Omega}\sigma dV \qquad \textbf{(2- 16)}$$

$$\varepsilon_e = \frac{1}{V_\Omega}\int_{V_\Omega}\varepsilon dV \qquad \textbf{(2- 17)}$$

Where V_Ω is the cell volume. It is noted that effective stress and strain are obtained by averaging the local stress and strain in the cell.

It can be seen that the results from improved cylinder models using both low bulk modulus and high bulk modulus for particles agree well with the experimental results.

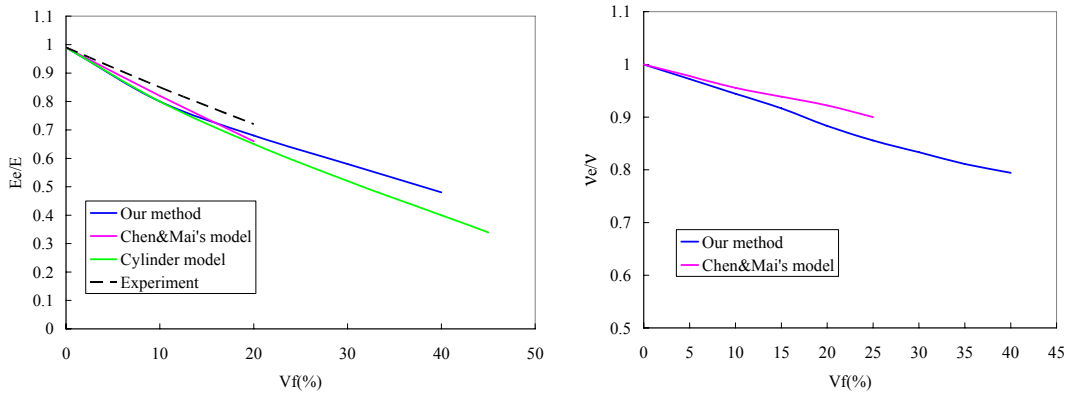

Figure 2. 15 Young's modulus and Poisson's ratio of materials with low bulk modulus rubber particle or void (Wang and Lee 1999)

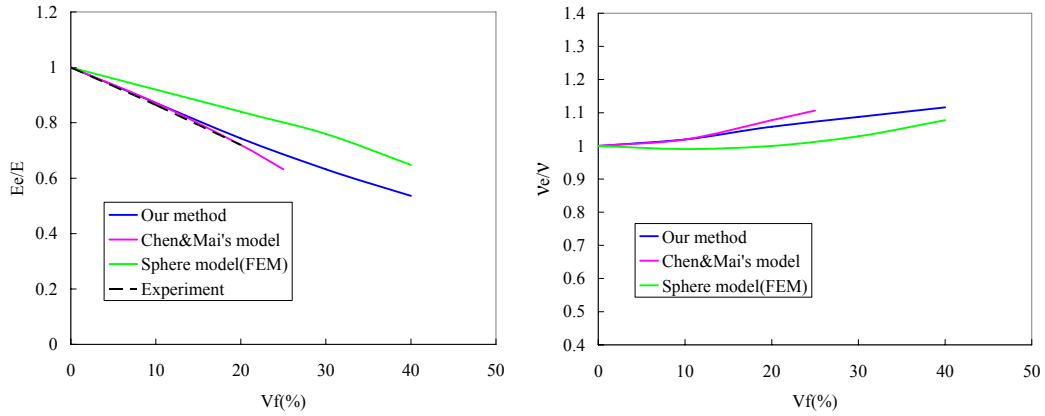

Figure 2. 16 Young's modulus and Poisson's ratio of materials with high bulk modulus rubber particle (Wang and Lee 1999)

The maximum Von Mises stress concentration factors of two kinds of rubber particles is shown in Figure 2. 17. Wang and Lee also found that the stress in rubber particle does not depend significantly on rubber volume fraction but depends on bulk modulus ratio of rubber particle to epoxy matrix ($\lambda=K_{rubber}/K_{epoxy}$). It is noted that this improved cylinder model is able to produce comparable results with the experimental observations. Moreover, improved cylinder model still can predict accurate results even for rubber volume fraction close to zero.

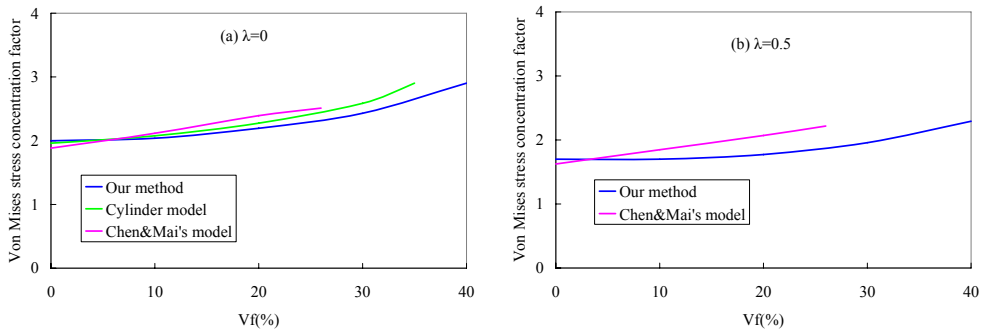

Figure 2. 17 Maximum Von Mises stress concentration factors under uniaxial tension (a: low bulk modulus rubber particle; b: high bulk modulus rubber particle) (Wang and Lee 1999)

2.5.3 The Single spherical cell model

Guild and Kinloch also developed a single spherical model which is similar to cylinder model (Guild and Kinloch 1995). The single spherical model is a one rubber particle ball enclosed by an annulus of polymer matrix. Due to symmetry only quarter of whole model is simulated. The structure of single spherical model is shown in Figure 2. 18.

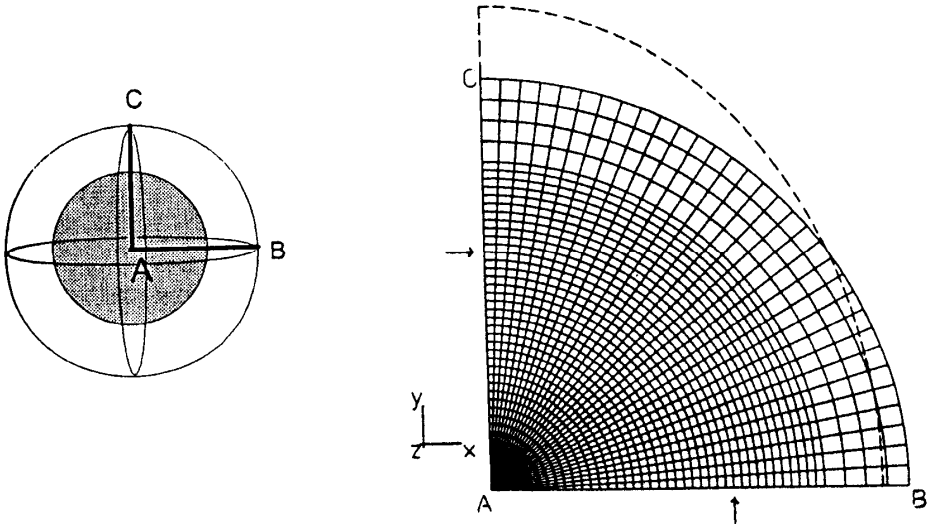

Figure 2. 18 Spherical model and its finite element mesh with deformed shape under unidirectional load (Kinloch and Guild 1996b)

In the spherical model, the same constraint conditions as cylinder model are applied. The lines of AB and AC are fixed due to symmetry, and the deformable BC is used to describe the deformed model under load. Because material is overall isotropic, the rubber toughened epoxy must deform in ellipsoid way. When unidirectional load is applied at the y-direction, Poisson's ratio and Young's modulus can be calculated from

the deformation of AB line. However, the Poisson's ratio is unknown for the rubber toughened system, and bulk modulus K is used to define the relationship between Young's modulus and Poisson's ratio. Thus an iterative procedure is required to analyse the spherical model under unidirectional load.

2.5.4 Statistical spherical cell model

Later, Poon et al. developed a statistical spherical cell model for particle-filled materials (Poon, Luk et al. 2002). The load and boundary conditions in statistical spherical cell model is shown in Figure 2. 19. Due to considering the statistical spatial distribution of particles in this model, Poon found that predictive results from glass-bead filled epoxy were closer to the experimental observations when compared with the results from single spherical cell model. He also found that this model is especially useful at predicting the Poisson's ratio values.

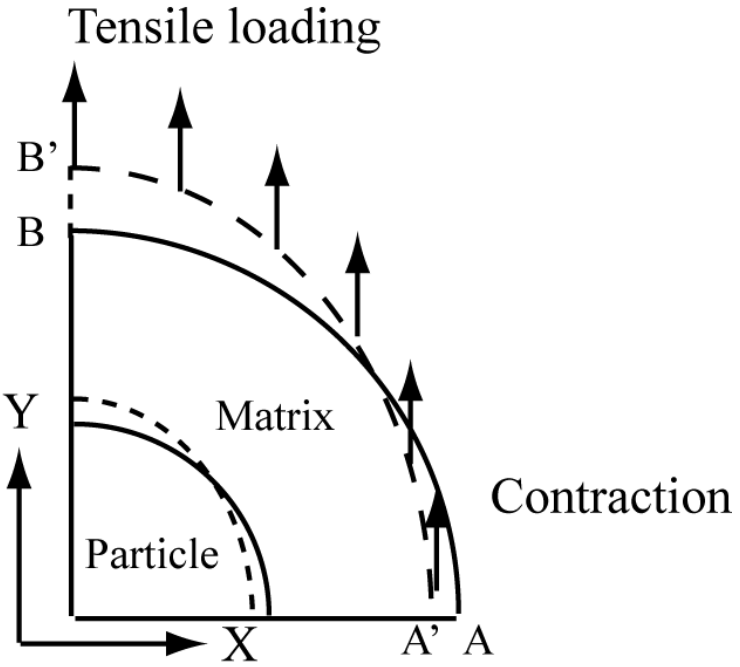

Figure 2. 19 Load and boundary conditions of the statistical spherical cell model (Poon, Luk et al. 2002)

In the single spherical cell model, the interaction between the particles has been assumed partially and indirectly by using the incorporation of the boundary conditions; however, statistical spherical cell model takes into account the inter-particle distance distribution and therefore has significant improvement in the prediction of Poisson's ratio. Figure 2. 20 demonstrates that the values from the statistical spherical model are closer to the experimental results than those from single spherical model (the

non-monotonic experimental results are un explained). However, Poon's works are limited to elastic properties calculation.

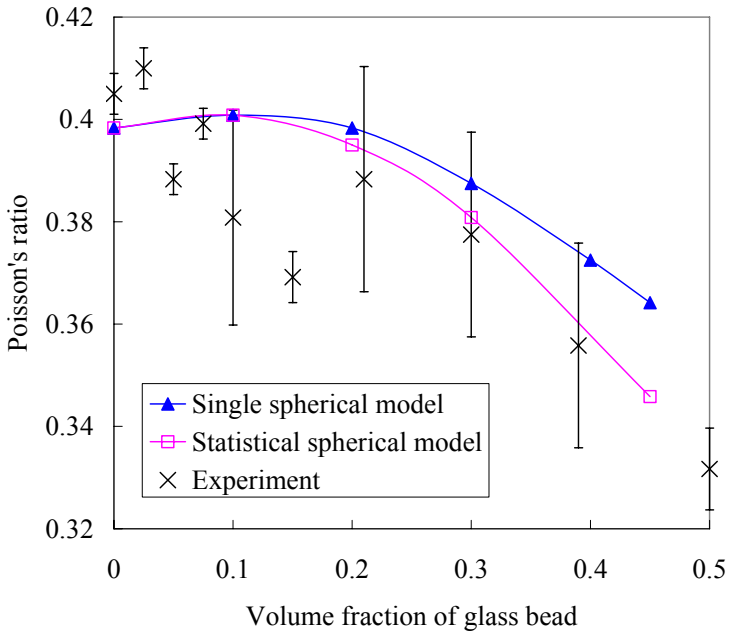

Figure 2. 20 Poisson's ratios calculated by statistical spherical cell model (cross: experimental data; triangle: single spherical model; square: statistical spherical model) (Poon, Luk et al. 2002)

2.5.5 Three-dimensional cell model for the particle-filled material

In order to obtain better and deeper understanding of particle toughening mechanism, Chen and Mai proposed a 3D micromodel using elastic-plastic properties to study the effects of phase morphology and mechanical properties of toughened system (Chen and Mai 1998b). They developed a 3D periodic cell model to study the local stress concentration and stress-strain states under various load. In their model, rubber particles are modelled with elastic behaviour and the epoxy matrix is modelled with elastic-plastic behaviour. Materials properties used in their model are listed in Table 2. 1. It is clear that the matrix is a typical epoxy resin.

Table 2. 1 Materials properties for matrix and particles (Chen and Mai 1998a)

Phase	Young's modulus (MPa)	Poisson's ratio	Yield stress (MPa)
Matrix	3500	0.25	80
Rubber particles	1-100	0.49-0.4999	/

The structure of periodic unit of the faced-centre cell (fcc) is shown in Figure 2. 21. Because of symmetry, back, left and bottom surfaces are fixed, other three surfaces are maintained straight under load. It is noted that Chen and Mai studied the effective stress-strain status and mechanical properties of system by changing particle volume fraction.

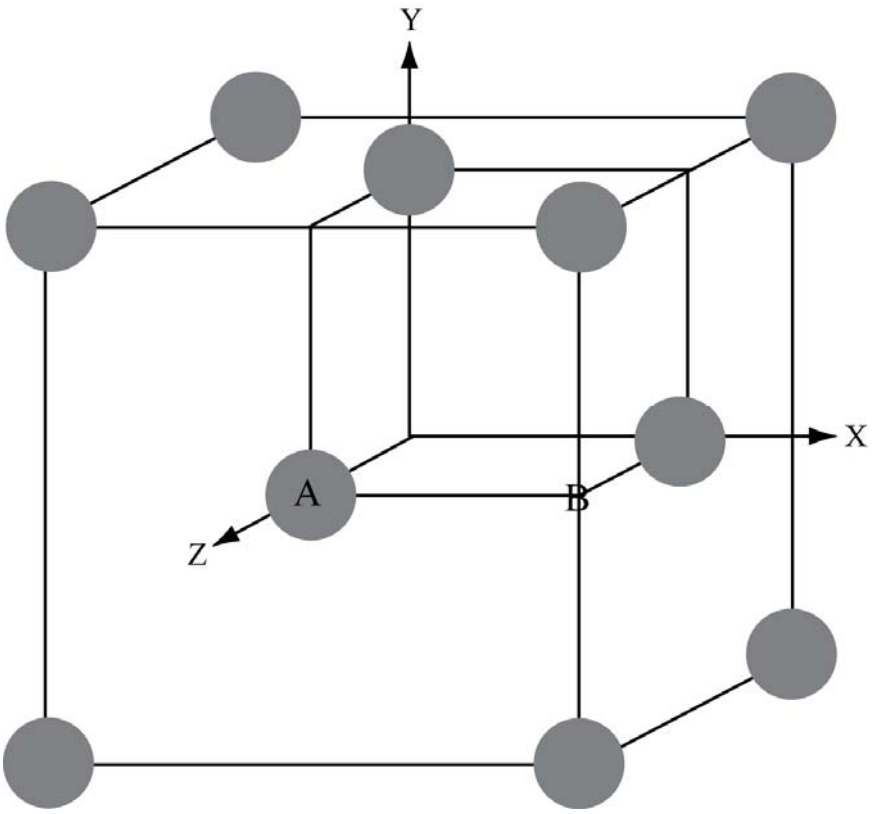

Figure 2. 21 The 3D schematic of periodic micromodel (Chen and Mai 1998b)

The effective stress-strain curves under global uniaxial tension for different rubber volume fractions are shown in Figure 2. 22. It is obvious that higher volume of rubber toughened system produce lower yield stress. The values of effective stress and yield stress decrease with increasing particle volume fraction and effective Poisson's ratio increase with increasing particle volume fraction. It is also found that the effective Young's modulus, Poisson's ratio and yield stress have a linear dependent relationship at the low volume fraction of particle which has been confirmed by Yee and Pearson's works (Yee and Pearson 1986a).

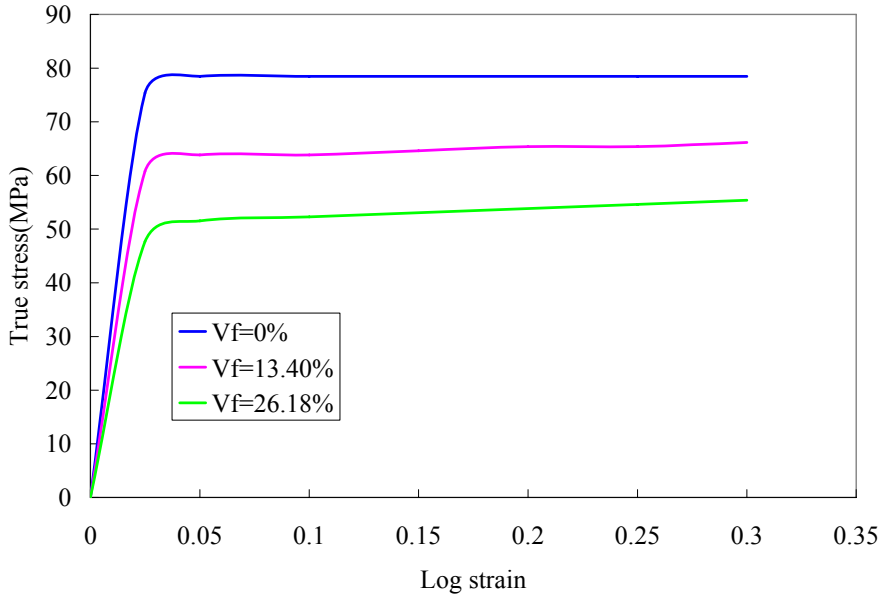

Figure 2. 22 Effective stress-strain curves under macroscopic uniaxial load at various rubber particle volume fractions (V_f) (Chen and Mai 1998a)

The curves of effective Young's modulus, Poisson's ratio and yield stress are shown in Figure 2. 23. It should be noted that all values were normalized by the matrix mechanical property at various particle volume fraction under global uniaxial tension. It is found that the effective Poisson's ratio increases with increasing particle volume fraction in the particle/matrix system but decreases in the void/matrix system.

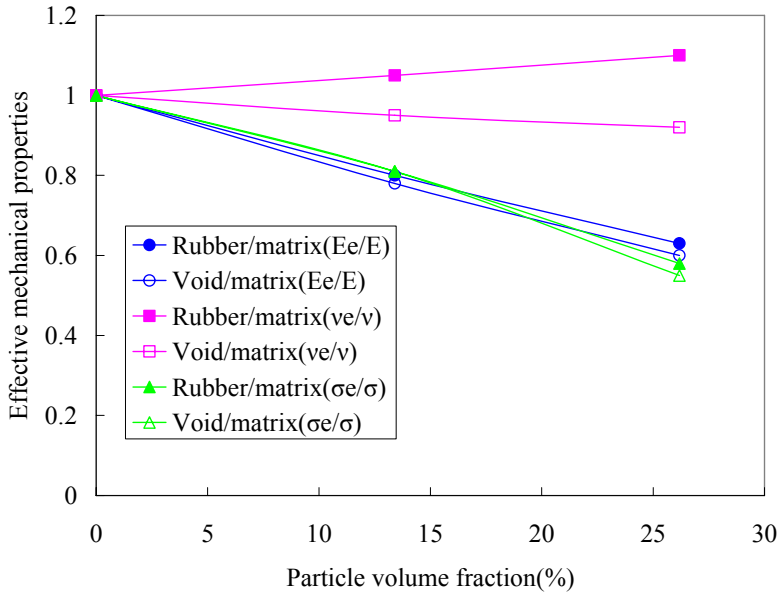

Figure 2. 23 Normalized effective Young's modulus, Poisson's ratio and yield stress versus particle volume fraction (solid tag: rubber/matrix system; hollow tag: void/matrix system) (Chen and Mai 1998a)

The relation between normalized effective yield stress and normalized effective dilatational stress in particle/matrix system is shown in Figure 2. 24. It should be noted that the effective stresses are obtained by averaging in the cell (see Eq.2- 16 and Eq.2-17) and σ_0 represents the applied stress. It is clear that there is difference between the shape of effective yield surface for particle/matrix and void/matrix system, and this difference becomes larger when the particle volume fraction increases. But it is also found that these two systems are similar under the triaxial load. It is also found that the effective yield stress of void/matrix system decreases more quickly than particle/matrix at high triaxiality load. This implies that the cavitation in rubber-toughened material is helpful for the occurrence of shear yielding at high triaxiality load (Chen and Mai 1998a).

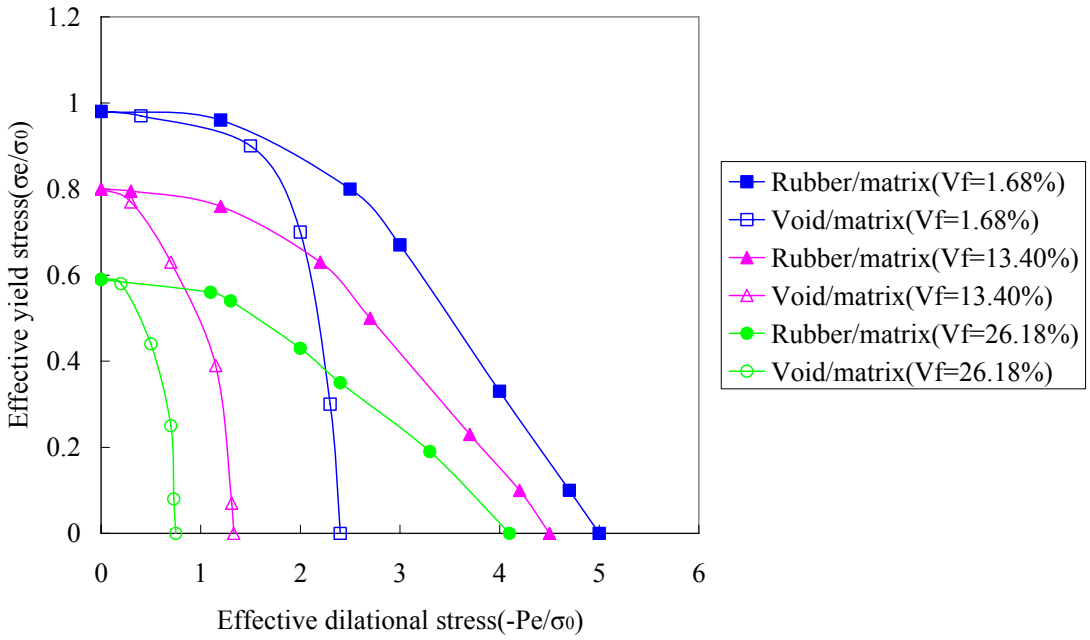

Figure 2. 24 Effective yield stress versus effective dilatational stress at various particle volume fractions (solid tag: rubber/matrix system; hollow tag: void/matrix system) (Chen and Mai 1998a)

The distribution of dilatational and Von Mises stress concentration along the path A-B is shown in Figure 2. 25 and Figure 2. 26, respectively. It is noted that the path A-B was chosen from the centre of one rubber particle to the nearest corner of the face centred cubical cell when model is under global uniaxial tension (see Figure 2. 21). It is also noted that stress concentration factor is defined as the ratio of local stress to corresponding average stress.

It is obvious that both factors increase with the increasing particle volume fraction and stress factors of void/matrix system are higher than those of particle/matrix system. Furthermore, there is a sharp change across the particle/matrix interface. They also found that the maximum Von Mises concentration factor in the rubber/matrix system is 1.91 at elastic stage with 0.21% particle volume fraction and increases to 2.29 and 2.58 with particle volume fractions of 13.4% and 26.2%, respectively (Chen and Mai 1998a). Compared with the stress concentration factors from Huang and Kinloch (Huang and Kinloch 1990), they predicted maximum Von Mises stress concentration factor to be 2.21 in axi-symmetric cylinder model and 3.81 in two-dimensional model when particle volume fraction is 19%.

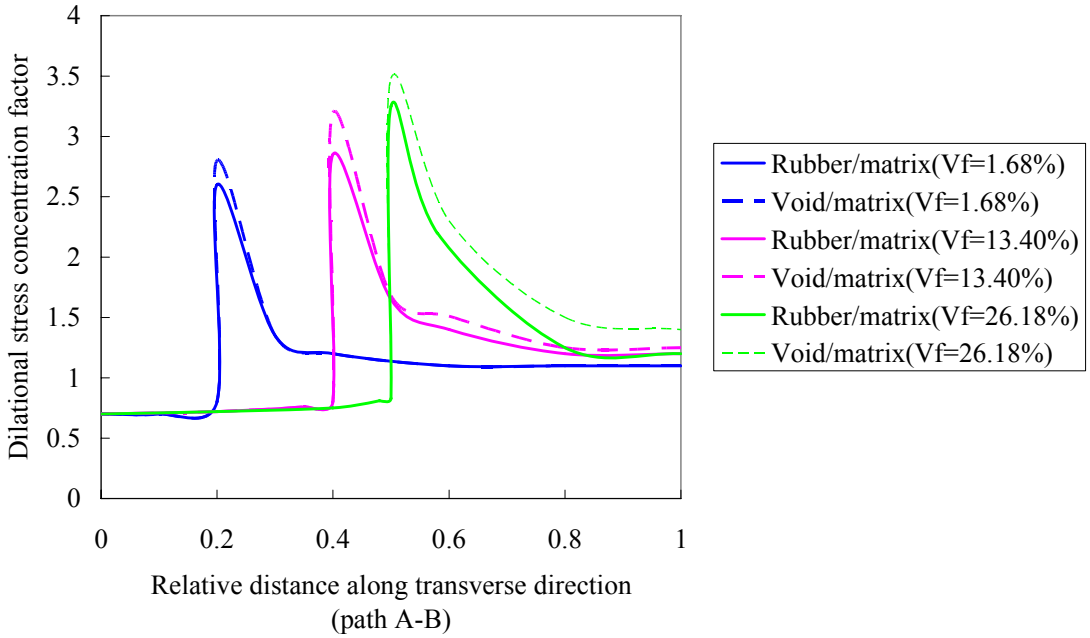

Figure 2. 25 Dilatational stress concentration factor versus relative distance along transverse direction under macroscopic uniaxial tension at various particle volume fractions (solid line: rubber/matrix system; dash line: void/matrix system) (Chen and Mai 1998a)

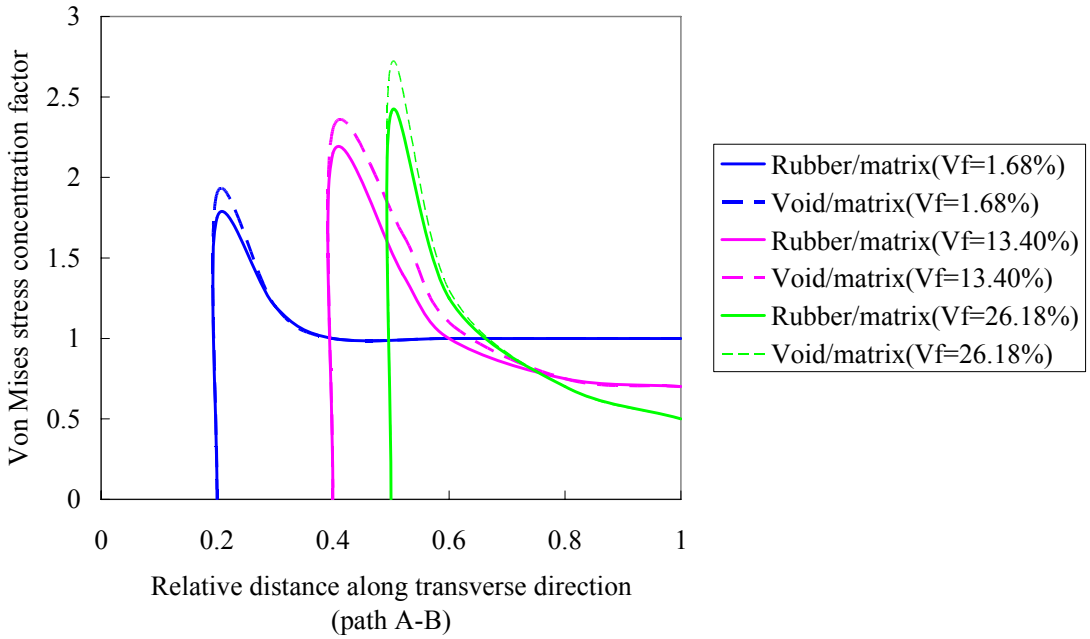

Figure 2. 26 Von Mises stress concentration factor versus relative distance along transverse direction under macroscopic uniaxial tension at various particle volume fractions (solid line: rubber/matrix system; dash line: void/matrix system) (Chen and Mai 1998a)

Chapter 3-Rubber toughened structural adhesive-AV119

3.1 General description

Araldite ® AV119 is rubber toughened epoxy adhesive produced by Huntsman Company in cartridge. This adhesive can be used in many applications as a structural adhesive. It is suitable for bonding of a wide variety of materials such as metals, glasses, plastics and ceramics, etc. Its curing temperature is in the range from 120 to 180℃ and heat resistance is up to 120℃ with very good bonding strength (HUNTSMAN 2004). Its gap filling is up to 3mm and no flow occurs during curing because of its thixotropic behaviour (no thixotropic agent is found according to Huntsman's data sheet). According to the published information from Huntsman Company, the AV119 adhesive is bisphenol-A epoxy resin toughened by liquid rubber particle. The recommended curing routes for AV119 are listed in Table 3. 1. It is noted that curing temperature below 120 ℃ will lead to inadequate cure even when cure time is prolonged. It can be stored for up to 2 years at 2-8 ℃.

Table 3. 1 Curing routes of AV 119 (HUNTSMAN 2004)

Temperatures (℃)	120	140	150	160	180
Curing time (mins)	60	45	30	20	10

3.2 Properties of AV119

The mechanical testing of AV119 adhesive have been performed by a few organizations, especially National Physical Laboratory (NPL), did large numbers of works to validate test methods for several adhesives including AV119 (Dean and Duncan 1995; Dean, Duncan et al. 1996b; Dean, Duncan et al. 1996a). Young's modulus, Poisson's ratio, stress-strain behaviour and associated hardening data can be obtained from tensile test of bulk specimens. NPL presents substantial details of bulk specimen's preparation and test (Dean, Duncan et al. 1996a); the tensile stress-strain curve of AV119 also can be found in Ozel's work (Ozel and Kadioglu 2002); more recently, Crocombe et al. investigated the mechanical properties of AV119 after environmental degradation (Crocombe, Hua et al. 2006).

3.2.1 Preparations and curing

Many types of manufacturing routes are available to prepare bulk specimen or joint specimen. The main problem associated with AV119 adhesive is removing the inclusion of air and to ensure the cure conditions are comparable to those in an adhesive joint. The material properties from bulk specimens are generally used to predict the strength of joints. There are two routes to manufacture bulk tensile specimens.

NPL used two plates to make a whole AV 119 plaque (Duncan 1999), then the plaque was cut into individual specimens. In order to remove air voids from the adhesive, vacuum stirring or centrifuging had been used before adhesive was moved into mould, and in the bottom plane mould, adhesive was spread in the same direction with spatula in order to introduce as little new air as possible. Finally the top plane mould is carefully laid on top, and then pressure was applied.

Another common method to manufacture bulk specimens is to use a cavity mould whose shape is exactly the same as bulk specimens. The thickness of specimens can be controlled by protruding mould which is fixed on the top of cavity mould. Compared with plane mould, it is difficult to remove all air voids via this method but it avoids the process of cutting specimen shape. Thus this method avoids internal stress introduced by cutting. Furthermore cavity mould is usually made from non-stick materials like bulk polytetrafluoroethylene (PTFE) which is hard and cannot bend easily, so it is difficult to remove specimen from mould after curing and the narrow part of specimen is easily damaged when getting out from mould. In order to avoid this drawing, cavity mould can be made from silicone rubber. However silicone moulds often have to be heated over 100 degrees in oven when curing bulk specimens, thus silicone may ages after repeated use and mould shape is distorted, which gives inaccurate shape of bulk specimens. Duncan et al. used three moulds made from mild steel, PTFE and silicone rubber to manufacture specimens (Duncan, Girardi et al. 1994b). Exothermal variations of these moulds were assessed. They found that mild steel mould was the best one to manufacture specimens.

It is well known that exothermic reaction will increase the temperature inside sheet

specimen, and the maximum sheet temperature depends on the curing temperature and thickness of sheet. Thermocouples have been used to measure difference between oven temperature and actual temperature inside sheet when curing. For instance, cure temperature at 120℃ for 60 mins caused maximum temperature of 138℃ inside 3 mm sheet specimens (Dean, Duncan et al. 1996a). Generally the thicker the sheet, the higher maximum temperature inside sheet, thus cycle curing method should be used if the sheet sample is too thick. Thus a temperature less than 120 ℃ should be set and post-cure should be applied to ensure that exterior thicker specimen completely react because the temperature in outer area is always lower than at the centre area in specimen. It was also found that curing temperature above 150℃ would cause degradation because the sheet sample was observed to be discoloured. Furthermore, curing temperature above 150 ℃ should be avoided because joining materials have different coefficients of linear thermal expansion.

Some sample have more voids than others although they were made by the same method, NPL suspected that this phenomenon may be caused by air entrapment in cartridges. Thus they suggested that cartridge should be emptied into a container under vacuum and stirring the adhesive until entrapped air was removed, then the cartridge was refilled under vacuum (Duncan, Girardi et al. 1994a).

After curing, the specimens should be assessed with respect to the location and quantity of voids. Usually voids in thin specimens are visible with strong light background. However, internal voids in thicker specimens are difficult to locate, thus non-destructive technology like visual inspection and ultrasonic C-scan may be used to detect voids. When the pulse of ultrasonic energy is incident on the sheet, the measured transmitted pulse is attenuated and influenced by voids. Thus the scanned image of sheet is able to reveal void-free area where the sheet can be cut for test specimens.

Shear properties of AV119 can be obtained from bulk or joint specimens, torsion and notched shear. NPL used V-notched specimen in bulk and joint form to determine shear properties (Duncan and Dean 1996). In their tests, the thickness of bulk specimens was controlled up to 4mm and the bonding thickness of joint specimens was set around 0.5mm which is similar to the real joint condition. Notched beam and notched plate

were studied; the curing conditions were the same as those of tensile specimens; the shear extensometer was developed for notched plate test because strain measurement in shear specimens is more difficult than in tensile test. They found that the notched plate test can obtain more accuracy in shear properties of stiff adhesive such as AV119 compared with compliant adhesive. Torsion test using butt joint was also implemented in NPL lab (see Figure 3. 1) (Dean, Duncan et al. 1996b).

3.2.2 Mechanical properties of AV119

Different bulk sheets with thickness ranging from 0.5mm to 4.00mm were made by NPL; 0.5mm thick sheet is able to compare to the adhesive thickness in bonded joints, and thicker sheets like 4.00mm are easy to test according to various international standards. Mechanical comparisons were applied to check if properties of bulk specimens are similar to those of adhesive layer in bonded joints. They found that the properties like modulus, failure tensile strength and strain of AV 119 are independent of specimen thickness. Moreover, thinner specimens are easy to test when contacting extensometers are used and thicker specimens are more difficult to manufacture because more air voids would be introduced. The stress-strain curves in tension and shear for AV119 adhesive are shown in Figure 3. 1. It is noted that the thickness of tensile specimen is 4mm and specimens were tested under the strain rate of 1%/min; the cross-section of butt joint was set to 15mm diameter (Dean and Duncan 1995; Dean, Duncan et al. 1996b). These curves present typical properties of rubber-toughened epoxy.

For shear test, other tests such as bulk notched beam, bulk torsion and thick adherend shear were also studied in NPL's work. The results show that the curves of various test methods agreed well with each other. Thus the basic mechanical properties can be obtained from above stress-strain curves. These properties were used to calculate the parameters of material model and compared with the results of micro model in the simulation (see Chapter 6).

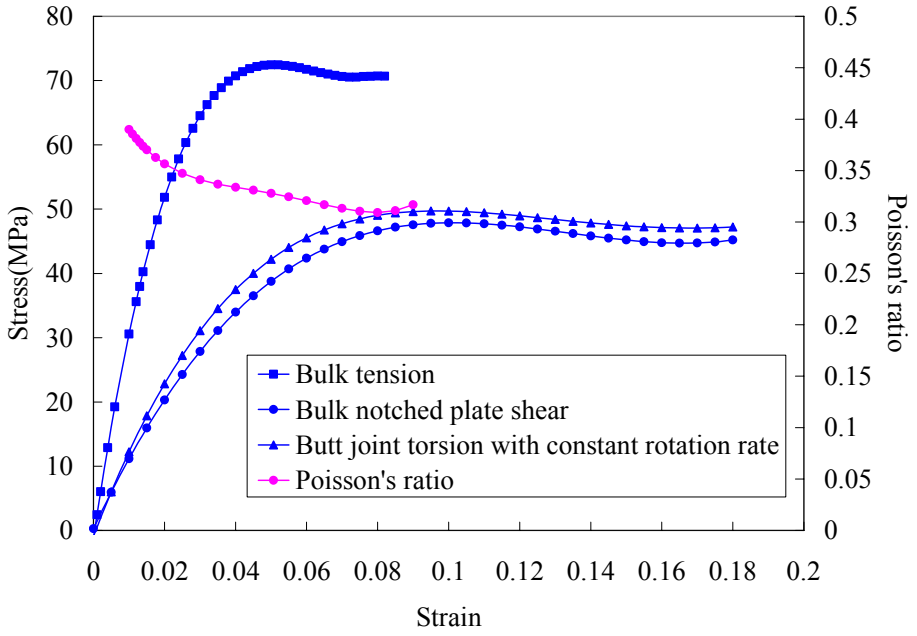

Figure 3. 1 Tensile and shear behaviour of AV119 adhesive (Dean and Duncan 1995; Dean, Duncan et al. 1996b)

Chapter 4-Experimental investigations of Double Lap Joints using AV119 adhesive

4.1 Introduction

There are many specimens used for testing adhesives. However lap joints are the most common form to be investigated and easiest to be prepared. Several joints such as Thick Lap Joint, Single Lap Joint and Double Lap Joint are popular test geometries. In this work Double Lap Joint (DLJ) was chosen to study the adhesive behaviour because this geometry minimizes bending moments.

DLJs were manufactured according to the ASTM standard-D 3528-76 (Re-approved 1981), the schematic is shown in Figure 4. 1. Thickness of outer adherends and inner adherend are 1.6mm and 3.2mm, respectively. It is noted that the strain gauge is glued at the middle of overlap area (the strain gauge parameters are described in Section 4.3). Extensometer covers the overlap range of joint.

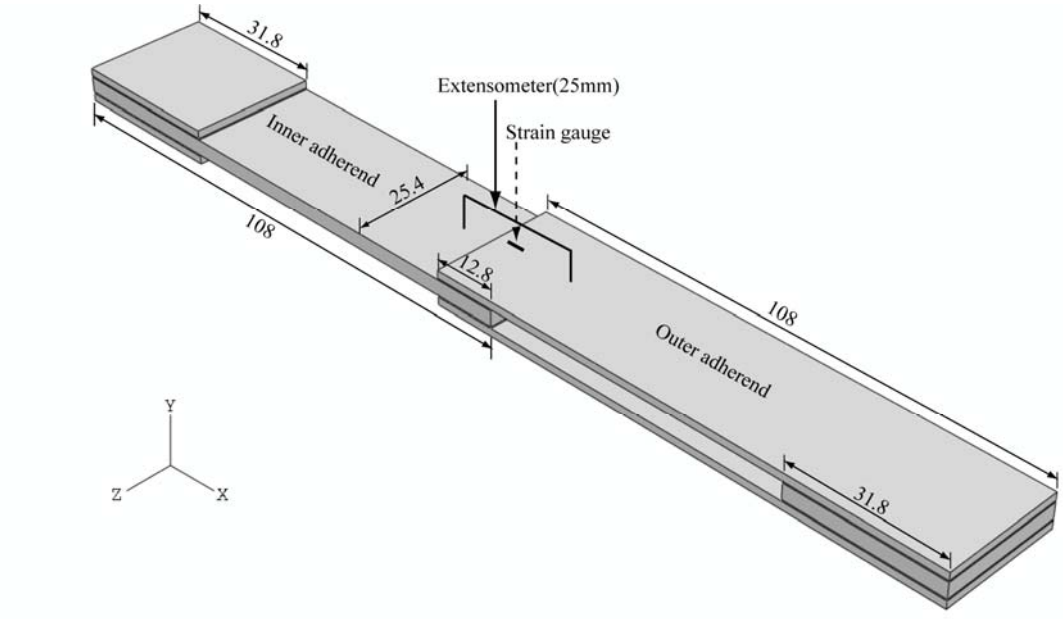

Figure 4. 1 Schematic illustration of DLJ (all dimensions in mm, not to scale)

One-part rubber toughened epoxy adhesive, AV119, was purchased from Aeropia Limited (UK) and used to bond the Double Lap Joints. Hardened steel was used for adherend to avoid plastic deformation during test. The adherend properties were

determined by testing the dog-bone specimens according to ASTM D638M-89.

4.2 Double lap joints (DLJs) preparation

Hardened steel was used for adherends due to its linear elastic response under load. This adherend can reduce the effects of plastic deformation in the experimental results. Hardened steel were tested under the same tensile load conditions as DLJ's in Instron 6025 in order to make sure the steel used for adherends have desired properties.

Grit blasting was used as surface preparation for adherends, spacers and tabs; degreasing agent (Acetone) was used to remove all traces of dirt and oil before and after grit blasting, the surface treatment effect is demonstrated in Figure 4. 2.

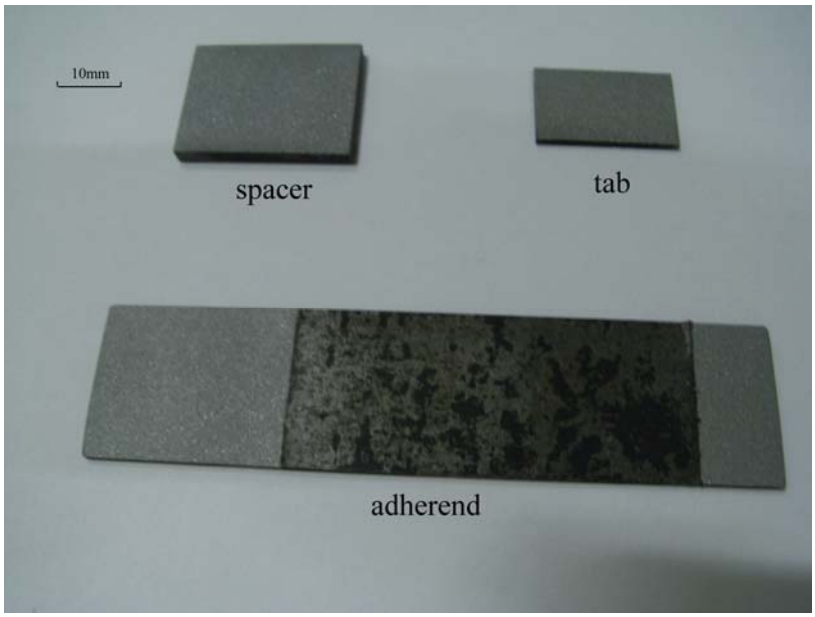

Figure 4. 2 Grit blasting treatment of adherend, spacer and tab

AV119 is paste adhesive which is embedded with lots of air bubbles, thus adhesive was extruded from the cartridge to a clean container then it was moved to vacuum for 30 mins in order to remove most air bubbles. 1% wt glass beads with 0.2mm diameter, 0.3mm diameter and 0.5mm diameter were added into adhesive to control layer thickness in joints, then adhesive was ready to be pasted to the surface of components. All components with adhesive were moved to vacuum for 50mins again to remove the rest of air bubbles because the process of pasting the adhesive to specimen surface introduced air to adhesive layer again. It is noted that the thickness of adhesive in specimen is much thinner than the bulk adhesive in container allowing further removal of air bubbles. After these two cycles of vacuuming, random samples of specimens

were observed under optical microscope to check the effect of vacuuming.

Adherends, spacers and tabs were heated to 50℃ prior to bonding in order to improve the wetting between adhesive and adherend. Joints were assembled into a jig as shown in Figure 4. 3.

Figure 4. 3 A jig used for DLJ's manufacture

The jig surface was cleaned by acetone and release agent was applied. The jig and all associated pins were treated with release agent as well to allow easy removal of the Double Lap Joints after manufacture. After all joints were fixed in the jig by the pins, a vacuum bag was made by tacky tape and plastic film. The whole mould was placed in the oven at 120℃ for one hour with vacuum pressure applied during the curing process. The vacuum mould is shown in Figure 4. 4. After curing process the joints were allowed to cool down slowly to ambient temperature in oven to avoid internal stress.

DLJs were removed from jig after cooling without clamping problem. It is found that nodules of adhesive protrude from the corner; this nodule is removed by using a fine file, leaving only very small fillets at the corners. Thus these lap joints are considered to have no fillets. Both side faces of DLJs were polished carefully in order to measure the adhesive thickness using a microscope.

Figure 4. 4 DLJ bonding manufacture using jig and vacuum bag

Compared with the method of vacuum bag, another assembling method used here is applying the weight to the specimens directly. Because AV119 adhesive has a high viscosity property, a sufficiently high external pressure must be applied to the joints to make sure adherends hold each other strongly and a predetermined thickness is achieved.

4.3 Strain gauge preparation

Strain gauges were used in DLJ testing. The position of strain gauge is shown in Figure 4. 1, the length of gauge is 3.0mm and supplied by Tokyo Sookki Kenkyujo Co., Ltd under the code of FLA-6-11-1L. It is important that the surface of adherend is clean and the gauge is perfectly bonded to the adherend. So the preparation procedure consisted of abrading the surface with fine emery paper and cleaning with acetone. Superglue was used to bond strain gauge to the adherend at the specified position. The strain results from the experiments could be compared with the FEA results.

4.4 Double lap joints testing procedure

All specimens were tested using Instron 6025 machine and associated data PC. Strain gauge was connected with another PC and associated mechanical software is CATMAN system. CATMAN catches the strain gauge signal and tracks the load of Instron machine. An Instron extensometer with 25mm gauge length was installed at the middle of specimen such that the gauge length covers the overlap of joint. All information of

strain gauge, extensometer and load are set to be synchronous before implementing the test. Load cell was set at 100KN load range and every load increment can be captured by PC. Cross-head speed was set to 2mm/min which results in tensile failure in several minutes.

4.5 Results and discussion

4.5.1 Properties of adherend

Adherends were made by hardened steel and tested using dog-bone specimen as shown at Figure 4. 5. Cross strain gauges were adhered to the centre of specimens and used to obtain the longitudinal and latitudinal strain when specimen was under tensile load.

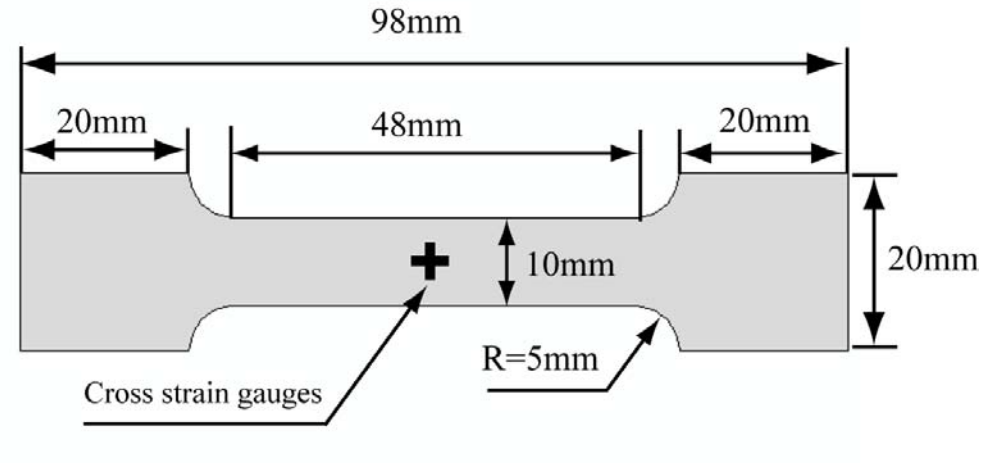

Figure 4. 5 Schematic of dog-bone specimen (specimen thickness=1.6mm)

The mechanical properties are shown in Table 4. 1. It is noted that in total five specimens were tested.

Table 4. 1 The properties of hardened steel used for adherends

Elastic	Young's modulus(MPa)	Poisson's ratio
	199300	0.30
Plastic	Yield stress(MPa)	Plastic Strain
	1400.20	0
	1580.61	0.000742
	1664.02	0.001101
	1734.77	0.001570
	1813.77	0.002320
	1871.73	0.003053

4.5.2 Manufacturing defeats

From the manufacture and test results, there are five major factors affecting joint strength. Desirable strength of DLJ can only be achieved when all factors are considered carefully. It is found that grit blasting plays a very important role in manufacturing DLJ, the bond surface is very weak if it was treated only with sand paper without any grit blasting. Then the strength of DLJ is around 4 times lower than that of DLJ treated with grit blasting.

Second factor significantly affecting the DLJ's strength is removing the air inclusion inside AV119 adhesive before bonding. Some paste adhesive like AV 119 which is stored in cartridge already contains air when it is filled in factory. These voids are the cause of promoting premature failure because of initiating and increasing stress concentration, thus the strength of DLJs is inevitably reduced. It is found that inadequate air removal reduced the strength up to 20%.

The third factor affecting the strength of joints is the curing temperature and process. It is found that curing temperature lower than 120℃ cannot give adequate curing and causes decrease in strength. However cure temperature exceeding 160℃ increases the residual stress in bonded joint because of different linear coefficients of thermal expansion in jointing materials (61.2e-5K^{-1} for adhesive and 11.1e-5K^{-1} for adherend (Loh and Crocombe 2002)), thus the strength of joints maybe decrease. It is found that the including of thermal strain does not affect the fracture energy obtained from Mixed Mode Flexure (MMF) test but affect the fracture energy obtained from Notched Coating Adhesion (NCA) (Giunta and Kander 2002; Loh and Crocombe 2002). Furthermore, most curing process of adhesive are exothermic so excessive heating may occur in bonded joint. Thus higher curing temperature will result in decomposition in adhesive because temperature singularity in joints and the colour of adhesive layer becomes darker than that of adhesive under lower curing temperature. Besides, the vacuum module should be left in oven to cool down slowly after whole curing process because quick cooling down may cause higher residual stress.

Last factor affecting the strength of joints is the parallel condition of adherends. If the adherends were not flat, the tensile load applied at the joints would not remain aligned

and it would introduce high cleavage stress into the bond area.

Some further factors like moisture content will affect the mechanical properties after curing; therefore, specimens should be stored in desiccator before test.

It is found that the process of adhesive degassing before bonding affects the fracture surface greatly. The failure surfaces of specimen with adequate and inadequate degassing are shown in Figure 4. 6. Sufficient void removal from the adhesive results in a smooth and continuous fracture surface. Voids in the adhesive trigger failure during load and the fracture surface exhibit tree form which is the trace of void enlarged by the application of vacuum bag during curing.

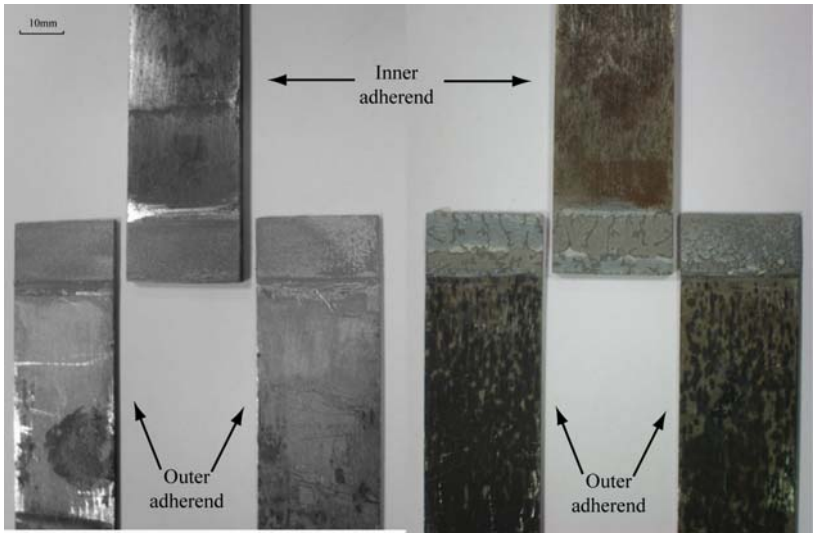

Figure 4. 6 Typical failure surfaces of DLJ (Left: adequately degassed. Right: inadequately degassed)

Comparing the load method of vacuum bag and weight pressure during curing, it is found that the specimens manufactured by vacuum bag have higher internal stress than those made by direct weight load because strong vacuum pressure was applied at top surface of specimen and caused a slight bending in the outer adherend. The effect of manufacture using vacuum bag is shown in Figure 4. 7. This method causes a slight deformation of top outer adherend in the overlap area and results in non-uniform adhesive thickness. Moreover, more internal stress exists in the adhesive after curing, thus the failure loads of specimens decrease slightly. However the test results showed that the relation of load and local strain is very stable when local strain is obtained from the bottom surface of specimen where good conditions exist.

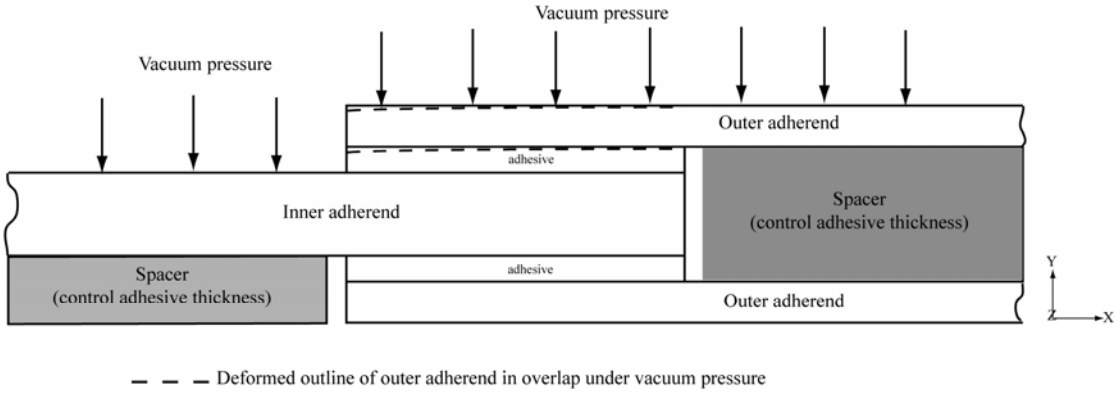

Figure 4. 7 Deformed outer adherend under vacuum pressure during manufacturing Double Lap Joints

4.5.3 Fracture paths

The failure morphology of specimens is illustrated in Figure 4. 8. It is noted that most specimens have adhesive failure but few specimens using 0.2mm adhesive thickness has cohesive failure.

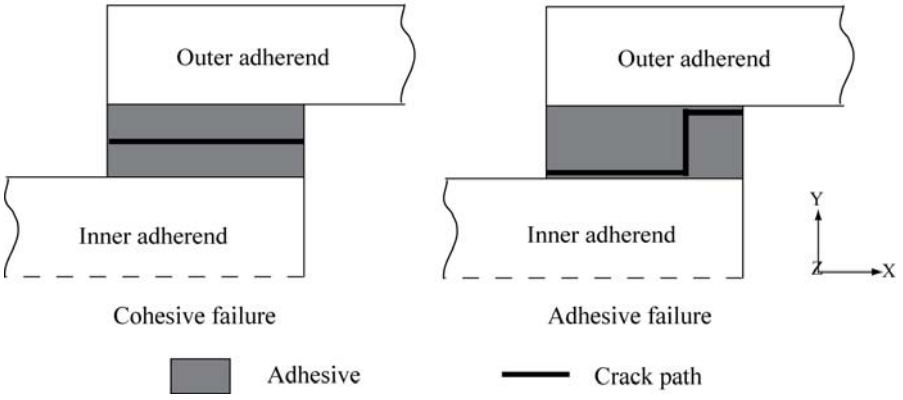

Figure 4. 8 Typical fracture path in DLJ specimens

Inspection of failure surface of DLJ using an optical microscope showed that there is a very thin adhesive layer remained at inner adherend as shown in Figure 4. 9; this thin adhesive layer almost covers the entire overlap joint area. The average measured thickness of this thin adhesive layer is around 10μm. This thin layer may be created by the inter-lock mechanics between adhesive and roughed steel surface caused by grit blasting treatment.

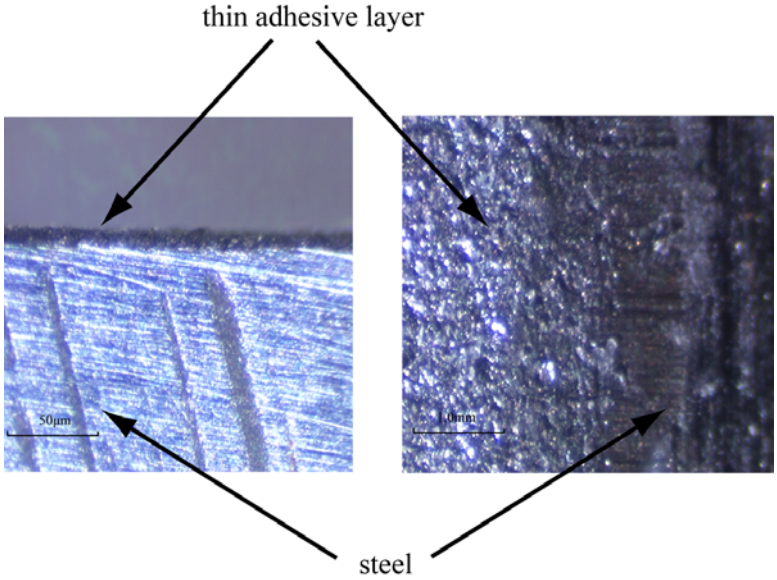

Figure 4. 9 Microscope images of failure surface

For specimens using 0.5mm thickness adhesive, adhesive mostly remained at surfaces of outer adherends and the surface of inner adherend only has a very thin trace of adhesive layer. Compared with the works done by Knox and Cowling (Knox and Cowling 2000), they used thick adherend lap shear joints (TAST) bonded by 0.5mm thickness adhesive and adhesive layer left at both fracture surfaces. This may be because TAST produce more pure shear than DLJ under load thus adhesive has the identical chance to remain at both thick adherend. Whereas outer adherend in DLJ undergoes a slight internal bending and inner adherend has zero bending under load, and the adhesive layer is found remain at outer adherend after failure. The failure surface of DLJs with 0.2mm thickness adhesive shows more complex fracture condition; the inner adherend has a few spots of adhesive layer left and most adhesive layers remain at outer adherend, moreover the adhesive layer has ragged edges indicating good adhesion, this fracture surface has the similar shape as found in the works of Knox and Cowling (Knox and Cowling 2000).

4.5.4 Joint strength

The failure loads and standard deviations (SD) of DLJ tests are shown in Figure 4. 10, the plot demonstrates the average failure load and standard deviation of joints using various adhesive thicknesses. It is noted that more than 15 specimens for each thickness were tested.

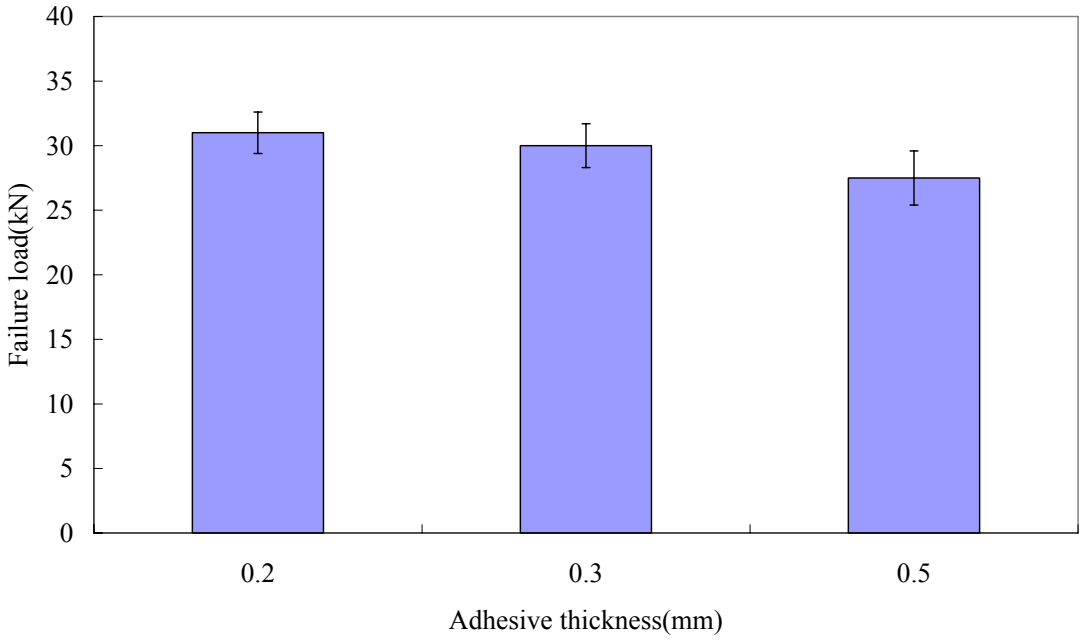

Figure 4. 10 DLJ's failure load using various adhesive thickness

As expected, thinner adhesive in joints produces higher tensile strength. It is noted that there is no significant difference of failure load between specimens using 0.2mm and 0.3mm adhesive thickness. This is because the adhesive thickness is less relevant to the joint strength in a specific thickness range. It is also found specimens using 0.5mm thickness adhesive have lower failure load than other specimens. Thicker adhesives usually bring in more defects in joints, thus quality control has to be taken into account in the manufacture of specimens.

Usually there are two classes of defects including surface defects and adhesive defects. Surface defects have no relation with adhesive thickness and can be eliminated before bonding. However adhesive defects are related to adhesive thickness because DLJ with thicker adhesive does introduce more voids inside adhesive because of the more relative displacement during bonding and more thermal shrinkage after curing than those with thinner adhesive. This increase in defects was observed. Furthermore, when the pressure is applied at the specimen during curing, overlap area of DLJ with thicker adhesive is easy to bend because of bigger gap between adherends, thus more unexpected nonlinear geometry is produced. Another main factor affecting the strength is poor curing. Thicker adhesive may change the curing properties and result in higher internal stress. In addition, thicker adhesive thickness gives rise to unaligned load in joints and increases the stress concentration at the corner of the adhesive-adherend and

enhances the bend moment in joints. DLJ test results show that failure load decrease when the adhesive thickness increase.

All these factors result in lower average failure load and bigger standard deviation of specimens which use thicker adhesive such as 0.5mm thickness specimens. But it should be noted that very small adhesive thickness tends to change the uniformity and homogeneity of joints, and gives rise to adhesive starvation in bond area, thus too thin adhesive thickness is not recommended. Other factors such as mismatch of adherend and using the bad adherend also result in high residual stress in adhesive layer and finally lead to low failure load in tests. It is known that the joint strength depends strongly on the substrate conditions. Morphology of adherend surface, metal component and oxidation condition, and carbon contamination after hardening play important role in adhesion capability. In this work, adhesive joint using polished adherends showed very low strength compared with other grit blasting joints because adhesive cannot create strong network in the adherend surface.

Chapter 5 Experimental methods to determine failure criteria

5.1 Introduction

Mode-I failure in adhesive joints has been investigated for many years. The Double Cantilever Beam (DCB) test and the peel test are two main tests to investigate this failure. In this work, Fixed Arm Peel test is chosen to obtain mode-I fracture energy due to its simplicity and extension from real application. There are many test methods to determine mode-II fracture energy; here 4 point End Notched Flexure (4p-ENF) test has been used to study pure mode-II fracture toughness because this test is stable and simple. This failure in practice is always combined with normal and shear stresses, thus the mixed-mode test must be implemented to investigate the initiation and propagation of failure. A lot of shapes of mixed-mode specimen have been designed to achieve above purpose, here the mixed-mode bending (MMB) is chosen to study mixed mode failure as it seems to be the best technology and is proved to be very powerful and successful in the applications of composite and adhesive.

5.1 Mode-I test (Fixed Arm Peel)

The AV119 adhesive-bonded Fixed Arm Peel specimen was employed to determine the mode-I fracture energy (G_{IC}). Adhesive thicknesses were chosen as 0.2mm and 0.5mm, respectively. The protocol and a macro of Excel from Imperial College were applied to carry out this experiment and calculate the results (ICpeel 2006). The schematic of Fixed Arm Peel test is shown in Figure 5. 1. It is noted that the specimen width is 25.4mm and the adhesive thickness is chosen as 0.2mm and 0.5mm.

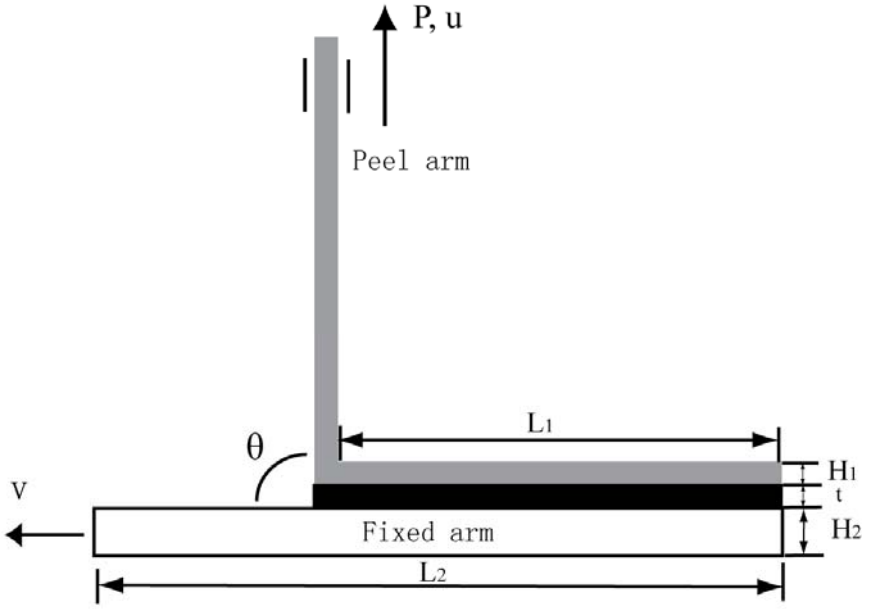

Figure 5. 1 Schematic of Fixed Arm Peel test (θ=90°), L_1=100mm, L_2=130mm, H_1=1.6mm, H_2=3.2mm, t (adhesive thickness)

The peel specimens were cut in the form of rectangular. The un-adhered region of peel arm has the same length as the length of adhered region (L_1).The load direction applied at the peel arm is unchangeable which requires the fixed arm to move towards left direction horizontally. The clip length of peel arm was set to 25mm.The peel angle θ is chosen as 90 degree. The fracture toughness of adhesive is described by the load (*P*), specimen geometry and dissipated bending energy in peel arm. i.e.

$$G_{adhesive} = G_{total} - G_{plastic} = \frac{P}{w}(1-\cos\theta) - G_{plastic} \qquad \textbf{(5- 1)}$$

Where G_{total} represents the input energy rate determined by load, specimen width (*w*) and peel angle (θ), $G_{plastic}$ represents the plastic dissipation rate of bending in the peel arm which is determined from the tensile behaviour of steel. The energy dissipation rate of peel arm has to be determined separately before or after the peel test. Thus two experiments must be implemented to obtain the adhesive fracture toughness: the Fixed Arm Peel test with specific peel angle and the tensile test of peel arm. It should be noted that the tensile strain of testing peel arm should exceed the specific strain which is typically 6% in the protocol of Imperial College (see Figure 5. 3). The fixed arm test was also used to determine the initial normal stress ($\sigma_{n,0}$) for the cohesive zone model (see Section 7.2.5.2).

5.1.1 Preparation of fixed-arm peel specimens and dog-bone specimens

The manufacture process of peel test specimens is similar to the process of Double Lap Joint. The same adhesive and hardened steel were used for glue layer and fixed arm, respectively. Every fixed arm has four holes which are used to fix at the peel table. The material of peel arm was chosen as gauge steel whose mechanical properties were tested using dog-bone specimens. The manufacturing procedure of peel testing specimens is as follows:

1) Before gluing together, both surfaces of peel arm and fix arm were grit blasted and then cleaned with acetone.
2) 1% glass beads by weight were mixed into AV119 adhesive to control the thickness. Both peel arm and fix arm were pasted with adhesive and then pre-heated at 50 ℃ prior to bonding the two parts together, and then clips were used to give pressure in the bonding area.
3) Specimens were cured at the temperature of 120℃ for one hour and cooled down to ambient temperature before moving them out of the oven. Redundant adhesive was removed from the specimen edge and edge surface was polished by fine emery paper. Thickness of adhesive was measured by optical microscope before test. the crack position was measured using ruled lines which marked on the specimens.

The test of peel arm material was implemented using dog-bone specimen. The dimension of dog-bone is shown at Figure 4. 5, but only longitudinal strain gauges were used instead of cross strain gauges. Precise dimensions of every specimen were measured by Vernier Caliper before test. The surface of dog-bones were polished with fine emery paper and cleaned with acetone. 1.00mm length strain gauge supported by Tokyo Sookki Kenkyujo Co., Ltd (code FLA-6-11-1L) was bonded to the centre of specimen.

5.1.2 Test processing of fixed-arm peel specimen

Both tests of Fixed Arm Peel and dog-bone specimen of gauge steels were conducted at constant tensile speed of the crosshead in Instron 5584 machine, all tests were implemented at ambient temperature with a relative humidity of approximately 55%.

The speed of crosshead was 1mm/min until the position in which a sufficient crack extension has evolved in peel specimen. For dog-bone test the load continued until the final fracture occurred and the test was conducted at the same test speed as the Fixed Arm Peel test.

The test apparatus is shown in Figure 5. 2. In order to maintain the constant peel angle, the fixed arm is attached to the peel table using four screws, and peel table is allowed to move along the low friction linear bearing jig which is fixed at the support head. Then the load force versus displacement curve ranging from the beginning to crack propagation was recorded. In the test more than 30mm fracture length should be created unless a flat plateau is found in the force-displacement curve. It is noted that five tests were performed for each 0.2mm and 0.5mm adhesive specimens since all tests showed consistent results. In addition, the peel angle was measured from each test and then used in calculation.

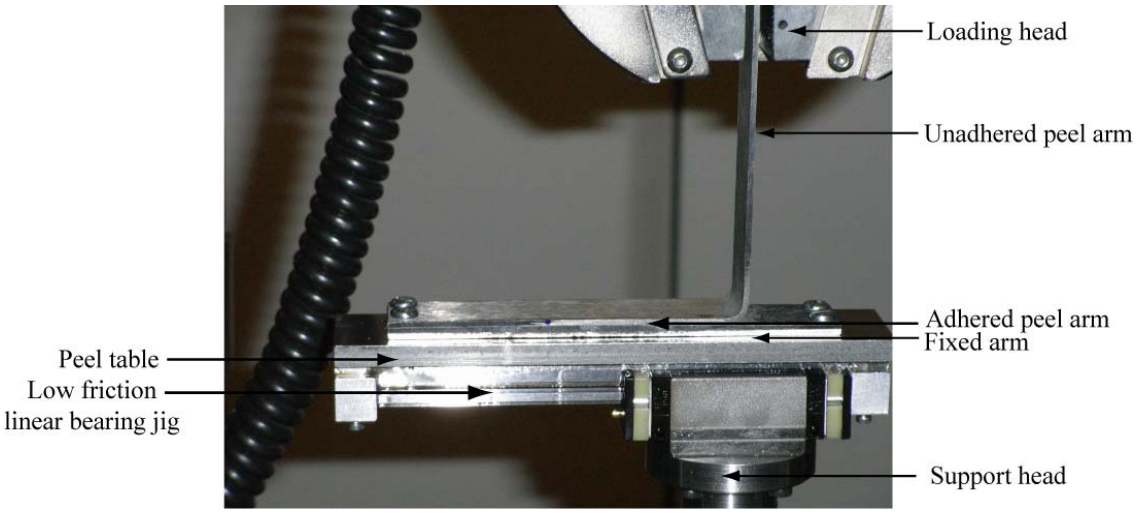

Figure 5. 2 Fixed arm peel fixture with linear bearing jig (90º peel angle)

5.1.3 Experimental results

5.1.3.1 Dog-bone test

In order to calculate the value of $G_{plastic}$ in Eq.5- 1, the stress-strain curve of peel arm material must be obtained, and then the plastic bending energy can be determined using large-displacement beam theory (Kinloch and Williams 2002; Kawashita, Moore et al. 2005). Here a bilinear fit tool was used to analysis the stress-strain curve of peel

arm material and calculate the $G_{plastic}$. The typical stress-strain curve from dog-bone test of gauge steel is shown in Figure 5. 3. It should be noted that total five specimens were tested and there is no significant difference between these curves of tests.

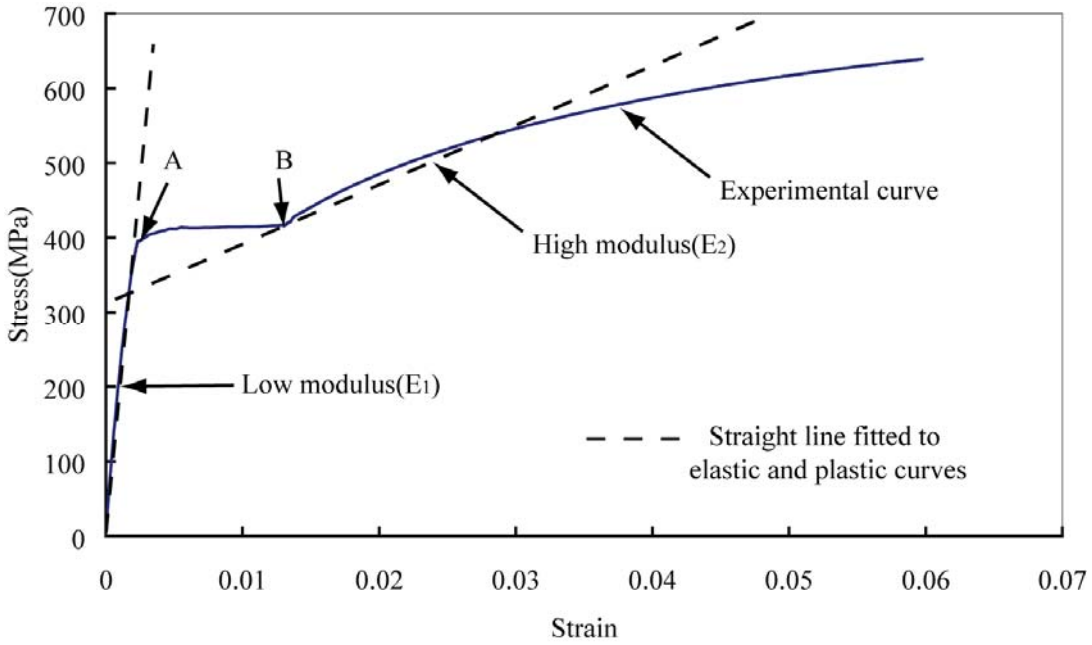

Figure 5. 3 Tensile test of peel arm material and the definition of modulus (E_1, E_2) using straight line fit

The curves were converted from engineering stress-strain to true stress-strain. Parameter α is defined as the ratio of high modulus (E_2) to low modulus (E_1), i.e. the ratio of plastic modulus to elastic modulus, because the curve of stress-strain exhibits a perfect plastic plateau (point A to B), thus the straight line fit to plastic was chosen starting from B and forward until ten times the yield strain which is recommended in the protocol of Imperial College. E_1 and E_2 are calculated to 199.3±1.1GPa and 7.5±0.3GPa from six specimens. Thus parameter α is determined to 0.038 averagely which is used in the peel test analysis. The power law fit was also used to compare the straight line fit (power law parameter N is 0.115 averagely) and it is found that both fit methods produced very similar adhesive fracture toughness.

5.1.3.2 Peel test

Peel test results showed that all specimens with 0.2mm adhesive thickness have the similar shape from the beginning of test to the end of test especially in the area of flat plateau. One typical curve is chosen to demonstrate the peel curve (Figure 5. 4). Point

A represents the onset of peel which requires the highest force to start the peel failure. There is an area of adhesive failure style from point A to point B according to experimental observation. When adhesive failure propagates, cohesive failure occurred starting from point B and forward to the final test (point D). The peel test was stopped at point C and then load continued in order to study the effect of load process to the force-displacement curve. It is found that the peel force decreases slightly but the trend of force versus displacement does not change and cohesive failure continued as well. It implies that cohesive failure in mode-I test is stable.

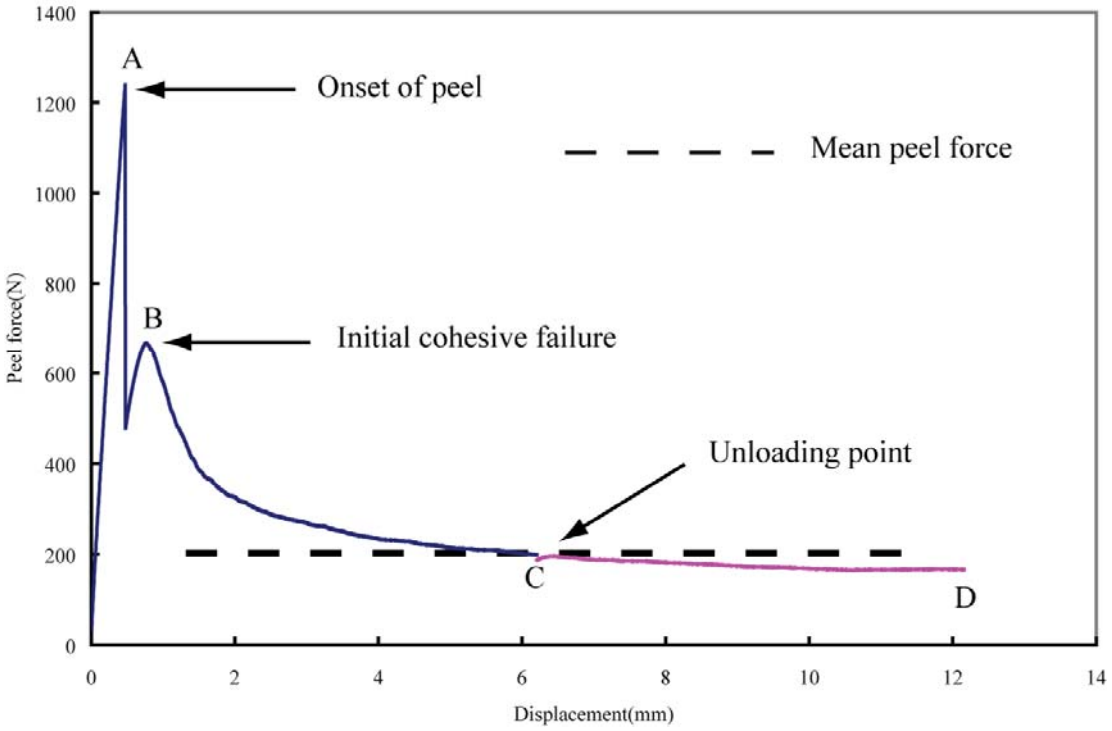

Figure 5. 4 Peel force versus displacement and force varies with different stage (0.2mm adhesive thickness)

The mean peel force in the flat plateau range is used to determine the adhesive fracture toughness individually. It is noted that the peel force at the point B is 650N averagely, and the section of peel arm is 25.4×1.6mm^2, thus the stress in the peel arm at point B is16.0MPa which is used as the initial tensile stress in cohesive zone modelling later. More details of failure locus are also displayed in Figure 5. 5. It shows that the failure is of cohesive style through the adhesive layer and main adhesive remained at the surface of fixed arm piece. Peel strength reached to the maximum value at point A because rich resin in the beginning of bonded area, then failure entered into adhesive style. In the range of A to B, most of adhesive remained at peel arm and strength reduced sharply then increased a little again because cohesive failure started from

position B. This AB range also can be considered as adhesive failure. Range of B to D is cohesive failure area but adhesive mainly remained at fixed arm. Test stopped at position D. It is noted that the stress at point B is found to be 16.0±0.4MPa.

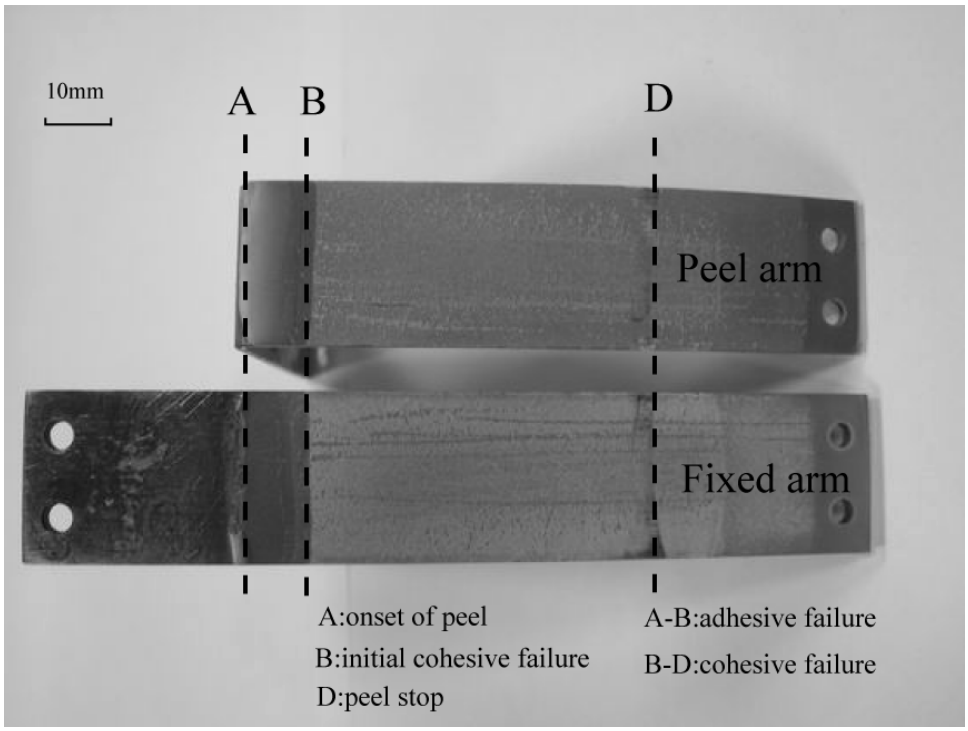

Figure 5. 5 Fracture surface of Fixed Arm Peel test (0.2mm adhesive thickness)

The software used to calculate the adhesive fracture toughness is supported by Imperial College, the input data and calculated results are shown in Table 5. 1

Table 5. 1 Fixed arm peel test parameters and results using 0.2mm thickness adhesive (Imperial College (ICpeel 2006))

Peel arm properties					Adhesive layer		Test parameters	
E Gpa	σ_y Mpa	α Bilinear	h mm	w mm	h mm	E GPa	P N	θ degree
199.3	400	0.038	1.6	25.4	0.2	3.0	215	91*
Results								
G_c N/mm	Gp N/mm	G_{total} N/mm	G N/mm	correction %	θ_0 degree	σ_{max} MPa	Load/unload condition	
1.37	7.24	8.61	8.61	84.06	2.37	200.88	Elastic-plastic	

* Angle θ is in the range of 90~92 degree during test and is chosen as 91 degree here

In the table above, G_{total} represents the input energy with correction of stored tensile elastic strain energy and dissipated tensile plastic energy in peel arm, G represents input energy without correction. It is cleared that both G_{total} and G have a very similar value which implies that the energy caused by tension in peel arm can be neglected.

Thus, only the bending plastic energy G_p is considerable. Cohesive fracture toughness G_c was obtained in term of the Eq.5- 1. θ_0 is the root rotation, i.e. the angle between the peel arm and fixed arm when testing. σ_{max} is the calculated maximum stress in fracture zone. Correction value of 84.06% describes the ratio of G_p to G_{total}. It should be appreciated that the comparisons of test geometries were complemented by Kinloch and Williams (Kinloch and Williams 2002). They found both Standard Tapered-Double Cantilever Beam (TDCB) specimen and Fixed Arm Peel specimen produced very similar fracture energy when the same rubber toughened epoxy was used. This gives confidence for the application of Fixed Arm Peel test.

Fixed arm peel with 0.5mm adhesive thickness has different curve compared with 0.2mm adhesive specimen and is shown in Figure 5. 6. The failure locus of 0.5mm adhesive specimen is shown in Figure 5. 7. It is found that the AB range of thicker adhesive specimen is longer than of thin adhesive specimen; this may be because that load force drops so quickly from maximum point to minimum point and causes unstable propagation.

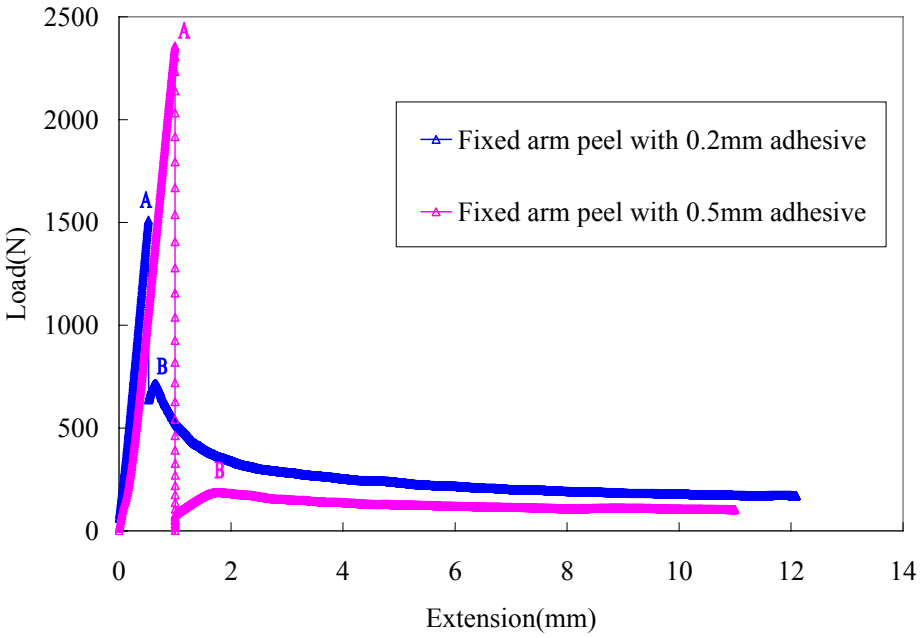

Figure 5. 6 Comparison of typical load-displacement between 0.2mm adhesive and 0.5mm adhesive

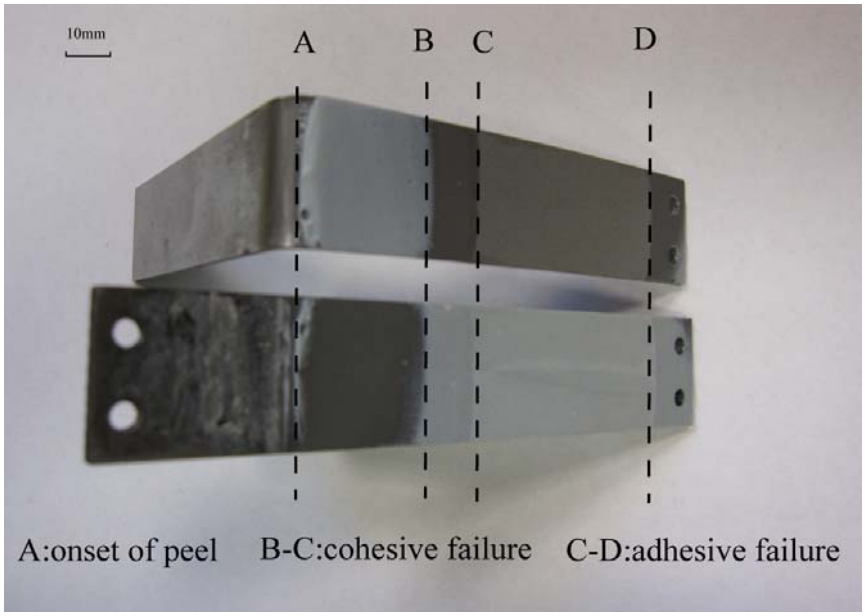

Figure 5. 7 Failure surface of Fixed Arm Peel with 0.5mm adhesive thickness

Because thicker adhesive was used between arms, it is difficult to trigger the onset of failure at the point A thus the onset peel load of 0.5mm adhesive specimen reaches higher values than 0.2mm adhesive specimen. After the onset of failure, load drops down very quickly till zero at point B. Range AB represents semi-cohesive failure and more adhesive remains on the fixed arm similar to the 0.2mm adhesive specimen. At the point B, failure steered toward to peel arm and most adhesive remained on peel arm. Starting from point C, failure steered toward peel arm more and a total adhesive failure style occurred. The higher onset failure load may be because thicker adhesive layer yields more plastic deformation and endures higher stress at the beginning, but failure changes from semi-cohesive style to adhesive style which implies that specimens with thicker adhesive have un-stable failure process. Thus specimens with 0.5mm adhesive thickness have lower energy release rate of 1.03 ± 0.23N/mm compared with 1.37 ± 0.20N/mm of 0.2mm adhesive thickness. However G_c of 0.5mm specimens is not much lower than that of 0.2mm specimens, this is because bigger plastic zone at the crack front and peel angle θ is a little more than 90° during peel test. The different failure paths of 0.2mm adhesive and 0.5mm adhesive are shown in Figure 5. 8. It is clear that thicker adhesive specimen tends to have adhesive failure and it is difficult to determine the energy release rate since there are three steps in the failure propagation.

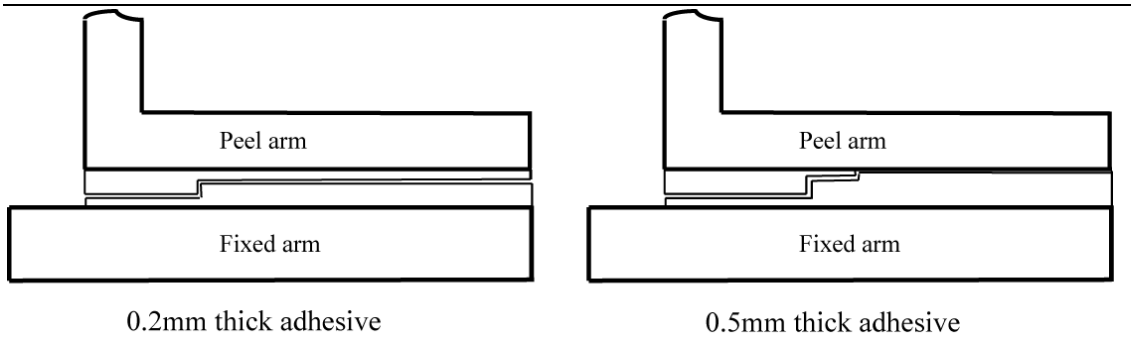

0.2mm thick adhesive 0.5mm thick adhesive

Figure 5. 8 Comparison of failure locus of 0.2mm specimen and 0.5mm specimen

5.2 Mode-II test (Four Point End Notched Flexure)

Three point ENF is commonly used for mode-II test but it has a shortcoming that the crack propagation in specimens is unstable and only one data point can be obtained to calculate the G_{IIc} (Schuecker and Davidson 2000). So the modified test of the 4 point End Notched Flexure specimens (see Figure 5. 9) was applied in this work which consists of two uniform hardened steel adherends bonded by one adhesive layer in the middle and a pre-crack was created artificially in one end of specimen. It is noted that the specimen width is 25.4mm. The initial crack length is 58mm which implies that the distance between left load roller of inner span to the crack tip is 10mm (usually 10-15mm is needed), this distance is designed to remove undesirable effects from the compressive stresses of the load roller. The inner span and outer span lengths were chosen as 94mm and 190mm, respectively, and the inner span locates at the centre position of outer span which leads to a 0.5 span ratio (d/L).

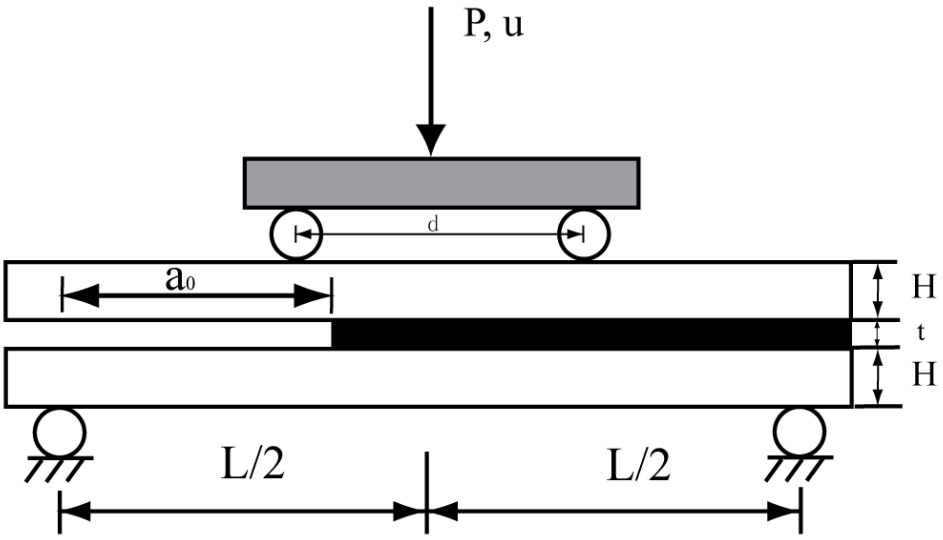

Figure 5. 9 Schematic of 4-point End Notched Flexure specimen. L=190mm, H=1.60mm, t=adhesive thickness, d=94mm, a_0 (initial crack length)

In this test, several data points can be obtained because crack growth is stable under displacement control. It should be noted that the yield stress and Young's modulus are 1400MPa and 199300MPa respectively which were obtained in previous tests (Chapter 4). In order to make beam theory valid in calculating the G_{II} of End Notched Flexure, several aspects must be taken into account carefully. First the adherends are only allowed to deform elastically through the whole test, thus the specimen's dimension and the distance between the load point and crack tip must be large enough to achieve the above purpose. Second the displacement of load point should be increased steadily in order that the shear deformation at the crack tip is developed at a comparatively constant speed. Third the crack propagation in ENF depends on its load condition according to other works. Carlsson et al. illustrated that the ENF is unstable when the pre-crack length, a_0, shorter than the 0.35L by adopting the elastic adherend elastic and rigid adhesive (Carlsson, Gillespie et al. 1986). Later Alfredsson developed the stability limit by considering the flexible behaviour of adhesive layer (Alfredsson 2004).

5.2.1 Preparation of 4 point ENF specimen

The same surface treatment was used for Double Lap Joint as described in Chapter 4; the specimen was chosen with 25.4mm width and 232mm long. A polytetrafluoroethylene film (PTFE) with 12μm thickness was inserted between the

two hardened steel adherends to make a mid-plane pre-crack which lead to the 79mm total initial crack at one end of specimen. The film was inserted without folding or crimping. Clips were used to add pressure to both surfaces of specimens after bonding, then specimens were moved to the oven for one hour curing at 120℃; after curing the specimens were cooled down slowly to avoid serious inner stress.

Both side-surfaces of the specimens were polished and measured to obtain the thickness of adhesive. The initial crack tip position was observed under the microscope and the PTFE film was found in the mid-position of the adhesive. One side surface of specimen was sprayed with white colour paint, and then the ruler was marked every 1mm starting from the tip of pre-crack for 60mm.

5.2.2 Test processing of 4 point ENF specimen

The Hounsfield machine was used to perform these quasi-static experiments, and the software of Hounsfield composite mode-I/II fracture toughness test was chosen to record the testing data. Figure 5. 10 shows the photograph of ENF test. A digital camera was used to capture the crack initiation and propagation; the pairs of crack length and corresponding load were recorded by software.

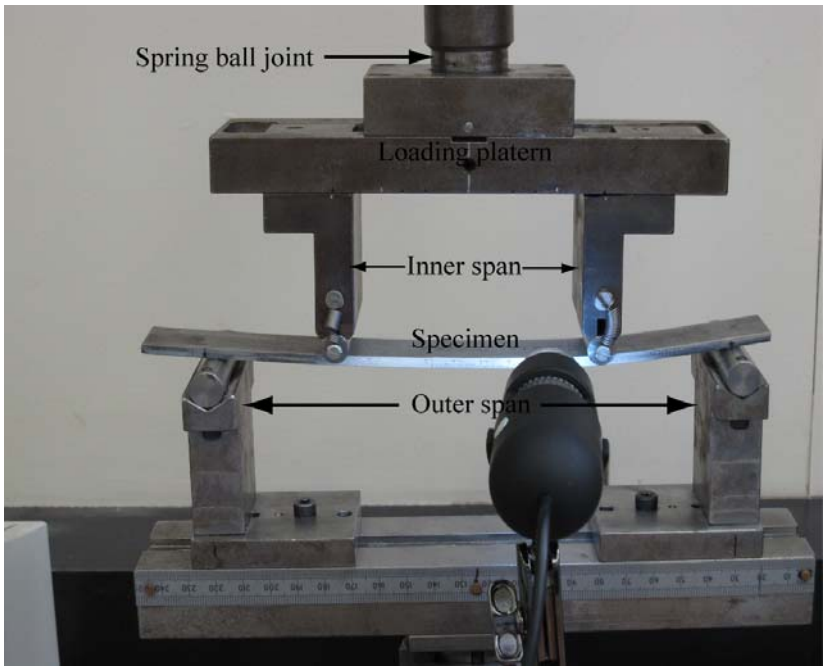

Figure 5. 10 4-point ENF apparatus and specimen

In order to make both load rollers which are attached with the load platen transmit the same amount of force to the specimen, the load is transferred to the load platen via a

spring ball joint, which allows load platen to adjust its angle freely about the axis perpendicular to the specimen's length. In addition, this spring ball joint also allows the load platen to adjust angle about the axis parallel to the specimen's length, thus even load is distributed across the specimen width. Rollers are designed to use bearing system to minimize the friction between parts of fixture and specimens.

Before test the specimen on the support roller was adjusted in line with support base to eliminate any load offset. High resolution digital camera was used to monitor the propagation in the front of crack tip during the experiment. Crack length is recorded on one side of specimen by use of optical equipment. The load and associated deflection values were recorded continually and at least 15 points of crack growths were recorded. The deflection can be recorded through the actuator displacement of machine. First, specimens were tested at a constant speed of crosshead at 0.5mm/min, as the crack occurred from the insert film at least 3 mm, the specimens were unloaded at the constant crosshead speed of 5mm/min and the new crack tip was marked which is considered as the initial pre-crack of next load. Then the specimens were reloaded continually at constant crosshead speed of 0.5mm/min until the crack tip reached to within approximately 15mm of the second load roller of outer span. Finally, the specimen was unloaded at the crosshead speed of 5mm/min to remove the load completely. Both first load and second load were recorded by load and deflection.

5.2.3 Data analysis

The compliance calibration (CC) technique was used to obtain the G_{Π} toughness in all tests. The fundamental equation came from Broek on base of the Griffith energy criterion and self-similar crack propagation (Broek 1986) or from Irwin-Kies equation, it should be noted that this equation is valid on the assumption of no excessive frictional effects between the cracked surfaces.

$$G_{\Pi c} = \frac{p_c^2}{2w}\frac{\partial C}{\partial a} \qquad \textbf{(5- 2)}$$

Where p_c is the critical load representing NL or 5%/Max value during test to calculate initial energy release rate or the average of all p values during crack propagation to calculate propagation energy release rate, w is the width of 4 point ENF specimen. C is the compliance which is defined as the ratio of maximum

displacement and load ($\frac{\delta_{\max}}{p_{\max}}$), a is the crack length. $\frac{\partial C}{\partial a}$ can be determined by the relation of compliance and crack length when crack grows.

The curve of compliance versus crack length was generated and a linear curve fit was used to this curve. Thus the relation between compliance and crack length is expressed as:

$$C = C_0 + C_1 a \quad \textbf{(5- 3)}$$

Substituting the Eq.5- 3 to Eq.5- 2, the fracture toughness of mode-II was obtained:

$$G_{\Pi c} = \frac{p_c^2}{2w} C_1 \quad \textbf{(5- 4)}$$

Thus C_1 is required to determine fracture toughness. The load versus deflection plots of two load cycles are shown in Figure 5. 11. It is obvious that the first load curve has slightly higher value of force than the second load curve. This may be because the crack onset in the first load generated from the inserted PTFE film and the crack onset of second load arose from the real pre-crack which is under self-similar condition. Furthermore, initiation G_{IIc} from insert film were higher than those from pre-crack, thus the second load curve was chosen to determine the fracture toughness.

5.2.4 Experimental results

Generally there are three methods to determine the initial $G_{II}c$ which are nonlinear (NL), 5% offset/maximum load (5%/Max) and visual measurement (VIS). It should be noted that the NL method is more conservative than other methods; while, the 5%/Max method is able to yield results more reproducibly. Because the visual measurement is difficult to practice in adhesively bonded specimens, here NL and 5%/Max were applied and shown in Figure 5. 11.

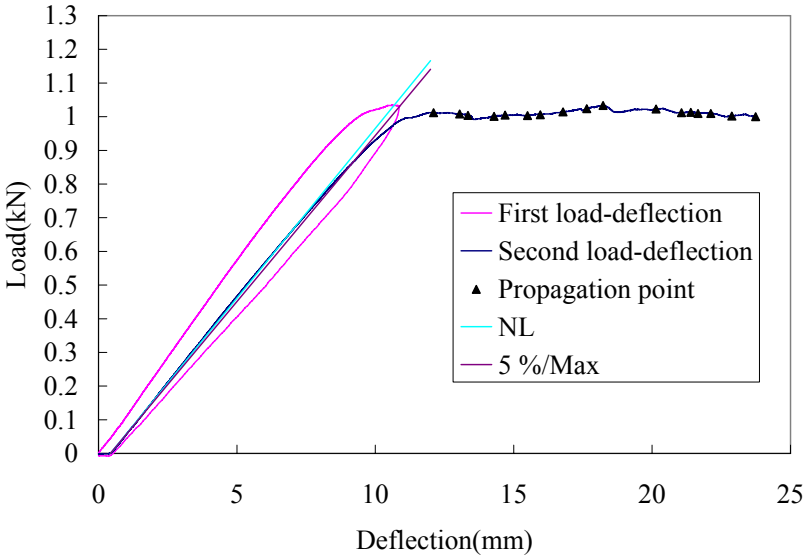

Figure 5. 11 Typical load vs. deflection curve from 4 point ENF test with 0.2mm AV119 adhesive

Compliance was calculated as shown in Figure 5. 12. In typical test, a value of C_1 is equal to 0.00021 which is used in Eq.5- 4 to determine G_{II} corresponding to various crack length. The typical R-curve of 4 point ENF using 0.2mm adhesive is shown in Figure 5. 13, R-curve is crack extension resistance curve which shows the increasing resistance to fracture with growing crack size in materials. A series of tests were performed for 0.2mm adhesive specimens, it is found that the initial G_{IIc} from NL and 5%/Max method have the average values of 3.47±0.25 N/mm and 3.85±0.18N/mm respectively when 0.2mm adhesive was used. These values seem to be a little high because the load did not drop sharply after the initiation of crack. As the crack grows, the fracture toughness exhibits a quasi-constant statue which implies the crack growth is stable. The initial G_{IIc} from 5%/Max result was used later in determining the parameters of mix-mode ratio and cohesive zone modelling.

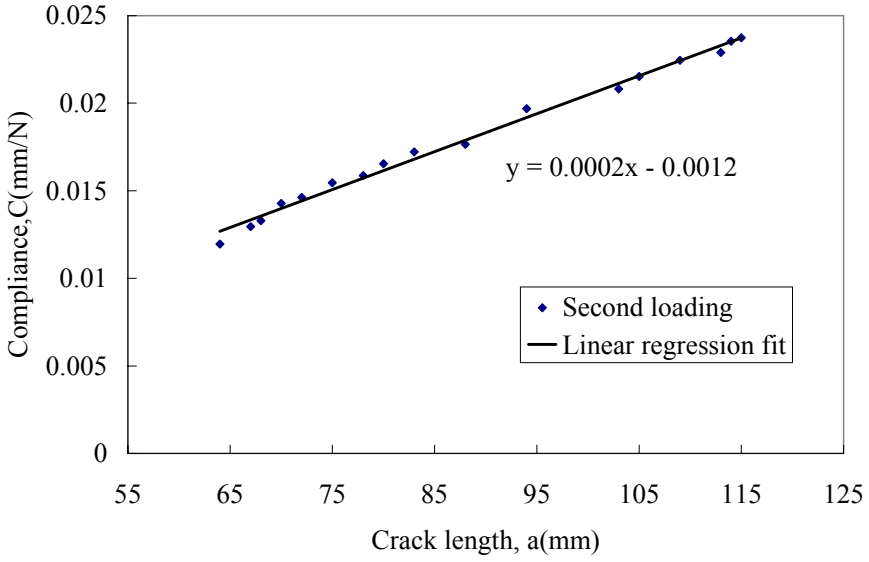

Figure 5. 12 Typical curve of compliance versus crack length from 4Point-ENF test using 0.2mm AV119 adhesive

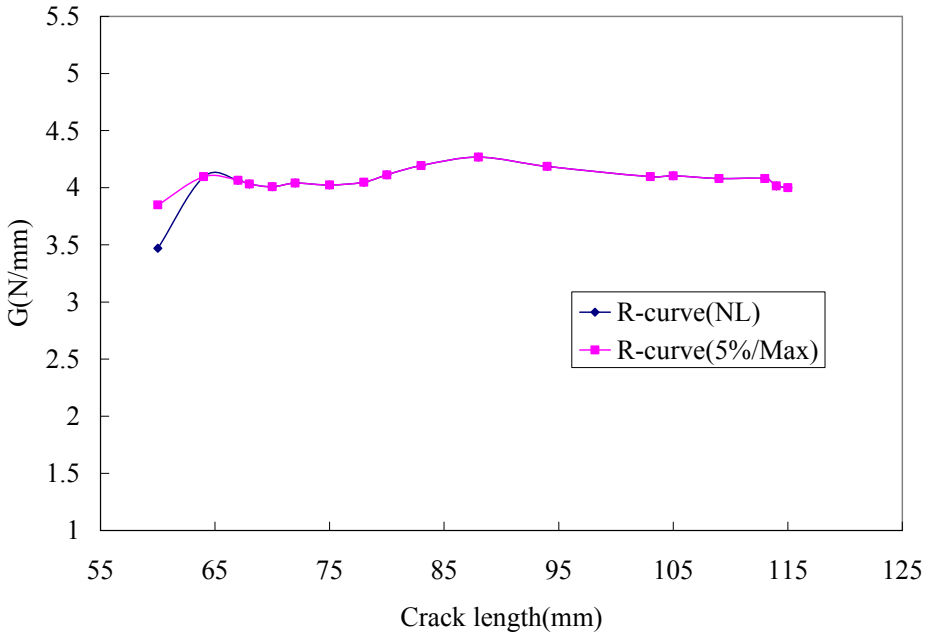

Figure 5. 13 Typical R-curve from 4 point ENF test using 0.2mm AV119 adhesive

The fracture surface of 4 point ENF specimen with 0.2mm adhesive is shown in Figure 5. 14. It is clear that the fracture is still a cohesive-domain failure but most of adhesive remained at the lower adherend.

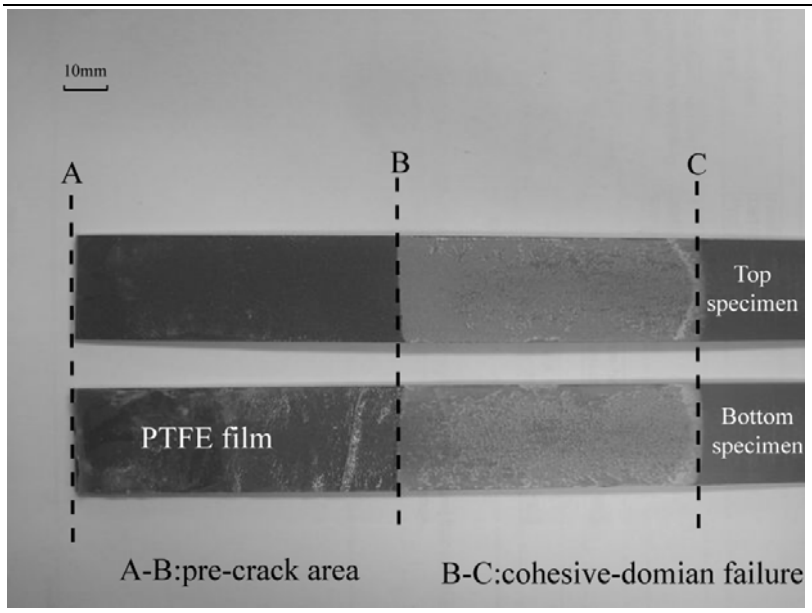

Figure 5. 14 Fracture surface of 4 point ENF test using 0.2mm adhesive

A series of tests were also performed for 0.5mm adhesive specimens. It was found that the fracture kinked into the interface after it started to propagate although the crack was initiated at the middle thickness of adhesive layer. It then propagated along the interface between the adhesive layer and top adherend (compressive adherend). Thus the failure of specimens with 0.5mm adhesive thickness demonstrated mainly interface fracture. The measured mode-II fracture energy of 0.5mm adhesive specimens was similar to the value of 0.2mm adhesive specimens. The measured G_{IIC} of 0.5mm thickness adhesive is 3.80±0.26N/mm using 5%/Max method.

In order to investigate the shear strain ahead of crack tip, one side surface of specimen was finely polished and straight lines were cut vertically through the direction of specimen thickness by sharp razor, different length of shear deformed zone were found in 0.2mm and 0.5 adhesive thickness specimens which is shown in Figure 5. 15. The shear deformed zone was measured from the crack tip to the farthest point with visible shear strain, it is found that specimen with 0.5mm thickness adhesive has longer shear deformed zone than specimen with 0.2mm adhesive thickness. This is because thicker adhesive layer has more freedom and less constraint from adherends to develop shear strain and gives rise to the plastic zone; furthermore increasing the adhesive thickness tends to increase the length of strain localization. However, largest local shear strain was found in the close vicinity of crack tip in both cases. The study of shear strain ahead of crack tip also provides a convenient method to determine the magnitude of

peak shear stress when applying cohesive zone model in other fracture analysis (see Chapter 7).

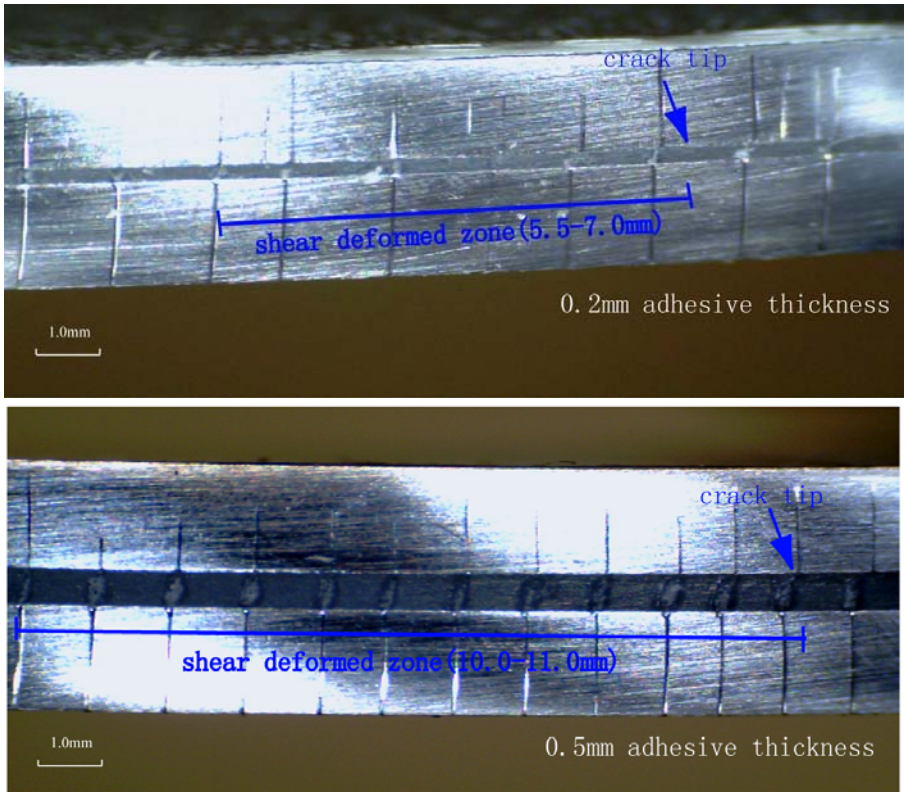

Figure 5. 15 Shear deformation zone ahead of crack tip

5.3 Mixed mode test (Mixed Mode Bending)

The Mixed Mode Bending (MMB) test is applied and is used to determine the mixed fracture of adhesive joints, and it should be noted that this test has been adopted as a standard of ASTM in 2003. The scheme of MMB test is shown in Figure 5. 16. It is noted that the outer span length ($2L$) is 140mm; adherend thickness (H) is 1.6mm, adhesive thickness (t) is 0.2mm; the specimen width (W) is 25.4mm, the initial crack length (a_0) is 35mm; the lever length (c) is adjusted to obtain various mixed mode ratio. It is known that the adherend's yield stress is 1400MPa and adherend Young's modulus is 199300MPa (see Chapter 4).

The mixed mode ratio is determined by the relative magnitudes of two loadings which are determined by the position c. When load is applied at the mid-span (c=0), MMB test becomes pure ENF test. When load lever is removed and load is applied at the hinge connector directly, DCB test occurs. The load lever is made by aluminium which only contributes 7N (this force comes from the mass of lever) to specimen and load

lever is much bigger than specimen in term of volume, thus the weigh of lever is assumed to be negligible and it is assumed to be much stiffer than specimen. Frictional force between apparatus and specimens are reduced via bearing mounted rollers. Specimen was held by the base of MMB apparatus stationary when the load lever loaded the specimen. The downward force is applied to the lever and an upward force is applied to the end of MMB specimens via hinge such that the load remains vertical during test. The lever may rotate during the test which results in unexpected geometric nonlinearity, thus specimen should be held on the base at a specific height such that the load is slightly higher than the mid-plane of specimen (Reeder and Crews 1992).

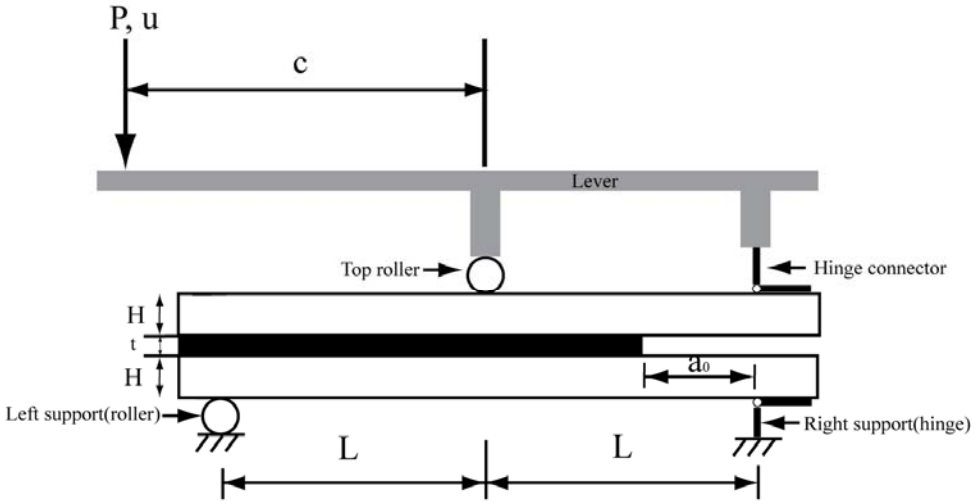

Figure 5. 16 Schematic of a Mixed Mode Bending (MMB) specimen

5.3.1 Preparation of MMB specimen

The manufacture of MMB specimens followed the same process as making 4 point ENF specimens. The two steel adherends of specimen has 1.6mm thickness, 25.4mm width and 232mm length. Adherends were made of gauge steel and then hardened. After surface treatment like ENF, AV119 adhesive was pasted to surfaces of both adherends, and then the adherends were degassed twice for 1 hour under 50℃. After degassing sufficiently, a Teflon film with 12μm thickness was inserted between two hardened steel adherends to make a mid-plane pre-crack which gave the 55mm total initial crack in one end of specimen. It is noted that the effective pre-crack length is 35mm. Clips were used to add even pressure to both surfaces of specimens after bonding, then specimens were moved in oven with one hours curing at 120℃, after

curing specimens were cooled down slowly to avoid higher inner stress.

All surfaces of specimens were polished especially for the side surfaces. The thickness of adhesive was measured under high resolution microscope. The initial crack tip position was found under microscope observation and the PTFE film was found at the mid-position of adhesive approximately.

Hinge tabs which are connected to MMB apparatus were made by gauge steel then hardened and have the same width as specimen. The hardened tabs can be reused many times since they are not deformed during test. It is noted that screws were used to connect the hinge tab and MMB apparatus. Hinge tabs which are connected to MMB specimens were made by commercial hinge piece. All pieces have more than 25mm width and 10mm length bonded with specimens. Before bonding, the bonding surfaces of tabs and specimens were given proper treatment such as combined degreasing and grit blasting to avoid debonding during test. The tabs were bonded to both top and bottom of specimen via two-part adhesive cured at room temperature for 48 hours which gave the 35mm effective pre-crack length (a_0) from the tab (hinge piece attached in MMB) to the end of inserted PTFE film. The effective pre-crack length is set to $0.45L<a_0<L-3h$ where h is the half thickness of MMB specimen and L is half span of two support roller in MMB apparatus.

It should be noted that the hinge piece bonded to MMB specimens will suffer from very strong force under high mode-II mode ratio test (for example, $G_{II}/G_T=0.8$), this force causes tab excessive deformation and then debonding occurs before the whole test is finished. Thus block steel is chosen to bond with tab to make compound tab in order to prevent any debonding problem in test.

One side surface of specimen was sprayed by white colour paint, and then the ruler was marked every 1mm starting from the tip of pre-crack for 60mm. In this test, the displacement was recorded from the crosshead of machine, thus the load system compliance must be subtracted from whole compliance by use of calibration MMB specimens. The calibration specimen was made by the same hardened steel as MMB adherend and bonded with tabs.

5.3.2 Test processing of MMB specimen

The MMB apparatus and specimens are shown in Figure 5. 17. A good calibrated machine of Instron 5584 machine was used to perform the quasi-static experiments. The high resolution optical microscope was used to monitor the crack initiation and propagation on one side of specimen. The crack front was observed by this equipment and selected propagations of crack length were recorded synchronously with load and displacement of load point. A constant displacement rate of 0.5mm/min was chosen to implement the test since it is closer to a quasi-static situation and allows more data to be captured. After crack reached the specific length, the crosshead of machine returned automatically at the speed of 5mm/min. The load returned to zero such that no damage occurred in the specimen. The load force and displacement of crosshead were recorded by software and all tests were performed at room temperature and 50±10% humidity. A series of tests were performed for 0.2mm adhesive specimens. Additionally, the calibration specimen was test independently at each mixed mode ratio.

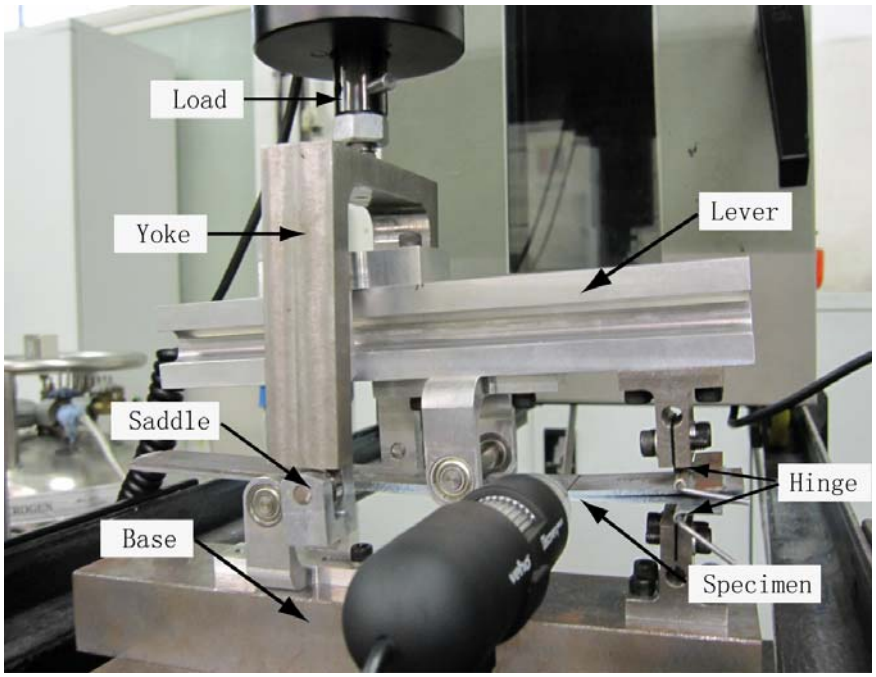

Figure 5. 17 MMB apparatus and specimen

5.3.3 Data analysis

Fracture initiation can be determined by both nonlinear criterion (NL) and 5% offset/maximum load criterion (5％/Max). It was found that visual observation criterion (VIS) is difficult to determine the initial crack especially at the high mode-II

regime. Fracture propagation toughness is collected when the fracture is processing in the stable way. The linear-elastic assumption is used to calculate the mixed-mode toughness of MMB specimen, which implies that the damage zone or plastic deformation at the debonding front, or both, must be small enough compared to the smallest dimension of specimen (typically this dimension refers to the thickness of MMB specimen). Thus, increasing the thickness of specimens or the use of stiffer materials for adherends of MMB specimen can produce more accurate results.

It should be noted that the calculations of mixed mode fracture energy was implemented in accordance with ASTM D6671-01 standard. It is well known that there is fracture process zone (FPZ) occurring ahead of crack front, thus energy dissipation caused by FPZ should be taken into account in the fracture energy calculation. Here a combination of compliance calibration method (CCM) and corrected beam theory (CBT) is introduced to data reduction scheme since pure CCM and CBT has their own disadvantages to locate the crack tip in fracture propagation. Thus to overcome this problem an equivalent crack length taking into account root rotation correction and FPZ effect and an equivalent Young's modulus were applied in this methodology.

It is noted that the analysis scheme is processed according to ASTM D6671-01 standard and Eq. 5- 5 to Eq.5- 13 are derived from this standard. The length of lever, *c*, and mixed mode ratio ζ is determined by the Eq. 5- 5. It is noted that Eq. 5- 5 is the curve fit to an iterative solution of Eq. 5- 8 and 5- 9 (Reeder 2003).

$$c = L(0.167 + 0.000137\tilde{a}^{2} - 0.108\sqrt{\ln(\tilde{a})^{2}}\zeta^{4} + \frac{01400 + 0.725\tilde{a}^{2} - 141\ln(\tilde{a}) - 302\ln(\zeta)}{219 - 5000\zeta + 55\ln(\tilde{a})}) \quad \textbf{(5- 5)}$$

Where $\zeta = \frac{G_{II}}{G} = \frac{G_{II}}{G_I + G_{II}}$; the term $\tilde{a}$ is the non-dimensional delamination length and equal to $\tilde{a} = \frac{a_0}{h\chi}$; The term a_0 is the initial crack length in specimen and *h* is the half thickness of specimen; the term χ is the crack length correction term which represents the shear deformation and bending deformation ahead of delamination front, and it is a function of material modulus and defined by the following equation (Hashemi, Kinloch et al. 1990; Kinloch, Wang et al. 1993):

$$\chi = \sqrt{\frac{E_{11}}{11G_{13}}\left\{3-2\left(\frac{\Gamma}{1+\Gamma}\right)^2\right\}} \quad \textbf{(5- 6)}$$

and

$$\Gamma = 1.18\frac{\sqrt{E_{11}E_{22}}}{G_{13}} \quad \textbf{(5- 7)}$$

Because MMB specimen is made by homogenous steel and adhesive, this implies that the specimen can be assumed as springs-in-parallel or springs-in-series. Thus E_{11} is dominated by steel Young's modulus and E_{22} is dominated by adhesive Young's modulus. In addition, G_{13}, is assumed equal to G_{12} and dominated by adhesive too.

The total mixed mode fracture toughness, G_c, is the sum of mode-I fracture toughness and mode-II from MMB test whose values are determined by the following two equations (Wang and Williams 1992; Kinloch, Wang et al. 1993):

$$G_I = \frac{12P^2(3c-L)^2}{16b^2h^3L^2E_{1f}}(a+\chi h)^2 \quad \textbf{(5- 8)}$$

$$G_{II} = \frac{9P^2(c+L)^2}{16b^2h^3L^2E_{1f}}(a+0.42\chi h)^2 \quad \textbf{(5- 9)}$$

Where P is the load applied at the MMB specimen via yoke, L is the half span of two support roller, a is the instantaneous crack length, b is the width of specimen and h is the half thickness of specimen. E_{1f} is the bending modulus of MMB specimen and is obtained by using back calculation method (Reeder 2003).

$$E_{1f} = \frac{8(a_0+\chi h)^3(3c-L)+[6(a_0+0.43\chi h)^3+4L^3](c+L)^2}{16L^2bh^3C_{MMB}} \quad \textbf{(5- 10)}$$

The parameter C_{MMB} is the compliance of MMB specimen which was obtained from the reciprocal slope of load-displacement curve and reduced from the system compliance. Thus, C_{MMB} is calculated by the following equations:

$$C_{MMB} = \frac{1}{m_{MMB}} - C_{sys} \quad \textbf{(5- 11)}$$

$$C_{sys} = \frac{1}{m_{cal}} - C_{cal} \quad \textbf{(5- 12)}$$

$$C_{cal} = \frac{2L(c+L)^2}{E_{cal}b_{cal}t_{cal}^{\ 3}} \quad \textbf{(5- 13)}$$

It is noted that m_{MMB} and m_{cal} are the slope of displacement-load curves of MMB specimen and calibration specimen under various mixed mode loadings, respectively. C_{cal} is the stiffness of calibration specimen and derived from simple beam theory by neglecting crack length term (Reeder 2003). E_{cal} is the Young's modulus of calibration specimen. b_{cal} and t_{cal} are width and thickness of calibration specimen.

When the force P is represented by P_{NL} or $P_{5\%/Max}$ and initial pre-crack length, a_0, is used, the initial fracture toughness can be obtained. When the force P is measured by load as the fracture propagates and instantaneous crack length, a, is used, the propagation fracture toughness is obtained.

5.3.4 Experimental results

A typical load-displacement curve from MMB test using 0.2mm adhesive thickness is shown in Figure 5. 18. Here the mixed mode ratio is defined as the ratio of mode-II fracture energy to total fracture energy. It was found that MMB specimen has unstable propagation toughness values in high mode-II regime.

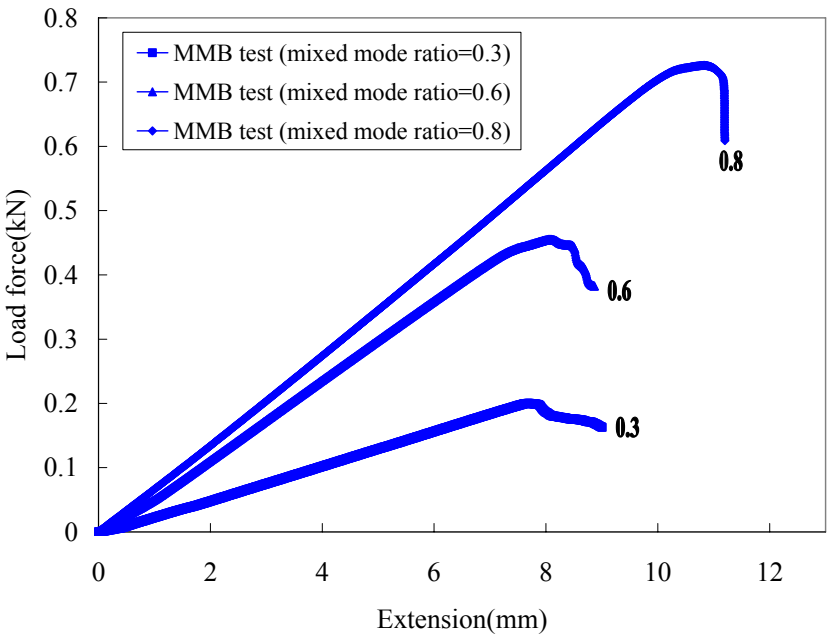

Figure 5. 18 Typical load force vs. load point extension of MMB test under 0.3, 0.6 and 0.8 mixed mode ratio (0.2mm adhesive thickness)

In this work, it is the major purpose to determine the initial fracture energy. The results of MMB test with various mixed-mode ratios are shown in Table 5. 2, the average load

forces were used for every mixed mode ratio and it is noted that the maximum difference of load force in all test is less than 0.02kN. The initial fracture toughness under various mixed-mode ratio tests was used to determine the BK ratio which was used for cohesive element application.

Table 5. 2 Results of MMB tests

Mixed mode ratio G_{II}/G	Crack initiation	Average P (N)	G_I (N/mm)	G_{II} (N/mm)	G_{total} (N/mm)
0.3	NL	205.15	1.02	0.43	1.45
	5%/Max	209.30	1.07	0.45	1.52
0.6	NL	422.20	0.90	1.37	2.27
	5%/Max	440.15	0.98	1.49	2.47
0.8	NL	702.65	0.60	2.44	3.04
	5%/Max	715.82	0.62	2.53	3.15

MMB test is easy to determine the fracture energy components at various mixed mode ratio, but it should be noted that this method is not very accurate to determine the energy distribution at both very high mode-I and mode-II regimes. There is no effect of friction since the surfaces are in opening mode. The MMB fracture surfaces are shown in Figure 5. 19. It is found that all specimens under three different mixed modes load demonstrate similar failure locus in which most of the adhesive remains on the bottom adherend and there is very little adhesive resin left on the top adherend. It is also found that the instantaneous crack front is parallel to the initial pre-crack front which implies that the crack grew uniformly under test.

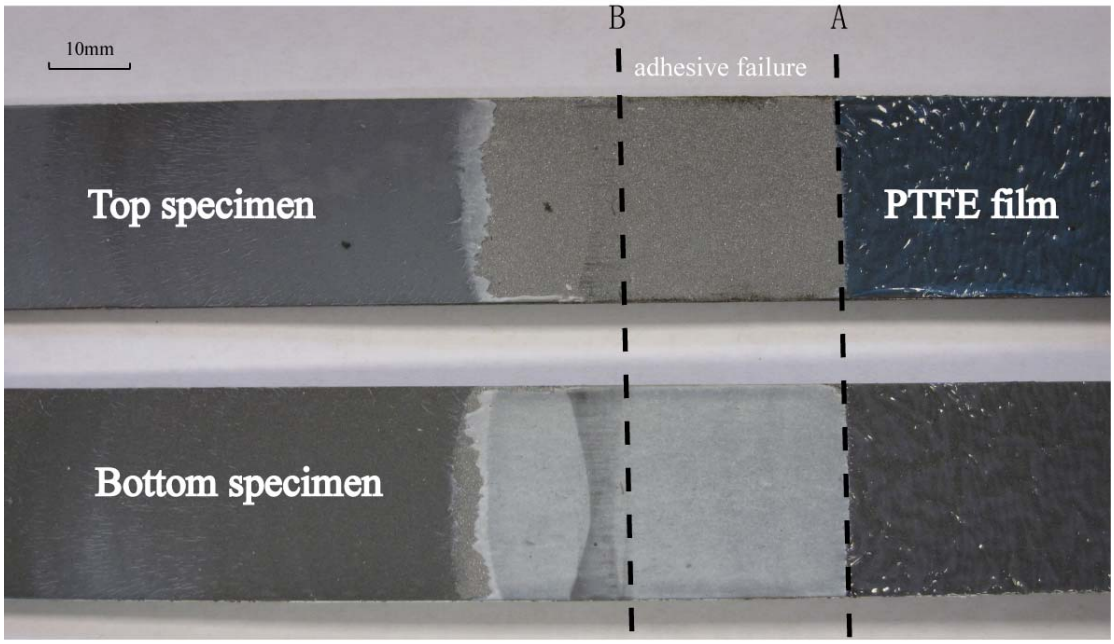

Figure 5. 19 Typical fracture surface of MMB test using 0.2mm adhesive

5.4 Results and discussions

Although the energy release rate G_{IC} is considered to be independent on the specimen thickness, it is found the adhesive thickness in specimen does affect the failure path of fixed arm test and then vary the energy release rate of mode-I slightly. The measured mode-I energy of 0.2mm adhesive specimen is slightly higher than it of 0.5mm adhesive specimen, and quicker fracture propagation in the beginning was found at the latter specimens. This implies that mode-I fracture energy decreases with increased adhesive thickness because of rapid crack tip opening under load. Failure path also demonstrates that specimens using thin adhesive layer has more stable fracture propagation than specimen using thick adhesive layer in Fixed Arm Peel tests.

Comparing pure mode-I fracture energy and pure mode-II fracture energy which were obtained from fixed-arm peel test and 4 point ENF test, respectively, it is found that mode-I fracture energy is much higher than mode-II fracture energy. This implies that the fracture energy is strongly dependent on mode of failure. This is because the adhesive layer is able to deform with higher plastic strain when it deformed by shear stress than deformation from tensile stress; this is confirmed by the basic mechanical test results. It is found that shear strain has twice the value than tensile strain at each corresponding maximum stress (see Figure 3. 1). The test of fixed-arm peel bonded by

0.2mm thickness adhesive has maximum normal stress of 16MPa before fracture propagation which is corresponding to 0.8% tensile strain in tensile test, while in the test of 4 point ENF used the identical adhesive thickness the maximum shear strain ahead of crack tip was around 5% as the corresponding shear stress is 43MPa (see Chapter 4). It is obvious that mode-II load causes failure at higher strain than mode-I load.

Large plastic zones were found at the very vicinity of crack tip in all specimens including 0.2mm and 0.5mm adhesive ENF specimens. ENF test shows that specimens with 0.5mm adhesive have longer shear deformed zone or plastic zone than specimens with 0.2mm adhesive. This is because that thicker adhesive layer is able to deform easier due to less constraint from top and bottom adherends, however, the fracture locus was dominated by interface failure and the measured mode-II energy is similar to those with 0.2mm adhesive thickness. This implies that the fracture energy is controlled by both fracture mode and plastic zone when the same adhesive and adherend is tested under the identical load condition. Other factors like voids in the adhesive layer may affect fracture energy. It is known that hydrostatic tension locates ahead of crack tip and decreases monotonically with increasing distance from the crack tip. This hydrostatic stress will cause failure though void growth or cavitation and plays an important role in adhesive layer. It is understandable that thicker adhesive layer possibly has more micro voids involved and is more sensitive to hydrostatic stress.

MMB test combined opening and shearing failure successfully, mode-I and mode-II fracture energy were separated from test data using the joint method of compliance calibration and modified beam theory. This test allows to investigate failure analysis in other adhesive applications. The test results of peel, 4-point ENF and MMB were applied at modelling applications (see Chapter 7).

Chapter-6 Constitutive response and microstructure model of rubber toughened epoxy system

6.1 Introduction

Most structural adhesives including AV119 are sensitive to the hydrostatic component of stress which implies that materials become stronger with increasing pressure; their compressive yield stresses are higher than tensile yield stresses. Thus the extended Drucker-Prager (D-P) model was chosen as yield criterion because of a few advantages. Drucker-Prager model allows materials to harden isotropically and is able to simulate inelastic dilation and volume change with inelastic behaviour and flow rule.

In order to understand the effects of material properties and rubber fraction to the mechanical behaviour, a 3D cube model was chosen to present the microstructure of rubber toughened system. In this model, rubber particles in epoxy matrix were assumed to distribute uniformly. Due to symmetry every cube model consisted of four 1/8 rubber particles.

It should be noted that the knowledge of constitutive response and application of Drucker-Prager model have been developed from books (Chen and Zhang 1991; Chen and Han 2007a), ABAQUS manual (ABAQUS Analysis User's Manual 2007b) and practice guide (Dean and Crocker 2001).

6.2 Constitutive response available to toughened structural adhesive

6.2.1 Yield criteria

The stress-strain curve of structural adhesive consists of elastic deformation under low load and plastic deformation after yielding. Normally there are two categories of yield criteria available to describe the behaviour of stress strain relationship after yielding which is shown in Figure 6. 1. It should be noted that I_1 is the first stress invariant and J_2 is the second deviatoric stress invariant. The axis of q represents the Von Mises

equivalent stress ($\sqrt{3J_2}$) and the axis of p represents the equivalent hydrostatic stress ($\frac{1}{3}I_1$).

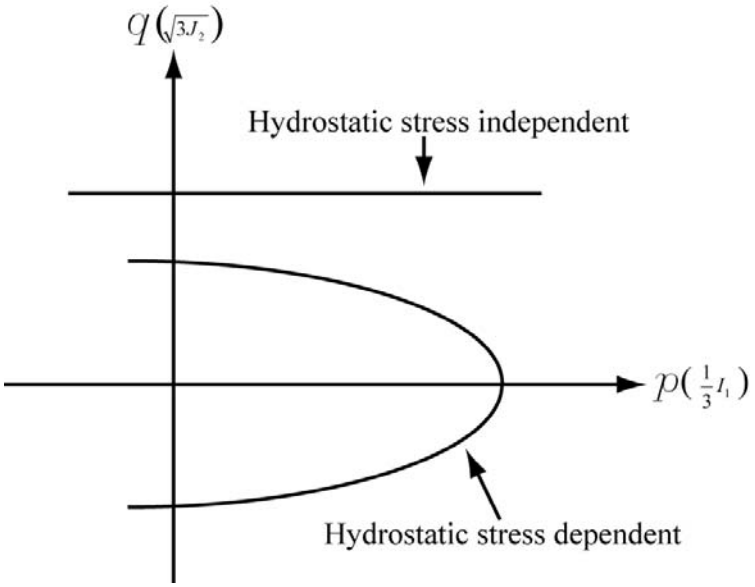

Figure 6. 1 General shapes of yield surface in meridian plane for hydrostatic stress dependent and independent materials

It is noted that any plane containing the hydrostatic stress is called meridian plane (Chen and Zhang 1991). For hydrostatic stress dependent materials their meridians are dependent on hydrostatic axis, and for hydrostatic stress independent materials, their meridians are straight lines parallel to the hydrostatic axis, which means that shear stress must be the main cause of yielding behaviour.

The Tresca yield criterion is the first hydrostatic stress independent yield criteria which comes from the study of metal and assumes that yielding will occur when the maximum shear stress reaches a critical value at one point. Thus in terms of principal stress (σ_i, i=1, 2, 3) this criterion is described as follows:

$$Max(\frac{1}{2}|\sigma_1-\sigma_2|,\frac{1}{2}|\sigma_1-\sigma_3|,\frac{1}{2}|\sigma_3-\sigma_1|)=\sigma_{cri} \quad \textbf{(6-1)}$$

Where σ_1, σ_2, σ_3 are the principal stresses. When yielding occurs, one-half of the maximum absolute value of the difference between three principal stresses must reach the σ_{cri} value. Furthermore in the plane stress condition, the yield locus is a hexagon. If three principal stresses are in the order of $\sigma_1>\sigma_2>\sigma_3$, the Eq.6-1 can be rewritten in the form as follows:

$$\frac{1}{2}(\sigma_1-\sigma_3)=\frac{1}{\sqrt{3}}\sqrt{J_2}\left[\cos\theta-\cos\left(\theta+\frac{2}{3}\pi\right)\right]=\sigma_{cri}\ (0\leq\theta\leq60^{o}) \qquad \textbf{(6- 2)}$$

It is known that the parameter θ is the angle between the projection of vector of a point and the projection of σ_1 on the deviatoric plane (any plane perpendicular to the hydrostatic axis is called deviatoric plane). In simple tension, the materials constant σ_{cri} can be determined by σ_{yt}. Then:

$$\sigma_{cri}=\frac{\sigma_{yt}}{2} \qquad \textbf{(6- 3)}$$

Combining Eq.6- 2 and Eq.6- 3 , the Eq.6-1 can be rewritten in the form as follows:

$$f(J_2,\theta)=2\sqrt{J_2}\sin\left(\theta+\frac{1}{3}\pi\right)-\sigma_{yt}=0\ (0\leq\theta\leq60^{o}) \qquad \textbf{(6- 4)}$$

Eq.6- 4 is the Tresca criterion in terms of the second deviatoric stress invariant. Tresca criterion does not include the influence of the intermediate principal stress although the maximum shear stress criterion is simple to use. The Von Mises criterion supplements the shortcoming of Tresca criterion using the maximum shear strain energy or octahedral shear stress (τ_{oct}) which reaches a critical value at a point of the materials. τ_{oct} can be expressed as follows:

$$\tau_{oct}=\frac{2}{3}\sqrt{\tau_{12}^2+\tau_{23}^2+\tau_{13}^2}=\sqrt{\frac{2}{3}J_2} \qquad \textbf{(6- 5)}$$

Where τ_{12}, τ_{23}, τ_{13} are the principal shear stresses. Von Mises criterion states that yielding happens as the octahedral shear stress reaches a critical value (σ_{cri}). So, Von Mises criterion can be rewritten to the form as follows:

$$f(J_2)=J_2-\sigma_{cri}^2=0 \qquad \textbf{(6- 6)}$$

Eq.6- 6 can be represented in terms of three principal stresses:

$$(\sigma_1-\sigma_2)^2+(\sigma_2-\sigma_3)^2+(\sigma_3-\sigma_1)^2=6\sigma_{cri}^2 \qquad \textbf{(6- 7)}$$

Where σ_{cri} is the yield stress in pure shear. When the material is under uniaxial tensile test ($\sigma_1=\sigma_{yt}$, $\sigma_2=\sigma_3=0$), σ_{cri} is determined as follows:

$$\sigma_{cri}=\frac{\sigma_{yt}}{\sqrt{3}} \qquad \textbf{(6- 8)}$$

So Eq.6- 8 can be expressed as follows:

$$J_2-\frac{\sigma_{yt}^2}{3}=0 \qquad \textbf{(6- 9)}$$

From Figure 6. 1, it is obvious that the elastic-plastic response in tension and

compression is equivalent for hydrostatic-pressure independent materials, which means tensile yield stress is the same as compressive yield stress. But polymers including adhesives show differences in yielding behaviour between tension and compression due to the nature of the chemical chain structure; hence a hydrostatic pressure dependent yielding criterion must be introduced to represent the mechanical behaviour of adhesive. Drucker-Prager model is the form of hydrostatic stress dependent criterion available in many FEA codes, and it is originally derived from the theories of soils (Jeong and Pan 1995).

The Drucker-Prager criterion is an extension of Von Mises criterion by taking account the influence of hydrostatic pressure on the yielding of materials. The extension is introduced by an additional term that is proportional to I_1 which is the first stress invariant. This criterion can be described as follows:

$$f(I_1, J_2) = \alpha I_1 + \sqrt{J_2} - k = 0 \qquad \textbf{(6- 10)}$$

Where α and k are material constants. Under uniaxial tension and uniaxial compression tests, both tensile yield stress (σ_{yt}) and compression yield stress (σ_{yc}) can be obtained:

$$\sigma_{yt} = \frac{\sqrt{3}k}{1+\sqrt{3}\alpha} \qquad \textbf{(6- 11)}$$

$$\sigma_{yc} = \frac{\sqrt{3}k}{1-\sqrt{3}\alpha} \qquad \textbf{(6- 12)}$$

and

$$\alpha = \frac{m-1}{\sqrt{3}(m+1)} \qquad \textbf{(6- 13)}$$

$$k = \frac{2\sigma_{yc}}{\sqrt{3}(m+1)} = \frac{2m\sigma_{yt}}{\sqrt{3}(m+1)} \qquad \textbf{(6- 14)}$$

Where m ($m = \frac{\sigma_{yc}}{\sigma_{yt}}$) is the ratio of the compressive yield stress to the tensile yield stress corresponding to the same equivalent plastic strain, ε_p^e, which is defined in Eq. 6- 27. So, Eq.6- 10 can be expressed in term of tensile yield stress σ_{yt} and ratio m as follows:

$$\sigma_{yt} = \frac{\sqrt{3}(m+1)}{2m}\sqrt{J_2} + \frac{(m-1)}{2m}I_1 \qquad \textbf{(6- 15)}$$

When m is chosen as 1, the Drucker-Prager criterion reverts to Von Mises criterion. The Drucker-Prager criterion including linear, hyperbolic and exponent form is based

on the shape of the yield surface in the meridian plane. An isotropic hardening rule is assumed to this criterion which implies all parameters are constant. These three Drucker-Prager models are shown in Figure 6. 2. These models are based on the shape of yield surface in the meridian plane (i.e. *t-p* or *q-p* plane). Thus *p* represents hydrostatic stress, *q* represents Von Mises equivalent stress and *t* is a function of second and third invariants of deviatoric stress. The symbol β is friction angle.

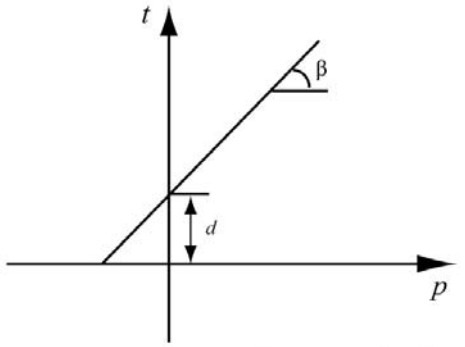

(a) Linear Drucker-Prager $F = t - p\tan\beta - d = 0$

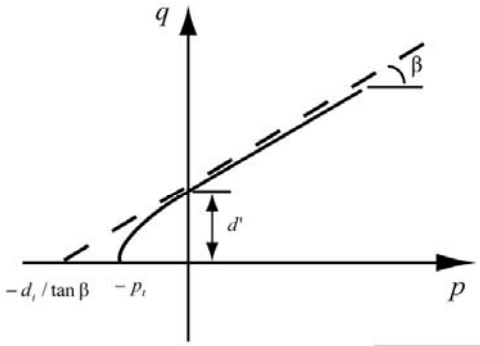

(b) Hyperbolic Drucker-Prager $F = \sqrt{(d^{'}|_0 - p_t|_0 \tan\beta)^2 + q^2} - p\tan\beta - d^{'} = 0$

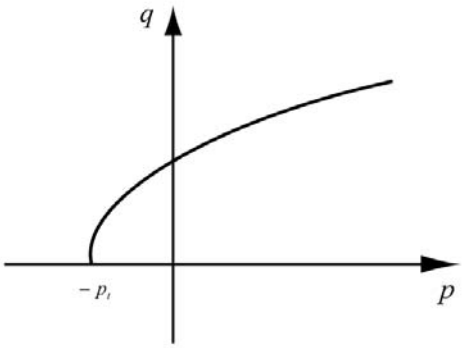

(c) Exponent Drucker-Prager $F = aq^b - p - p_t = 0$

Figure 6. 2 Yield surfaces of three Drucker-Prager models in the meridian plane (ABAQUS Analysis User's Manual 2007b)

6.2.2 Flow criteria

The linear model may have a noncircular yield surface in the deviatoric plane or

π-plane and the accuracy of linear model is limited because it assumes linear dependence of deviatoric stress on hydrostatic stress. So the linear Drucker-Prager criterion cannot describe the behaviour accurately in adhesive bonding area because the bonding interface is highly constrained by the adherends. However this linear criterion is useful for applications where the stresses are mostly compressive.

The hyperbolic and exponent models provide a circular section in the deviatoric plane and both models use the same hyperbolic flow potential. Usually the hyperbolic model is powerful for brittle materials. It is noted that exponent model is much more accurate than hyperbolic model because the latter only provides nonlinear relations between hydrostatic stress and deviatoric stresses at low confining pressures and linear response in high confining pressures.

The flow rule is necessarily introduced to describe the plastic behaviour of materials after yielding, Von Mises proposed a plastic potential function, $g(\sigma_{ij})$, which is a scalar function of the stress tensor (Chen and Han 2007c) Thus, the plastic flow equation can be expressed in the form as follows:

$$d\varepsilon_{ij}^{p} = d\lambda \frac{\partial g}{\partial \sigma_{ij}} \qquad \textbf{(6- 16)}$$

Where dλ is a positive scalar and non-zero only when plastic deformations happen; $d\varepsilon_{ij}^{p}$ presents the plastic strain increment vector in the strain space ε_{ij}. The simplest case of plastic flow is to choose the yield function *f* as plastic potential function. It implies that the direction of increment of plastic strain is the same as the normal direction of yield surface, i.e., *g=f*, thus Eq.6- 16 becomes:

$$d\varepsilon_{ij} = d\lambda \frac{\partial f}{\partial \sigma_{ij}} \qquad \textbf{(6- 17)}$$

The application of above equation means associated flow rule is assumed. If yield function is not chosen as plastic potential function, i.e., *g≠f*, so the non-associated flow rule is assumed. Thus, the flow function $g(\sigma_{ij})$ can be chosen as yield function or an independent function, however, the scalar $d\lambda$ can be obtained by squaring both sides in Eq.6- 17, then:

$$d\varepsilon_{ij} d\varepsilon_{ij} = (d\lambda)^2 \frac{\partial f}{\partial \sigma_{ij}} \frac{\partial f}{\partial \sigma_{ij}} \qquad \textbf{(6- 18)}$$

and

$$d\lambda = \frac{\sqrt{d\varepsilon_{ij}^{p} d\varepsilon_{ij}^{p}}}{\sqrt{\frac{\partial f}{\partial \sigma_{ij}} \frac{\partial f}{\partial \sigma_{ij}}}} \quad \textbf{(6- 19)}$$

Thus, the factor $d\lambda$ is related to the stress and strain invariant. Furthermore, the factor $d\lambda$ can be applied to determine the equivalent plastic strain, In general, there are two different definitions of equivalent plastic strain ε_{p}^{e}; one is based on the accumulated plastic strain, and another is defined in terms of plastic work increment (*dWp*).

The plastic work theory is more general than accumulated plastic strain theory in most cases. dW_p can be defined using the equivalent stress as follows:

$$dWp = \sigma_e d\varepsilon_p = \sigma_{ij} d\varepsilon_{ij}^{p} \quad \textbf{(6- 20)}$$

Where $\sigma_e = \sqrt{3J_2}$, determined by Von Mises equivalent stress which is originally derived from the hardening rule.

$$F(\sigma_{ij}) = C\sigma_e^n \quad \textbf{(6- 21)}$$

Where $F(\sigma_{ij})$ is an isotropic hardening function; C and n are constants. For Von Mises surface case, $F(\sigma_{ij}) = J_2$, and in uniaxial tension, $\sigma_e = \sigma_1$, $\sigma_2 = \sigma_3 = 0$, so C=1/3, n=2, then, $\sigma_e = \sqrt{3J_2}$.

Substituting Eq.6- 17 into Eq.6- 20, it leads to:

$$dWp = d\lambda \sigma_{ij} \frac{\partial f}{\partial \sigma_{ij}} \quad \textbf{(6- 22)}$$

Generally, f is a homogeneous function of degree n of stresses (a function $f(x_1, x_2, ..., x_n)$ of variables x_1, x_2,…x_n is called a homogeneous function of degree n in these variables) (Chen and Han 2007d), thus the above equation can be rewritten as:

$$\sigma_{ij} \frac{\partial f}{\partial \sigma_{ij}} = nF \quad \textbf{(6- 23)}$$

So substituting Eq.6- 19 and 6- 23 to Eq.6- 22, the dWp becomes:

$$dWp = \frac{\sqrt{d\varepsilon_{ij}^{p} d\varepsilon_{ij}^{p}}}{\sqrt{\frac{\partial f}{\partial \sigma_{ij}} \frac{\partial f}{\partial \sigma_{ij}}}} nF = \sigma_e d\varepsilon_p^e \quad \textbf{(6- 24)}$$

If Von Mises model is used which implies that n=2, f =F=J_2, and $\frac{\partial F}{\partial \sigma_{ij}} = s_{ij}$, s_{ij} is deviatoric stress tensor, then $d\varepsilon_p^e$ is determined.

$$d\varepsilon_p^e = \sqrt{\frac{2}{3} d\varepsilon_{ij}^p d\varepsilon_{ij}^p} \quad \textbf{(6- 25)}$$

And equivalent plastic strain ε_p^e is determined by principal plastic strain.

$$\varepsilon_p^e = \sqrt{\frac{2}{3}\varepsilon_{ij}^p \varepsilon_{ij}^p} = \frac{\sqrt{2}}{3}\sqrt{\left[\left(\varepsilon_1^p - \varepsilon_2^p\right)^2 + \left(\varepsilon_2^p - \varepsilon_3^p\right)^2 + \left(\varepsilon_3^p - \varepsilon_1^p\right)^2\right]} \quad \textbf{(6- 26)}$$

It is noted that for Von Mises condition the plastic-incompressibility condition is assumed in Eq.6- 26, i.e., $d\varepsilon_1^p + d\varepsilon_2^p + d\varepsilon_3^p = 0$, in the case of uniaxial tension, it is $\varepsilon_2^p = \varepsilon_3^p = -\frac{1}{2}\varepsilon_1^p$, then $\varepsilon_p^e = \varepsilon_t^p$. Likewise, if plastic-compressibility condition is assumed in Eq.6- 26 (i.e., $d\varepsilon_2^p = d\varepsilon_3^p = (1+v^p)d\varepsilon_1^p$), equivalent plastic strain ε_p^e in shear, tension and compression conditions become:

$$\varepsilon_p^e = \frac{2}{3}(1+v_t^p)\varepsilon_t^p = \frac{2}{3}(1+v_c^p)\varepsilon_c^p = \frac{2}{\sqrt{3}}\varepsilon_s^p = \frac{1}{\sqrt{3}}\gamma_s^p \quad \textbf{(6- 27)}$$

Where v_t^p and v_c^p are plastic components of Poisson's ratio from tension and compression. ε_s^p (Defined as average plastic shear strain), ε_t^p and ε_c^p are shear, tension and compression strains, γ_s^p is defined as engineering plastic shear strain and is equal to $2\varepsilon_s^p$.

6.3 Applications in ABAQUS

6.3.1 Simple elastic-plastic model

When elastic-plastic behaviour is assumed to adhesive materials and Von Mises yield criterion is used, the constitutive response of adhesive can be described by following form:

$$\sigma_{yt} = \left[\left(\sigma_1 - \sigma_2\right)^2 + \left(\sigma_2 - \sigma_3\right)^2 + \left(\sigma_1 - \sigma_3\right)^2\right]^{\frac{1}{2}} = \sqrt{3J_2} \quad \textbf{(6- 28)}$$

Where σ_1, σ_2, σ_3 are the principal stresses. σ_{yt} is the tensile yield stress. J_2 is the second invariant of the deviatoric stress tensor.

6.3.2 Linear Drucker-Prager model

The linear Drucker-Prager model can be defined when the friction angle β, dilation angle φ, flow stress ratio r and related hardening curve are determined. When the frictional angle β reduces to zero, the linear Drucker-Prager model becomes the von Mises model. The linear Drucker-Prager model is represented as follows (ABAQUS Analysis User's Manual 2007b):

$$F = t - p\tan\beta - d = 0 \qquad \textbf{(6- 29)}$$

Where

$$t = \frac{1}{2}q\left[1 + \frac{1}{r} - \left(1 - \frac{1}{r}\right)\left(\frac{J_3}{q}\right)^3\right] \qquad \textbf{(6- 30)}$$

Parameter J_3 is the third invariant of the deviatoric stress tensor; r is the ratio of the yield stress in tension to the yield stress in compression which controls the section shape of yield surface in the deviatoric plane; q is the Von Mises equivalent stress, $q = \sqrt{\frac{3}{2}(S:S)} = \sqrt{3J_2}$; p is the equivalent hydrostatic stress, $p = -\frac{1}{3}trace(\sigma) = -\frac{I_1}{3}$; β is the friction angle of the material which is the slope of the linear yield surface in the t-p plane; d is the cohesion of the materials; S is deviatoric stress tensor.

When r=1, Eq.6- 30 shows that t equals to q which means yielding is not relevant to the third deviatoric stress invariant. Thus Eq.6- 29 can be rewritten as follows:

$$d = \sqrt{3J_2} + \tan\beta\frac{I_1}{3} \qquad \textbf{(6- 31)}$$

Multiplying with the factor $\frac{m+1}{2m}$ in Eq.6- 31, it becomes:

$$d\left(\frac{m+1}{2m}\right) = \sqrt{3J_2}\left(\frac{m+1}{2m}\right) + \tan\beta\frac{I_1}{3}\left(\frac{m+1}{2m}\right) \qquad \textbf{(6- 32)}$$

Comparing Eq.6- 32 with Eq.6- 15, we can obtain the following parameter:

$$\tan\beta = 3\left(\frac{m-1}{m+1}\right) = 3\left[\frac{\frac{\sigma_{yc}}{\sigma_{yt}} - 1}{\frac{\sigma_{yc}}{\sigma_{yt}} + 1}\right] \qquad \textbf{(6- 33)}$$

Where σ_{yc} and σ_{yt} are yield stresses from compression and tension test. It is also known that the Drucker-Prager criterion in the σ-τ (I_1=σ, J_2=1/3σ^2+τ^2) sub-space is an ellipse,

see Figure 6. 3.

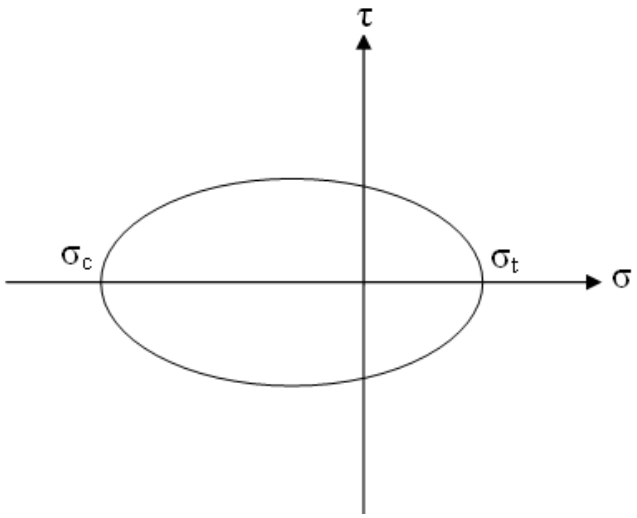

Figure 6. 3 Shape of Linear Drucker-Prager criterion in σ-τ plane

And the equation of this ellipse is shown in Eq.6- 34:

$$\left[\frac{\sigma+\frac{3k\alpha}{1-3\alpha^2}}{\frac{\sqrt{3}k}{1-3\alpha^2}}\right]^2+\left[\frac{\tau}{\frac{k}{\sqrt{1-3\alpha^2}}}\right]^2=1 \qquad \textbf{(6- 34)}$$

Where parameters α and k are defined in Eq.6- 13 and Eq.6- 14. In the pure shear load condition, σ is equal to zero and yield shear stress $\sigma_{ys}=\tau_y$ can be obtained from Eq.6- 34 and Eq.6- 10 as follows:

$$\sigma_{ys}=k=\sqrt{J_2}\text{ , }I_1=0 \qquad \textbf{(6- 35)}$$

Substituting Eq.6- 35 in Eq.6- 14, we also can obtain the following equation:

$$\frac{\sigma_{yt}}{\sigma_{ys}}=\frac{\sqrt{3}(m+1)}{2m} \qquad \textbf{(6- 36)}$$

Substituting Eq.6- 36 to Eq.6- 33, the relationship between tanβ and $\frac{\sigma_{ys}}{\sigma_{yt}}$ can be obtained as follows if the uniaxial tensile and shear tests are available.

$$\tan\beta=3\left(\sqrt{3}\frac{\sigma_{ys}}{\sigma_{yt}}-1\right) \qquad \textbf{(6- 37)}$$

Likewise, the relationship between tanβ and $\frac{\sigma_{ys}}{\sigma_{yc}}$ can be obtained as well.

$$\tan\beta = 3\left(1-\sqrt{3}\frac{\sigma_{ys}}{\sigma_{yc}}\right) \qquad \textbf{(6- 38)}$$

It must be noted that above σ_{ys}, σ_{yt} and σ_{yc} are associated with the same equivalent plastic strain ε_p^e which is defined in terms of principal plastic strain. Another parameter that must be determined is the dilation angle φ. This angle is used to determine whether the flow rule is associated or non-associated. $\varphi = \beta$ means associated flow used. Otherwise, the non-associated flow is applied.

The tangent of φ is defined as the ratio of volumetric plastic strain to the equivalent plastic strain.

$$\tan\varphi = \frac{I_1^{'}}{\varepsilon_p^e} \qquad \textbf{(6- 39)}$$

Where $I_1^{'}$ is the first invariant of plastic strain tensor and ε_p^e is equivalent plastic strain whose form depends on the selected criterion. The definition of dilation angle φ in Eq.6- 39 can also be illustrated in Figure 6. 4. The flow increment vector $d\varepsilon_{ij}^p$ of any point in a meridian plane can be decomposed into the vertical and horizontal components $d\varepsilon_{ij}^{pv}$ and $d\varepsilon_{ij}^{ph}$, respectively. Thus the horizontal component $d\varepsilon_{ij}^{ph}$ parallels to hydrostatic axes and represents the plastic volume changes.

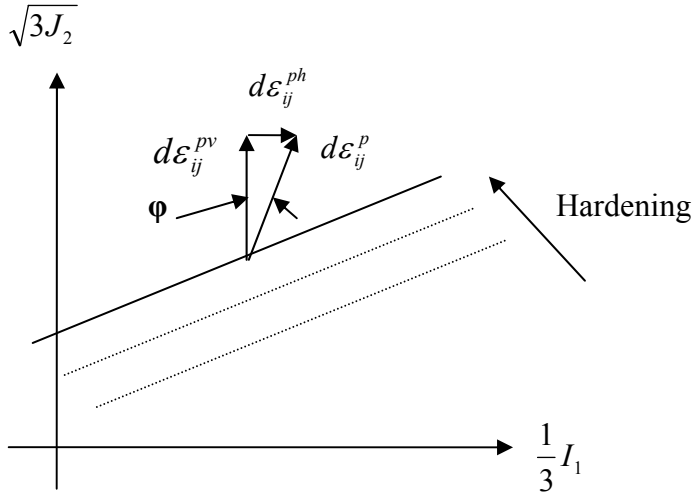

Figure 6. 4 Dilation angle φ in a meridian plane

If Drucker-Prager model $F = \alpha I_1 + \sqrt{J_2}$ is used, Eq.6- 24 becomes:

$$dw_p = \frac{\sqrt{d\varepsilon_{ij}^p d\varepsilon_{ij}^p}(1)\left(\alpha I_1 + \sqrt{J_2}\right)}{\sqrt{3\alpha^2 + \frac{1}{2}}} = \sigma_e d\varepsilon_p \quad \textbf{(6- 40)}$$

Where $\frac{\partial F}{\partial \sigma_{ij}}\frac{\partial F}{\partial \sigma_{ij}} = 3\alpha^2 + \frac{1}{2}$ and n=1. It is noted that the equivalent Drucker-Prager stress (σ_e) can be obtained from Eq.6- 21 by setting n=1 and $C = 1 - \frac{1}{\sqrt{3}}$ (Chen and Han 2007b). Thus equivalent stress σ_e is calculated as follows:

$$\sigma_e = \frac{\sqrt{3}\alpha I_1 + \sqrt{3J_2}}{1 + \sqrt{3}\alpha} \quad \textbf{(6- 41)}$$

So, comparing Eq.6- 40 and Eq.6- 41, the Drucker-Prager equivalent plastic strain ε_p^e can be obtained by:

$$\varepsilon_p^e = \frac{\alpha + \frac{1}{\sqrt{3}}}{\sqrt{3\alpha^2 + \frac{1}{2}}}\sqrt{\varepsilon_{ij}^p \varepsilon_{ij}^p} \quad \textbf{(6- 42)}$$

Then Drucker-Prager dilation angle can be obtained from $\tan\varphi = \frac{I_1^{'}}{\varepsilon_p^e}$. It is obvious that the calculation of dilation angle of Drucker-Prager model is complex because it is the function of α, i.e. tanβ, and non-associated flow is always assumed. However the Von Mises equivalent plastic strain applied here can simplify the parameter calculation and it should also be noted that in ABAQUS package the yield surface of all three Drucker-Prager criteria make use of Von Mises equivalent stress to determine the parameters. In the case of uniaxial tension, i.e., $\varepsilon_{2p} = \varepsilon_{3p} = -v_p\varepsilon_{1p}$, $\varepsilon_{1p} = \varepsilon_{yt}$, so the $I_1^{'}$ and ε_p^e becomes:

$$I_1^{'} = (1 - 2v_p)\varepsilon_{yt} \quad \textbf{(6- 43)}$$

$$\varepsilon_p^e = \frac{2}{3}(1 + v_p)\varepsilon_{yt} \quad \textbf{(6- 44)}$$

Where ε_{yt} is the plastic strain in tension direction; v_p is the plastic Poisson's ratio, i.e., $\frac{\varepsilon_{trans,p}}{\varepsilon_{axial,p}}$. Substituting Eq.6- 43 and Eq.6- 44 to Eq.6- 39, the relationship between dilation angle φ and v_p is obtained.

$$\tan\varphi = \frac{3(1-2v_p)}{2(1+2v_p)} \quad \textbf{(6- 45)}$$

The adhesive materials generally show non-associated flow behaviour which leads to a non-symmetrical stiffness matrix and results in non-convergence problems in some FEA. So for simplicity reason and sacrificing the accuracy calculation, or the difference between β and φ is not too large and the plastic deformation is limited, the associated flow can be assumed by setting $\beta=\varphi$ if possible which will give an acceptable rate of convergence and the unsymmetrical matrix may not be needed. This assumption has been validated by modelling results in this work.

Thus, summing up the above understanding, the parameters of friction angle β and dilation angle φ can be determined.

6.3.3 Exponent Drucker-Prager model

As mentioned before, linear Drucker-Prager model includes some sensitivity of hydrostatic stress; however it cannot model the behaviour of stress state for high hydrostatic stresses. Such hydrostatic tension often occurs in the bonding interface caused by constraint imposed by rigid adherends. So the exponent Drucker-Prager criterion is introduced to produce more accuracy for FEA modelling.

In ABAQUS code, the exponent Drucker-Prager yielding criterion is written as follows (ABAQUS Analysis User's Manual 2007b):

$$F = aq^b - p - p_t = 0 \quad \textbf{(6- 46)}$$

Parameter b is often defined as 2, and p_t is the hardening parameter which represents the hydrostatic tension strength of materials as shown in Figure 6. 2. Furthermore, p_t value can be determined by different uniaxial tests, if hardening is defined by the uniaxial compression yield stress (σ_{yc}). p_t can be represented as follows:

$$p_t = a\sigma_{yc}^{\ 2} - \frac{\sigma_{yc}}{3} \quad \textbf{(6- 47)}$$

If hardening is defined by the uniaxial tension yield stress (σ_{yt}), p_t can be represented as follows:

$$p_t = a\sigma_{yt}^{\ 2} + \frac{\sigma_{yt}}{3} \quad \textbf{(6- 48)}$$

So the parameter of *a* can be determined by subtracting Eq.6- 47 to Eq.6- 48

$$a = \frac{1}{3(\sigma_{yc} - \sigma_{yt})} \quad \textbf{(6- 49)}$$

When hydrostatic stress sensitivity parameter *m* is used, which is equal to $\frac{\sigma_{yc}}{\sigma_{yt}}$, then the parameter *a* becomes:

$$a = \frac{1}{3\sigma_{yt}(m-1)} \quad \textbf{(6- 50)}$$

and

$$p_t = am\sigma_{yt}^2 = \frac{m\sigma_{yt}^2}{3\sigma_{yt}(m-1)} \quad \textbf{(6- 51)}$$

Like linear Drucker-Prager criterion in σ-τ (I_1=σ, J_2=1/3σ^2+τ^2) sub-space is an ellipse, exponent Drucker-Prager shows the similar geometrical figure under σ-τ plane, it is known that $q = \sqrt{3J_2} = \sqrt{\sigma^2 + 3\tau^2}$ and $p = -\frac{1}{3}\sigma$, then Eq.6- 46 becomes:

$$a(\sigma^2 + 3\tau^2) + \frac{1}{3}\sigma - p_t = 0 \quad \textbf{(6- 52)}$$

Substituting $p_t = a\lambda\sigma_t^2$ to Eq.6- 52 then an ellipse equation becomes as follows:

$$\left(\frac{\sigma + \frac{1}{6a}}{m\sigma_t^2 + \frac{1}{36a}}\right)^2 + \left(\frac{\tau}{\sqrt{\frac{m\sigma_t^2}{3} + \frac{1}{108a}}}\right)^2 = 1 \quad \textbf{(6- 53)}$$

The relations between σ_{ys}, σ_{yt} and σ_{yc} under uniaxial shear, tension and compression can be determined by Eq.6- 52 or Eq.6- 53, and displayed as follows:

$$m = \frac{\sigma_c^2}{3\sigma_s^2} = \frac{3\sigma_s^2}{\sigma_t^2} \quad \textbf{(6- 54)}$$

In ABAQUS code, the exponent Drucker-Prager model is always using non-associated flow, and the flow potential of exponent model is the same as hyperbolic model's whose flow potential approaches the linear Drucker-Prager flow potential asymptotically at high confining pressure stress, thus the dilation angle φ of exponent model can be replaced by dilation angle of non-associated linear Drucker-Prager model, i.e. calculating from Eq.6- 45.

Thus all three parameters of exponent Drucker-Prager model required by ABAQUS package can be determined from any two uniaxial tests.

6.4 Parameters of rubber particle in modelling

It is known that the rubber particle in adhesive exhibits hyperelastic behaviour; in addition, it is assumed that this material behaviour is isotropic and incompressible when rubber is simulated in ABAQUS package; the incompressible behaviour results in unchangeable volume except for thermal expansion. Thus normal constitutive response is unable to describe the rubber behaviour.

For hyperelastic materials, strain energy potential (U) is used to relate stresses to strains instead of using Young's modulus and Poisson's ratio. Generally, four different strain energy potential models including polynomial model, Ogden model, Arruda-Boyce model and Van der Waals model are used to describe rubber's mechanism (ABAQUS Theory Manual 2009b), the polynomial model also can be simplified to forms such as Mooney-Rivlin model and Neo-Hookean. In this work, the polynomial model is applied for the rubber particle in the epoxy form which is described as follows (ABAQUS Analysis User's Manual 2007a):

$$U = \sum_{i+j=1}^{N} C_{ij} (\bar{J}_1 - 3)^i (\bar{J}_2 - 3)^j + \sum_{i=1}^{N} \frac{1}{D_i} (J_{el} - 1)^{2i} \qquad \textbf{(6- 55)}$$

Where U is strain energy potential per unit of reference volume; C_{ij} represents the shear property of rubber material; $\bar{J}_1$ and $\bar{J}_2$ are the first and second deviatoric strain invariants and measure the distortion in rubber material; J_{el} is the elastic volume ratio which relates the total volume ratio and the thermal volume ratio; the parameter N can be up to six but values of N bigger than 2 are rarely used. It is noted that C_{ij} and D_i are temperature-dependent material parameters. In addition, the D_i values determine the compressibility of the material. In this modelling, polynomial strain energy potential with order 2 was used and associated parameters are listed as follows:

Table 6. 1 The parameters of polynomial model used for rubber particle (Guild 2004)

Polynomial strain energy function with N=2				
Parameters	D_1(MPa^{-1})	C_{10}(MPa)	C_{01}(MPa)	/
	D_2(MPa^{-1})	C_{20}(MPa)	C_{11}(MPa)	C02(MPa)
Value	0.0008	-0.4682973	0.877016	/
	0.0016	0.0006046	-0.00309817	0.135766

For rubber, rubber-like materials and some materials in state of plasticity, there is a volumetric locking problem which affects the convergence of simulation because the volume of these materials cannot be changed. However the unique definition of locking does not exist, the most general viewpoint of the volumetric locking is expressed that *'locking is the effect of a reduced rate of convergence in dependence of a parameter, in the case of volumetric locking, this parameter is bulk material'* (Felippa 1986). In order to eliminate volumetric locking, refining mesh and introduction of a small amount of compressibility into rubber materials (i.e. setting the material parameter D_1 to non-zero value) are employed. In polynomial modelling, the initial shear modulus and bulk modulus are expressed by (ABAQUS Theory Manual 2009b):

$$\mu_0 = 2(C_{10} + C_{01}), K_0 = \frac{2}{D_1} \quad \textbf{(6- 56)}$$

Also, the relation between Poisson's ratio (ν), initial shear modulus (μ_0) and initial bulk modulus (K_0) is used to measure the compressibility. The equation is described as follows (ABAQUS Theory Manual 2009b):

$$\nu = \frac{3(\frac{K_0}{\mu_0}) - 2}{6(\frac{K_0}{\mu_0}) + 2} \quad \textbf{(6- 57)}$$

When the material constants in Table 6. 1 is substituted into Eq.6- 56 and 6- 57, the Poisson's ratio is calculated as 0.4998 which is very close to 0.5. In this case, the results obtained with a small amount of compressibility will be in close agreement with those obtained with total incompressibility.

6.5 Micro model description

6.5.1 Geometry of micro model

In this FEA model, rubber particles were distributed uniformly which implies that the distance between rubbers particles is equal. The face centred cubic (fcc) cell was used to describe the model structure which is shown in Figure 6. 5. Due to the mirror symmetry, only one eight fcc cell including four 1/8 rubber particles was chosen for FEA simulation.

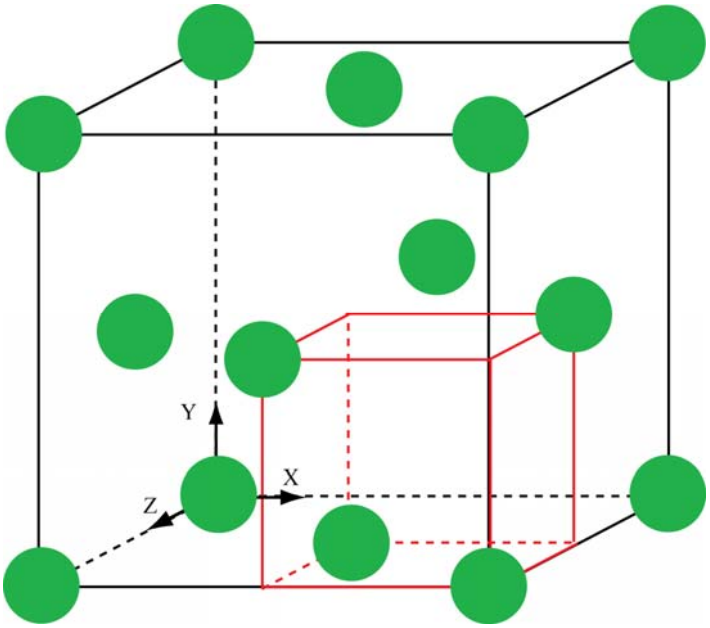

Figure 6. 5 Distributions of rubber particles (green balls) in epoxy matrix and typical geometry of one eight face centred cube (red cell)

6.5.2 Boundary conditions and element used in micro model

The selected one-eighth fcc cell is shown in Figure 6. 6. The volume fraction of rubber particles was determined by the ratio of particle radius to cell length (i.e. b/a), thus two models with 13.4% (b/a =0.4) and 20.0% (b/a=0.457) rubber fraction were studied.

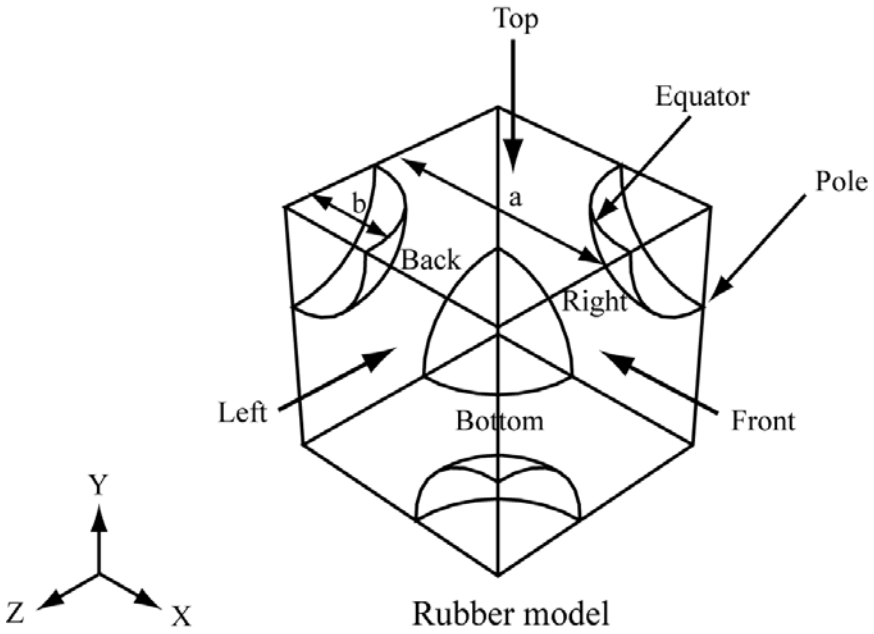

Figure 6. 6 One-eight face centred cubic cell for FEA simulation

In modelling, the right, back and bottom surfaces were not allowed to move along –Z, -X, -Y axis respectively, thus all these three surfaces were constrained by symmetry boundary conditions. The front and left surfaces were constrained by equation function such that both surfaces move parallel to their initial shape. The uniaxial tensile or compressive displacements were applied at the top surface. It is noted that rubber part must employ the hybrid element because rubber has nearly uncompressible behaviour and no compressible stress can be obtained if using normal 3D element. The idea of hybrid element is to couple the independent interpolation of pressure stress-based solution and typically displacement-based solution to resolve the incompressibility problem (ABAQUS Theory Manual 2009a). Thus, 16984 quadratic tetrahedral (C3D10) elements were used for epoxy matrix and 3336 hybrid quadratic tetrahedral (C3D10H) elements were used for rubber particles in 13.4% rubber fraction model. 18484 C3D10 elements were used for epoxy matrix and 6372 C3D10H elements were used for rubber particles in 20.0% rubber fraction model. It should be noted that the mesh size in models is small enough to provide good resolution for stress distribution.

6.5.3 Material properties used in micro model

The property of rubber particle was described in Table 6. 1. The epoxy matrix used in this simulation was considered as exponent Drucker-Prager behaviour whose properties are listed in Table 6. 2.

Table 6. 2 The properties of pure epoxy using exponent Drucker-Prager behaviour (Guild 2004)

Elastic	Young's modulus(MPa)	Poisson's ratio	
	3000	0.30	
Drucker-Prager plastic (exponent form)	Dilation angle	a	b
	12.6	0.116	2
Drucker-Prager plastic (tension behaviour)	Yield stress(MPa)	Plastic strain	
	51.797	0.000	
	62.552	0.004	
	72.135	0.006	
	80.788	0.013	
	81.417	0.018	
	77.541	0.031	
	75.328	0.039	
	72.473	0.053	
	69.604	0.066	
	67.254	0.091	
	69.215	0.126	
	72.349	0.260	
	76.859	0.209	
	94.541	0.400	
	113.028	0.600	
	131.514	0.800	
	150.000	1.000	
	196.216	1.500	

6.6 FEA modelling of 13.4% and 20.0% rubber toughened epoxy model

Different rubber fraction toughened epoxy show different behaviour under load. In order to distinguish this difference, two rubber models with different rubber particle volumes are simulated under uniaxial tensile and compression load to determine elastic and plastic properties which are used in global and associated simulations later. The results of two models under uniaxial load are shown in Figure 6. 7. So the basic strain-stress curves are obtained which are ready for further analysis. It should be noted that all stress and strain used in analysis were converted to true values.

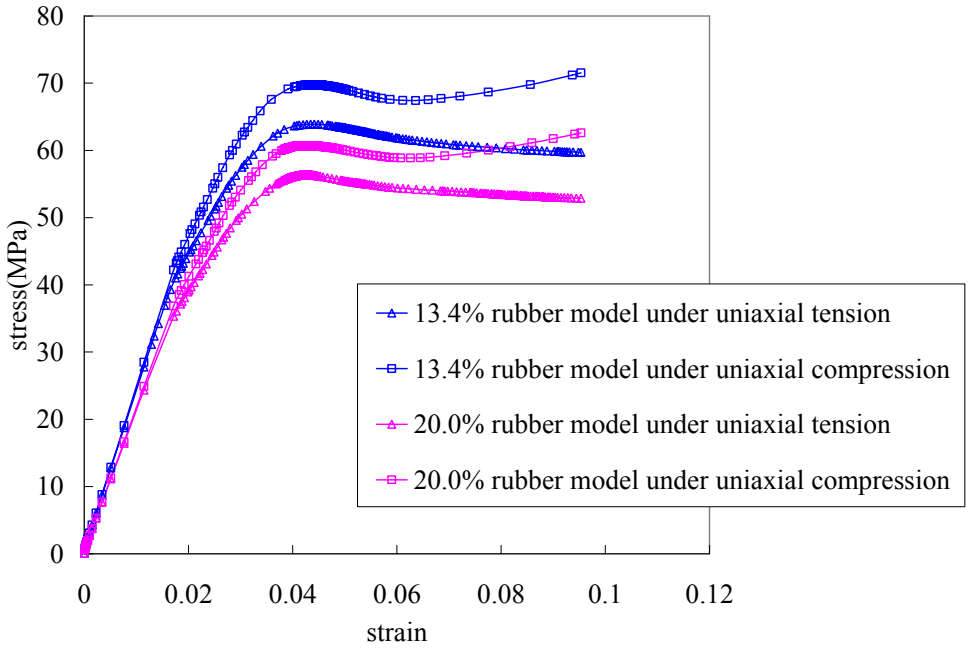

Figure 6. 7 Stress-strain curves of 13.4% and 20.0% Rubber model under uniaxial load

6.6.1 Elastic properties derived from model results

For static or low-rate modelling, elastic properties including Young's modulus and elastic Poisson's ratio are easy to calculate from tensile strain-stress curve in linear region. It is obvious that 13.4% rubber toughened epoxy has a higher Young's modulus than 20.0% rubber toughened epoxy. The Young's modulus is 2850 MPa for 13.4% Rubber model and 2400 MPa for 20.0% Rubber model, respectively. Poisson's ratio is 0.38 for 13.4% Rubber model and 0.40 for 20.0% Rubber model. All values of elastic properties are measured below the strain level of 0.02 to ensure that the linear region of curves is used.

6.6.2 Hardening data of two models

Generally, the hardening curves of many adhesives can extend to large strain value, thus the cross sectional area of the test sample reduce significantly with increasing strain. Both engineering stress (σ_{eng}) and strain (ε_{eng}) should be converted to true stress (σ_{true}) and strain (ε_{true}) through following equations:

$$\varepsilon_{true} = \ln(1+\varepsilon_{eng}) \quad \textbf{(6- 58)}$$

and

$$\sigma_{true} = \sigma_{eng}(1+\varepsilon_{eng}) \quad \textbf{(6- 59)}$$

The hardening curve required by ABAQUS is in the tabular form of yield stress and plastic strain, and the first pair of data must be the initial stress which corresponds to zero plastic strain. It should be noted that extended Drucker-Prager criterion in ABAQUS is unable to model the strain softening behaviour, and in some cases to make the analysis running smoothly more data may be required because the analysis assumed no hardening occurs with additional extension if strains in the analysis exceed the maximum strain in defined data, which often causes non-convergence problem in the solution. Thus, Eq.6- 60 is chosen to extrapolate or fit the hardening curve to higher strain state or remove soften region in hardening curve to avoid the convergence difficulty in analysis without significant loss of predictive accuracy (Dean and Read 2001).

$$\sigma = \left[\sigma_y + (\sigma_f - \sigma_y)(1-\exp-(\frac{\varepsilon_p}{\varepsilon_{ps}})^{\psi}\right](1+\rho\varepsilon_p) \quad \textbf{(6- 60)}$$

Where σ_y is the initial yield stress corresponding to zero plastic strain; σ_f is the initial flow stress corresponding to the plateau stress; ε_{ps} is a parameter indicating mean strain within the strain range where the stress increases rapidly between σ_y and σ_f; ψ is the parameter which influences the strain width of that range, and parameter ρ describes the small increase of stress at higher plastic strain beyond the strain where the flow stress occurs. All these parameters must be chosen to fit the data from micro Rubber model or experimental data. The shape of hardening curve after fit is very sensitive to chosen σ_y and σ_f. Figure 6. 8 shows the comparison between original hardening curve and fit hardening curve, the fit hardening data is used in smear model and the loss of accuracy need to be investigated. Furthermore, combining with well known Eyring equation which is able to describe the rate-dependent behaviour of polymers (Eyring 1936), Eq.6- 60 can produce more hardening data responding to various strain rates $\dot{\varepsilon}_p$. The Eyring equation is written as follows:

$$\sigma = a + b\log\dot{\varepsilon}_p \quad \textbf{(6- 61)}$$

Where parameter *a* and *b* are temperature related constants. When determining *a* and *b* in rate-dependent plastic theory, parameter *a* becomes yield stress and parameter *b* can

be resulted by linear fitting the curve plotted by stress vs. $\log \dot{\varepsilon}_p$.

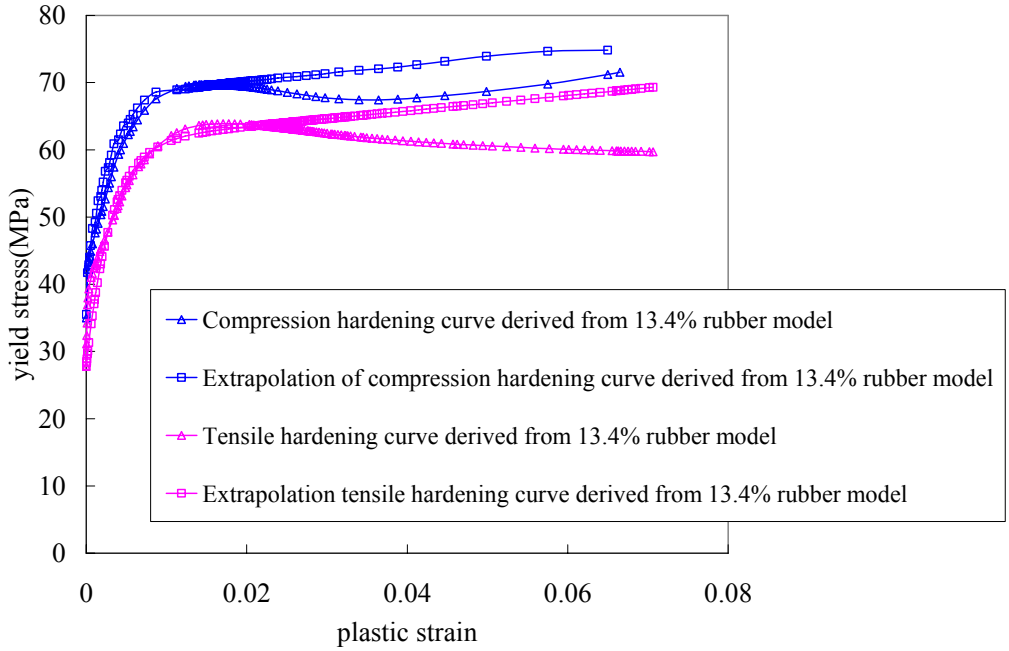

Figure 6. 8 Fit and original hardening curves derived from 13.4% Rubber model

6.6.3 Determination of Linear Drucker-Prager model (β,φ, r)

When uniaxial tension and compression data are available and all data are converted to true stress and strain, Eq.6- 62 is applied to plot both tensile and compressive yield stress vs plastic strain curves.

$$\varepsilon_p = \varepsilon_T - \frac{\sigma}{E} \qquad \textbf{(6- 62)}$$

Where ε_p is plastic strain, ε_T is total strain, and σ is the stress corresponding to present strain. According to the definition of parameter m defined previously, σ_{yt} and σ_{yc} are chosen at the same equivalent plastic strain (Gali, Dolev et al. 1981), i.e. $\frac{\sigma_{yc}}{\varepsilon_p^c} = \frac{\sigma_{yt}}{\varepsilon_p^t}$ is imposed. Alternatively the Eq.6- 27 is used to locate the same equivalent plastic strain point in both tension and compression curves where yield stresses are derived to calculate parameter $\tan\beta$.

Then Eq.6- 33 is used to calculate parameter $\tan\beta$ which is a function of the equivalent plastic strain, the average result of $\tan\beta$ can be used if the dependence of m

on equivalent plastic strain is not too significant, or $\tan\beta$ corresponding to the interested range of plastic strain can be chosen. It should be noted that the friction angle will not vary too much in the higher plastic strain. In the case yield stress curves have plateau in both tension and compression where yield stresses do not change significantly with equivalent plastic strain, then $\tan\beta$ is able to be determined in this region without loss of accuracy. It is clear that the plateau regions of tension and compression start from plastic strain around 0.02 in Figure 6. 8, where equivalent plastic strain should be a little larger than 0.02, thus the value of equivalent plastic strain ε_p^e is chosen as 0.02 in this analysis. Plastic Poisson's ratio in tension is around 0.33 and 0.34 in compression at the point of 0.02 plastic strain, then the values of ε_p^t and ε_p^c calculated from Eq.6- 27 are 0.0225 and 0.0224, respectively. Finally, the yield stress of tension and compression can be determined from Figure 6. 8 at the same equivalent plastic strain of 0.02. The values are 63.15MPa for tension yield stress and 70.26MPa for compression yield stress. Thus parameter *m* is 1.11 and $\tan\beta$ is obtained by Eq.6- 33 at the value of 0.16, i.e., friction angle β is 9.0 degree derived from 13.4% Rubber model.

Another parameter of linear Drucker-Prager is dilation angle φ, which is able to be calculated by Eq.6- 45 when plastic Poisson's ratio v_p is known. It is obvious that the plastic Poisson's ratio is the function of plastic strain. Generally plastic Poisson's ratio decreases with increasing of plastic strain and tends to the constant value in the large plastic strain stage. ABAQUS package does not allow plastic Poisson's ratio to vary in analysis, thus an average value of v_p or the value at a region where the stress-strain stage is interesting can be chosen as the constant plastic Poisson's ratio in analysis. It is noted that the validity of this assumption was examined. When true uniaxial tensile curve is available, plastic Poisson's ratio is calculated by:

$$v_p = \frac{\varepsilon_2^p}{\varepsilon_1^p} \qquad \textbf{(6- 63)}$$

Where ε_1^p is plastic strain in the tensile direction, and calculated by:

$$\varepsilon_1^p = \varepsilon_1 - \varepsilon_1^e = \varepsilon_1 - \frac{\sigma}{E} \qquad \textbf{(6- 64)}$$

ε_2^p is transverse plastic strain, and determined by:

$$\varepsilon_2^p = \varepsilon_2 - v_e \varepsilon_1^e \quad \textbf{(6- 65)}$$

Therefore dilation angle φ is 19.86 degrees derived from 13.4% Rubber model corresponding to the plastic Poisson's ratio of 0.33

The last parameter in Linear Drucker-Prager model is flow stress ratio *r*, which is the ratio of tensile yield stress to compressible yield stress and controls the dependence of the yield surface on the value of the intermediate principal stress (ABAQUS Analysis User's Manual 2007b), the value of *r* is between 0.778 and 1.0 to make sure the yield surface remains convex. For the reason of simplification in this analysis, *r* is set to 1 which implies that the yield surface in deviatoric plane is a Von Mises circle because t=q when *r*=1 in Eq.6- 30.

Thus, for linear Drucker-Prager model derived from 13.4% Rubber model, all parameters are determined and it is found friction angle is not equal to dilation angle that means non-associated flow rule is applied here. Appling the same methodology, friction angle and dilation angle derived from 20.0% Rubber model are 7.2 and 26.50 degrees, respectively. Flow stress ratio *r* was also set to the value of 1. It should be appreciated that friction angle is generally larger than dilation angle in Drucker-Prager model (Runesson 2005; Malm 2009), however it is found that friction angle calculated from rubber model is smaller than dilation angle. This is because tension and compression curves tend to produce small friction angle and some part of curves used in calculation produce small friction angle as well. Thus, the small friction angle implies that linear Drucker-Prager model may be not accurate enough to study rubber model under complicated load conditions.

6.6.4 Determination of exponent Drucker-Prager model (a,b,φ)

Parameter *a* in exponent Drucker-Prager model in calculated by Eq.6- 50 where *m* must be determined first. It should be noted that parameter *m* in exponent Drucker-Prager has the same definition in linear Drucker-Prager, thus the same pair in yield stress of tension and compression are selected like its in linear Drucker-Prager to calculate parameter *a* at the level of 0.02 of equivalent plastic strain. Generally parameter *b* of exponent model is set to the value of 2. Furthermore, the flow potential is similar to that used in the linear

model as mentioned before, thus both exponent model and linear have the same parameter of yield stress ratio *m* and dilation angle φ.

The calculated parameters *a*, *b* and dilation angle for exponent model derived from 13.4% Rubber model are 0.048, 2, and 19.86, respectively. From the analysis of 20.0% Rubber model results, the parameter *a* is 0.053 and dilation angle is 26.50 degree. Parameter *a* is always set to 2.

6.7 Parameters and properties validation through smear model

Finally, a smear panel (60×30mm) model was applied to validate those parameters and properties derived from two Rubber models and the simulation results of smear panel model were compared with real bulk tensile test of AV 119 adhesive. Due to symmetry, only 1/4 panel was simulated which is shown in Figure 6. 9, thus symmetry boundary conditions were applied at the left and bottom line and uniaxial displacement load was applied at the top line. 5000 generalized plain strain (CPEG4) elements were used in this model. The material properties used in smear model were derived from 13.4% and 20.0% Rubber models; materials behaviour was described by simple elastic-plastic, linear Drucker-Prager model and exponent Drucker-Prager model.

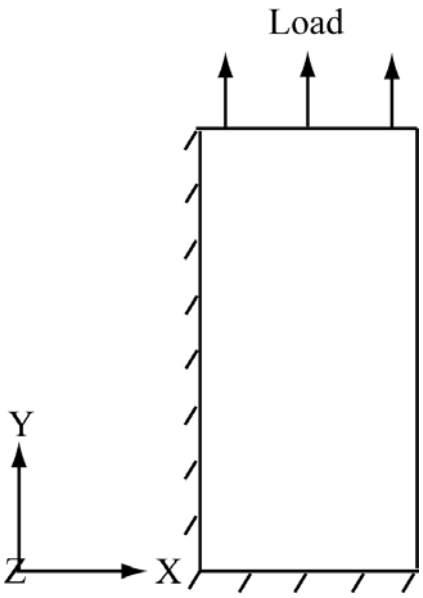

Figure 6. 9 Geometry of one-fourth smear panel model

The modelling results are shown in Figure 6. 10 and Figure 6. 11, respectively. Unless otherwise stated, all stress and strain are converted to true stress and strain, respectively. It should be noted that the tensile test of bulk AV119 are the experimental

results from Dean and Duncan's works (Dean and Duncan 1995).

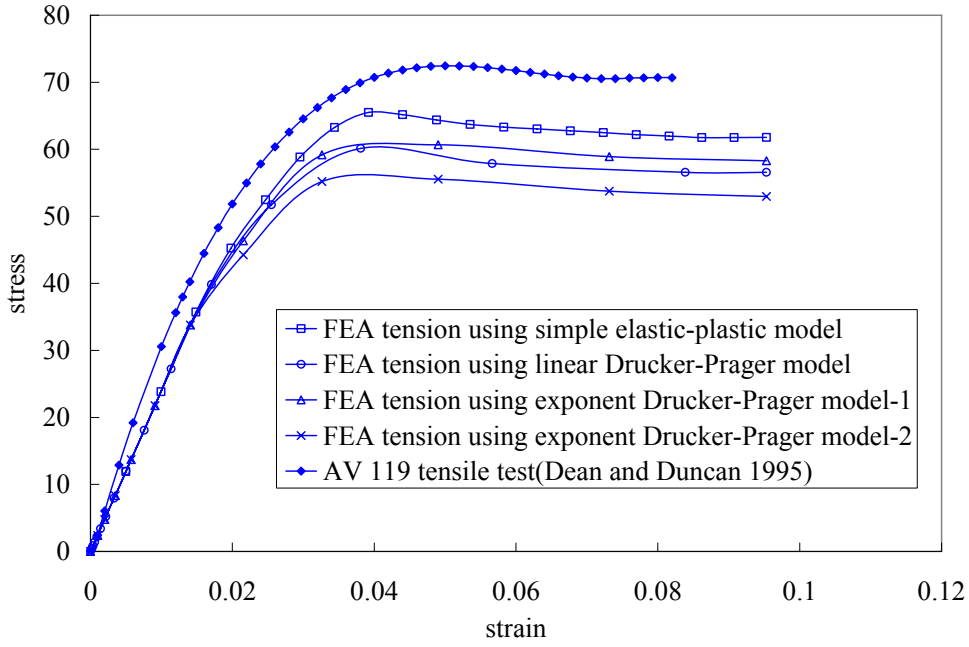

Figure 6. 10 Smear model using 20.0% rubber toughened epoxy properties under macroscopic uniaxial tension

It is found that tensile strength of AV 119 is higher than any model derived from 20.0% Rubber model which implies this model is unable to describe the behaviour of AV 119 adhesive. All models use the same Young's modulus and elastic Poisson's ratio and hardening data as well. It is also found that exponent Drucker-Prager model is sensitive to parameters m (here $m = \frac{\sigma_c}{\sigma_t}$) or parameter a. In Figure 6. 10, exponent Drucker-Prager model-2 use smaller parameter a value (a=0.03), while exponent Drucker-Prager model -1 use a=0.053 which was calculated from 20.0% Rubber model. Thus the difference between two exponent models means the strength increases when parameter a increases or m decreases. If m descends to 1, i.e. compression strength is equal to tension strength, the exponent Drucker-Prager tend to be simple elastic-plastic model, and in this case, the coincide between exponent Drucker-Prager and simple elastic-plastic model would be expected.

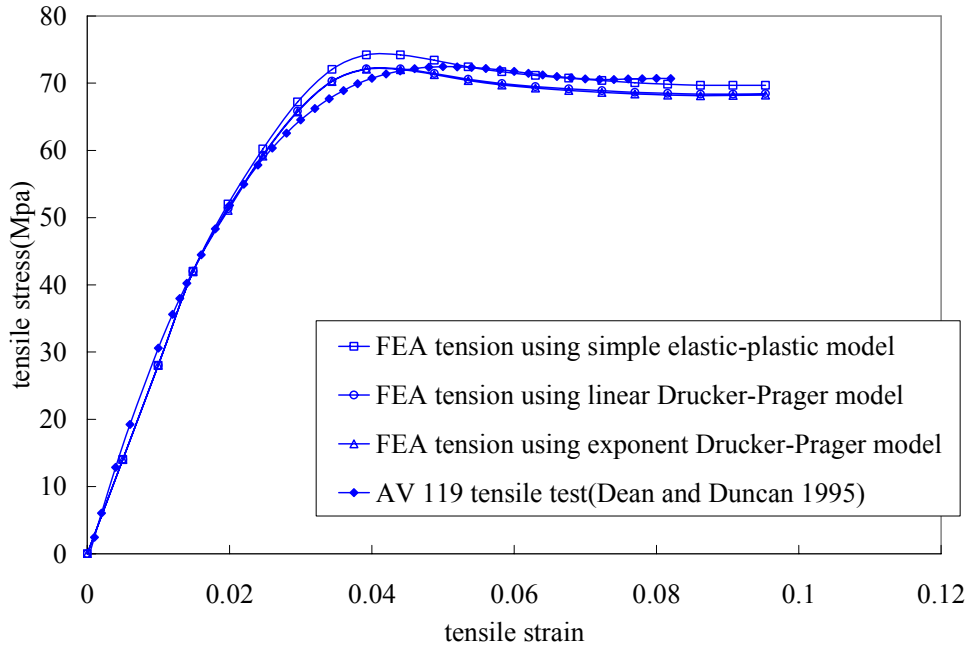

Figure 6. 11 Smear model using 13.4% rubber toughened epoxy properties under macroscopic uniaxial tension

The 13.4% Rubber model shows its stress-strain behaviour is very close to real AV119 bulk tensile result. It is found that stress-strain curves using linear Drucker-Prager and exponent Drucker-Prager derived from 13.4% Rubber model are very similar, this may be because both materials properties used same dilation angle and hardening data. The simple elastic-plastic model have similar behaviour as AV 119's in high strain, however this model only shows stress-strain response in the case of without high constraint. It is known that while high constraint from adherends always happens in bonding area of joints, thus modelling adhesive behaviour in bonded joint should choose Drucker-Prager model instead of simple elastic-plastic criterion. The modelling results also agrees with the experiment tensile result from another work (Ozel and Kadioglu 2002), specially both modelling and experiment demonstrate that material has a soft character after yielding. The FEA of smear model also shows that the maximum tensile and compressible strength occur around 4% strain.

6.8 Conclusions

Structural adhesives always demonstrate hydrostatic stress dependent behaviour, and this phenomenon is more notable in adhesive joint applications. Thus Drucker-Prager model was chosen to describe the behaviour of epoxy in Rubber model. Since the

accuracy of Drucker-Prager application is mostly controlled by friction angle, dilation angle and flow stress ratio, a systemic deduction of determining Drucker-Prager parameters was established via careful numerical analysis. Furthermore, a fit of hardening data was used in order to simulate FEA modelling smoothly without losing too much accuracy. Exponent Drucker-Prager form may be the best criterion to model epoxy properties in Rubber model and whole properties in smear model because this criterion is able to produce more accuracy in high hydrostatic stress region.

The FEA results of Rubber models show that the volume fraction of rubber particle always plays the key function to determine the mechanical properties. When the system is under macroscopic uniaxial load, both yield stress and effective Young's modulus of system decrease with the increasing of particle volume fraction; the effective Poisson's ratio increases when the particle volume fraction increases.

Although Rubber model applied the typical properties to epoxy matrix and rubber particle and the difference must exist between the assumed regular rubber distribution in FEA and real rubber particle's distribution in AV119 adhesive, the stress-strain curves of smear model using the properties of 13.4% Rubber model show a very well agreement with the curves of AV119 adhesive. Thus the 13.4% Rubber model is confidently considered as the micro model of AV119 adhesive and this Rubber model can be used to investigate the deeper and further stress states of adhesive under more complicated load condition. It is found that the smear model using simple elastic-plastic properties also produced similar stress-strain curves as those of AV119 test, but this is considered to be valid only under simple load conditions such as uniaxial tension and compression.

Chapter-7 Finite element analysis of Double Lap Joints

7.1 Introduction

In order to obtain accurate predictions and cut the expense of repeated testing, 3D models with Cohesive Zone Model (CZM) are presented in this chapter to simulate global and local response of Double Lap Joints (DLJ) under tensile load. Since CZM played very important role in simulations, all parameters of CZM were determined via a series of numerical analysis and experimental results (see Chapter 5) and used in 3D DLJ without further modification. FEA results were compared with experiments and numerical analysis. The effects of CZM parameters on predicted failure load are studied by changing maximum shear stress and maximum normal stress; the sensitivities of FEA results to constitutive law and materials properties are also explored. Details of fracture energy and stress distributions are exposed via 2D models. In particular, the technique of sub-modelling was employed which is powerful to present much deeper details of stresses in joints.

7.2 Three dimension DLJ model

7.2.1 Geometry of 3D DLJ model

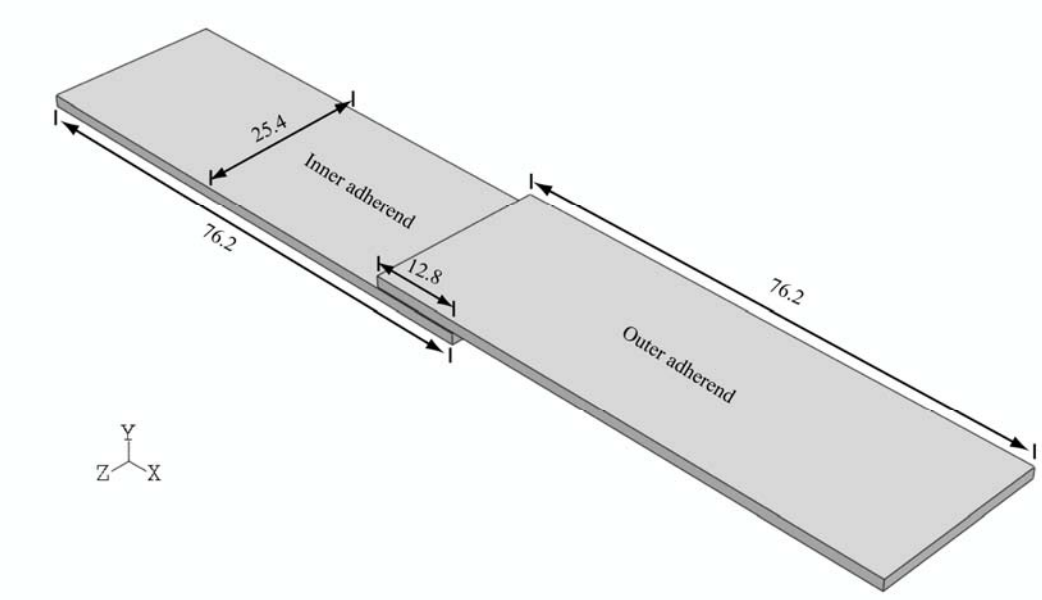

Figure 7. 1 Geometry of DLJ model (dimension unit: mm)

Half DLJ was modelled due to its geometrical symmetry through thickness direction. The geometry of DLJ model is shown in Figure 7. 1: both inner and outer adherends have 1.6mm thickness; the thickness of adhesive was chosen as 0.2mm and 0.5mm respectively. It should be noted that tab and spacer were not included in this model.

Under observation of high resolution microscope, it was found that very thin adhesive layer with around 10μm thickness remained on the surface of inner adherend in most specimens. Thus cohesive zone elements were applied along the fracture surface. Some specimens using 0.2mm adhesive thickness show typical cohesive failure. In order to compare with cohesive failure, model using pure adhesive failure was simulated as well. All these DLJ models are shown in Figure 7. 2.

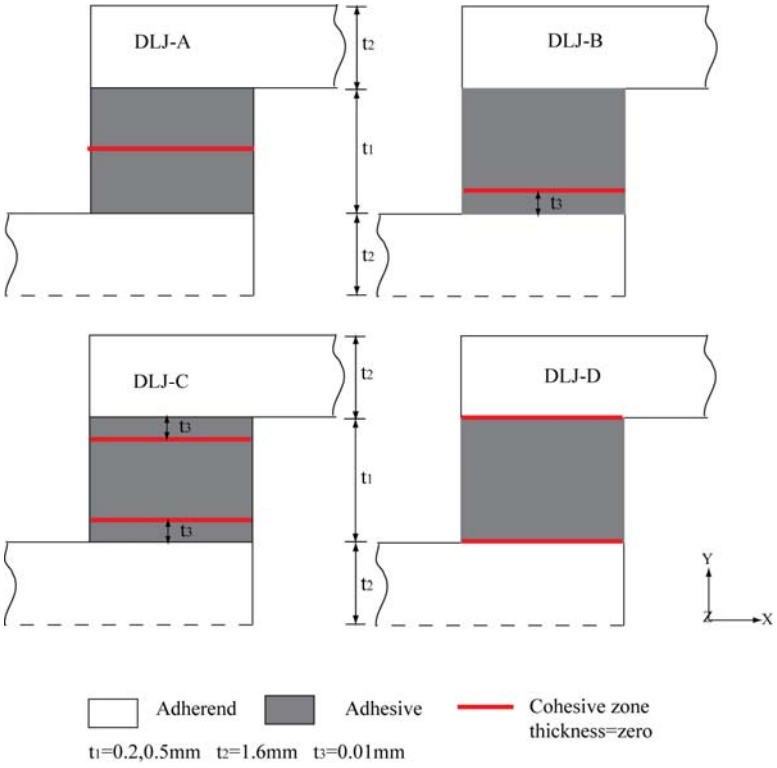

Figure 7. 2 Schematic of failure modes in FEA simulations

It is noted that DLJ-A represents typical cohesive failure; DLJ-B and DLJ-C represent another cohesive failure where it occurs close to interface; DLJ-D represents typical adhesive failure; the thickness t_3 was measured from experimental observation. In the simulation, DLJ with 0.2mm adhesive thickness was modelled by DLJ-A, -B and –C; DLJ with 0.5mm adhesive thickness was modelled by DLJ-B and -C, in addition, in order to investigate the effect of failure locus to maximum load, DLJ with 0.5mm adhesive thickness was also modelled by DLJ-D.

7.2.2 Analytical solution

An analytical solution is presented here which assumes linear elastic behaviour for adhesive and adherends. It is noted that only half DLJ is studied due to geometrical symmetry. The displacements along x-axis are shown in Figure 7. 3.

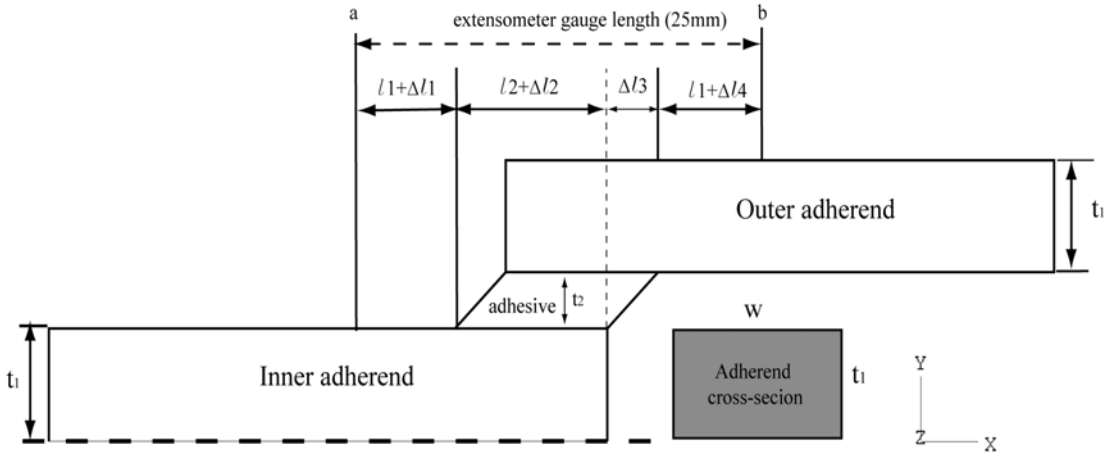

Figure 7. 3 Illustration of half deformed DLJ used in analytical solution

It is noted that a gauge length of 25mm is chosen for the analysis; this length cover the overlap of joint and has the same position as extensometer in experiment. Thus the undeformed distance between point a and point b is equal to $l_1+l_2+l_1$. The value of t_2 represents adhesive thickness and t_1 represents the thickness of outer adherend and half inner adherend; the value of w represents the width of specimen.

It is noted that half inner adherend has the same thickness and length as outer adherend. Adherend is modelled by hardened steel with Young's modulus E=199300MPa, and adhesive has shear modulus, G=1100MPa. Specimen has width of 25.4mm, both half inner and outer adherend has thickness of 1.6mm and the thickness of adhesive has 0.2mm and 0.5mm, respectively. The total force applied at the end of half inner adherend and outer adherend is *F/2*. It is also assumed that the cross-section of adherend suffer from the same force of *F/2* and adherend in the overlap area suffers the same force on the assumption of the linear distribution of force from bonded end to free end. This force causes four displacements in the leg of inner adherend (Δl_1), overlap in inner adherend (Δl_2), adhesive (Δl_3) and leg of outer adherend (Δl_4). It should be noted that the overlap of outer adherend has the same axial deformation as the overlap of inner adherend such that its displacement does not contribute to the total displacement (Xiao, Foss et al. 2004).

This analytical solution assumes pure shear stress state and no bending moment in specimen. Thus, the displacement in half inner adherend is calculated as:

$$\Delta l_1 = \varepsilon_1 \times l_1 = \frac{F}{2wt_1E} \times l_1 \quad \textbf{(7- 1)}$$

The displacement in overlap of inner adherend is calculated as:

$$\Delta l_2 = \varepsilon_2 \times l_2 = \frac{F}{2wt_1E} \times l_2 \quad \textbf{(7- 2)}$$

The shear displacement in adhesive is calculated as:

$$\Delta l_3 = \gamma \times t_2 = \frac{F}{2wl_3G} \times t_2 \quad \textbf{(7- 3)}$$

The displacement in outer adherend is calculated as:

$$\Delta l_4 = \varepsilon_4 \times l_1 = \frac{F}{2wt_1E} \times l_1 \quad \textbf{(7- 4)}$$

Thus the load (F) and the global displacement (Δl) using 25mm gauge length have the following relation via analytical solution:

$$\Delta l = \Delta l_1 + \Delta l_2 + \Delta l_3 + \Delta l_4 = \frac{F}{wt_1E} \times l_1 + \frac{F}{2wt_1E} l_2 + \frac{F}{2wl_3G} t_2 \quad \textbf{(7- 5)}$$

In this case, l_1 has length of 6.1 mm; l_2 has length of 12.8mm. Thus the predicted curve of load-displacement can be obtained.

7.2.3 Mesh of 3D DLJ model

All 3D models used the same mesh techniques such that models are able to be compared with each other directly without further modification because stress depends on the size of elements at singular points. A fine mesh seed was assigned to the end of adhesive layer which is adjacent to the end of outer adherend, thus unsymmetrical element distribution was applied at overlap area in order to avoid non-convergent problem and reduce computer time as well. A typical meshed DLJ model is shown in Figure 7. 4.

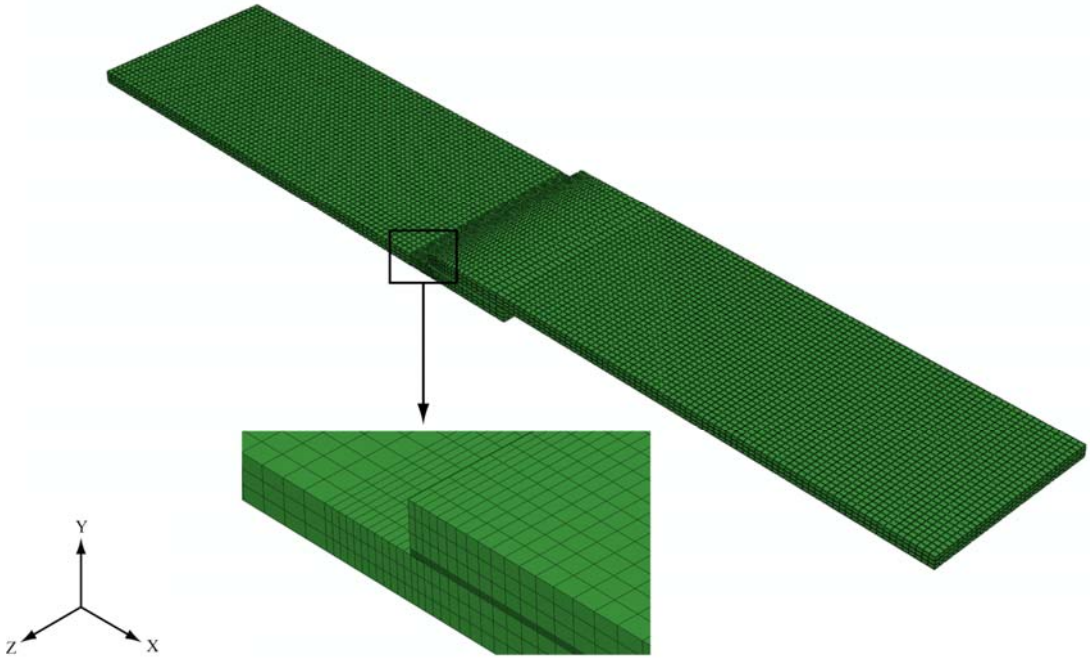

Figure 7. 4 A typical mesh of 3D DLJ model

A mesh technology using orphan part allows model to employ a zero thickness cohesive zone layer and avoids using interface constraint (Tie function) which often causes convergency problem. Element of C3D8I (linear incompatible brick element) were used in all adherends and adhesive layer except cohesive zone. Generally the application of incompatible element can avoid shear locking in modelling and produce similar simulation result as second order element but reduce the cost of computation significantly. Element of COH3D8 (8 node cohesive element) was used in zero thickness cohesive zone. The number of elements used in the models is shown in Table 7. 1.

Table 7. 1 Element number in DLJ models

Adhesive thick(mm)	Model	Adherend	Adhesive	Cohesive layer
0.2	DLJ-A	20100	2720	680
	DLJ-B	20100	3400	680
	DLJ-C	20100	4080	1360
	DLJ-D	20100	2720	1360
0.5	DLJ-A	20100	6800	680
	DLJ-B	20100	7480	680
	DLJ-C	20100	8160	1360
	DLJ-D	20100	6800	1360

7.2.4 Boundary conditions of 3D DLJ model

Because of symmetry, symmetry boundary condition was applied at the bottom surface of inner adherend; Encastre (built-in) boundary condition was applied at end of outer adherend which constrained all six degree of freedom. A displacement load was applied at the end of inner adherend. The boundary conditions of DLJ model are shown in Figure 7. 5.

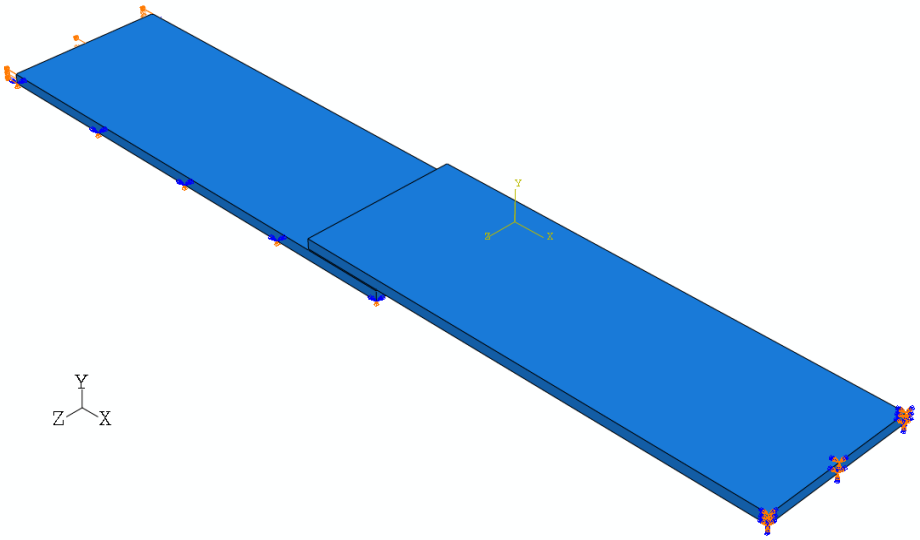

Figure 7. 5 Boundary conditions and load of DLJ model

7.2.5 Cohesive Zone Model (CZM) applied for fracture criterion

In this simulation, CZM parameters consist of penalty stiffness (k), three nominal stresses ($\sigma_{n,0}$, $\tau_{s,0}$, $\tau_{t,0}$), three independent mode fracture toughness (G_I, G_{II}, G_{III}) and mixed-mode ratio (η) of BK criterion. BK criterion is described in detail later. It is noted that nominal stress ($\tau_{t,0}$) and fracture toughness (G_{III}) can be ignored in DLJ simulations. Thus nominal stresses ($\sigma_{n,0}$, $\tau_{s,0}$), and fracture toughness (G_I, G_{II}) were measured and determined from Fixed Arm Peel (FAP) tests and 4 point End Notched Flexure (ENF) tests; The mixed-mode ratio (η) was calculated from MMB tests; The penalty stiffness (k) was calculated using effective Young's modulus which has substantial physical meaning. All parameters are considered as the intrinsic properties of adhesive which can be used for other modelling. Traction-Separation (T-S) law is the core of CZM application, the description of T-S law is shown in Figure 7. 6. It is noted that the single T-S law image is shown in Figure 2. 3.

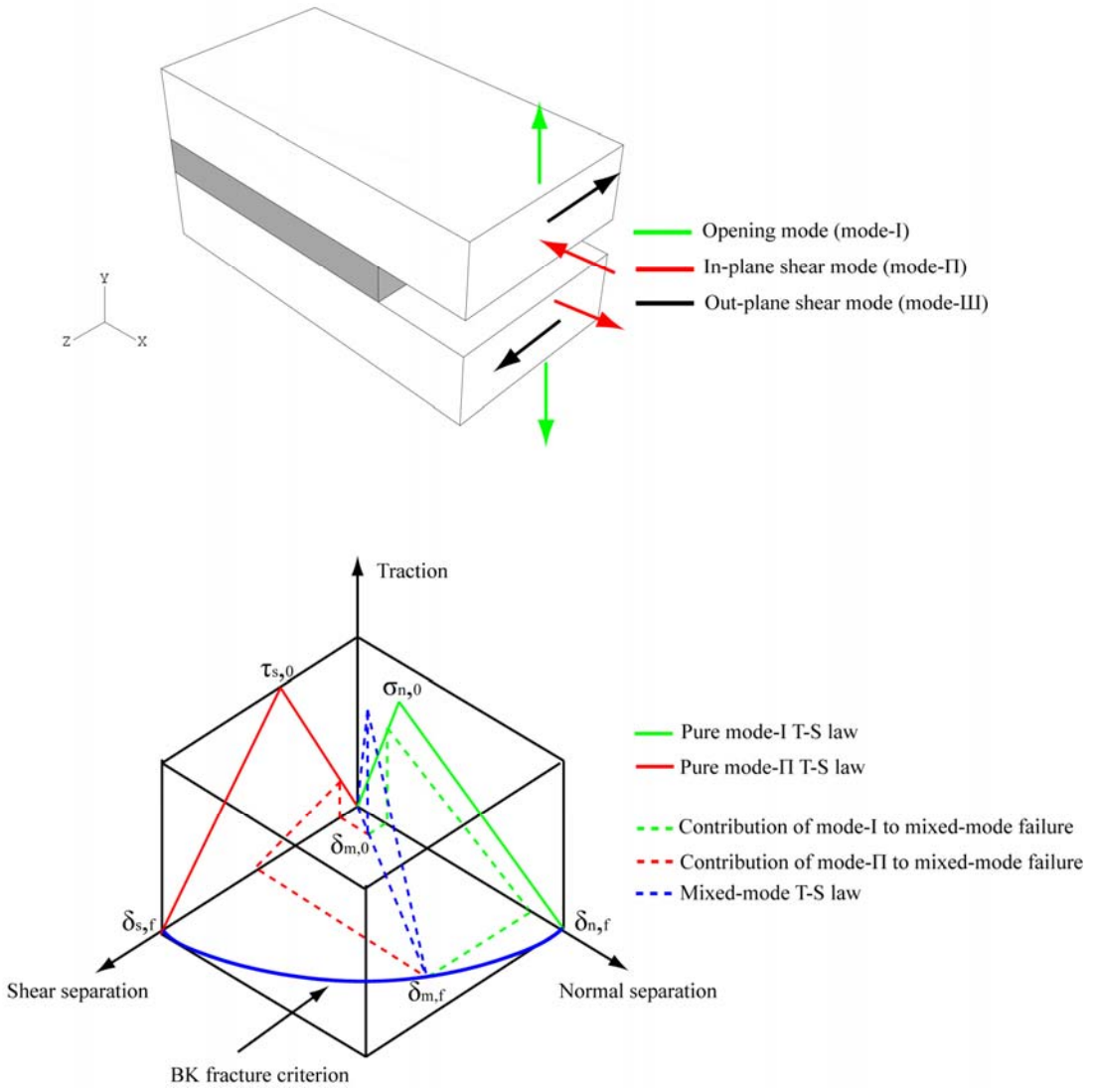

Figure 7. 6 Illustration of three fracture modes at the crack tip (top image) and mixed-mode Traction-Separation law in CZM (bottom image)

In CZM application, three maximum stresses and associated displacements are fundamental parameters. The constitutive responses of cohesive zone are defined by the terms of traction versus separation. In general, there are three possible fracture modes at the crack tip, opening mode (mode-I), in-plane shear mode (mode-II), and out-plane shear mode (mode-III). Again due to the symmetrical geometry of DLJ, the out-plane shear mode is small enough to be negligible, and only opening mode and in-plane shear mode are considered in this work. Every mode has its corresponding T-S law.

From the bottom image (see Figure 7. 6), the vertical axis represents the magnitudes of normal stress ($\sigma_{n,0}$) and shear stress ($\tau_{s,0}$) and two horizontal axes represent the

corresponding separation. The triangles drawing by solid line are pure mode-I and -II T-S laws and their areas are pure mode-I and –II fracture toughness; the dashed triangles represent the T-S law under mixed mode condition and many dashed triangles form the BK fracture criterion. In T-S law, the damage initiation and evolution are less important thus they are assumed to perform linearly. The most important parameters are two maximum traction stress ($\sigma_{n,0}$, $\tau_{s,0}$) and two corresponding failure displacement ($\varepsilon_{s,f}$, $\varepsilon_{n,f,}$) which define the shape of triangle in pure mode and mixed mode. The slope of mode triangle is defined as penalty stiffness (k) and determined by numerical analysis.

7.2.5.1 Determination of penalty stiffness (k)

Observed from failure locus of lap joints, the fracture always occurs very close to the interface between inner adherend and epoxy adhesive. In this case, the geometry of CZM can be demonstrated in Figure 7. 7.

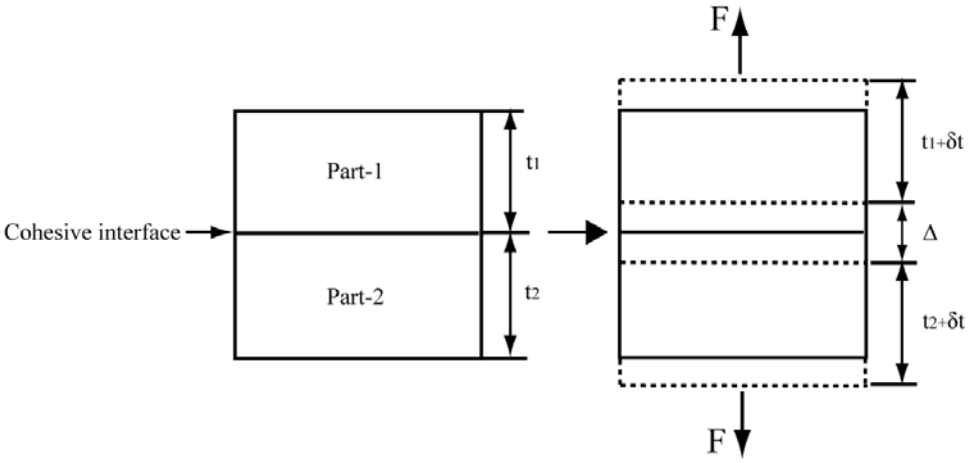

Figure 7. 7 Cohesive interface located inside adhesive under load

Cohesive interface locates inside adhesive which implies both part-1 and part-2 are identical materials and have the same mechanical properties such as Young's modulus. It should be noted that thickness t_1 represents the thicker layer of adhesive which remained at outer adherend and the thickness of t_2 represents a very thin adhesive layer at inner adherend. According to Hooke's law cohesive interface and effective Young's modulus have the relation shown in Eq.7- 6:

$$\sigma = E_1\varepsilon_1 = E_2\varepsilon_2 = k\Delta = E_{eff}\varepsilon_{eff} \qquad \textbf{(7- 6)}$$

Where σ is the traction caused by load F; E_1 and E_2 are through thickness Young's modulus of part-1 and part-2 respectively, because part-1 and part-2 are both isotropic

materials, their Young's modulus are represented by normal tensile modulus; k is stiffness of cohesive interface and Δ is opening displacement of bottom and top surface of cohesive interface; thus due to load F, there are three parts of displacement $(\delta t_1 + \delta t_2 + \Delta)$ contributing to the effective strain in Eq.7- 7:

$$\varepsilon_{eff} = \frac{\delta t_1 + \delta t_2 + \Delta}{t_1 + t_2} \quad \textbf{(7- 7)}$$

The thickness t_1 and t_2 can be measured by DLJ using optical microscopy. Here it is assumed that $t_2 / t_1 = e$, e is a factor and can be measured from experiment. It is noted that $\varepsilon_1 = \frac{\delta t_1}{t_1}$ and $\varepsilon_2 = \frac{\delta t_2}{t_2}$, then the effective strain ε_{eff} can be expressed as follows:

$$\varepsilon_{eff} = \frac{1}{1+e}\varepsilon_1 + \frac{e}{1+e}\varepsilon_2 + \frac{\Delta}{t_1 + t_2} \quad \textbf{(7- 8)}$$

Substituting Eq.7- 8 to Eq.7- 6, the effective Young's modulus becomes:

$$E_{eff} = \frac{1}{\frac{1}{1+e}\frac{1}{E_1} + \frac{e}{1+e}\frac{1}{E_2} + \frac{\Delta}{(t_1 + t_2)\sigma}} \quad \textbf{(7- 9)}$$

Because $\sigma = k\Delta$, and both E_1 and E_2 are equal to the adhesive Young's modulus $E_{adhesive}$ in case the fracture occurs inside adhesive thus Eq.7- 9 can be written as follows:

$$E_{eff} = E_{adhesive}\left[\frac{1}{1 + \frac{E_{adhesive}}{k(t_1 + t_2)}}\right] \quad \textbf{(7- 10)}$$

It is obvious that the effective Young's modulus is independent with the position of cohesive interface (i.e. independent to e) in case of cohesive failure, and the thickness of adhesive is $t_1 + t_2$. In addition, the effective Young's modulus will be close to adhesive Young's modulus $E_{adhesive}$ if the part of $\frac{E_{adhesive}}{k(t_1 + t_2)}$ tends to zero. The ratio of $\frac{E_{eff}}{E_{adhesive}}$ (ω) can be written as follows:

$$\omega = \frac{E_{eff}}{E_{adhesive}} = \frac{1}{1 + \frac{E_{adhesive}}{k(t_1 + t_2)}} \quad \textbf{(7- 11)}$$

In case the adhesive style failure occurs, Part-1 and Part-2 have different mechanical properties. In terms of DLJ, Part-1 is epoxy adhesive with Young's modulus ($E_{adhesive}$) and Part-2 represents inner adherend with Young's modulus ($E_{adherend}$), thus another effective Young's modulus E'_{eff} is introduced to compare with E_{eff} referred in Eq.7-9. It is noted that E_1 is equal to $E_{adhesive}$ and E_2 is equal to E_{steel}, then E'_{eff} is written as follows:

$$E'_{eff} = \frac{E_{adherend} E_{adhesive} (t_1 + t_2)}{E_{adherend} t_1 + E_{adhesive} t_2} \quad \textbf{(7- 12)}$$

Thus the ratio of $\frac{E_{eff}}{E'_{eff}}$ can be defined as follows:

$$\omega = \frac{E_{eff}}{E'_{eff}} = \frac{(E_{adherend} t_1 + E_{adhesive} t_2)(1+e)}{(t_1 + t_2)(E_{adherend} + eE_{adhesive}) + \frac{(1+e) E_{adherend} E_{adhesive}}{k}} \quad \textbf{(7- 13)}$$

The ratio of $\frac{E'_{eff}}{E_{eff}}$ is a function of the Young's modulus of adherend and adhesive and their thickness. Thus two kinds of penalty stiffness of cohesive interface are calculated and listed in Table 7. 2.

Table 7. 2 Penalty stiffness of cohesive interface in different adhesive thickness (ω=98%, $E_{adhesive}$=3000MPa, $E_{adherend}$=199300MPa)

Adhesive (mm)	Failure	Part-1	Part-2	t_1 (mm)	t_2 (mm)	e	k (MPa/mm)
0.2	cohesive	adhesive	adhesive	/	/	/	7.4E+05
	adhesive	adhesive	inner-adherend	0.2	1.6	8	6.6E+05
0.5	cohesive	adhesive	adhesive	/	/	/	2.9E+05
	adhesive	adhesive	inner-adherend	0.5	1.6	3.2	2.8E+05

When the ratio of ω is chosen as 98% which means the loss of stiffness for effective modulus is 2%. The penalty stiffness of cohesive interface use the value of 7.4E+5 MPa/mm for cohesive failure and 6.6E+5 MPa/mm for adhesive failure when 0.2mm adhesive is used in DLJ simulation. When 0.5mm adhesive was used in DLJ simulation, the penalty stiffness of cohesive interface is 2.9E+5 MPa/mm and 2.8E+5 MPa/mm for cohesive failure and adhesive failure, respectively. These calculated values are comparable with the cohesive stiffness published by Camanho (Camanho and Davila 2002) who use 1.0E+6 MPa/mm and Zou (Zou, Reid et al. 2002) whose k

value is in the range from 4.5E+5 to 4.5E+8 MPa/mm. According to Eq.7- 11 and 7- 13, the relation between stiffness k and the ratio of ω can be plotted in Figure 7. 8. It is obvious that cohesive interface have similar penalty stiffness when ratio ω exceeds the value of 0.98. Penalty stiffness does not change significantly when adhesive thickness changes.

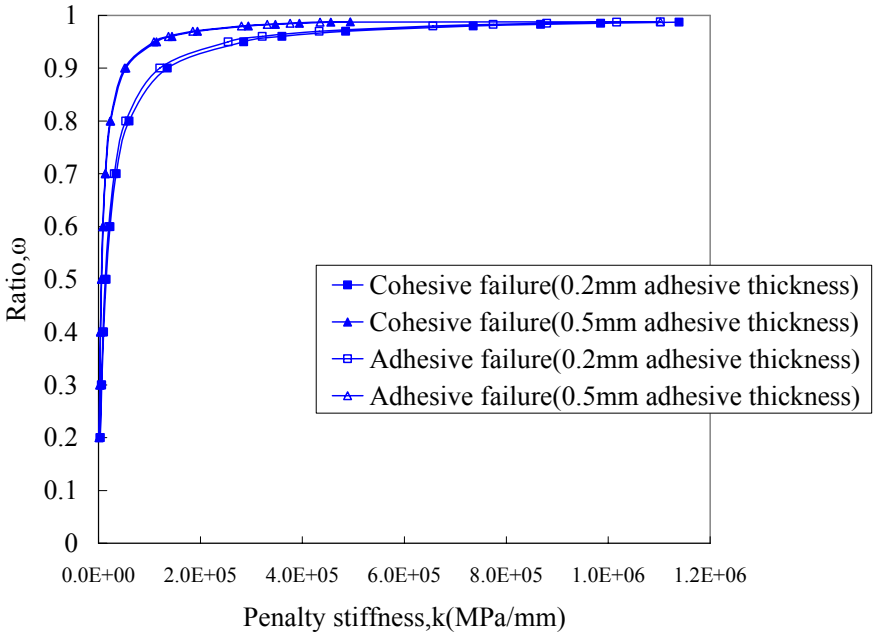

Figure 7. 8 The relation between ratio (ω) and penalty stiffness (k) of cohesive interface for two failure modes

The relation of the penalty stiffness varying with the adhesive thickness is shown in Figure 7. 9. It is cleared that thicker adhesive will decrease the penalty stiffness and the relation between penalty stiffness (k) and adhesive thickness (t) is nonlinear descending. A similar trend is recommended in ABAQUS's theoretical manual which uses a simplified relation of $k=E/t$ (E is Young's modulus of adhesive and t is the thickness of adhesive). This calculation method does not consider the position of cohesive interface which implies that k value is identical in the cases of cohesive failure and adhesive failure.

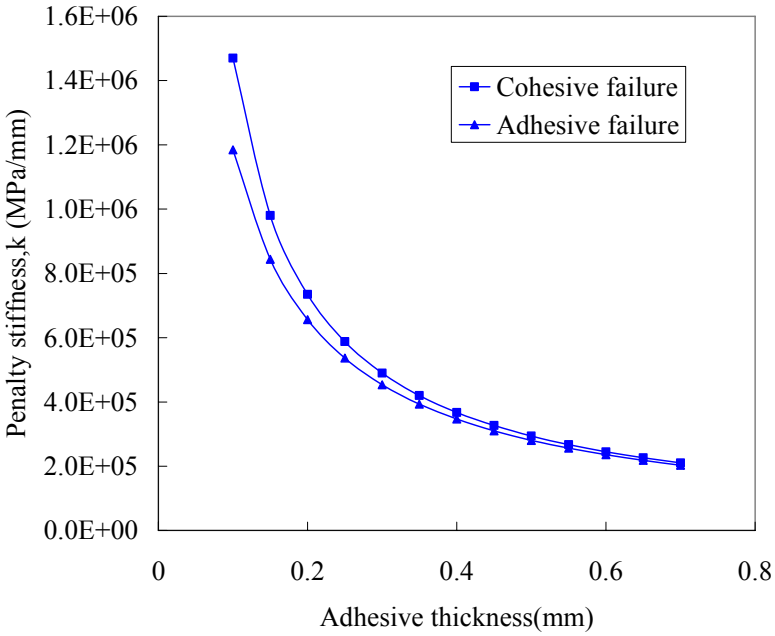

Figure 7. 9 The plot of penalty stiffness varying with adhesive thickness (adhesive Young's modulus E=3000MPa)

7.2.5.2 Determination of initial fracture parameters ($\sigma_{n,0}$, $\tau_{s,0}$, $\tau_{t,0}$)

The maximum normal stress ($\sigma_{n,0}$) in pure opening mode is determined by the Fixed Arm Peel tests, and the maximum shear stress ($\tau_{s,0}$) in pure in-plane mode is resolved by the test of 4 point End Notched Flexure (ENF) and bulk tensile property of AV119. It should be appreciated that these initial stresses are intrinsic properties of materials and are independent of mesh size in FEA and the fracture toughness of experiment (Liljedahl, Crocombe et al. 2006). A typical load-displacement curve of FAP test using 0.2mm thickness adhesive is shown in Figure 5. 4. It is clear that point B is the initiation of cohesive failure, thus the stress at this point can be confidently considered as the maximum normal stress ($\sigma_{n,0}$) which is used in CZM. It was calculated that the value of $\sigma_{n,0}$ is 16.0±1.2MPa when 0.2mm thickness adhesive is used. Unfortunately load-displacement curves of FAP specimens using 0.5mm thickness adhesive did not show clear point B; this may be because a very fast failure at the beginning of test eliminates the observation of point B. However $\sigma_{n,0}$ can be chosen as the same value as specimens using 0.2 thickness adhesive because normal stress is not affected by adhesive thickness generally.

It should be noted that maximum shear stress ($\tau_{s,0}$) in CZM is lower than the stress measured from failure load of DLJ test. It was found that the curves of load-displacement from the Instron machine cannot display an expected turning point because the global displacement consists of high compliance from test machine and the global displacement covers up the very tiny change at the initial failure point (see Figure 7. 10). It is clear that all curves have similar failure load but the displacement shows big scatters. The sharp change in the beginning may be caused from slight sliding between DLJ specimen and jig. There is no change from linear to nonlinear in all curves before the failure point. Thus the maximum shear stress ($\tau_{s,0}$) cannot be detected from these curves.

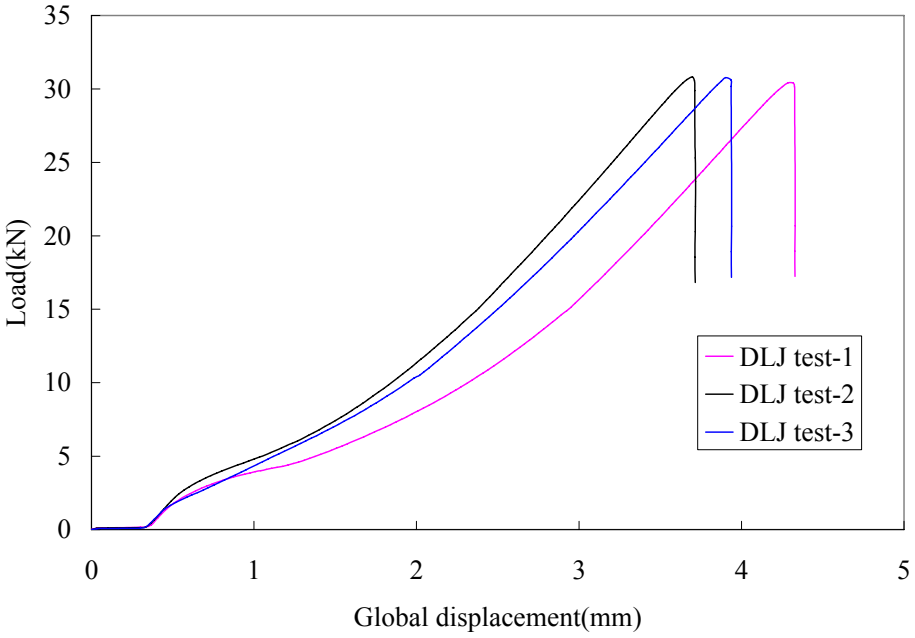

Figure 7. 10 Curves of load vs. displacement of DLJ using 0.2mm thickness adhesive (measured from Instron machine)

Local strain ahead of crack tip of ENF specimens is shown in Figure 5. 15. It was found that local strain ranges from 5% to 10% for specimen with 0.2mm thickness adhesive. According to butt joint test in Figure 3. 1 (Chapter 3), maximum shear stress ($\tau_{s,0}$) in pure in-plane mode is set to 43.0±1.2 MPa at the point of 5% shear strain. Although local strain of ENF specimen using 0.5mm thickness adhesive showed slightly higher value than specimen using 0.2mm thickness adhesive, the same value of maximum shear stress ($\tau_{s,0}$) is used for 0.5mm adhesive thickness specimen without losing accuracy. The value of maximum shear stress ($\tau_{s,0}$) in 0.5mm adhesive thickness can also be confirmed by DLJ tests with extensometer. The curves of

load-displacement measured from extensometer are shown in Figure 7. 11. In this work, adherend using hardening steel has much higher yield stress than adhesive and is not contributing to the nonlinear behaviour of experimental curve. All nonlinear behaviour is arising from adhesive alone. When the initial crack starts, the plastic zone is triggered by the crack tip and develops as reflected by the curve. Thus it is considered that crack starts as curves changes from linear to nonlinear where maximum shear stress ($\tau_{s,0}$) is measured. It is found that the measured shear stress range is 40.0±3.0MPa which is calculated from failure load of specimens.

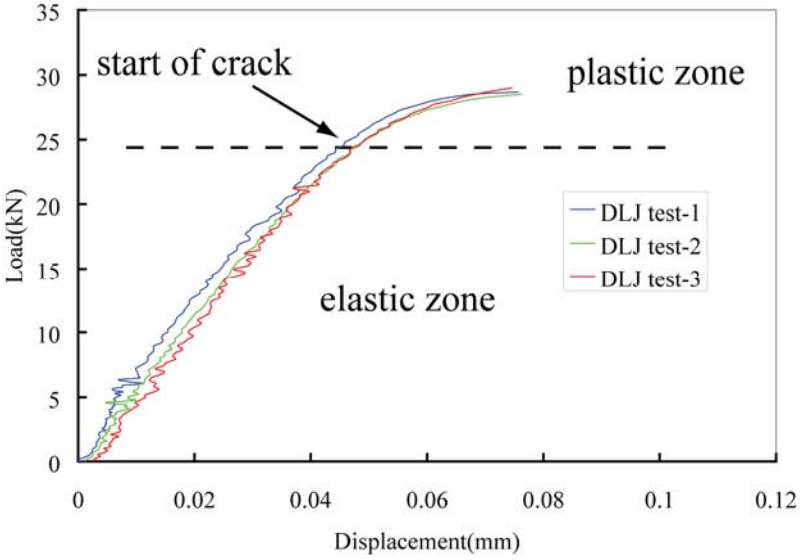

Figure 7. 11 Typical curves of load vs. local displacement of DLJ using 0.5mm thickness adhesive (extensometer gauge length=25mm)

7.2.5.3 Determination of fracture propagation parameters (G_I, G_{II}, G_{III}, η)

Mode-I fracture toughness was determined by Fixed-Arm Peel (FAP) tests and mode-II fracture toughness was obtained via 4 point End Notch Flexure (ENF) tests in previous experiments (see Chapter 5). Mode-III fracture toughness is difficult to determine because there is no reliable test to combine mode-III and other failure modes so far. Some methods such as Edge Crack Torsion (ECT) have been proposed to determine mode-III fracture toughness (Lee 1993), however this method requires transverse shear modulus which is an unclear parameter itself (Camanho, Davila et al. 2001). Therefore, in the crack propagation of DLJ, mode-III fracture toughness is assumed equal to mode-II fracture toughness due to DLJ's geometrical symmetry. Furthermore, mode-III fracture toughness is less important in DLJ simulation because shear stress along the lap width direction is small enough to be neglected.

Much work has been done in order to choose a proper criterion and formulation for fibre-reinforced composites (Camanho and Davila 2002). So far the power law criterion, which is established by Wu and Reuter (Wu and Jr. Reuter 1965), is the most used criterion to predict the crack propagation, which is expressed by the following equation:

$$\left(\frac{G_I}{G_{IC}}\right)^{\alpha}+\left(\frac{G_{II}}{G_{IIC}}\right)^{\alpha}=1 \qquad \textbf{(7- 14)}$$

Reeder successfully used power law criterion with α=1 to predict the failure of polyetheretherketone (PEEK) matrix composites but failed to accurately predict the epoxy matrix composites using α=1 and α=2, respectively (Reeder 1992). It is obvious that power law is convenient but parameter α is chosen randomly. Later, Benzeggagh and Kenane developed another widely used criterion (BK criterion) which is expressed as a function of fracture toughness (Benzeggagh and Kenane 1996). The form of BK is presented as follows:

$$G_{IC}+\left(G_{IIC}-G_{IC}\right)\left(\frac{G_{II}}{G_T}\right)^{\eta}=G_C \qquad \textbf{(7- 15)}$$

Where G_T=G_I+G_{II}, and $\left(\frac{G_{II}}{G_T}\right)$ means the mixed mode ratio. The parameter η was calculated by an interpolation polynomial function. The equation is written at the following form:

$$p\left(\frac{G_{II}}{G_T}\right)=G_{IC}+\left(G_{IIC}-G_{IC}\right)\left(\frac{G_{II}}{G_T}\right)=G_C \qquad \textbf{(7- 16)}$$

It is noted that values of G_{IC} and G_{IIC} were obtained from Fixed Arm Peel and 4 point ENF tests. Pairs of $\left(\frac{G_{II}}{G_T}\right)$ and G_C can be obtained from MMB tests. The above equation can be rewritten as the following equation which is expected to reach a minimum:

$$q=\sum_{i}^{n}\left[G_{IC}+\left(G_{IIC}-G_{IC}\right)\left(\frac{G_{II}}{G_T}\right)_i^{\eta}-\left(G_T\right)_i\right]^2 \qquad \textbf{(7- 17)}$$

Number of *i* is considered as the data pairs of test. Considering $\frac{dq}{d\eta}$ to be zero, the parameter η can be obtained. The comparison of experiment and BK fitting is shown in

Figure 7. 12. It is obvious that both curves start from pure mode-I and end at pure mode-II. The parameter η was calculated as 1.70 which means the q has value of 0.03981. In addition, the largest difference between BK fitting and experimental curve happens at the mixed ratio of 0.3.

It is known that mode-I fracture energy is 1.37 N/mm and mode-II fracture energy is 3.85 N/mm (referred to Chapter 5); mode-III is assumed 3.85 N/mm which is equal to mode-II fracture energy.

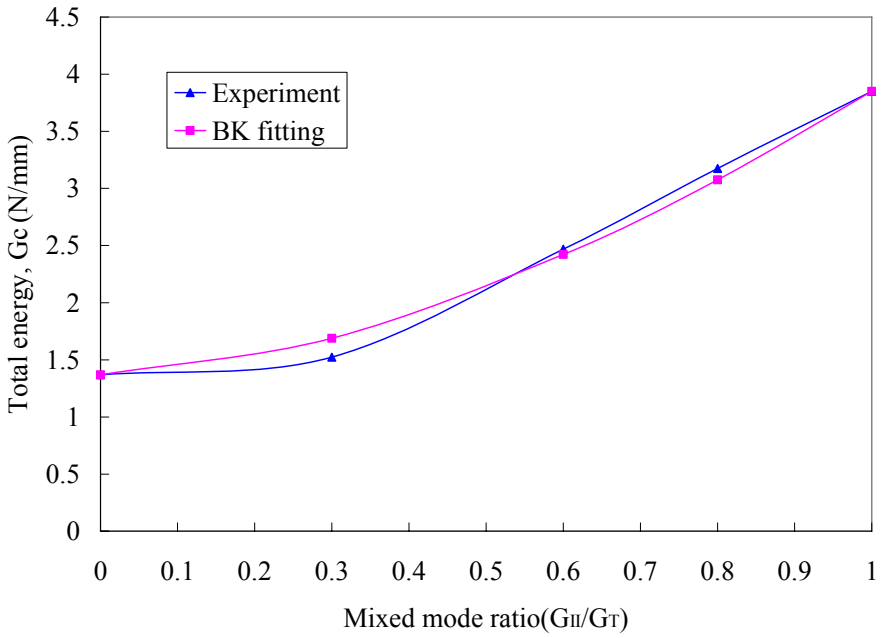

Figure 7. 12 Curves of experiment and BK criterion as a function of mixed-mode ratio

7.2.6 Materials properties of DLJ model

In the simulations, adherend was modelled by simple elastic-plastic behaviour and isotropic hardening behaviour. Adhesive part except for cohesive zone was modelled by exponential Drucker-Prager behaviour and associated tensile hardening after yielding. The properties of adherend were tested and listed in Table 4. 1 (see Chapter 4); adhesive properties are calculated from published basic tests (see Chapter 3) and listed in Table 7. 3; properties of CZM are determined in previous section of this chapter. It should be noted that DLJ-D used the same CZM properties as other models except for G_I and G_{II}. Compared with other models, adhesive failure model (DLJ-D) used mode-I fracture energy of 0.45N/mm (Curley, Hadavinia et al. 2000; Abdel Wahab, Ashcroft et

al. 2002). However the mode-II fracture energy is assumed as twice the value of mode-I fracture energy since FEA results proved that this assumption did not affect the modelling results too much.

Table 7. 3 Mechanical properties of adhesive

Elastic	Young's modulus(MPa)	Poisson's ratio	
	3000	0.39	
Drucker-Prager plastic (exponent form)	Dilation angle	a	b
	24.29	0.01	2
Drucker-Prager plastic (tension behaviour)	Yield stress(MPa)	Plastic strain	
	37.97	0	
	44.46	0.00077	
	51.83	0.0022	
	57.82	0.0042	
	62.58	0.0066	
	66.23	0.0093	
	68.90	0.012	
	70.73	0.016	
	71.84	0.019	
	72.37	0.023	
	73.00	0.027	
	73.70	0.031	
	75.70	0.042	
	76.80	0.052	
	78.30	0.060	
	81.00	0.080	
	83.00	0.10	
	87.55	0.15	

The determined CZM parameters of 0.2mm and 0.5mm adhesive thickness are listed in Table 7. 4. For the simplified reason, the modelling of 0.3mm adhesive thickness is assumed to use identical parameters as 0.2mm adhesive thickness since there is no notable difference from experiments. It should be noted that all models use the same BK parameter of η=1.70. The parameter η does not affect the simulation results significantly, while the fracture energies and initial failure stresses are the main factors to affect simulation results.

Table 7. 4 Determined CZM parameters from experiments and analysis

Adhesive thickness t(mm)	Failure	k (MPa)	$\sigma_{n,0}$ (MPa)	$\tau_{s,0}$ (MPa)	G_{IC} N/mm	G_{IIC} N/mm	BK(η)
0.2	cohe	7.4E+05	16	43	1.37	3.85	1.70
	adhe	6.6E+05	16	43	0.45*	0.90	1.70
0.5	cohe	2.9E+05	16	40	1.03	3.85	1.70
	adhe	2.8E+00	16	40	0.45*	0.90	1.70

* G_{IC} value of 0.45N/mm is obtained from Curley's work (Curley, Hadavinia et al. 2000)

7.2.7 3D DLJ model analysis

7.2.7.1 Comparison of FEA, experiment and analytical solution

In order to validate the application of CZM, FEA results are compared with the analytical solution and experimental results. Firstly the failure load from both experiment and FEA were compared; second, local displacement of FEA compared with the results of experiments because extensometer and strain gauge were applied. In addition, analytical solution is employed as well. The failure loads from prediction and experiment are listed in Table 7. 5.

Table 7. 5 Experimental tensile failure load and 3D prediction of DLJ

Adhesive thickness (mm)	Experimental failure load[#] (kN)	FEA failure prediction* (kN)
0.2	31.0±1.6	30.2
0.5	27.5±2.1	27.1

[#] More than 15 specimens were tested for each adhesive thickness

*FEA failure prediction used DLJ-B model (i.e. failure close to interface)

It is clear that the failure load predicted by FEA agrees with the experimental results very well. It is appreciated that the cohesive zone in FEA plays a very important role because the failure of cohesive layer is controlled by T-S law; other factors such as the elastic and plastic behaviour of adherend and adhesive usually affect the local and global strain behaviour in the FEA. As demonstrated previously, the parameters of T-S law used in cohesive zone were obtained from experiments and the position of cohesive layer was observed from the morphology of failure surface of DLJ. Thus it is proved that cohesive zone application and its definition in this work are correct.

The load versus displacement from experiment, FEA and analytical solution are shown

in Figure 7. 13, It should be noted that the displacement value in all curves are obtained from relative displacement of two points which are located in the midline of top surface of FEA since the moment and transverse shrinkage of adherend does change the relative displacement slightly. In this way, the relative displacement can be compared by the extensometer which measured the same two positions in DLJ test symmetrically using 25mm gauge length (referred to Chapter 4).

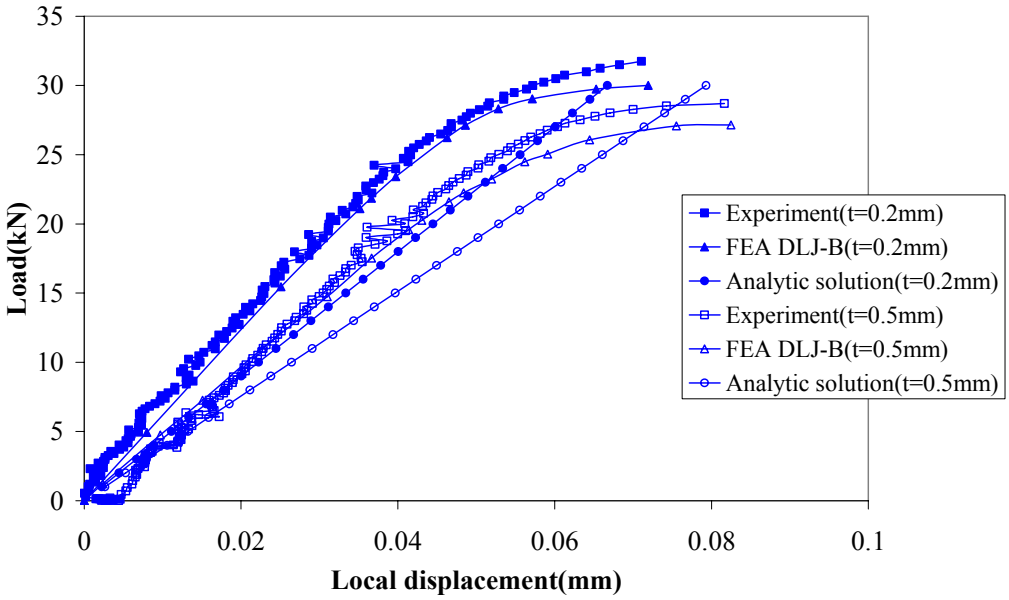

Figure 7. 13 Typical curves of load vs. displacement from DLJ experiment, FEA and analytical solution method

It is found that DLJ-B model (i.e. crack close to interface, see Figure 7. 2) is able to simulate the local displacement of DLJ very well for both 0.2mm and 0.5mm adhesive thickness; both experiment and FEA model show similar displacement trend and demonstrate that 0.5mm adhesive thickness specimen has bigger displacement than 0.2mm adhesive thickness specimen at their failure point. The curves from experiment consist of two parts: first part is linear then changes to nonlinear after initial failure; the slope of linear portion represent the stiffness of joint. It is obvious that FEA curves match the experimental curves very well in both linear part and nonlinear part. The nonlinear part in FEA is contributed by cohesive elements whose failures start to propagate after initial crack. Thus, FEA is able to model the DLJ excellently with respect to the global response. It should be appreciated that the slope of FEA curve is mainly controlled by parameters of CZM, so the good agreement between experimental curves and FEA curves means the definition of CZM in this work is validated.

In addition, the diversion point from linear part to nonlinear part varies with the thickness of adhesive slightly. The diversion points of specimens with 0.2mm and 0.5mm thick adhesive are at local displacement of 0.045 and 0.05mm, respectively, but after the diversion point, specimen with 0.5mm adhesive has longer curve before final failure. This is because thicker adhesive layer can develop more plastic zone under load which gives rise to the global extension, while plastic zone in thin adhesive layer cannot expand fully due to the high constraint of adherend. This trend is also revealed by FEA model.

However the analytical solution fails to predict displacement development because this method uses elastic properties only. The curve of analytical solution is seen to be far away the experimental curves and does not show any nonlinear part which really exists in practice. Thus, the analytical solution can only predict the initial stiffness. In this work, the analytical solution is able to predict that 0.2mm adhesive thickness specimens have higher stiffness than 0.5mm adhesive thickness specimens. In both cases, the predicted stiffness using analytical solution are lower than those from experiment and FEA.

7.2.7.2 Failure analysis of joints

Many failure criteria which are classified as stress or strain criteria and fracture mechanics criteria have been proposed and developed for many years. Widely used failure criterion such as maximum von Mises stress is easiest to use but it does not take account of hydrostatic stress although the behaviour of adhesive within the joint is affected by this stress significantly. In general, principal stress or strain is used as failure criterion. Principal stress is used widely because adhesive failure in joints is mostly caused by tension. For ductile adhesive, principal strain criterion may be preferred. In some cases, the choice of criterion depends on the comparison of the behaviour of bulk adhesive and bonded adhesive (Adams, Comyn et al. 1997). However, it is difficult to determine which one should be used; moreover, the criteria always depend on the element size. The critical stress or strain criterion has been used by Lee and Lee (Lee and Lee 1992), but their criterion cannot predict the joints with arbitrary thickness adhesive. All above criteria are based on stress or strain. A criterion based on critical plastic energy density was proposed by Harris and Adams who

introduced a tiny roundness into adherend corners (Harris and Adams 1984), however it is unclear how the degree of roundness affects the energy density.

An alternative fracture criterion is the application of fracture energy (G_c) or toughness of materials. This criterion is independent of the geometry and used to predict the failure of adhesive joints (Kinloch 1997). It is noted that the cohesive element is the most close to the fracture energy approach by prescribing the failure behaviour ahead of the crack tip through the relation of fracture energy (G_c) and maximum stress (σ_{max}).

The failure predicted by the simulation of a typical DLJ model (DLJ-C) is shown in Figure 7. 14. The failure status is demonstrated by SDEG (scalar stiffness degradation at integration points) which is used to describe the process of damage evolution. It is found that failure always occurs first in the bottom cohesive layer since SDEG value reaches 1 earlier than in the top cohesive layer; thus top cohesive layer does not affect predicted failure load. It is proved that FEA model using two cohesive layers has the same results as FEA model using one cohesive layer. Thus DLJ-B has similar results as DLJ-C when same adhesive thickness is used. However DLJ-A has higher predicted failure load than all other DLJ models because it is typical cohesive failure. Furthermore, DLJ-C has similar results as DLJ-D when identical cohesive zone parameters are used which implies that slight change of the position of cohesive zone do not affect modelling results significantly.

There are three stresses- σ_y , σ_{xy} , σ_{yz} in cohesive element which are the direct through-thickness stress, first transverse shear stress and second transverse shear stress, respectively. It was found that σ_{yz} is very small compared with σ_y and σ_{xy} ranging from the beginning of tension to the final failure. Thus the shear part σ_{yz} can be neglected. Since stress σ_{yz} represents mode-III failure style, the failure of DLJ arises from the mixed mode-I and mode-II failure. Thus it is justified that mode-III failure is not considered in this work.

It is noted that a refined mesh was used at one end of overlap area where failure occurs firstly, thus this model displays no spurious mesh dependency.

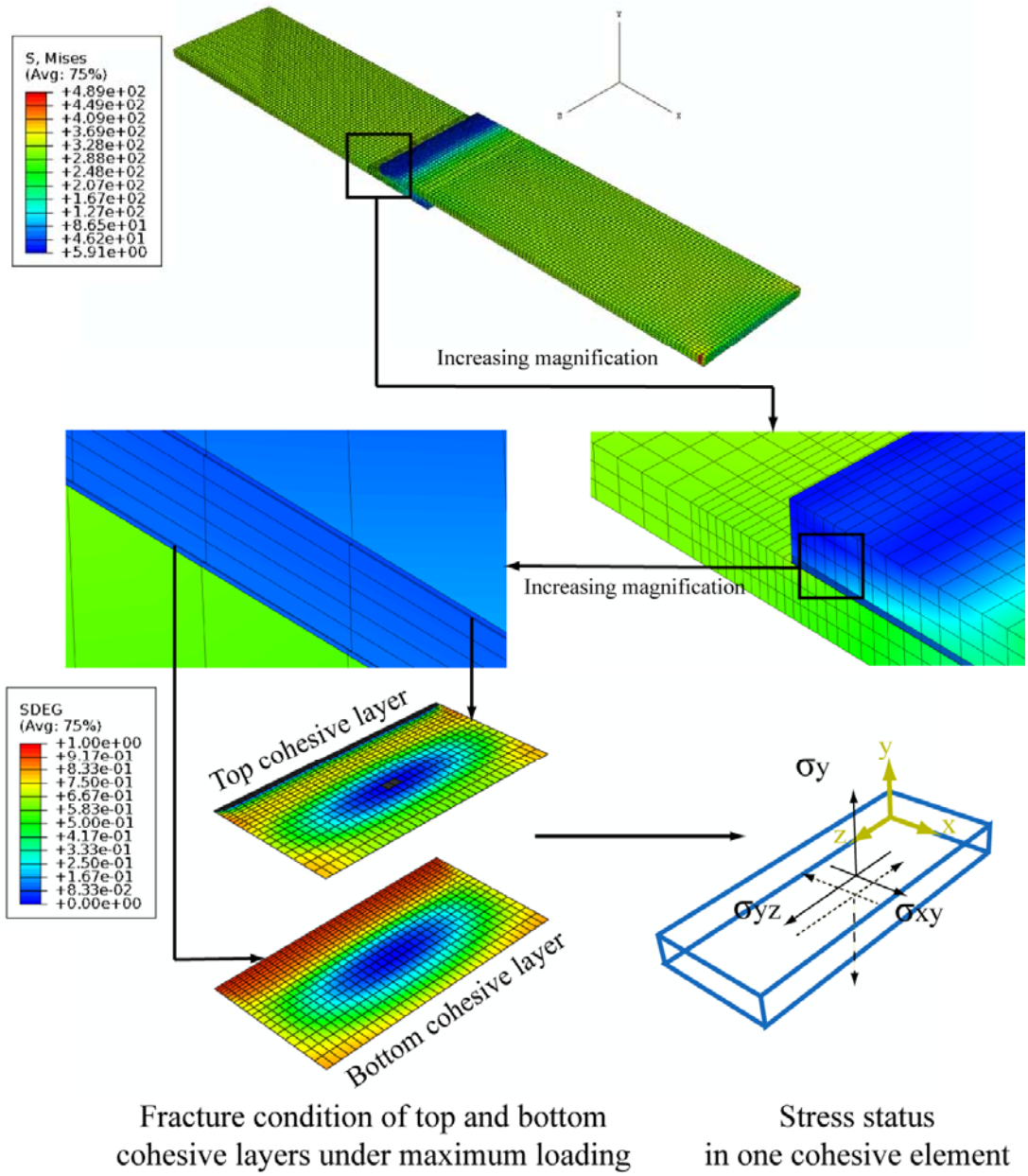

Figure 7. 14 Typical cohesive zone layers in DLJ and stress status in one cohesive element

The cohesive modelling has an advantage to show the failure initiation and propagation and the value of SDEG in cohesive zone can be employed to display the joint failure history. Unlike the Single Lap Joint whose crack grows symmetrically from both ends of joint (Abdel Wahab, Ashcroft et al. 2002), the crack growth in DLJ starts from the end of joint which is close to inner adherend and then crack occurs in the joint's other end which is close to outer adherend. This phenomenon is confirmed by both experimental observation and FEA modelling, the reason is highest stress

concentrates at the joint end and crack always initiates there in priority, thus the area of adhesive adjacent to inner adherend is mostly investigated.

0.2mm adhesive thickness:

Two DLJ models using 0.2mm adhesive thickness under their maximum load are shown in Figure 7. 15, it is noted that the figures are displayed using the SDEG parameter.

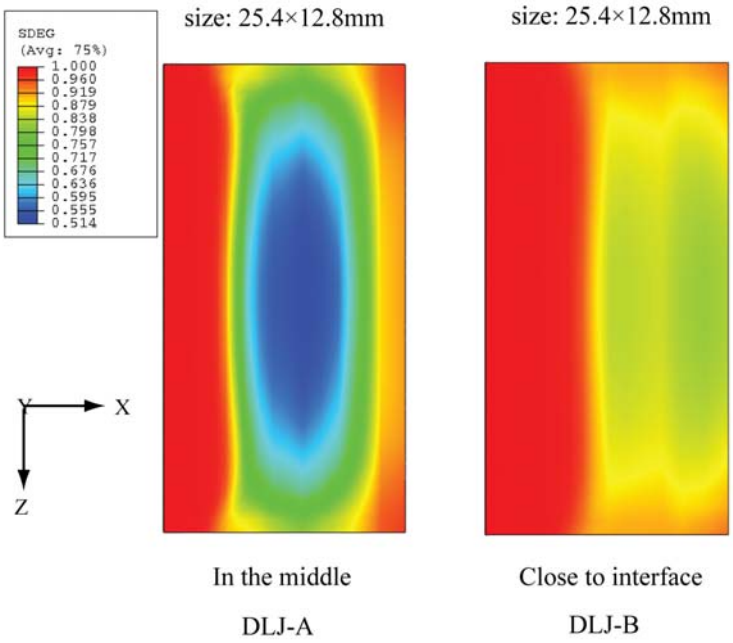

Figure 7. 15 Damage distribution in cohesive zone layer (0.2mm adhesive thickness)

It should be noted that these images show the SDEG distributions at the moment when maximum loads are achieved. It is clear that in the case of DLJ-A the failure is completed in the left part which is close to the end of outer adherend; the top right corner and bottom right corner nearly reach the final failure; the centre area of cohesive zone surface is far away from the final failure status and is still bonded by adhesive. Damage surface develops from both left area and right area to the centre when failure propagates after the maximum load.

For the case of DLJ-B, cohesive zone has a little larger failure area than DLJ-A at the maximum load. The failure also starts from the left part which is close to end of outer adherend and develops in the right direction after the maximum load. But the uncompleted failure part in DLJ-B is much closer to final failure than DLJ-A. This implies that DLJ-B develops to the final failure much quicker than the DLJ-A. Thus

DLJ-A (failure along the middle of adhesive layer) not only has higher capacity of load but also can delay the crack propagation.

0.5mm adhesive thickness:

Three DLJ models using 0.5mm adhesive thickness under their maximum load are shown in Figure 7. 16. It should be noted that only bottom cohesive layers are demonstrated in this figure. It is found that all three models have very similar damage condition when the loads achieve the maximum load. This is very beneficial for the use of CZM because failure always occurs at the position where the crack is most easy to develop and extra cohesive zone does not affect the modelling results. Thus more than one cohesive zone can be applied to one model to predict the failure path if the path of the crack is unclear or difficult to determine. Furthermore, the similar results of DLJ-B, DLJ-C and DLJ-D imply that Virtual Crack Closure Technique (VCCT) (referred to Section 8.3.1) is valid using crack path which has tiny distance (0.01mm) from adherend since this technique encounters the problem of stress oscillation if crack is assumed at the interface directly. This tiny distance was introduced and confirmed by other works previously (Raju, Crews et al. 1988; Dattaguru, Venkatesha et al. 1994).

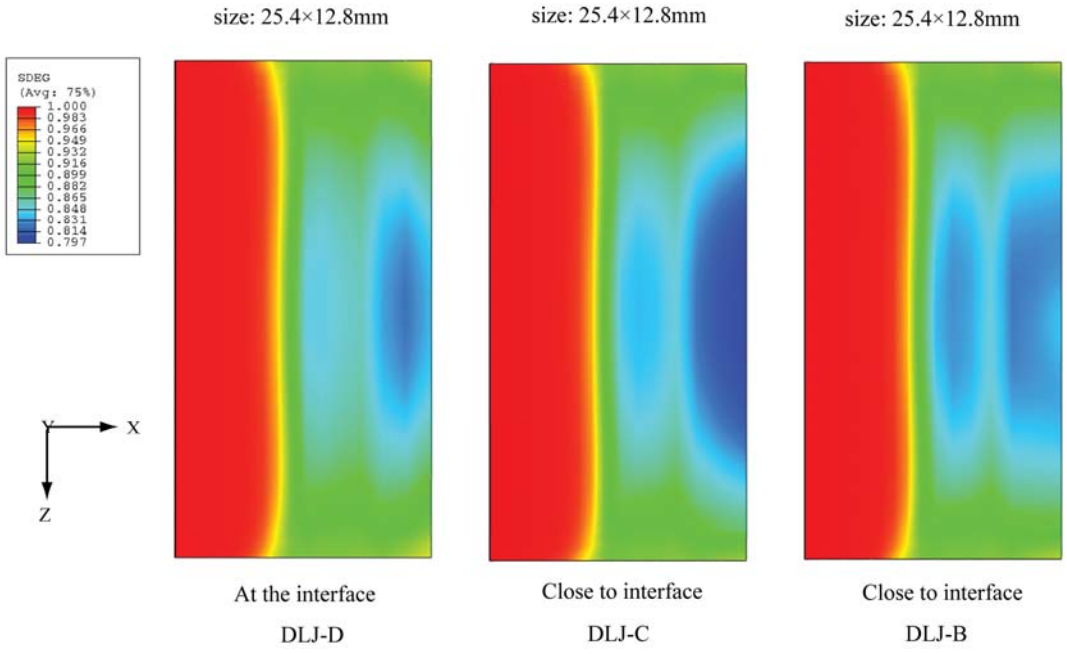

Figure 7. 16 Damage distribution in cohesive zone layer (0.5mm adhesive thickness)

7.2.8 Effect of modelling parameters

7.2.8.1 The effect of number of cohesive zones

Since DLJs bonded by 0.5mm thickness adhesive generally have cohesive failure which is very close to the inner adherend, it is necessary to investigate the difference between models which apply the cohesive layer in different positions. According to Figure 7. 2, DLJ-B implies that only one cohesive zone has been applied at the position where failure is 0.01mm distant from the inner adherend; DLJ-C uses two cohesive zones such that one zone is 0.01mm distant from outer adherend and another zone is 0.01mm distant from the inner adherend; while DLJ-D applies both two cohesive zones at the interfaces directly. All three models employed identical material properties, element type and mesh density. Their load-displacement behaviour is shown in Figure 7. 17. It should be noted that displacements are obtained from 25mm gauge range of models.

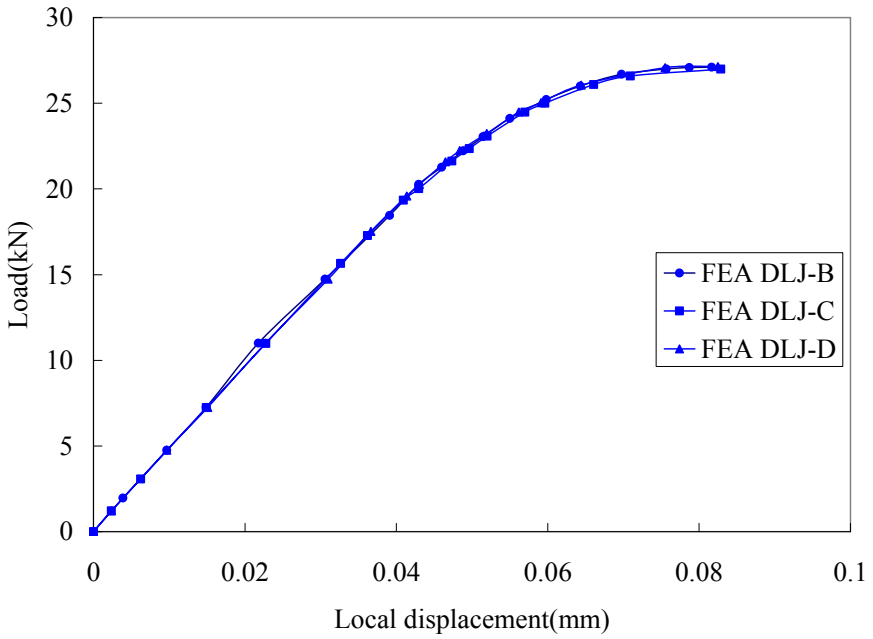

Figure 7. 17 Comparison of load-displacement curves of different failure models

It is obvious that all three models have the same curves; the values of failure load and failure displacement only have very slight differences which are shown in Table 7. 6. Thus it can be considered that the number of cohesive zones does not affect the modelling and the slight change of cohesive zone position also has no effect on the results of modelling. This conclusion is significantly useful to predict adhesive joints

or other structures since the failure path in practice is not clear and structures have very complicated geometry.

Table 7. 6 Comparison of FEA results using different model

Model	Failure displacement(mm)	Failure load(kN)
DLJ-B	0.0816	27.10
DLJ-C	0.0828	26.98
DLJ-D	0.0824	27.14

7.2.8.2 The effects of cohesive zone type on predicted failure load

It should be appreciated that the maximum stresses in T-S law play the most important role in the approach of CZM as the choice of these values will affect the predicted failure load significantly. For DLJ modelling, mode-III shear stress is less relevant and ignored usually, thus the effects of the maximum opening stress ($\sigma_{n,0}$) in mode-I and maximum shear stress ($\tau_{s,0}$) in mode-II are demonstrated in this work. Furthermore, the failure of DLJ under tensile load is always an opening style. Thus maximum opening stress ($\sigma_{n,0}$) is especially important. The predicted failure load varying with maximum opening stress ($\sigma_{n,0}$) and maximum shear stress ($\tau_{s,0}$) is shown in Figure 7. 18. The relation between failure load and maximum opening stress is shown when the maximum shear stress ($\tau_{s,0}$) is fixed at 40MPa. In the same way, maximum opening stress ($\tau_{s,0}$) is fixed at 16MPa then the curve of failure load vs. maximum shear stress is obtained.

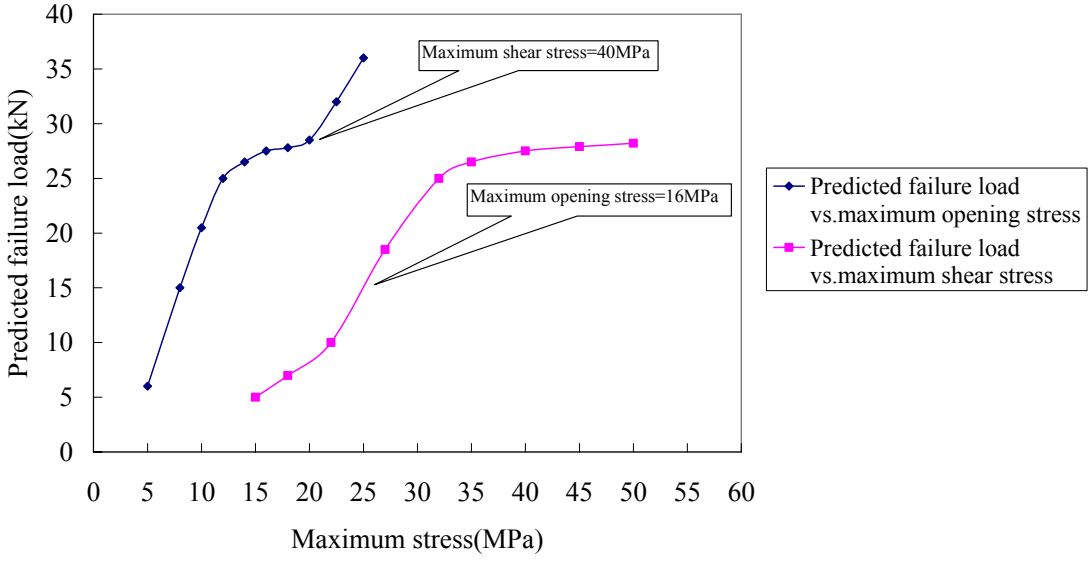

Figure 7. 18 The effects of maximum stress to the predicted failure load (DLJ-B with 0.5 mm adhesive thickness)

It is obvious that the predicted failure load depends on the maximum opening stress ($\sigma_{n,0}$) especially in the range of low and high magnitude of $\sigma_{n,0}$, in addition there is a plateau in the middle range where the failure load depends less on $\sigma_{n,0}$. This is attributed to the fact that most cohesive elements along overlap length are starting to operate together in the low range of $\sigma_{n,0}$, meantime few cohesive element exceed the maximum stress and start to unload. In the range of high $\sigma_{n,0}$, many cohesive elements along the overlap exceed the maximum stress and start to unload together; these cohesive elements form the process zone length (Liljedahl, Crocombe et al. 2006). Obviously the process zone length is dependent on the value of $\sigma_{n,0}$, especially in the high range of $\sigma_{n,0}$, thus the failure load varies with $\sigma_{n,0}$ sharply again. In the range of platform, the value of initial fracture toughness affects the failure load via BK criterion; it is obvious that failure load increases if high initial fracture toughness is used because initiation of fracture in joint requires more energy and more force. As result, the failure load increases. This effect of initial fracture toughness to failure load is dependent on the mode-I, mode-II and mixed-mode ratio together; however the collective trend of failure load upon initial fracture toughness is increased.

Regarding effect of the maximum shear stress to the failure load, it is seen that failure load decrease sharply in the low range of shear stress but failure load exhibits a stable value after the point of shear stress of 32MPa. This is because failure in DLJ is always an opening style even if it is mixed-mode failure. The fact is that high shear stress does not give rise to the failure load because the contribution amount of shear stress to failure is controlled by BK criterion. However, if the first shear stress is too small (even its value is bigger than normal stress) then the failure style in DLJ is no longer a mode-I domain failure (opening failure), the failure becomes the mode-II failure style because the cohesive element is very easy to be triggered, thus the failure load is dependent on the shear stress strongly. For example, the modelling results show that the failure load is only around 10kN, which is much lower than the experimental result, when 22MPa shear stress is used. The values of $\sigma_{n,0}$ and $\tau_{s,0}$ were determined from experiment in this work and are shown in Table 7. 4.

7.2.8.3 The effects of cohesive zone position

DLJ-B is the main FEA model for all DLJs; DLJ-A, DLJ-C and DLJ-D were used to

obtain knowledge of effect of cohesive zone position on load-displacement behaviour. The effect of DLJ model and adhesive thickness on load-displacement curves are shown in Figure 7. 19. It is noted that FEA and analytical solution used the same gauge length and position as experiments. The parameters of CZM in these models are shown in Table 7. 4.

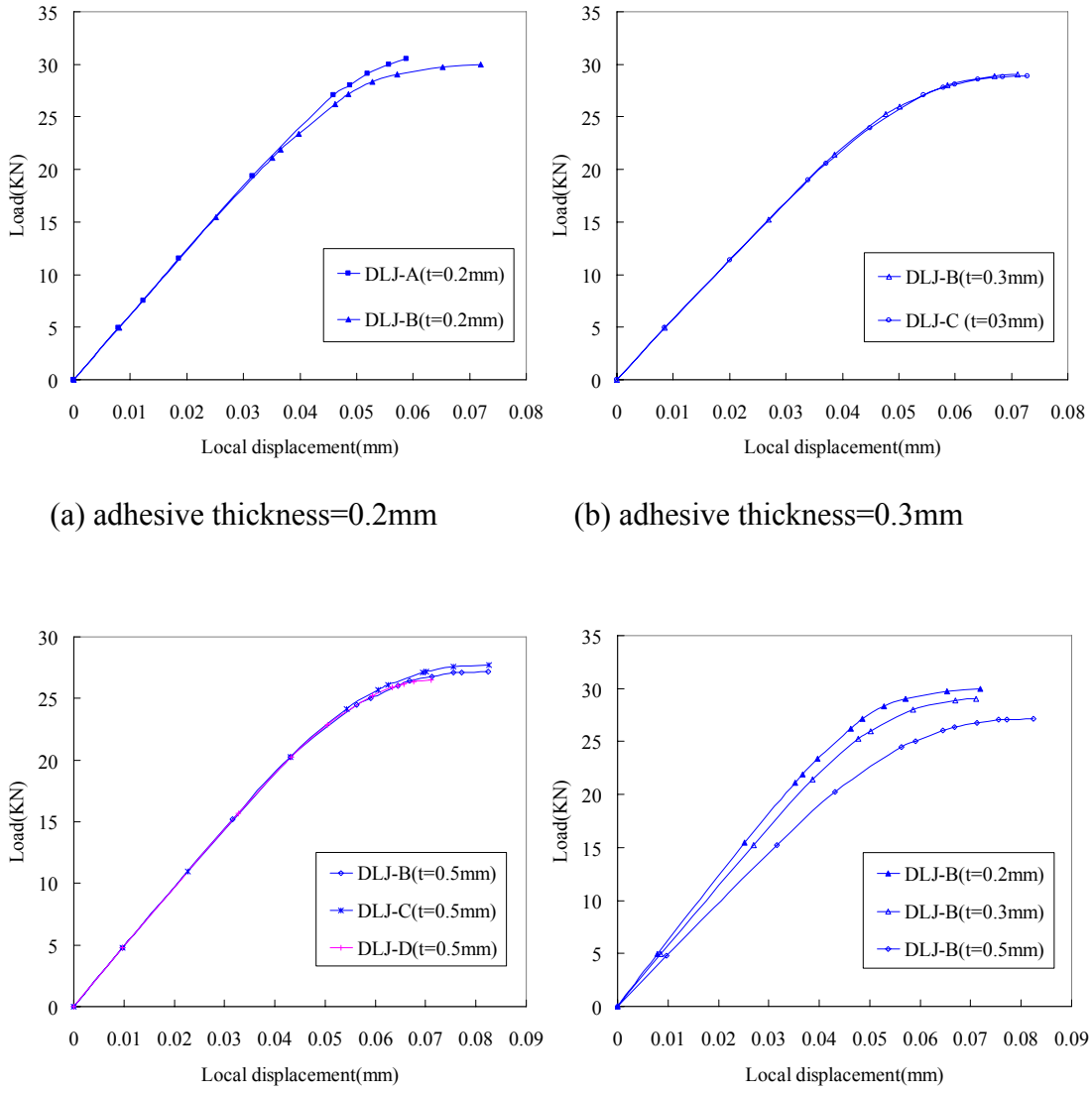

(a) adhesive thickness=0.2mm (b) adhesive thickness=0.3mm

(c) adhesive thickness=0.5mm (d) various adhesive thickness(DLJ-B)

Figure 7. 19 Effect of DLJ model and adhesive thickness to the curves of load-displacement

For the models using 0.2mm thick adhesive, it is found that DLJ-B has a little lower failure load than DLJ-A but has much higher displacement at failure point which was confirmed by experiments. Thus DLJ-A cannot predict the deformation behaviour of 0.2mm adhesive thickness specimen under tensile load and DLJ-B is the best model to predict the specimen using 0.2mm adhesive. For the models using 0.3mm thick

adhesive, both DLJ-B and DLJ-C have the same predicted behaviour of load-displacement, which implies that the additional top cohesive zone layer does not change the character of failure initiation and propagation. In addition, the failure always occurs along the bottom cohesive zone layer under the observation of FEA results. However, this additional top cohesive zone layer provides a method to investigate the stress field where it is very close to the thin adherend (i.e. outer adherend).

For the models using 0.5mm thick adhesive, the DLJ-B and DLJ-B$^{\#}$ models have similar results. DLJ-B$^{\#}$ predicted a slightly higher failure load than DLJ-B, this is attributed to the fact that the first shear stress ($\tau_{s,0}$) is used as 43MPa instead of 40MPa in DLJ-B$^{\#}$. However but both have similar local displacement. DLJ-D^{+} is pure adhesive failure model, thus the parameters used in this model are partially different from those used in other cohesive models. Because the cohesive zone layer does not suffer from damage under pure compression, and it is well known that the stress field in the vicinity of the end of inner adherend is compression and shear, therefore it is difficult to initiate failure at this corner since the component of shear is not high enough to do so. The details of failure load and corresponding displacement are listed in Table 7. 7.

Table 7. 7 Failure load and displacement in different CZM models

Name	Adhesive t (mm)	Failure style	CZM position	Failure (kN)	Local displacement* (mm)
DLJ-A	0.2	cohesive	middle	30.50	0.05875
DLJ-B	0.2	cohesive	bottom	30.20	0.07191
DLJ-B	0.3	cohesive	bottom	29.05	0.07107
DLJ-C	0.3	cohesive	bottom and top	28.91	0.07277
DLJ-B	0.5	cohesive	bottom	27.14	0.08249
DLJ-B$^{\#}$	0.5	cohesive	bottom and top	27.73	0.08262
DLJ-D^{+}	0.5	adhesive	bottom and top	26.53	0.07108

*Local displacement measured at the same range of extensometer (25mm)

$^{\#}$This DLJ-B use $\tau_{s,0}$=43MPa, other properties are identical to DLJ-B with 0.5mm

$^{+}$This DLJ-D use G_{IC}=0.45N/mm and G_{IIC}=0.90N/mm, other properties are identical to DLJ-B with 0.5mm

7.2.8.4 The effects of constitutive laws and adhesive properties on modelling

Hardened steel was used as adherend and its properties are not taken into account further since its high yield stress (Table 4. 1) ensures there is no plastic deformation. Thus it is assumed that adherend does not affect the modelling behaviour. However adhesive and cohesive interfaces are very complex, and any change of their material models and constitutive laws definitely affect the modelling results. Further attention should be paid to those factors, so that deeper understanding about modelling can be established and useful instructions can be obtained to design and apply FEA modelling. It should be noted that definition of T-S law is based on ABAQUS code in this work, thus study of cohesive interface can be referred to its theory manual. It is known from previous chapter that Drucker-Prager model has different representations due to the choice of yield criterion. Generally, three yield criteria are provided in Drucker-Prager model which are linear, hyperbolic and exponent forms. Here linear and exponent Drucker-Prager models are chosen to represent adhesive properties. Hyperbolic Drucker-Prager model is not taken into account since it is similar to the exponent form. Besides, another factor needed to be considered is the flow law in linear Drucker-Prager model which can be defined as associated or non-associated flow dependent on whether the frictional angle (β) and dilatational angle (φ) are equal to each other or not.

In order to investigate the effects of adhesive properties on the overall results, the properties of adherend and cohesive interface were fixed. It is found that the modelling result is very sensitive to the choice of flow rule; if the frictional angle was set equal to dilatation angle, the model fails to converge. This implies that the non-associated flow is realistic. When non-associated flow was used, the difference between linear Drucker-Prager and exponent Drucker-Prager model is not significant as shown in Table 7. 8 and Figure 7. 20.

Table 7. 8 Description of various model and failure load

Name	adhesive material	Mixed mode	Damage initiation*	Damage softening	Failure(kN)
mode-1	elastic-plastic	BK	QUADS	linear	28.42
mode-2	linear D-P	BK	QUADS	linear	30.59
mode-3	exponent D-P	BK	QUADS	linear	30.50
mode-4	exponent D-P	BK	QUADS	exponent	32.26
mode-5	exponent D-P	independent	QUADS	linear	29.26
mode-6	exponent D-P	power law	QUADS	linear	30.37
mode-7	exponent D-P	BK	MAXS	linear	32.35

* QUADS and MAXS are defined at Eq.7-18 and 7-19.

It should be noted that displacement was measured from 25mm gauge length and DLJ-A model with 0.2mm adhesive thickness was studied for easy convergence in simulation. Both linear and exponent Drucker-Prager has similar behaviours of load-displacement whose response is represented by model-2 and model-3, respectively; model-1 represents simple elastic-plastic properties which was used for adhesive, it is obvious that model-1 yields higher elongation at failure point and failure load is lower than other models; this is because adhesive using simple elastic-plastic properties cannot represent real adhesive and yields easier than Drucker-Prager models since no pressure-sensitivity was considered. Simple elastic-plastic behaviour also implies that its yielding is caused by shear stress since its meridian is parallel to hydrostatic axis. For Drucker-Prager materials, yield stress is related to first invariant (hydrostatic stress or pressure stress) which gives rise to the anti-yield ability because shear stress is not the only cause of yielding.

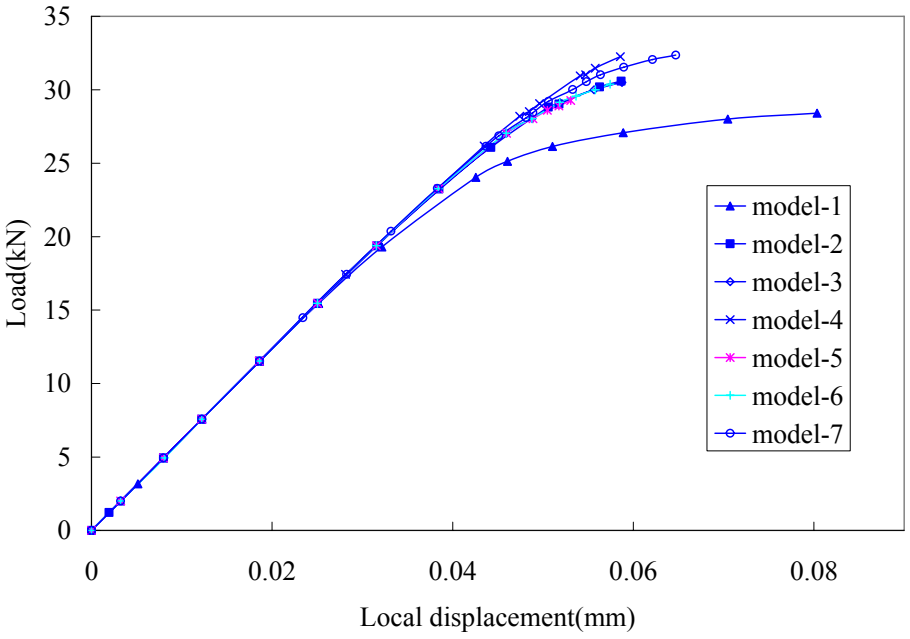

Figure 7. 20 Load-displacement behaviours using various constitutive rules

7.2.8.5 The effect of cohesive interface

The properties of cohesive interface are much more complicated than adhesive properties; complexity arises from various definitions of its behaviour. Since Traction-Separation law consists of both damage initiation and damage evolution which may affect the element behaviour as failure occurs, the beginning of failure can be based on strain or stress criterion, but both strain and stress criterions are able to convert to each other because they have relationship based on stiffness and energy release rate. Thus only damage initiation based on stress was applied here since those stresses are obtained from experiments. Initiation damage criterion based on stress is specified on the terms of maximum nominal stress (Maxs) and quadratic nominal stress (Quads) criterion, respectively (ABAQUS Analysis User's Manual 2007d). They are represented as follows:

$$\max\left\{\frac{\langle t_n \rangle}{t_n^0}, \frac{t_s}{t_s^0}, \frac{t_t}{t_t^0}\right\} = 1, \text{ Maximum nominal stress criterion} \qquad \textbf{(7- 18)}$$

$$\left\{\frac{\langle t_n \rangle}{t_n^0}\right\}^2 + \left\{\frac{t_s}{t_s^0}\right\}^2 + \left\{\frac{t_t}{t_t^0}\right\}^2 = 1, \text{ Quadratic nominal stress criterion} \qquad \textbf{(7- 19)}$$

Where t_n^0, t_s^0 and t_t^0 are the maximum stresses referring to Figure 2. 3; these stresses

are either normal to cohesive interface or in the first or the second shear direction. It is noted that the symbol $\langle\ \rangle$ represents Macaulay bracket which interpreted as follows:

$$\langle x \rangle = \begin{cases} 0, x < 0 \\ x, x \geq 0 \end{cases} \quad \textbf{(7- 20)}$$

Thus, the Macaulay bracket means a pure compressive stress state does not initiate damage.

It is obvious that Maxs assumes that the failure initiates as the maximum nominal stress ratio reaches one, while Quads assumes that failure initiates as the nominal stress ratios weighted by quadratic interaction function reaches one. Both criteria use the same nominal stresses appearing in the denominators of above equations, thus the definition for both initial damage criteria are the same but the behaviour of cohesive elements should be different. Fixing all other parameters and properties of model, the difference between Maxs and Quads is shown in Figure 7. 20. Model-7 uses Maxs criterion and other models use Quads criterion. Comparing model-3 and model-7, model-7 has higher failure load and longer failure displacement. This is because peel stress is the major factor to cause failure in bonded joint, and Maxs criterion requires that peel stress has slightly higher value to trigger failure initiation than Quads criterion. Thus it is best to choose a reasonable initiation damage criterion to predict the behaviour of bonded joint. In this work, the Quads criterion is the best one to describe joint failure.

The damage evolution is another field to consider about the cohesive application. After damage initiation completes, damage evolution determines how the stiffness degrades. The damage status is defined by overall scalar stiffness degradation (*D*) (Davila, Camanho et al. 2001; Lee, Rus et al. 2007; Erlicher, Bursi et al. 2008); before damage evolves, the value of *D* is zero; during the damage process *D* value increases till it reaches one which means final damage. The stress component of cohesive elements determined by this *D* value and predicted stresses ($t_n^{'}$, $t_s^{'}$ and $t_t^{'}$) corresponding to current strain status. Their definitions are shown as follows (ABAQUS Analysis User's Manual 2007d):

$$t_n = \begin{cases} (1-D)t_n^{'}, & t_n^{'} \geq 0 \\ t_n^{'}, & otherwise \end{cases} \quad \textbf{(7- 21)}$$

$$t_s = (1-D)t_s^{'}$$
$$t_t = (1-D)t_t^{'} \quad \textbf{(7- 22)}$$

Generally the stiffness can degrade on the various softening forms which affects the movement of *D* value possibly, then affects the failure process of modelling. Linear softening and exponent softening have different definitions of *D* value shown as follows (ABAQUS Analysis User's Manual 2007d):

$$D = \frac{\delta_m^f(\delta_m^{\max} - \delta_m^0)}{\delta_m^{\max}(\delta_m^f - \delta_m^0)}, \text{ Linear softening} \quad \textbf{(7- 23)}$$

$$D = 1 - \left\{\frac{\delta_m^0}{\delta_m^{\max}}\right\}\left\{1 - \frac{1-\exp\left(-\alpha\left(\frac{\delta_m^{\max} - \delta_m^0}{\delta_m^f - \delta_m^0}\right)\right)}{1-\exp(-\alpha)}\right\}, \text{ Exponential softening} \quad \textbf{(7- 24)}$$

Where material parameters α is used to determine the exponential shape (i.e the damage rate), the parameter $\delta_m^{\max}$ is the maximum effective displacement during deformation, the initiation effective displacement (δ_m^0) and failure effective displacement (δ_m^f) are shown in Figure 7. 21. It should be noted that the effective displacement was introduced by Camanho and Davila and defined as $\delta_m = \sqrt{\langle\delta_n\rangle^2 + \delta_s^2 + \delta_t^2}$ (Camanho and Davila 2002), δ_n, δ_s, and δ_t are displacement at the directions of mode-I, mode-II and mode-III respectively. Also, the softening behaviour can be defined by the *D* directly if possible, and this *D* value is a function of effective displacement.

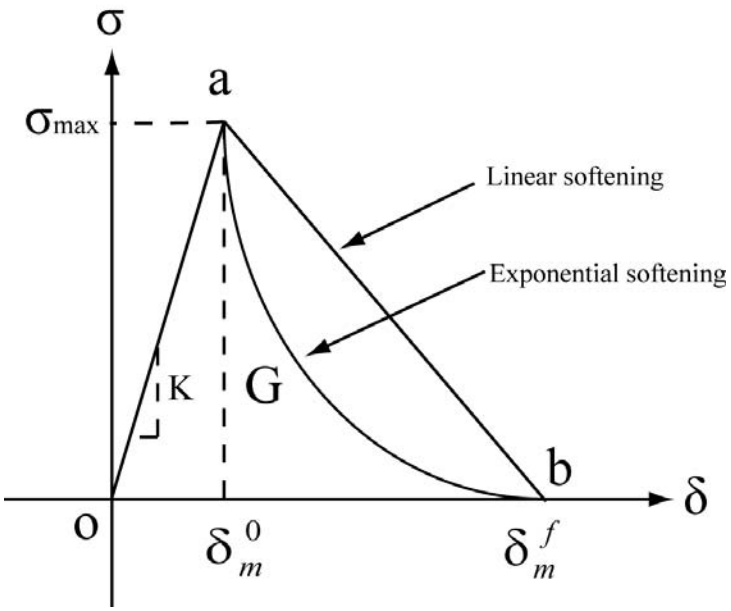

Figure 7. 21 Linear damage evolution and exponent damage evolution

Thus linear and exponent degradation can be considered for the same modelling; again, fixing all other parameters and materials properties, the effective of softening criterion is compared between model-3 and model-4 shown in Figure 7. 20. It is clear that both linear softening evolution (model-3) and exponent softening evolution (model-4) produce similar final displacement at failure point. However, model-4 has slightly higher failure load than model-3. It should be noted that the same fracture energy is used for both model-3 and model-4, and due to the difference of shape, exponent softening should have bigger value of δ_m^f than that of model-3 in order to maintain the same enclosed area which represents fracture energy. This delays the final failure of cohesive element and leads to higher failure load in global model.

Mode-independent failure is not general in practice; however this can reduce the complexity of modelling and may produce acceptable results. It should be noted that BK law is useful especially in the case of equal critical energies of first shear and second shear direction. Power law may be more general in use, so both laws have advantages in some applications. Model-3, model-5 and model-6 represent BK, power law and mixed-mode independent criterion, respectively. Figure 7. 20 shows that model-3 (BK criterion) and model-6 (power law criterion) have very similar curves which implies that both criteria are useful in this work, but model-5 (mixed-mode independent) has both lower failure load and failure displacement. It should be noted

that the curves of these three models are superposed which implies that the failure of cohesive elements is triggered mainly by the same stress component which should be peel stress.

Generally all models agree to each other in the beginning of curves shown in Figure 7. 20, and do not have very different failure loads. This is because cohesive element in these models has similar behaviour in the process of initial damage, and exhibits different behaviour after stress reaches to the maximum value. It is noted that the model-3 is chosen to present joint simulation in this work because this model can represent the realistic condition very well.

7.3 Two dimension DLJ model and submodel

In order to investigate the detailed stresses ahead of crack tip and values of fracture energy, 2D models and submodels have been developed. In practice, DLJ test is subjected to in-plane deformation, thus conventional plain strain elements were applied to DLJ model. Contour integral was used to present the fracture energy. Models with various adhesive thicknesses were simulated. In order to ensure accuracy of simulation, the artificial strain energy of whole model was monitored since artificial strain energy means the magnitude of hourglass force in the model. It is assumed that surface created by crack is traction free thus the frictional effect is ignored.

7.3.1 Geometry, boundary conditions, mesh and materials properties of 2D models

7.3.1.1 Geometry of 2D DLJ model

Like the 3D model, only half geometry was modelled, 2D DLJ geometry is shown in Figure 7. 22. It should be noted that adhesive thickness was chosen as 0.2, 0.3 and 0.5mm.

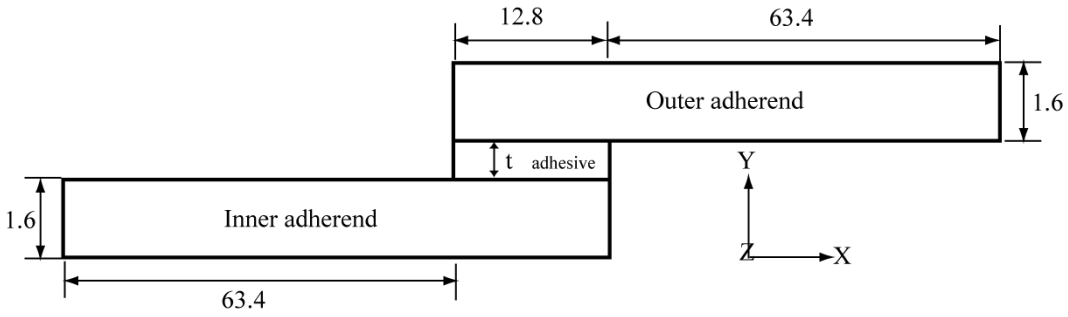

Figure 7. 22 Geometry of 2D DLJ (dimension unit: mm)

Observation of DLJ specimens showed that in most specimens the crack path is 0.01mm distance from the inner adherend. Thus 2D model with pre-crack in this model was simulated. In order to investigate the effect of crack position to FEA results, another 2D model was simulated with crack in middle of adhesive layer. Both 2D models are shown in Figure 7. 23. It is noted that the crack length of 2D model ranges from 0.05mm to 1.2mm because 3D DLJ models show that under maximum load the crack length is up to 1.16 mm in cohesive zone layer. This can be confirmed by value of SDEG (scalar stiffness degradation at integration points) under maximum load in 3D models.

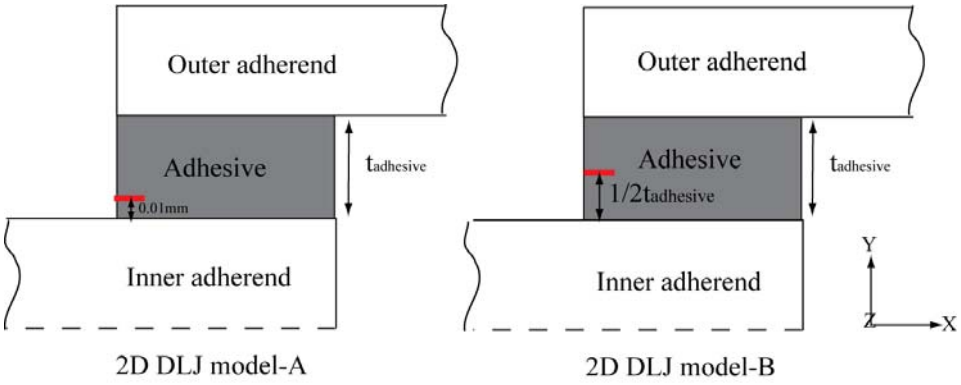

Figure 7. 23 2D DLJ model with different crack position

7.3.1.2 Mesh of 2D DLJ model

Plane strain elements (CPE4) were used for all 2D models. Plane strain is a state where its Z-direction (out-of-plane) strain normal to X-Y plane and two shear strain (γ_{xz} and γ_{yz}) are considered be zero. From the viewpoint of geometry, plane strain is suitable to represent the body because the stress in Z-direction cannot be ignored compared to stresses in other directions when load is applied on X-Y plane. For DLJ model, width

is not small enough to ignore, furthermore σ_z is expected to be significant because of constraints in Z-direction. In contrast, plane stress state is used to describe a thin body whose Z-dimension is very small. However plane stress model is able to overcome the convergence problem around crack tip much easier than plane strain modelling and much less computer time is used. The number of elements used in models is listed in Table 7. 9.

Table 7. 9 Element number in 2D DLJ

Adhesive thickness t(mm)	Element No. of adherend	Element No. of adhesive
0.2	97536	1270
0.3	97536	1778
0.5	97536	2794

7.3.1.3 Boundary conditions of 2D DLJ model

The boundary conditions (BC) applied to 2D DLJ model were identical to the conditions used for 3D DLJ models (see Figure 7. 5). Encastre BC was used at the end of outer adherend; Y-symmetry BC was used at the bottom of inner adherend, and displacement load was applied at the end of inner adherend. It should be noted that the magnitudes of displacement load were derived from results of 3D DLJ joints at their failure point. The loads are listed in Table 7. 10.

Table 7. 10 Displacement load used in 2D models

Adhesive thickness(mm)	0.2	0.3	0.5
Displacement load(mm)	0.273	0.274	0.276

7.3.1.4 Material properties of 2D DLJ model

Materials properties used in 2D models are identical with 3D DLJ models. Adherend properties are listed in Table 4. 1 and adhesive properties are listed in Table 7. 3.

7.3.2 Effects of contour path to fracture energy

Because of the existence of singularity at the crack tip, J-integral values depend on contour path especially very near the tip. Thus five contours were chosen to investigate the singularity effect upon J-integral. Each contour consists of a ring of elements which encircle the crack tip from one crack surface to opposite crack surface. First

contour surrounds the crack tip directly and other four contours surround previous contours recursively; each contour yields a J-integral. The FEA results show that first contour has the lowest value compared with other four contours because this contour connects to the crack tip directly, but there is no significant difference between other four contours as shown in Figure 7. 24.

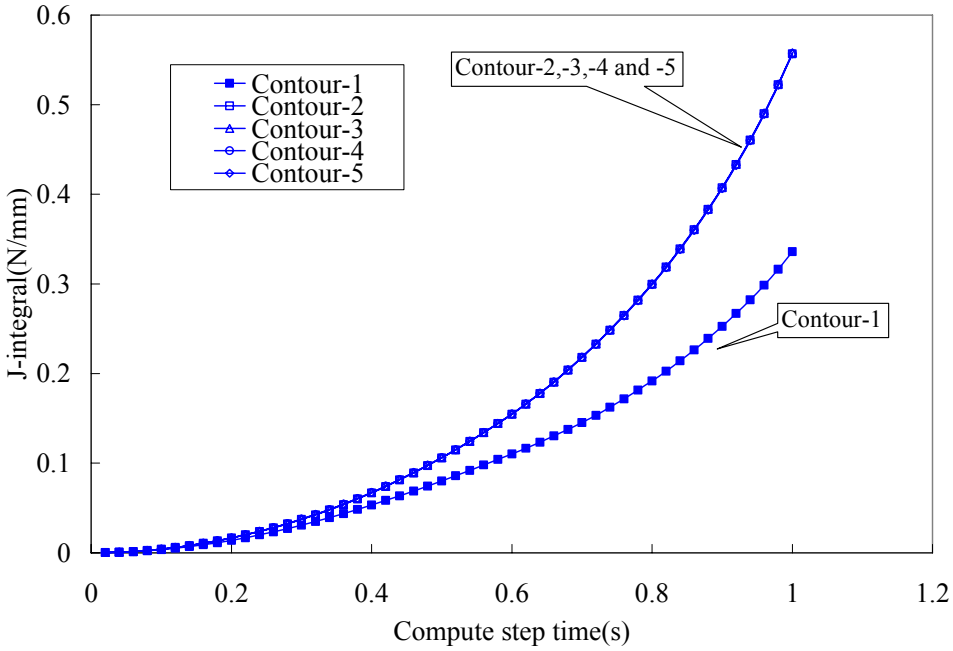

Figure 7. 24 Typical five contours surrounding the crack tip

It is obvious that the gap between the first contour and other four contours broaden when the simulation goes further along computer step time. In this work, the fifth contour of model was chosen for investigation in order to avoid the effect caused by singularity around crack tip.

7.3.3 Effects of pre-crack length on J-Integral (R-curve)

J-integral values affected by crack length are shown in Figure 7. 25. It should be noted that these J-integral values were obtained from 2D DLJ model-A (see Figure 7. 23, crack close to interface). It is obvious that DLJ using thicker adhesive has higher J-integral at the same crack length, J-integral increases when crack length increases which implies the typical R-curve. R-curve is formed because plastic zone is developed which led to energy dissipation when the crack length increases. However it is found that J-integral decreases with increasing crack length for small crack lengths. This may be because nonlinear materials and geometry were used in 2D model. Thus singular stress or strain exists around the sharp crack which causes oscillation and

unreasonable trend in the short crack range. In practice, sharp crack does not happen and some tiny rounding must exist; in addition, refined mesh used in this area maybe a benefit. Thus sub-model can be used for this situation in order to avoid singularity. The J-integral became stable after long enough crack because the plastic zone had fully developed. Furthermore, at the 1.2mm crack length, J-integral value with 0.5mm adhesive thickness is close to the G_{IC} experimental results (1.37N/mm). This implies that crack in Double Lap Joint with 0.5mm thickness adhesive would approach mode-I failure when crack length reaches a specific length. It is noted that J-integral values are not sensitive to the element size.

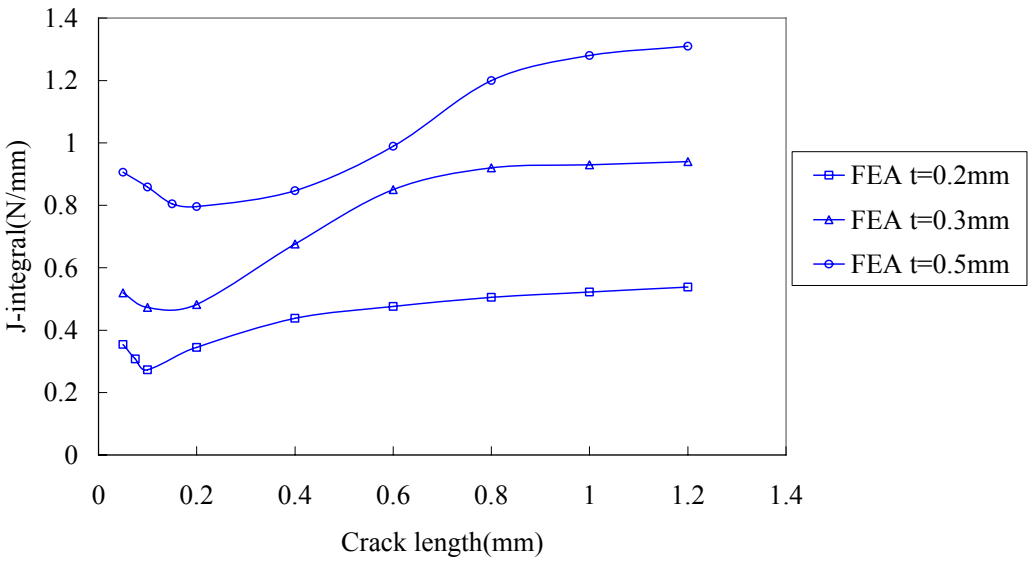

Figure 7. 25 J-integral values vary with crack length under maximum load

It is known that the J-integral represents mixed-mode fracture toughness in DLJ modelling. Because all three failure modes (mode-I, II, III) are dependent on many factors including the load rate and magnitude, constraints acting on the failure area, thermal factors and geometry nonlinear factors (Lim, Hatano et al. 1994; Cavalli and Thouless 2001), thus the J-integral values are not a unique material property. Compared with experimental results from fracture test (see Chapter 5), the J-integral value from 2D modelling is much lower than those from mixed-mode fracture toughness.

7.3.4 High solution around crack tip using submodels

In order to obtain more accurate results, the displacement of nodes in 2D global model was used as driving force in submodel. Global model always uses relatively coarse

mesh to save the computer time and obtain satisfactory global results. It was found that 2D DLJ models have very similar global displacement and load using different mesh density; however the solution near detailed geometry such as corner or crack tip cannot provide accurate details in global model because there is severe stress or strain singularity occurring there. Thus submodel technique is introduced to obtain more details of crack tip in this work. ABAQUS provides two kinds of submodel which are node-based and surface-based. Here the node-based submodel was chosen to analyse the stress condition around the crack tip, and this is based on the interpolation of the node displacement from global model onto the boundary of submodel. Driven variables are defined as the submodel boundary condition and constrained to match the results from the global model in the same increment.

Here 2D global models with different adhesive thickness but with the same crack length (0.1mm) were investigated using submodel. Only regions (see Figure 7. 26) around crack tip were extracted for submodel analysis. It should be noted that two submodels with different crack position were simulated; one used the crack path which is at the middle of adhesive and another used the crack path which is close to the interface (see Figure 7. 23). All models used the same crack length which is set to 0.1mm.

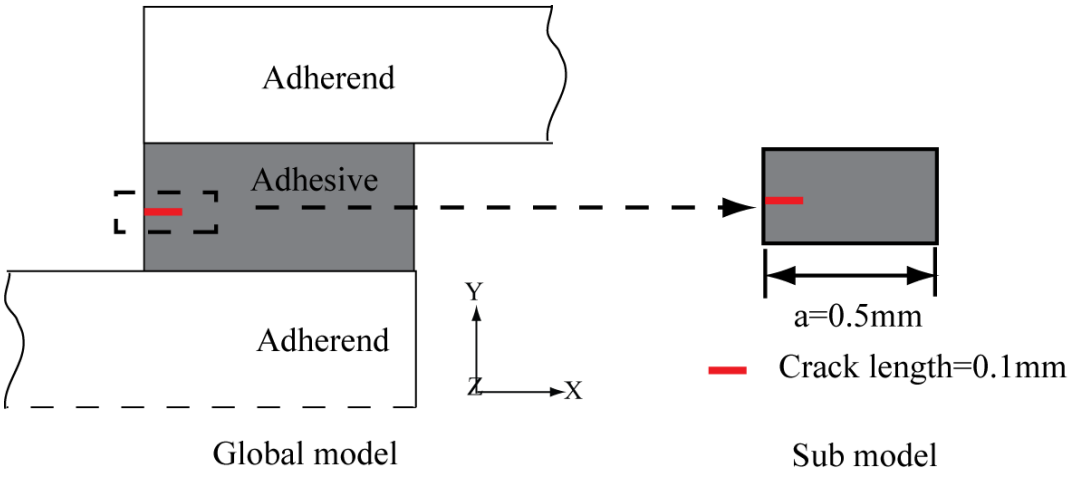

Figure 7. 26 Global model and submodel of 2D DLJ

The element size in global model is 0.05×0.05mm, and element size in submodel is 0.001×0.001mm which is 50 times smaller than global model element. Both models used the same plain strain element (CPE4) and sharp crack is embedded in submodels. The length of submodel is 0.5mm which means the analysis focus on a range of 0.4mm

ahead of crack tip. Submodels provide clear and non-singular results which are illustrated in Figure 7. 27. It is noted that curves of global model start from the crack tip and curves of submodel start from two elements away from crack tip. All models are applied with maximum load, 2D DLJ model-A represents the crack position in bottom and 2D DLJ model-B represents the crack position in the middle of adhesive (see Figure 7. 23)

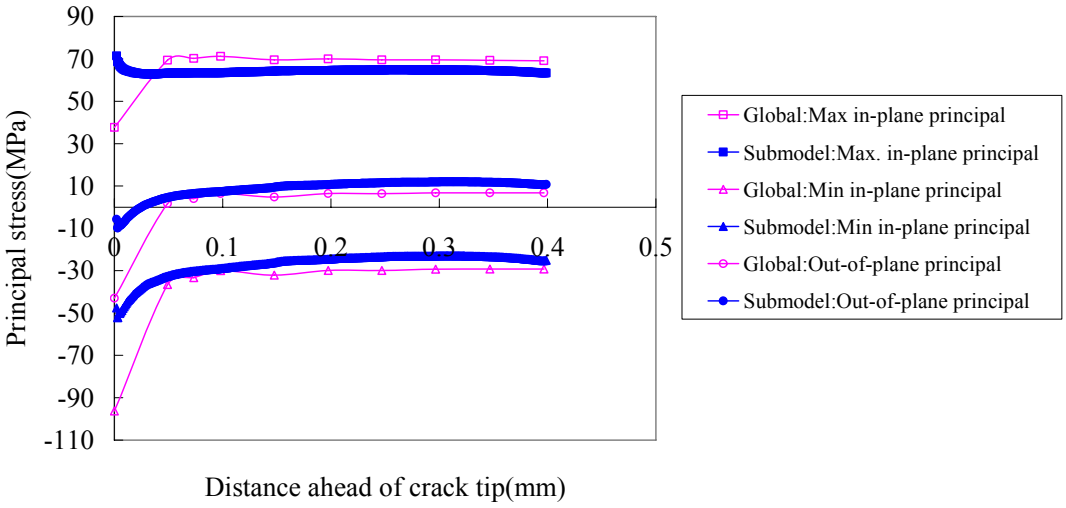

(a) 2D DLJ model-B and its submodel (t=0.2mm)

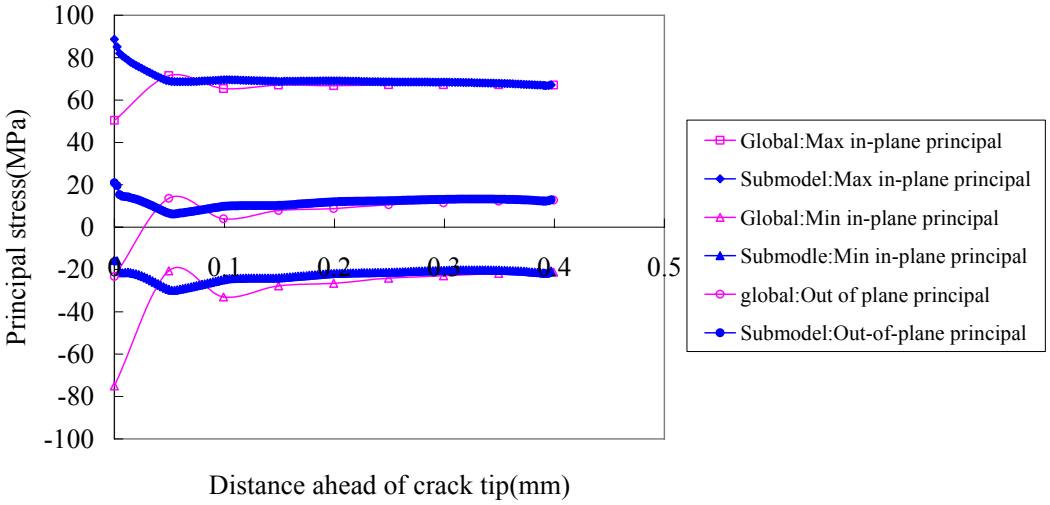

(b) 2D DLJ model-A and its submodel (t=0.2mm) (continued)

Figure continued

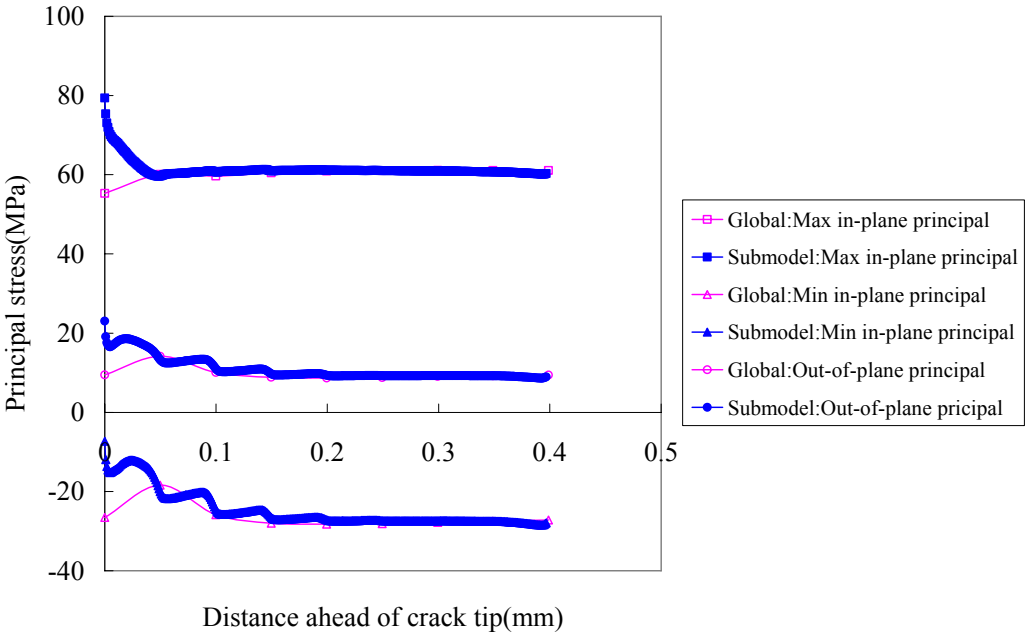

(c) 2D DLJ model-B and its submodel (t=0.5mm)

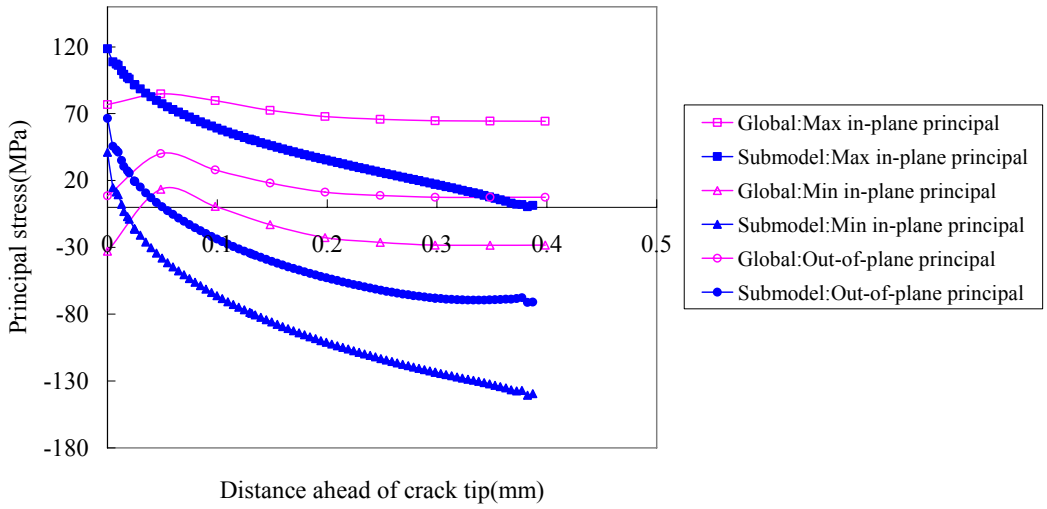

(d) 2D DLJ model-A and its submodel (t=0.5mm)

Figure 7. 27 Comparison of stress conditions ahead of crack tip from global model and submodel

It is obvious that there is serious stress singularity in the vicinity of crack tip of global model, especially at the crack tip itself. Thus the stress condition obtained from global model is not acceptable for further analysis; submodel avoids this shortcoming and supplies good solution. Furthermore, in the vicinity of interface, the stress field of adhesive is affected by hard adherend significantly because of the high constraint of steel which does not allow adhesive to deform freely. Obviously, the adhesive in this

area suffers higher pressure than in the middle area. Submodel also shows that stress distribution is similar for both adhesive failure in the interface and cohesive failure close to interface.

The element size also affects the solution ahead of crack tip which is demonstrated in Figure 7. 28. It is noted that all curves were obtained from submodels using 0.2mm adhesive thickness and 0.1mm crack locating in the middle of adhesive.

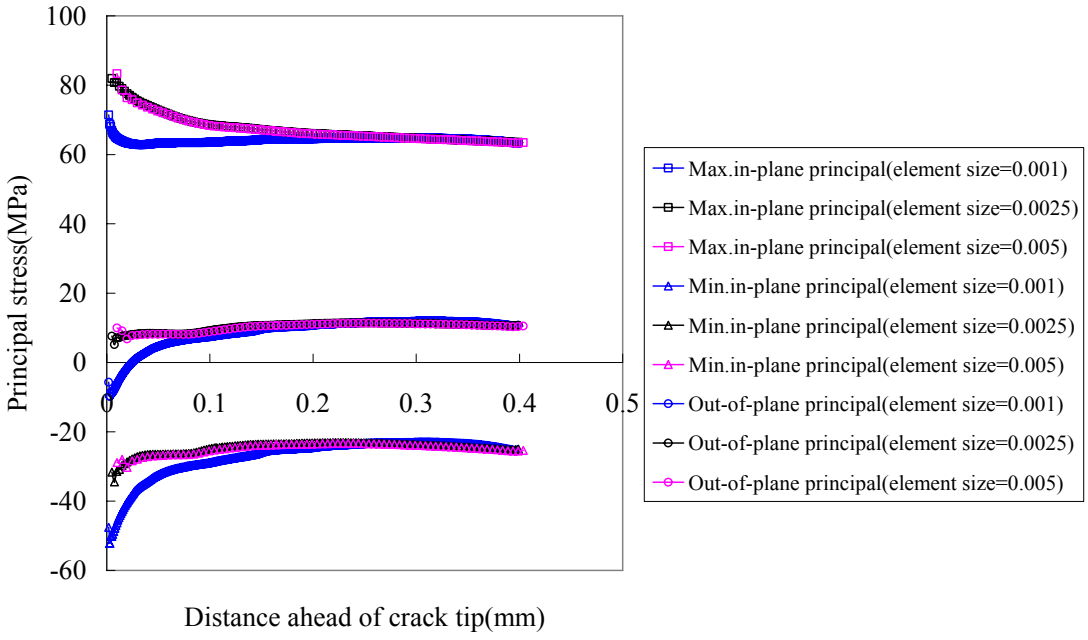

Figure 7. 28 Submodel affected by element size

It is noted that all curves agree with each other far away from crack tip, but in the vicinity of crack tip, the curves are distinct because different element sizes were used. It should be appreciated that smaller element in submodel is able to provide more accurate results than bigger elements. Furthermore, submodel using smaller elements can demonstrate the sharp-details of stress which is much closer to the crack tip. It is found that submodels are not sensitive to mesh when element length is smaller than 0.001mm.

All above submodels are based on the sharp crack tip; a submodel with blunt crack tip also was modelled to compare the strain condition around crack tip. The model with sharp crack tip is easy to mesh and achieve the final convergence, but strain condition around crack tip is not clear; when the model is analyzed by blunt crack tip, strain condition is more explicit, but more complicated mesh technique such as mixed mesh

controls and mixed element type must be applied for this geometry in order to complement J-integral technique; thus convergence problem always comes with this model. The difference of principal strain between submodels using blunt and sharp crack tip is shown in Figure 7. 29. It is noted that the circle radius in blunt crack submodel is 0.01mm which is obtained from global model. Both submodels were simulated with 0.1mm crack length and crack position at middle of adhesive.

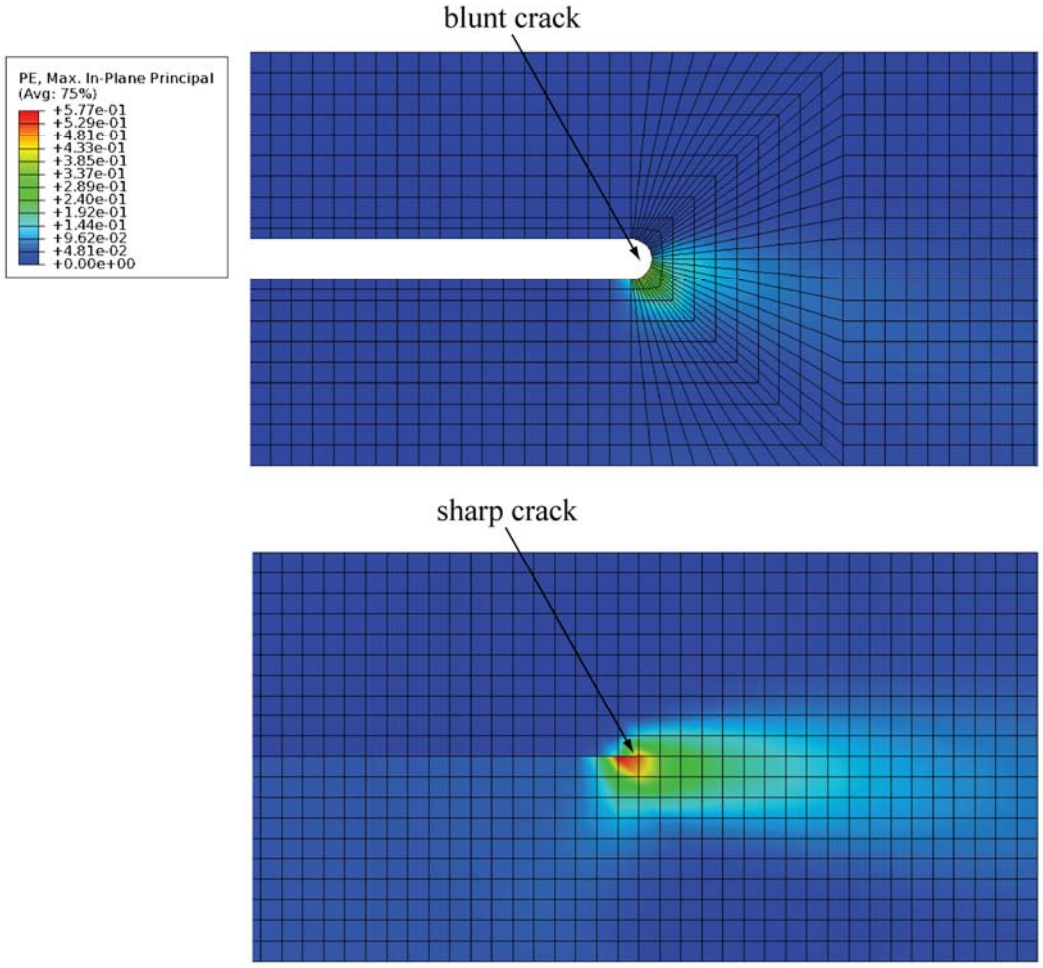

Figure 7. 29 Different crack shapes in submodels (Top: blunt crack tip; Bottom: sharp crack tip)

It is obvious that maximum strain principal locates at the bottom half-circle ahead of crack in blunt model which has value of 0.47. In the sharp crack tip model, the maximum principal strain has value of 0.58 which exists in the whole element and this element distorts significantly because of stress concentration. Generally this element is not used in analysis.

7.4 Conclusions

3D DLJ model:

It was found that DLJ-B model (crack close to interface) is the main FEA model for all DLJ simulation. 3D model using cohesive zone approach shows very good agreement with experimental failure and displacement, simulation yields better results than the traditional analytical solution methods and it is shown that it is an excellent predictive approach to model DLJ. Deeper details of failure propagation can be released though study of cohesive zone layer in modelling. Thus it is proved that determination of CZM parameters is correct and its application also can be used in other simulations.

Through studying geometry of DLJ model, it was found that the number of cohesive zone does not affect the FEA results significantly and slight change of cohesive zone position also has no effect to the results of modelling. This conclusion is significantly useful to predict adhesive joints or other structures since the failure path in practice is not clear and structures have very complicated geometry.

Maximum opening stress in CZM plays more important role than maximum shear stress. It was found predicted failure load is sensitive to low and high range of $\sigma_{n,0}$, higher $\tau_{s,0}$ does not affect FEA results significantly because it is controlled by BK criterion. It is found that material property affects FEA results mainly through adhesive behaviour. The Traction-Separation law also affects FEA results significantly through cohesive layer behaviour which is the core of CZM application.

2D DLJ model:

It was found that the total fracture energy in 2D model depends on the thickness of the adhesive layer, but compared with the experiments in this work, the fracture energy is less sensitive to the adhesive thickness. This is attributed to the fact that constraints in Double Lap Joint are much stronger than in the ENF specimen or Fixed Arm Peel specimen; thus there are more plastic zone developing in the bonded joint which gives rise to the total fracture energy(R-curve) and total fracture energy become stable because the plastic zone is completely developed. Furthermore, the extra fracture energy caused by plastic zone increase sharply when the size of plastic zone matches with the thickness of adhesive.

Submodel has significant advantage to present sharp-details of stress condition ahead of crack tip; this technique is able to demonstrate the distribution of principal stresses which global model fail to present. The accuracy of stress ahead of crack tip is affected by the element size; the model using blunt crack shape presents more explicit strain distribution than model using sharp crack shape. The results from submodels will be used further in micromodels.

It is found that element size around crack tip plays important role in finite element analysis. As the ratio of element size to the adhesive thickness decreases, the analysis convergence becomes more difficult. When this ratio is less than 0.05, complex singularity occurs and this leads to oscillatory behaviour of stresses and displacement around the crack tip.

Chapter-8 Finite element analysis of mixed-mode bending (MMB)

8.1 Introduction

In practice, material fracture is always controlled by mixed failure; so mixed-mode bending (MMB) is widely used to investigate the fracture initiation and propagation in many materials. The MMB test combines Double Cantilever Beam (DCB) and End Notched Flexure (ENF) which represent pure mode-I and mode-II, respectively. It is notable that significant details of fracture can be found from the MMB test since real fracture is seldom in pure mode. The full description of MMB experiments has been presented at Chapter 5. Presently, researchers have done much FEA works on the mode-I and mode-II but little on mixed mode failure. In this chapter, MMB modelling was performed to reproduce the experiments and the modelling results were compared with numerical calculations and experimental results. Modelling is able to demonstrate the distribution of energy release rate and undesired mode-III fracture. Furthermore, the plastic zone ahead of crack front was also obtained for plastically deformed adhesive. Two pure mode fracture parameters and the BK criterion parameters obtained from experiments have been applied in these simulations (see Chapter 7); quadratic stress criterion was used to describe the relationship between normal and shear stress. The failure paths of MMB models are defined on the base of experimental observation. The Virtual Crack Closure Technique (VCCT) method based on stress components was applied to calculate fracture energy release rates.

8.2 FEA analysis

8.2.1 Geometry of MMB modelling

The geometry of MMB modelling is demonstrated previously in Figure 5. 16(see Chapter 5). It should be noted that modelling whole MMB apparatus is not necessary. In order to simulate the real test conditions, all apparatus except for MMB specimen is modelled by rigid body since the components of MMB apparatus are much stiffer than MMB specimen. The load can be transferred to MMB precisely as long as all positions

of rigid body and connection and contact relationships between each part are correct. All sizes of parts were modelled according to measured dimensions in order to obtain the most accurate modelling results.

Only half MMB specimen was chosen to simulate the real mixed-mode test because of symmetry in the width direction. According to the MMB test (see Figure 5. 16), the span distance between left support (roller) to right support (hinge) is set to 140mm, the initial crack is set to 35mm, the distance between top roller to lever hinge is 70mm, the length of the lever c which presents the distance between yoke and top roller varies in order to create different mixed mode ratio. The radius of top roller and left roller is 5mm and the radius of both hinges at the right end is 2mm. The initial height difference between the bottom surface of yoke and the bottom surface of top roller is set to 12mm because this is corresponding to the real test condition and affects the load-displacement curve. The load was applied at the reference point of yoke and then transferred to the lever, as result, opening force was created at the right end of MMB and compressive force was created at the middle of MMB.

Two MMB specimens with different geometry were modelled which are shown in Figure 8. 1. One model consists of 0.2mm thickness adhesive layer and zero thickness cohesive elements, cohesive zone locates at the interface which is between adhesive and top MMB adherend. Another model only consists of zero thickness cohesive elements between two MMB adherends.

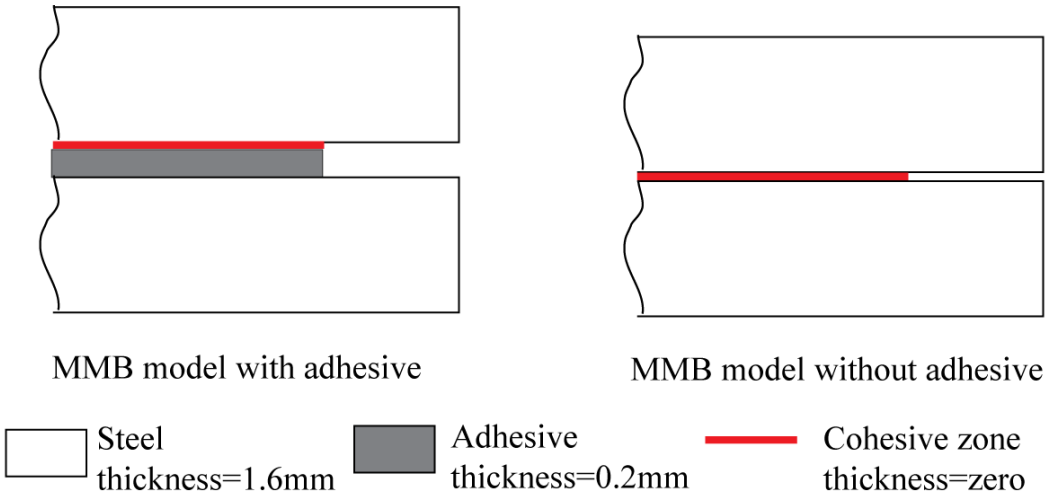

Figure 8. 1 MMB models with adhesive and without adhesive

8.2.2 Element formulation and mesh techniques

ABAQUS package provides a number of elements for 3D simulation and choosing suitable element for model becomes more important. It was found that the accuracy of modelling strongly depends on the type of element used. This arises since the modelling contains high degree of nonlinearity including material nonlinearity, geometrical nonlinearity and boundary nonlinearity in the structural simulation. Nonlinearity is caused by the structure's stiffness changes when it deforms either by change in material properties or change in geometrical shape. In the MMB modelling, there is much nonlinearity arising from material failure in interface, large deflection and rotation of steel pieces and contact problem between rollers and MMB specimen. Therefore the choice of element for MMB modelling should be carefully considered in order to avoid convergence difficulties and obtain accurate modelling results. Since this model consists of a huge number of elements, 3D linear element was chosen to model the steel of MMB instead of 3D quadratic element in order to reduce the total computational time. However, 3D linear element with full integration (C3D8), which has $2 \times 2 \times 2$ array of integration points in one element, experiences shear locking in bending problem, even more elements used through the thickness direction of specimen may not resolve this problem smoothly. This is because C3D8 element is too stiff in bending since the element edges are unable to curve. Another 3D linear element is reduced integration element (C3D8R) which has single integration point at the centre to element, but this element is too soft because it suffers from hourglassing numerical problem, this problem is caused by the zero strain energy in the integration point. Thus ABAQUS uses a small quantity of artificial “hourglass stiffness” to limit the hourglassing problem, but effective restriction of the hourglassing depends on huge number of elements used in model which increase the cost of simulation significantly. In this model, 3D linear incompatible element (C3D8I) was used for parts of MMB steel and adhesive; the application of C3D8I is based on the Wilson’s theory which makes use of an extra displacement and non-node component in interpolation function. The advantage of incompatible element subjected from bending is demonstrated in Figure 8. 2 (Wang 2003). It is obvious that element in Figure 8. 2 (a) shows correct deformation under bending, however element in Figure 8. 2 (b) shows incorrect deformation under bending.

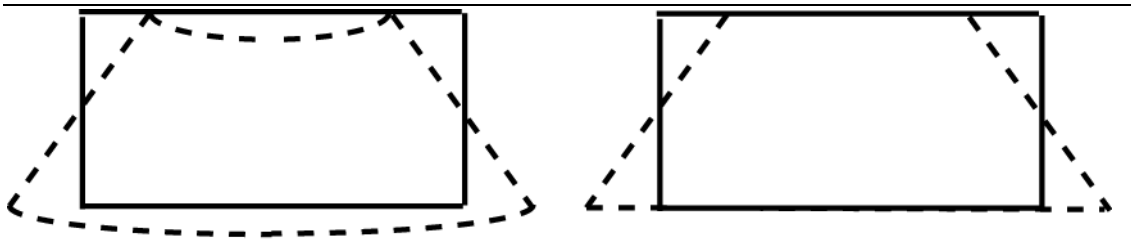

(a) element deforms correctly (b) element deforms incorrectly

Figure 8. 2 Brick element subjected from bending ((a): incompatible element ;(b): normal element))

The precise displacement of correct deformation using incompatible element is calculated by Eq.8- 1. It is noted that u and v are defined in natural coordinate system; x and y are defined in Cauchy coordinate system.

$$u = \alpha xy$$

$$v = \frac{1}{2}\alpha(a^2 - x^2) + \frac{1}{2}\gamma(b^2 - y^2) \quad \textbf{(8- 1)}$$

The bending condition modelled by normal four-node brick element is shown in Figure 8. 2 (b) and its displacement is calculated by Eq.8- 2.

$$u = \alpha xy$$

$$v = 0 \quad \textbf{(8- 2)}$$

It is clear that normal brick element is unable to model the bending condition because its interpolation function lacks a second order component. In order to model bending precisely, two extra interpolation components, $\alpha_1(1-\xi^2)$ and $\alpha_2(1-\eta^2)$, are added to the interpolation function and the equation form is shown in Eq.8- 3. It is noted that ξ and η are defined in natural coordinate system.

$$u = \sum_{i=1}^{4} N_i u_i + \alpha_1(1-\xi^2) + \alpha_2(1-\eta^2)$$

$$v = \sum_{i=1}^{4} N_i v_i + \alpha_3(1-\xi^2) + \alpha_4(1-\eta^2) \quad \textbf{(8- 3)}$$

Where $\alpha_1, \alpha_2, \alpha_3, \alpha_4$ are internal degree of freedoms, the interpolation function N_i satisfy the Eq.8- 4.

$$N_i = \frac{1}{4}(1+\xi_i\xi)(1+\eta_i\eta) \text{ (i=1,2,3,4)} \quad \textbf{(8- 4)}$$

It should be noted that the displacement of $\alpha_1(1-\xi^2)$ and $\alpha_2(1-\eta^2)$ are zero in all four node points which implies these extra components do not affect the node

displacement and only affect the internal displacement, besides, more precise results can be obtained by adjusting the value of parameters α_1, α_2, α_3 and α_4.

Therefore this C3D8I is able to overcome shear locking in bending problem by introducing additional degrees of freedom into element and enhance the deformation gradients. In this way C3D8I elements can produce modelling results which are comparable to quadratic elements but reduce computational cost significantly.

The element used for yoke, lever, hinge and supporter roller can be any type of 3D solid element since these parts are modelled by rigid body and are not involved in the calculation of integration point. The 3D cohesive element (COH3D8) is used for the failure interface. It should be noted that top MMB steel was created first and then imported into new model as orphan mesh part in order to create zero geometrical thickness layer of cohesive element. The benefit of zero thickness cohesive layer is to overcome the penetration problem between the surfaces of cohesive element under compressive load. The mesh edit method is used to create the rest of MMB specimen which includes cohesive layer and bottom MMB steel, and then the whole MMB was assembled. The meshed MMB part is shown in Figure 8. 3. In this FEA, there were two MMB model studied, thus total 33280 C3D8I elements were used for MMB adherend and 3520 COH3D8 elements were used for cohesive layer in MMB without adhesive layer; in the MMB model with 0.2mm adhesive layer, there were 7040 C3D8I elements used for adhesive layer and other parts used the same amount and type elements as MMB model without adhesive layer. In both MMB models, MMB adherend was meshed into 4 layers and cohesive was meshed into 1 layer. Adhesive was meshed into two layers in the MMB model with adhesive. The area ahead of initial crack tip and two contact areas were modelled by higher density elements where element size is 0.8× 0.4 × 0.2 mm. It should be noted that rigid body can be meshed with any elements since it is not involved in computable calculation. Thus the sweep mesh control and wedge elements were used for the rollers and hinges, all other parts use structural mesh control and normal brick element.

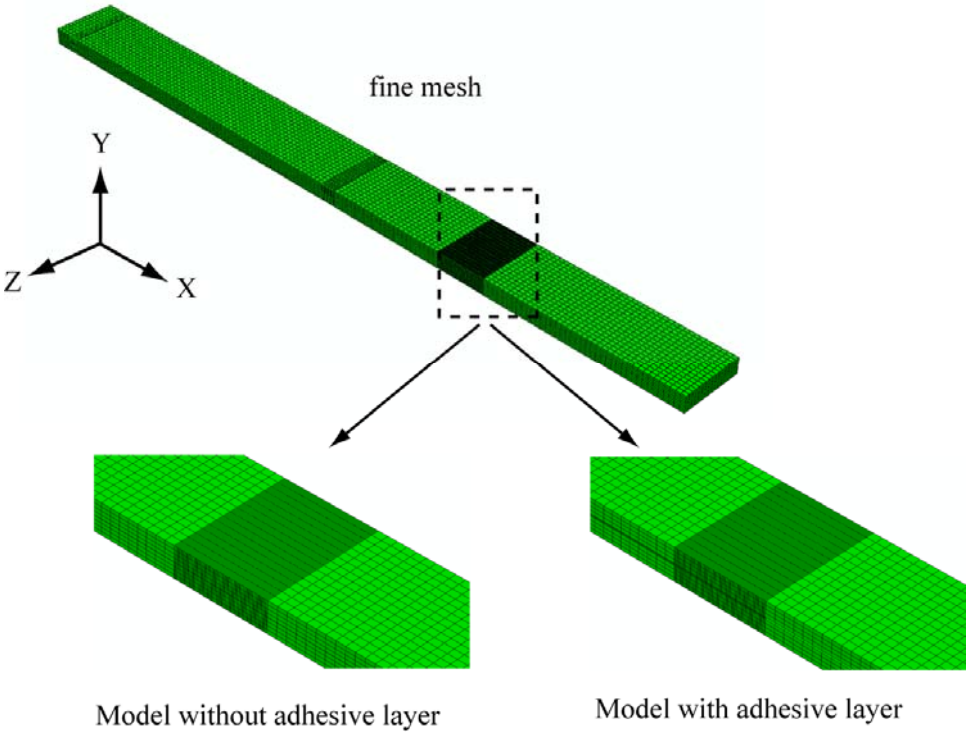

Figure 8. 3 Meshed MMB part in FEA

8.2.3 Boundary, constraint and load conditions

The boundary, constraint and load conditions are shown in Figure 8. 4. The whole model consists of MMB specimen, lever, yoke, top roller and two supports.

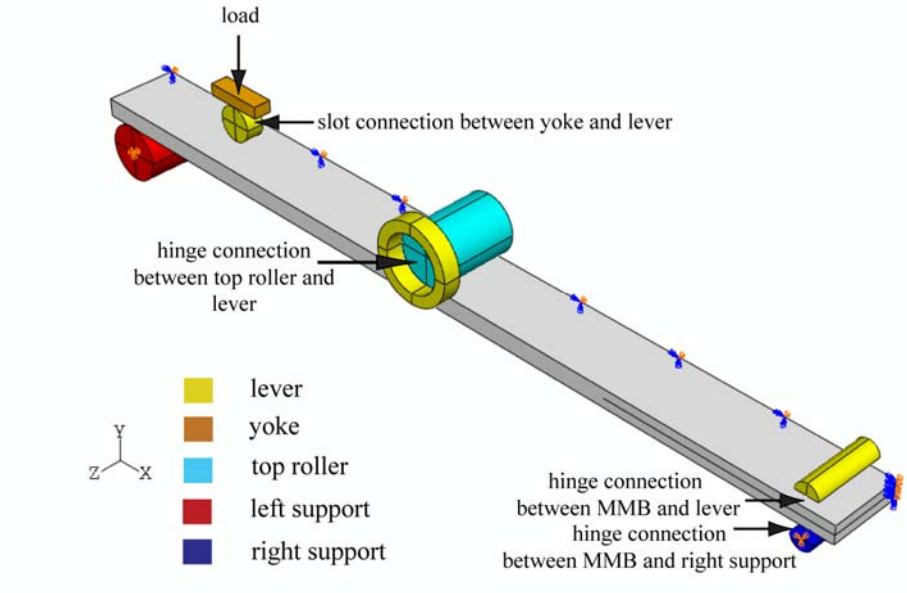

Figure 8. 4 Scheme of MMB simulation

Because only half MMB specimen was modelled and the width direction of MMB parallels with the Z-direction of global coordinate, thus symmetrical surface of MMB specimen was constrained in this direction. MMB specimen was modelled as deformable body and lever, top roller, yoke, and two supports were modelled as rigid bodies. The centre of left support is constrained with movements of all three directions such that the support was fixed but allowed to rotate only around z-direction of global coordination system. The right support was constrained at all six degrees. In this model, hinge connector and slot connector elements were used which are shown in Figure 8. 5.

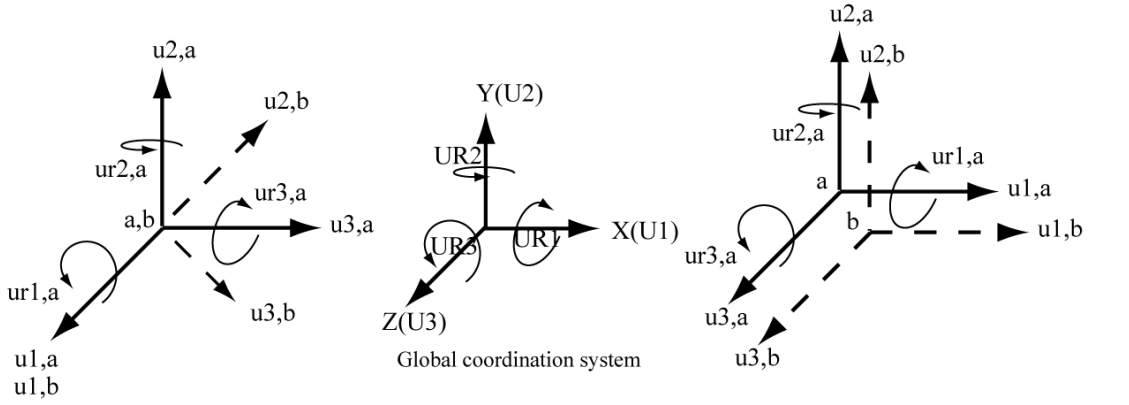

Local coordination system(hinge) Local coordination system(slot)

Figure 8. 5 Schematic of hinge connector and slot connect in local and global coordination system

The hinge connector does not allow any relative displacement and rotation between point a and point b in local coordination system except the rotation of point b to point a around the 1-direction, thus the relative freedom of ur1 is allowed. While the slot connector only allows point b to move along the 1-direction of point a and forbid other relative freedoms between point a and point b in local coordination system.

The MMB specimen was connected to right support and lever by hinge connector and allowed to rotate around the 1-direction of local coordination which is equal to the z-direction of global coordination. The top roller was contacted with top surface of MMB specimen and connected to lever by the same hinge connector which allowed rotate around the z-direction of global coordination too. The relation between yoke and lever was modelled by slot connector which allowed them move to locally in the 1-direction which is equal to the x-direction of global coordination.

Displacement load was applied at the yoke reference directly then translated to lever.

When yoke goes down, MMB specimen starts to open at the right end and top roller goes down to make MMB specimen bend. Thus mixed mode load is established. Furthermore, mixed mode ratio will change as the position of load point changes. Reaction force and vertical displacement can be extracted from yoke reference which can be compared with experimental data. It should be noted that each increment of displacement load is set to be small in order to obtain smooth propagation process; thus the initial displacement load is 0.01mm and the maximum displacement load does not exceed 0.03mm.

In order to simulate the real test conditions, contact conditions are created between top roller and top surface MMB specimen in the middle, left support and bottom surface of MMB specimen in the left (see Figure 8. 4). Those contact conditions allow limited sliding and no friction as observed from experiment and then defined by contact property in simulation.

It should be noted that contact conditions are much more complicated than other boundary conditions, thus more attention has to be paid to these conditions in order to obtain accurate modelling results because contact may not be established properly in the beginning even though their surfaces locate coincidently. This incorrect contact problem will cause rigid body motion or contact oscillation between open and closed, which is known as *chattering* (ABAQUS Analysis User's Manual 2009). Therefore, an initial displacement (0.01mm) is applied at the load point to avoid rigid body motion and chattering problems, and then the rest of displacement load continues at the load point. Since this model contains multiple bodies and each body has six degrees of freedom (three motions and three rotations), the boundaries and constraints have to satisfy the following relationship (ABAQUS Analysis User's Manual 2007c):

$$6 \times N_{nody} = N_{boundary} + N_{constraint} \quad \textbf{(8- 5)}$$

Where N_{nody} is the amount of bodies in model, $N_{boundar}$ and $N_{constraint}$ are the total amount of boundary conditions and total amount of constrained degree of freedom of connectors, respectively. The total boundary and connector conditions are demonstrated in Table 8. 1. It is noted that the U1,U2,U3,UR1,UR2,UR3 are the freedoms of body in global coordination system and u1,u2,u3,ur1,ur2,ur3 are the freedoms of connectors in local coordination system (see Figure 8. 5). It should be noted that the load condition is not involved in the above equation.

Table 8. 1 Boundary and load conditions

Part	Boundary condition
MMB	U3=0
yoke	U1=U3=UR1=UR2=UR3=0,U2=load
left support	U1=U2=U3=UR2=0
right support	U1=U2=U3=UR1=UR2=UR3=0
lever	/
top roller	/
Connector	Constrains condition
slot between yoke and lever	u2=u3=ur1=ur2=ur3=0
hinge between right support and specimen	u1=u2=u3=ur2=ur3=0
hinge between lever and specimen	u1=u2=u3=ur2=ur3=0
hinge between lever and top roller	u1=u2=u3=ur2=ur3=0

8.2.4 Mechanical properties in MMB model

In this model, MMB substrates were modelled by hardened steel whose Young's modulus is 199300MPa and Poisson's ratio is 0.3 for all MMB models, the tensile test of hardened steel was presented previously (see Chapter 4). The mechanical properties of cohesive zone are obtained and determined from experiments previously (see Chapter 5 and 7) and shown in Table 8. 2, these cohesive properties were used for all MMB models.

Table 8. 2 Mechanical properties of cohesive zone

Damage initiation	σ_I(MPa)	τ_{II}(MPa)	τ_{III}(MPa)	Criterion
	16	43	43	quadratic
Damage evolution	G_{IC}(KJ/m)	G_{IIC}(KJ/m)	G_{IIIC}(KJ/m)	BK
	1.37	3.85	3.85	1.70

In the MMB model with adhesive, exponent Drucker-Prager properties were used for adhesive and shown in Table 7. 3. The method to determine adhesive properties was demonstrated in Chapter 6. All other components in MMB modelling were modelled by rigid bodies.

8.3 FEA modelling analysis

8.3.1 MMB model without adhesive layer

MMB modelling with different mixed mode ratio (mixed ratio is defined by the ratio of mode-II energy release rate to total energy release rate. i.e. G_{II}/G) are compared with MMB test and numerical analysis. Three different mixed ratios of MMB model

are simulated which are 0.3, 0.6 and 0.8, respectively. The comparison between MMB test and simulation is shown in Figure 8. 6. It should be noted that all modelling in Figure 8. 6 do not include adhesive layer. It is clear that all MMB models agree with MMB test very well at different mixed ratio. After load force reach the maximum, curves of MMB test show rapid fall except for MMB test at mixed ratio of 0.3 (i.e. mode-I dominant failure), this agrees with test results that mode-II fracture propagation is unstable in most cases and mode-I tend to be more stable. Because a fined mesh is applied along the crack path, this model displays mesh independency at various mixed mode ratios.

However, MMB models demonstrate stable crack propagation in all mixed ratio cases. After fracture occurs, curves of MMB models descend quickly in the case of high mixed ratio and slowly at the low mixed ratio that agree with the experimental observation. The extension magnitude corresponding to the maximum load force increase with the increasing of mixed ratio because fracture is more difficult to start under mode-II domain than under mode-I domain.

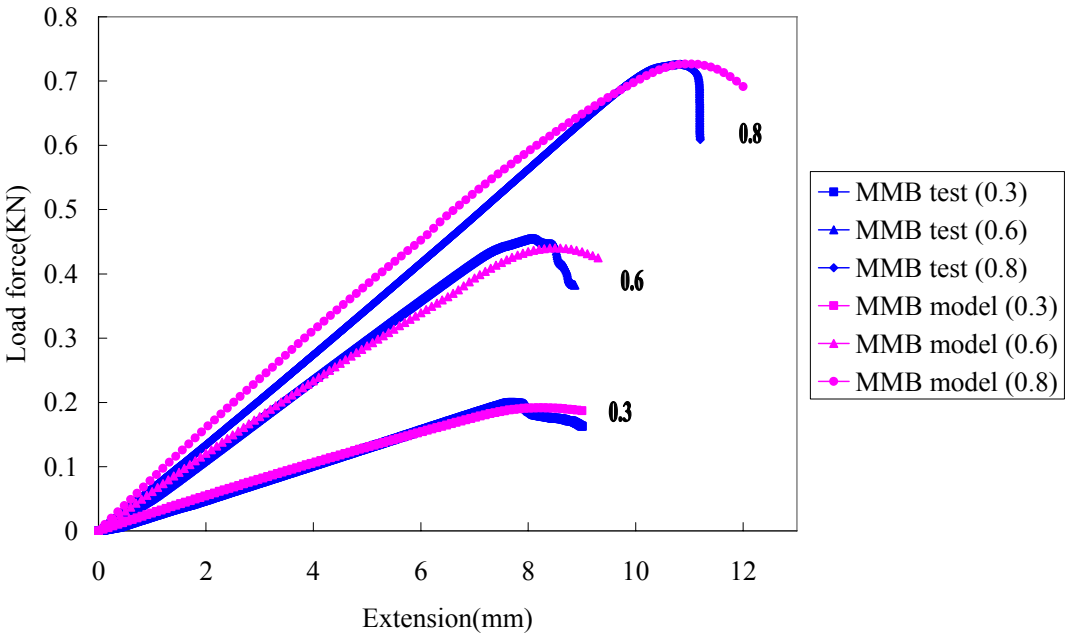

Figure 8. 6 Comparison between MMB tests and models without adhesive layer

Since the mode-I and mode-II components of force in the MMB specimen can be separated (see Figure 8. 7), these forces can be related to the total applied force. Thus mode-I and mode-II forces were extracted from MMB models to verify its accuracy. The reaction forces are obtained from the connector of MMB model at different mixed

ratio load, these forces then can be compared with forces from the simple beam theory. The numerical solution of MMB test is demonstrated in Figure 8. 7,

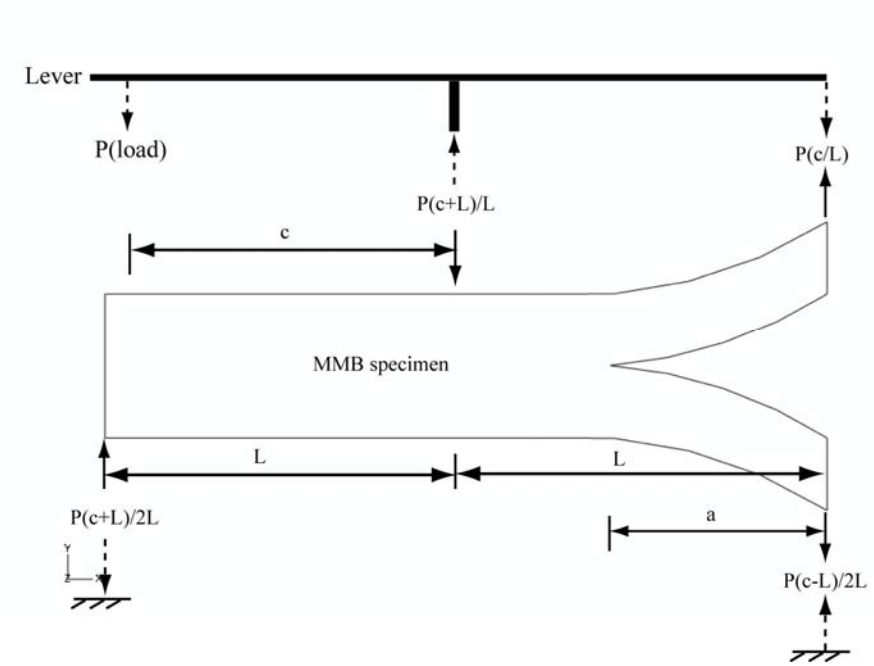

Figure 8. 7 Numerical solution of reaction force in MMB test

According to moment equilibrium of lever, the forces applied at the top middle and top right end of MMB specimen are *P(c+L)/L* and *P(c/L)*, respectively. It should be noted that the force of *P(c+L)/L* is also the force to cause pure mode-II load in MMB test. According to force and moment equilibrium of MMB specimen, the forces of left bottom and right bottom are *P(c+L)/2L* and *P(c-L)/2L*, respectively. Because the forces applied at the end of top and bottom of DCB test is identical, the force contributed to pure mode-I load in MMB test is *P(3c-L)/4L* which is the average force of right end in MMB test.

The MMB test then can be separated into pure mode-I load and mode-II load, respectively. Those components are expressed at Eq.8- 6 and 8- 7, respectively. Then energy release rate of mode-I load and mode-II can be calculated by simple beam theory.

$$P_I = \left(\frac{3c - L}{4L}\right)P \qquad \textbf{(8- 6)}$$

$$P_{II} = \left(\frac{c + L}{L}\right)P \qquad \textbf{(8- 7)}$$

The top-middle of MMB suffers from compressive force and the right-end of MMB

suffers from tensile force, numerical analysis demonstrates these forces are constant in the process of test, thus the ratios between these forces to load force do not change along the crack propagation. The force ratios obtained from MMB modelling are shown in Figure 8. 8. it is clear that result from model agree with numerical analysis very well, thus the force components of tension and compression from MMB are available to investigate the mode-I and mode-II fracture, respectively. All ratios remain constant even after the crack propagates which implies that the crack propagation does not affect the load history and distribution.

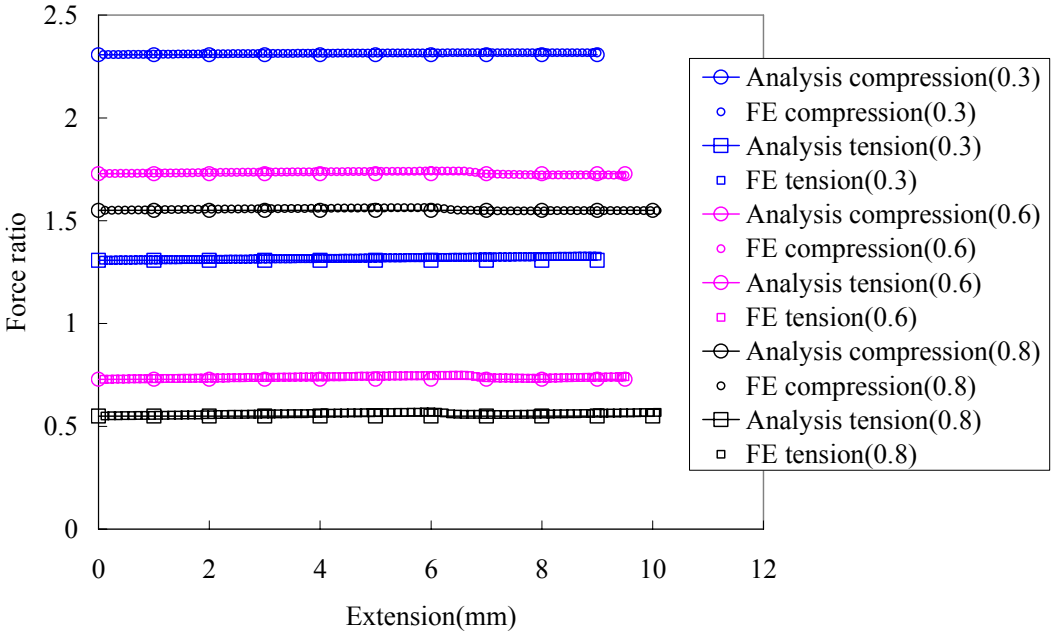

Figure 8. 8 Comparison of force ratio between FE model and numerical analysis

In the MMB test, mode-III component is caused by the contraction of steel and magnitude of mode-III decreases from the free edges to centre of MMB specimen according to MMB modelling. The mode-III varied with mixed-mode ratio can be calculated by Virtual Crack Closure Technology (VCCT) based on nodal stresses instead of nodal forces (Oliveira, de Moura et al. 2007). This VCCT can be applied at the first load step and can analyse complete crack propagation. The calculation form is shown in Figure 8. 9.

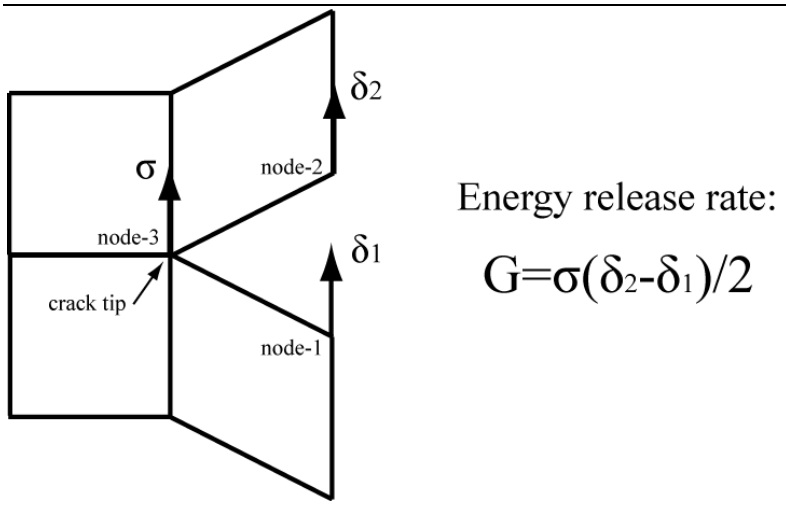

Figure 8. 9 Schematic of Virtual Crack Closure Technique (VCCT)

Where σ is nodal stress at crack tip, δ_1 and δ_2 are displacement of nodal pair which is closest to the crack tip. It should be noted that mode-III energy is calculated when σ is replaced by shear stress and δ_1 and δ_2 are replaced by shear displacement. Thus the mode-III energy release rates at free edge and central region of MMB are demonstrated in Figure 8. 10.

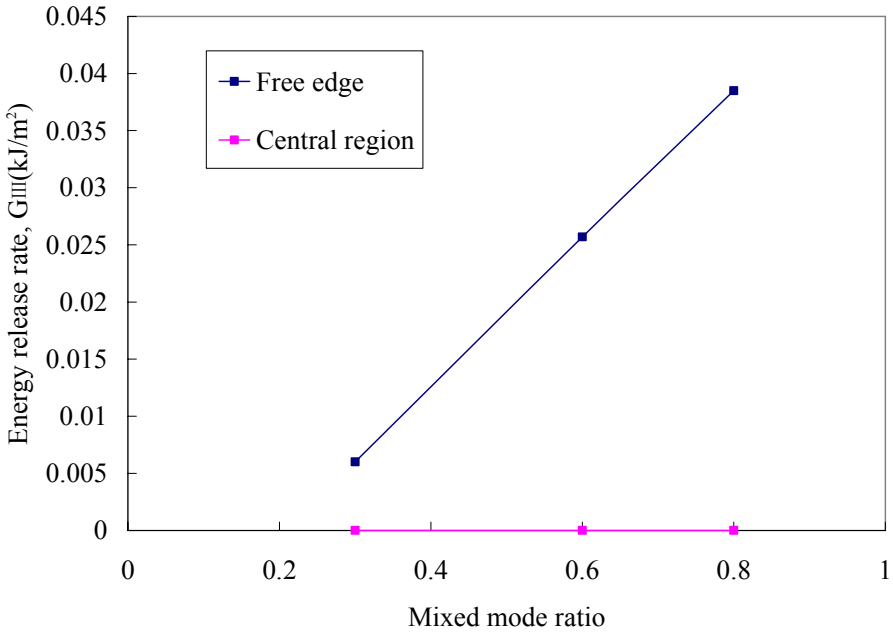

Figure 8. 10 Distribution of mode-III energy release rates along mixed mode ratio

It is clear that mode-III energy release rate is non-zero at free edge and zero at the central region; furthermore, mode-III component increases linearly with the mixed mode ratio. It is also found that the ratio of mode-III component to total energy release rate range from 0.4% to 1.2% which also increases with the increasing of mixed ratio. Thus the mode-III component is small enough to be ignored in mixed mode analysis.

8.3.2 MMB model with adhesive layer

Many workers assumed that adhesive layer only plays the role of providing tractions between adherends and neglect the adhesive layer itself (Yang and Thouless 2001; Oliveira, de Moura et al. 2007). Generally, adhesive layer between MMB steel undergoes plastic deformation when displacement load reaches a specific value, thus MMB model with adhesive layer is performed to study plastic dissipation situation during the test. The plastic strain distribution ahead of crack front at 0.6 mixed-mode ratio is shown in Figure 8. 11. The component PE22 (plastic strain in Y-direction) represents mode-I plastic deformation and PE12 (plastic strain in XY plane) represents mode-II plastic deformation, respectively. It is found that both PE22 and PE12 concentrate at the free edge; particularly PE12 has very high value at the region of free edge. Plastic strain distributes linearly along the width direction except for free edge which is caused by Poisson's ratio of MMB steel. PE12 has much higher magnitude and size than PE22 since plastic deformation is mostly caused by shear stress. Furthermore, it is found that PE23 representing mode-III component only exists at the free edge and has zero value in the central region. Compared with other two plastic strains, mode-III has negligible value and can be ignored. It is noted that other MMB models with adhesive have similar plastic strain distribution in adhesive layer.

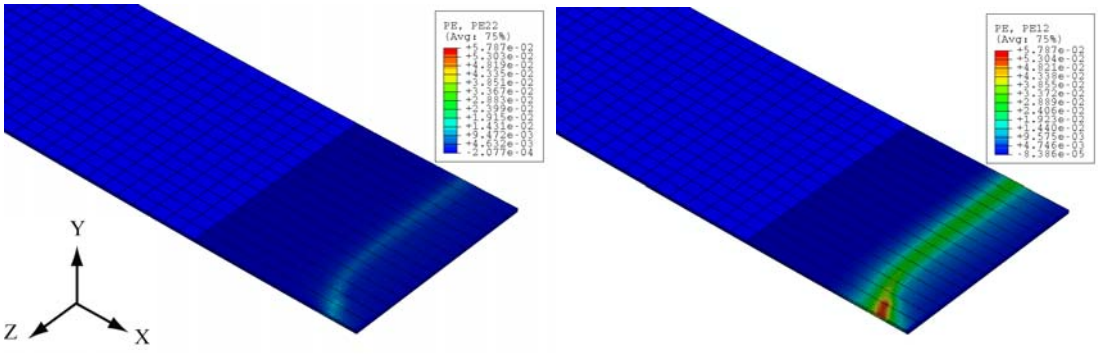

Figure 8. 11 Plastic strain distributions ahead of crack front in adhesive layer at 0.6 mixed-mode ratio

The plastic deformation also can be analysed by the plastic dissipation for different mixed-mode ratio; the plastic dissipation is shown in Figure 8. 12. When mixed ratio increases, more plastic dissipation occurs which also implies plastic dissipation is mostly caused by shear stress, i.e. mode-II fracture.

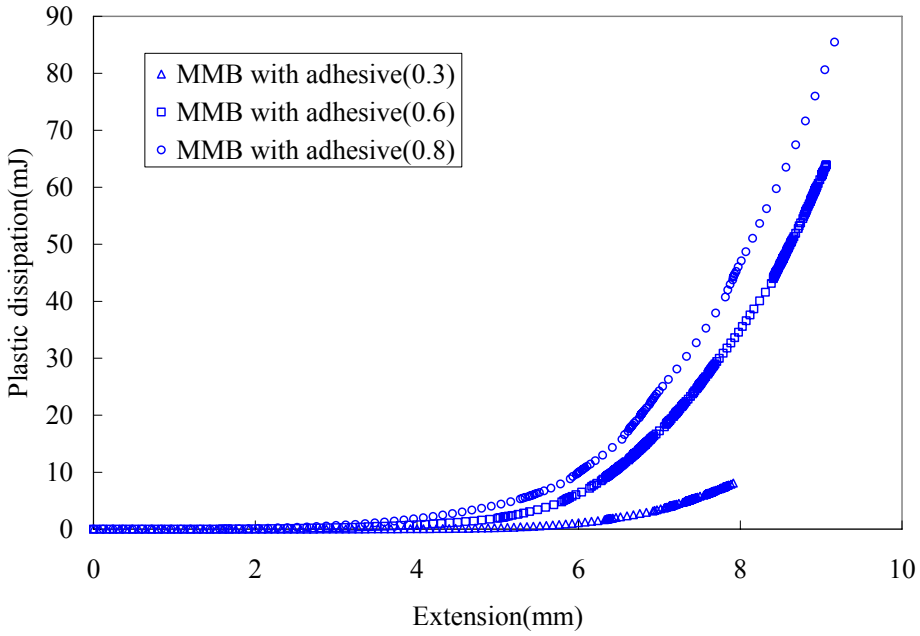

Figure 8. 12 Plastic dissipation of adhesive layer varies with displacement load

8.4 Conclusions

Cohesive element models of MMB were performed; all parameters of MMB models were determined from experiments, in particular, constitutive law of cohesive element determined by quadratic stress criterion and BK criterion showed that it is powerful to investigate the failure initiation and propagation in mixed mode failure. There is good agreement between modelling and experiment which implies that the method to determine mechanical properties of cohesive element and modelling creation of complicated multi-part are correct. Thus, this method can be extended into other modelling study such as DCB, ENF and other complicated failure model, etc. MMB models were also compared with numerical study and it is proved both analyses agree well. Furthermore, the VCCT analysis based on nodal stress was performed to study the value and distribution of un-wanted mode-III energy release rate and it is revealed that the mode-III component ahead of crack front is a small quality compared with total energy release rate and can be ignored. VCCT also shows that mode-I and mode-II components are uniformly distributed ahead of crack front but localize at the free edges.

Since cohesive zone approach always neglects the thickness of cohesive layer where

failure occurs and does not take into account the inclusion of deformed materials around cohesive layer, the presence of plastic zone and its energy dissipation are not disclosed by such models. Thus in this work, another MMB model which considered the adhesive layer was performed in order to overcome the disadvantage of general cohesive zone model. It is found that most plastic deformation ahead of crack front was caused by second shear stress and its maximum magnitude focuses on the free edge where plastic zone is free to develop. It is also found that plastic zone yields early when mode-II component dominates and the plastic dissipation increases quickly as the mode-II component increases. However, in the high mode-II range, the plastic dissipation is not distinct under different mixed mode ratio; this maybe implies that there is threshold of mixed mode ratio which controls the development of plastic zone. Thus, it can be concluded that plastic zone is easy to be developed at higher mode-II mixed ratio than lower ratio.

Chapter-9 Morphologic effects of microstructure models

9.1 Introduction

The 2D global models and associated sub models were investigated for several factors including thickness of adhesive, crack length and crack position: at the middle or close to the interface. The stress status ahead of the crack tip changed significantly by changing these factors. Thus microstructure would be subjected to different stresses from the different conditions and must present various responses according to morphology. These details have been studied around the crack tip and stress status derived from the area ahead of tip has been applied to microstructure. Mainly there are two factors affecting the cavitation of the rubber particles in the model: One is the geometry of the model and another is the load condition.

For modelling in FEA, three micro structural models including Rubber model, Onion model and Void model were studied. It is noted that the Onion model includes different core-shell thickness of rubber and epoxy. The load conditions in this chapter consist of two kinds: one is derived from the infinite centre crack panel; another is derived from the 2D joint modelling with crack in the middle of adhesive and crack close to the interface. Onion model which is a core-shell model has been paid more and more attention lately because core-shell particles have outstanding toughening effect (Day, Lovell et al. 2001; Mafi and Ebrahimi 2008). Thus, in this work, Onion model was investigated deeply compared with traditional Rubber model and Void model.

9.2 FEA analysis of micro models in the centre cracked panel

9.2.1 Geometry of the models

Geometrical dimensions of Rubber model, Onion model and Void model are shown in Figure 9. 1. The dimension ‘a’ represents the length of cube, ‘b’ means the radius of core part in Rubber model and Onion model, the dimension of ‘c-b’ represents the thickness of rubber shell in Onion model only, ‘c’ is the radius of void in Void model.

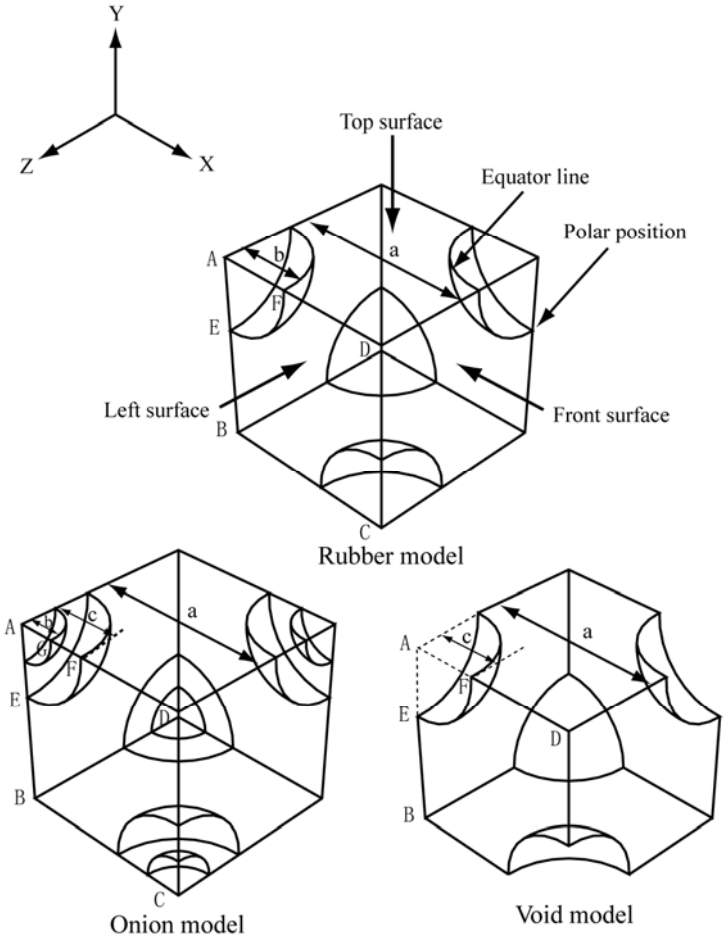

Figure 9. 1 Geometrical structure of Rubber model (top), Onion model (left bottom) and Void model (right bottom)

For all three models, the cell length of 'a' is fixed at the value of 10μm, so the ratio of $\frac{b}{a}$ (the ratio of rubber particle radius to cell length) and $\frac{c}{a}$ (the ratio of void radius to cell length) are equal to $\frac{4}{10}$ which result in 13.4% rubber volume fraction in Rubber model and 13.4% void volume fraction in Void model; the Onion models have fixed ratio of $\frac{c}{a}$ which is 0.4, however the ratio of $\frac{b}{c}$ is varying when changing the thickness of rubber shell. Four different Onion models are studied as the ratio of $\frac{b}{c}$ is $\frac{2}{4}$, $\frac{3.5}{4}$, $\frac{3.75}{4}$ and $\frac{3.85}{4}$, respectively. Thus, the thicknesses of rubber shell are 2μm, 0.5μm, 0.25μm and 0.15μm, respectively. As result, Rubber model contains 13.4% volume fraction of rubber particle and Void model contains 13.4% volume fraction of void. Onion models have totally different structure from both Rubber model and Void

model. It is noted that the total volume fraction of core and shell is constant at 13.4% which is same as Rubber model and Void model. The volume fraction of all models is listed in Table 9. 1

Table 9. 1 The volume fraction of epoxy core and rubber shell in Onion models

Name	Core radius b (μm)	Shell thickness c-b (μm)	Epoxy core (%)	Rubber shell (%)
Onion model-1	2.0	2.0	1.7	11.7
Onion model-2	3.5	0.5	9.0	4.4
Onion model-3	3.75	0.25	11.0	2.4
Onion model-4	3.85	0.15	11.9	1.5
Rubber model	4.0	/	13.4	/
Void model	4.0*	/	13.4	/

*It is noted that void radius is represented by ‘c’ instead of ‘b’ in Void model

9.2.2 Elements and material property

It is found that tetrahedron element and free mesh technology used in models cannot provide accurate FEA results when micro models are subjected to strong load conditions. Thus, in this work, hexahedral elements with sweep mesh technology are used for rubber shell and hexahedral elements with structural technology are used for epoxy part, then continuous contours can be obtained. Furthermore, the cavitation effect in Onion models is controlled by the thickness of rubber shell which implies that more cavitation occurs with the decrease of the thickness of rubber shell; however it results in more elements to be used and then needs more computer resource to complete the analysis. The typical element numbers used for these micro models are listed in Table 9. 2. C3D8 elements were used for epoxy matrix in all models and epoxy core in all Onion models; C3D8H hybrid elements were used for rubber particle in Rubber model and rubber shell in all Onion models.

Table 9. 2 Typical element numbers in micro models*

Model name	Rubber partial	Epoxy matrix	Epoxy core	Rubber shell
Rubber model	3336	16984	/	/
Void model	/	16984	/	/
Onion model-1	/	18198	3888	7776
Onion model-2	/	28464	8640	6912
Onion model-3	/	28646	8640	3456
Onion model-4	/	27648	12096	3456

*Element size in all models is approximately 0.3mm and modelling results display no mesh-dependency when element size is smaller than 0.35mm

The properties of rubber part and epoxy part are shown in Table 6. 1 and Table 6. 2, respectively.

9.2.3 Boundary conditions

In these models, back, right and bottom surface are constrained with symmetrical boundary conditions, and top, front and left surfaces are available to be loaded (see Figure 6. 6). However, these three surfaces are constrained by linear equations in order to maintain surfaces planar under load.

9.2.4 Load conditions

It is obvious that the stress state ahead of crack tip is always non-hydrostatic. A loaded infinite panel with through-thickness crack was investigated which is shown in Figure 9. 2. A 6000×6000mm size plane with 100mm crack in the centre was chosen to model this infinite plane so that there is no crack effect to the whole panel. Only quarter of this panel was modelled due to symmetry, thus 3000×3000mm size plane with 50mm crack was simulated.

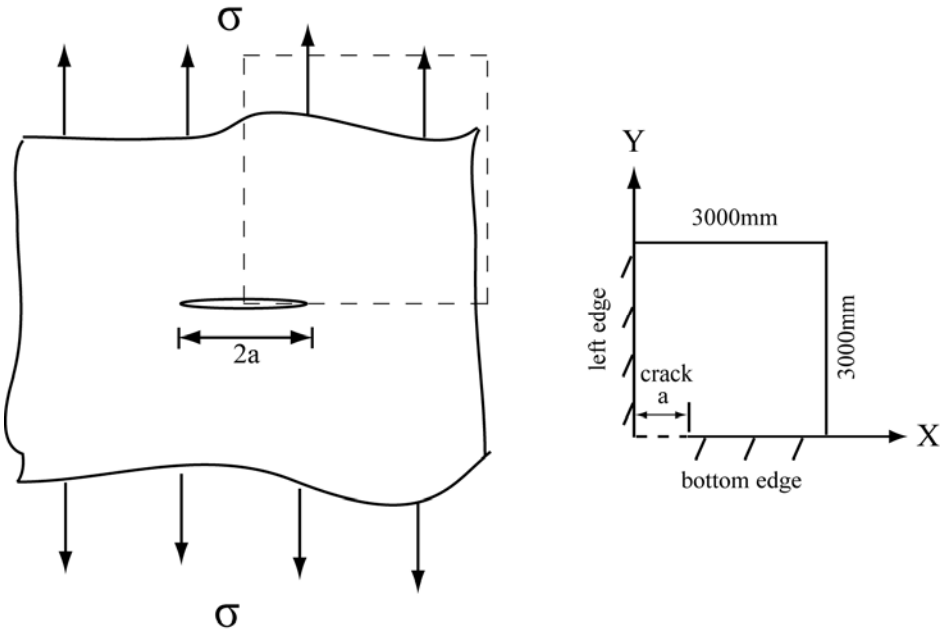

Figure 9. 2 A tiny crack in a loaded infinite panel and quarter panel for simulation

Symmetrical boundary conditions were imposed on the left and bottom edges, and a displacement of 20mm was loaded on the top edge which provides 16MPa stress representing the far field load (see Figure 9. 2). AV119 properties are chosen as the properties of this model. Generalized plane strain elements are used so that three

principal stresses are available from this model, thus all three principal stresses ahead of crack tip are 68.40MPa, 34.23MPa and 35.48MPa in the order of max, min and mid, and these stresses were applied to all micro models which are listed in Table 9. 3. It is noted that these stresses were selected two elements away from crack tip since the stress in the crack tip is not meaningful. Unless otherwise stated, all micro models are loaded with those three principal stresses.

Table 9. 3 Three principal stresses derived from global model and applied to micro models

Stress(derived from infinite plane)	Value and position(applied to micro model)
max in-plane principal	68.40MPa(top surface)
min in-plane principal	34.23MPa(front surface)
mid out-plane principal	35.48MPa(left surface)

9.2.5 FEA results

9.2.5.1 Morphologic effects

It is noted that the adhesive is considered as isotropic response. However in the level of micro structure, the micro models exhibit anisotropic character. The contours of pressure stress for all models are shown in Figure 9. 3. It is noted that all models adopt the same legend which ranges from -81.61MPa to -12.81MPa. The minimum pressure stress of -12.81MPa (negative symbol represents dilation) occurred at the epoxy matrix (interface) of Rubber model and the maximum pressure stress of -81.61MPa occurred in the rubber shell of Onion model-4 whose rubber shell thickness is 0.15μm. More details of models are shown in Table 9. 4. Unless otherwise stated, all modelling results are base on the perfect bonding assumption; it implies that rubber particle is bonded with epoxy matrix perfectly.

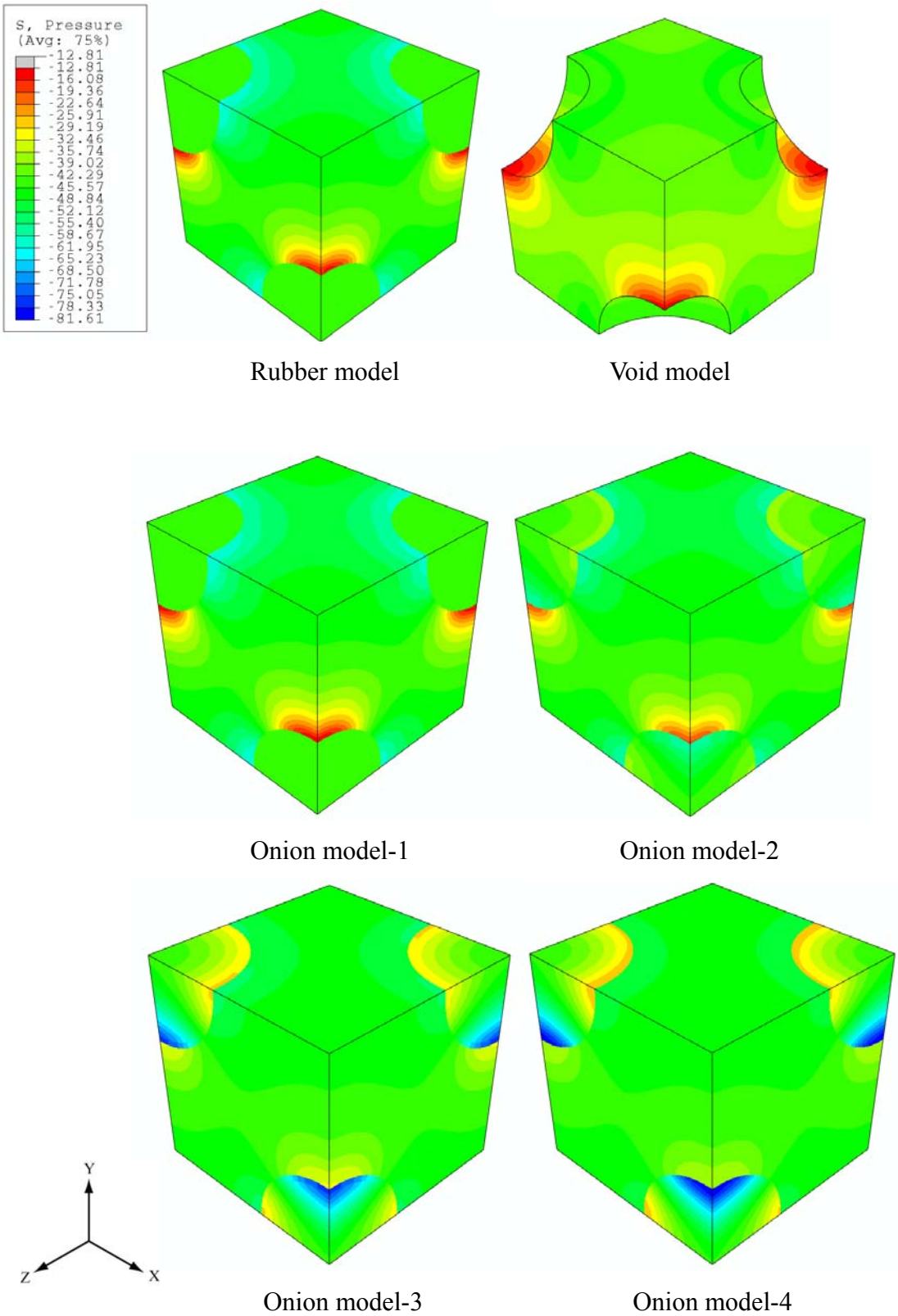

Figure 9. 3 Comparison of pressure contours between Rubber model, Void model and Onion model

The values of pressure and Von Mises stresses in different models are listed in Table 9. 4. It is noted that all models are loaded with the same load conditions.

Table 9. 4 Hydrostatic and Von Mises stresses in models

Component	Name	cube length a(μm)	Radius b(μm)	Thickness c-b(μm)	Max -P (MPa)	Min -P (MPa)
Pressure stress in rubber part	Rubber model	10	4	0	42.67	41.54
	Onion model-1	10	2	2	42.95	42.69
	Onion model-2	10	3.5	0.5	56.45	37.89
	Onion model-3	10	3.75	0.25	76.05	28.47
	Onion model-4	10	3.85	0.15	81.61	26.3
Von Mises stress in epoxy part	Name	cube length a(μm)	Radius b(μm)	Thickness c-b(μm)	Max σ (MPa)	Min σ (MPa)
	Rubber model	10	4	0	60.73	17.2
	Onion model-1	10	2	2	60.67	0.25
	Onion model-2	10	3.5	0.5	58.55	2.13
	Onion model-3	10	3.75	0.25	61.6	2.25
	Onion model-4	10	3.85	0.15	63.43	2.25
	Void model	10	/	/	73.20	2.47

It is obvious that maximum hydrostatic stress increases significantly with decreasing thickness of rubber shell. The thickness of rubber shell in Onion model-1 has value of 2μm, and this model has similar hydrostatic stress around 42MPa as pure Rubber model which implies that Onion model-1 does not lead to increase in hydrostatic stress as the rubber shell is thick when compared to other Onion models. The maximum hydrostatic stress occurs at the polar position whose axis is equal to the direction of maximum load stress, and the minimum hydrostatic stress locates at equator of rubber close to epoxy matrix. Maximum hydrostatic stress in rubber part increases as the shell thickness of rubber decrease, however the minimum hydrostatic stress exhibits the opposite tendency. This leads to more debonding between rubber and epoxy.

Rubber model has smaller maximum Von Mises stresses than Void model, but Rubber model has much higher minimum Von Mises stress than Void model. For all Onion models, maximum Von Mises stress always occurs in the epoxy matrix and minimum Von Mises stress occurs at the epoxy core, this means the interaction force mostly occurs at the interface between rubber shell and epoxy matrix instead of rubber shell and epoxy core. In addition, for Onion models, the value of maximum Von Mises stress tends to be the value of Rubber model and the value of minimum Von Mises stress tends to be the value of Void model when the thickness of rubber shell decreases.

More details can be unveiled by plotting the stress versus path in models. Figure 9. 4 illustrates that hydrostatic stress distributes along the path of AB (see Figure 9. 1), the position at value of 4 represents the interface between rubber core and epoxy matrix in Rubber model or rubber shell and epoxy matrix in Onion models.

It is very clear that Onion model-1 has very similar hydrostatic stress distribution as Rubber model. In Onion model-2, -3 and -4, the hydrostatic stresses increase along the point A to point of 4, and remain constant ahead of interface between rubber and matrix: the stress is constant in rubber shell. Thus, cavitation should be more notable if the shell thickness could be reduce to near zero, so the hydrostatic stress is expected to reach a very high value theoretically.

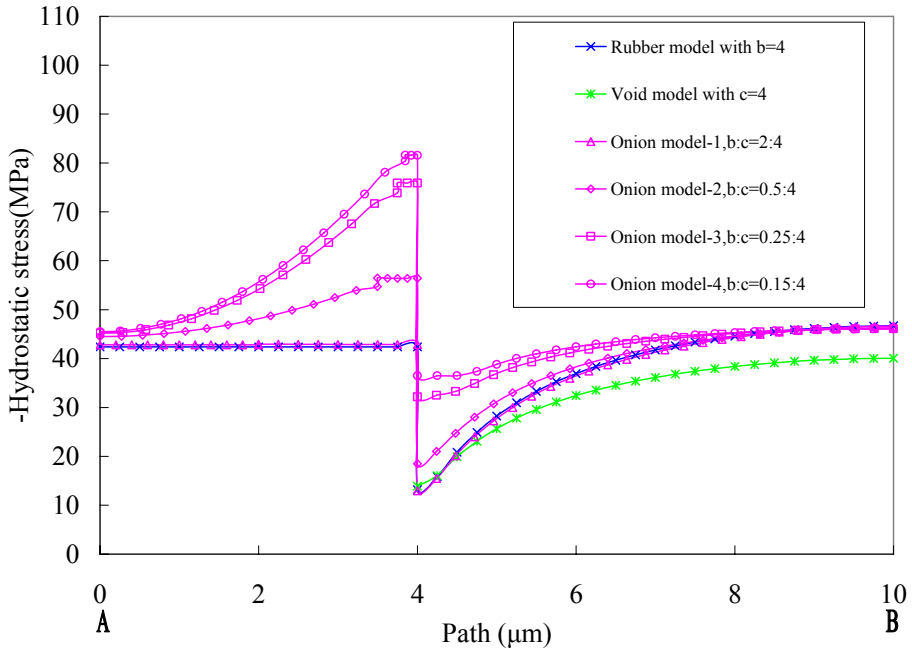

Figure 9. 4 Hydrostatic stress distributed along the path A-B (see Figure 9. 1)

It is known that the debonding of rubber particle is caused by high pressure difference in interface (Fond 2001); Rubber model can be considered as a special Onion model because its rubber shell thickness is considered as 4μm and larger than all other Onion models. The pressure differences of Rubber model and Onion models are shown in Figure 9. 5. It is noted that rubber debonding is much easier to be produced at polar position than equator because of higher pressure stress difference there. However this is based on the assumption that the interface force between rubber shell and epoxy matrix is not strong enough to hold two parts together, otherwise, debonding would occur at the equator position due to rubber's incompressibility.

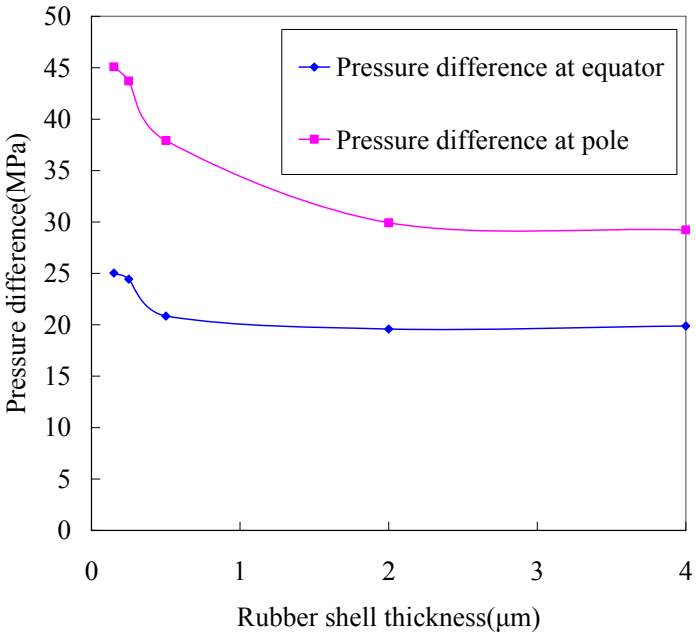

Figure 9. 5 Pressure difference at equator and polar position between interfaces of rubber shell and epoxy matrix

The maximum principal stress along path FE is shown in Figure 9. 6. Points F and E locate at the equator and pole, respectively. Void model shows it has the lowest maximum principal stress at equator and polar position in all models. For Onion models, the maximum principal stress at the equator decreases with the decreasing thickness of rubber shell, whereas the maximum principal stress at polar position increases when rubber shell thickness decreases. Rubber model has highest maximum principal stress at equator, furthermore it has the similar distribution of principal stress as Onion model-1; this demonstrates again that thick rubber shell does not change stress distribution. It is expected that the stress can be released after rubber cavitation in all Onion models and Rubber model, especially, Onion model with very thin rubber shell like Onion model-4 is able to release maximum principal stress from 71.44MPa to 20.91MPa at polar position after the rubber particle debonding. Thus this Onion model can dissipate more energy than any other models.

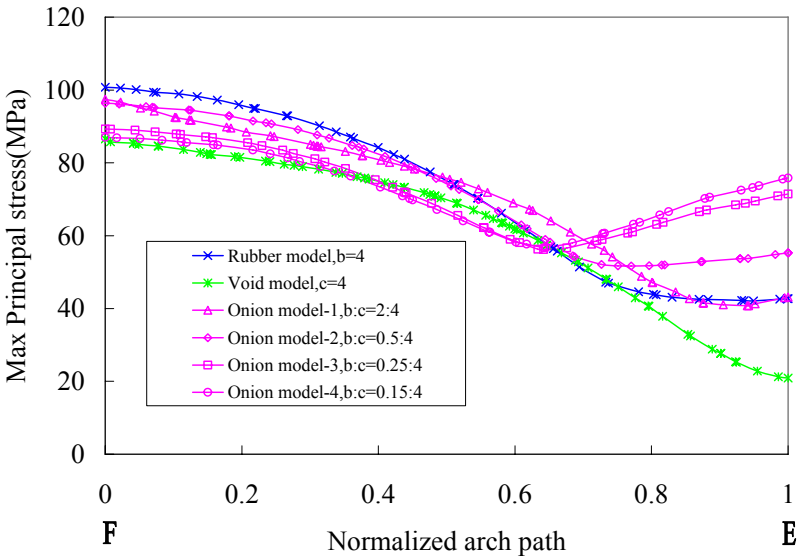

Figure 9. 6 Maximum principal stress distributed along the normalized arc path F-E (see Figure 9. 1)

It is known that rubber cavitation will induce shear yielding in matrix, and then the maximum stress in matrix will decrease. The maximum principal stresses changed by rubber shell thickness are shown in Figure 9. 7. It is found that both Rubber model and Onion model with 2 μm shell thickness have the same maximum principal stress in matrix whose value is equal to 100.90MPa, and have constant maximum principal stress of 43.00MPa in rubber part. While Onion models with thin shell show that maximum principal stress in matrix decreases with deceasing shell thickness but maximum principal stress in rubber part increases with decreasing shell thickness. Furthermore, in Onion models with thin shell, the maximum principal stresses in rubber part have wide distribution while Rubber model has constant distribution (see Table 9. 5). It is noted that maximum principal stress in matrix occurs at the equator and maximum principal stress in rubber part take place at the polar position in all models.

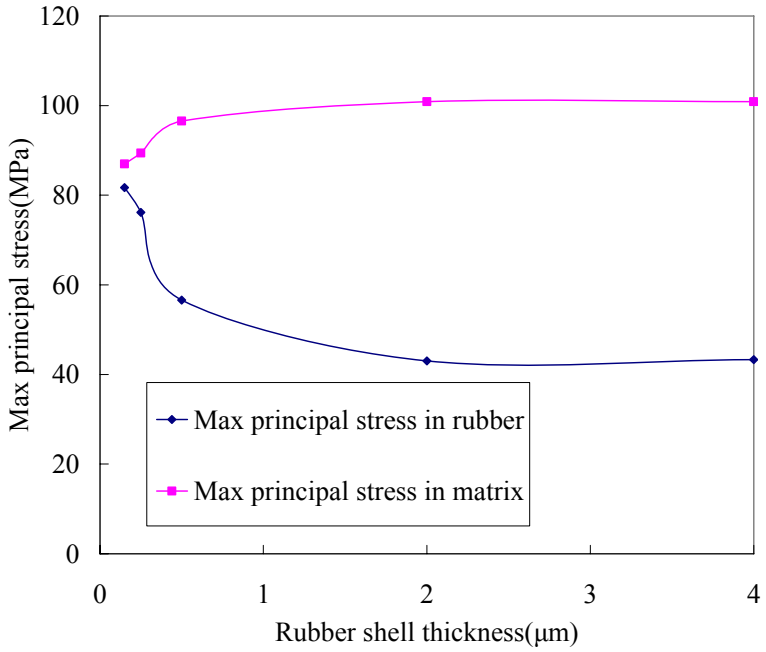

Figure 9. 7 Maximum principal stress in rubber and matrix vary with the thickness of rubber shell thickness

Table 9. 5 Max principal stress in matrix and rubber part

Component	Name	Shell thickness (μm)	Maximum (MPa)	Position	Variation (MPa)
Epoxy	Rubber model	4	100.94	equator	34.87-100.94
	Void model	/	86.59	equator	20.71-86.59
	Onion model-1	2	100.85	equator	38.07-100.85
	Onion model-2	0.5	96.57	equator	42.75-96.57
	Onion model-3	0.25	89.39	equator	37.20-89.39
	Onion model-4	0.15	87	equator	34.78-87.00
Rubber	Rubber model	4	43.3	pole	constant
	Void model	/	/	/	/
	Onion model-1	2	43	pole	constant
	Onion model-2	0.5	56.62	pole	37.91-56.62
	Onion model-3	0.25	76.17	pole	28.49-76.17
	Onion model-4	0.15	81.68	pole	26.30-81.68

According to the mechanism of toughening, shear yielding will occur in epoxy matrix, and the position of yielding is close to the interface between rubber and epoxy matrix or void and epoxy matrix. The location and magnitude of shear yielding are represented by PEEQ (Equivalent plastic strain at integration points) in ABAQUS. The contours in Figure 9. 8 illustrate the distribution of PEEQ in Rubber model, Void

model and Onion models. It is found that, for Rubber model, Void model and Onion model-1 and model-2, the maximum PEEQ value is at the equator of top surface because of maximum load applied there, but Onion model-3 and model-4 have the maximum PEEQ in polar position. Furthermore, it is noted that Void model has the highest PEEQ value of 0.00774 of all models.

In Onion model's series, maximum PEEQ of 0.00442 is found for Onion model-4. It should be noted that no shear yielding occurs at the polar position expect for Onion model-3 and model-4. The shear yielding happens and increases at the polar position when the shell thickness deceases in Onion model-3 and -4. Furthermore, the position of maximum PEEQ is changed from equator to polar position.

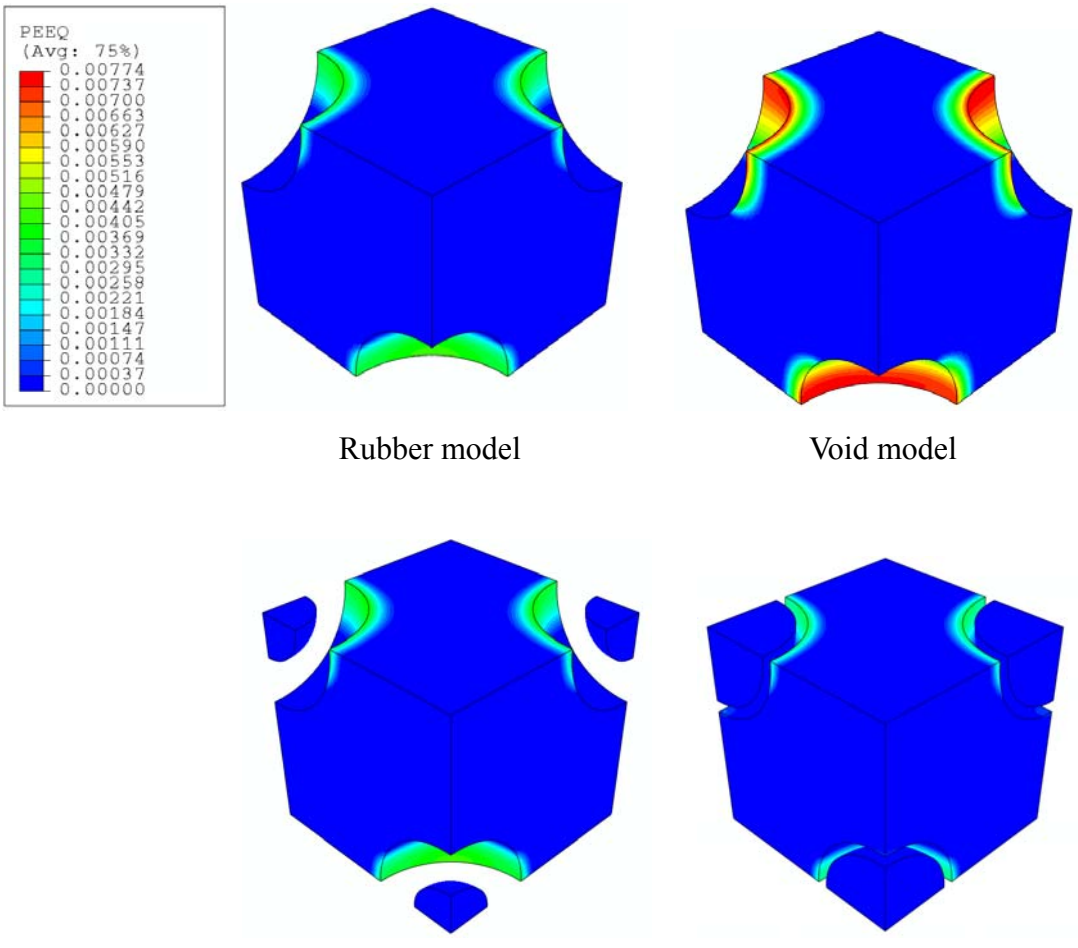

Figure continued

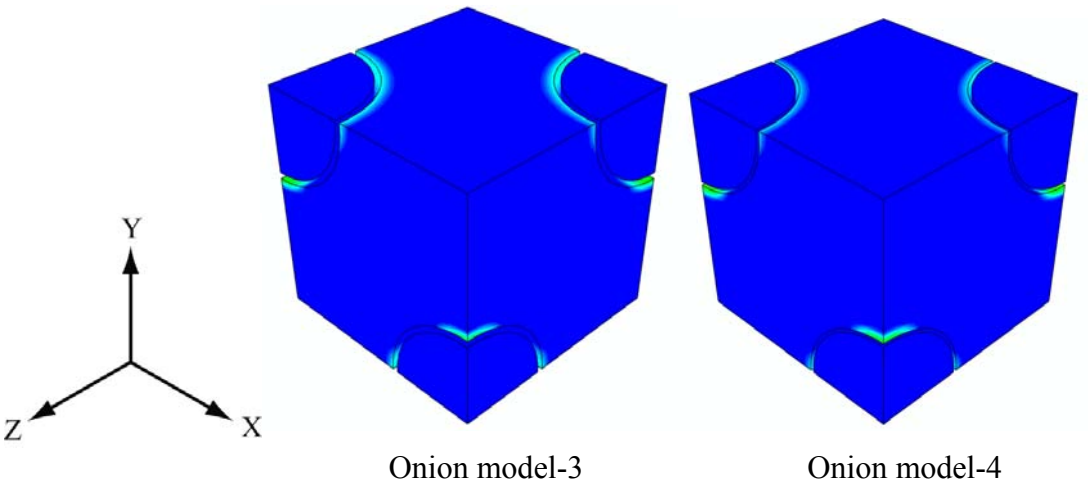

Figure 9. 8 Comparison of pressure contours in various models

The position and magnitude of maximum PEEQ in matrix which varies with the thickness of rubber shell is shown in Figure 9. 9. Again Rubber model can be treated as a special Onion model by considering the thickness of rubber shell as 4 μm. It is found that a critical shell thickness exists where Onion model has a lowest value of maximum PEEQ in matrix, then PEEQ increases with increased shell thickness and the value reaches to 0.00545 which means a special Onion model, i.e. Rubber model. Below the critical thickness point, it is expected that PEEQ will increase quickly by reducing the shell thickness. This is because the thin rubber shell is constrained by rigid epoxy core and epoxy matrix.

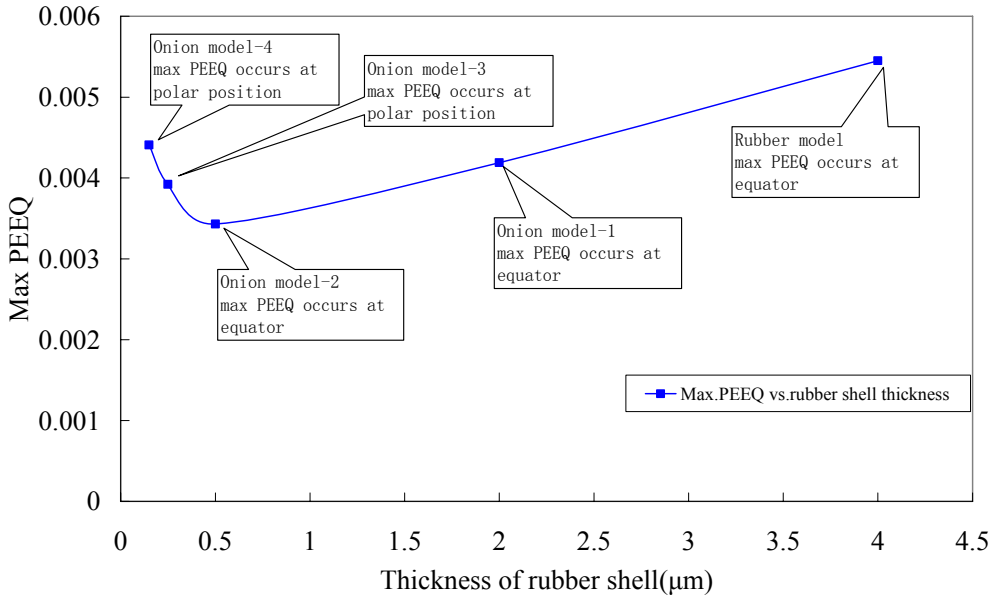

Figure 9. 9 Position of maximum PEEQ in Rubber and Onion models

The significant change of PEEQ in matrix also can be seen through the arc path of EF

(path is illustrated in Figure 9. 1) in Figure 9. 10. Point E represents the pole and point F locates at the equator. Onion model-3 shows the maximum PEEQ no longer occurs at equator. For Rubber model and Onion model-1, PEEQ value is equal to zero at the pole which means no shear yielding is produced, also it should be noted that maximum PEEQ does not take place at the point of F, but at the crossing point between equator and diagonal of core to core of top surface. It is clear that shear banding position in matrix varies with the thickness of rubber shell, and for Onion models with thin rubber shell there are two places including equator and polar areas which can produce shear yielding, while Rubber model and Onion model with thick rubber shell only have shear yielding at equator areas.

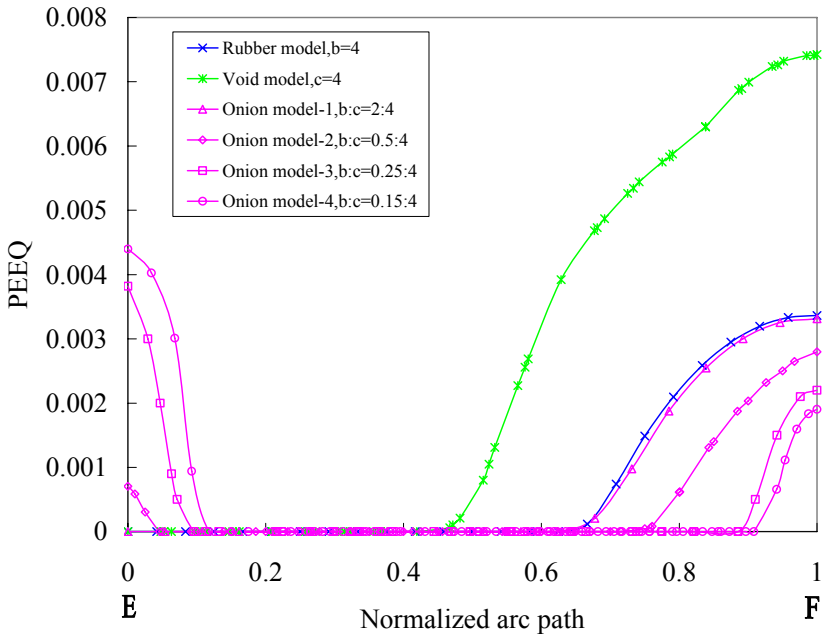

Figure 9. 10 Distribution of PEEQ along the arc path of E-F (see Figure 9. 1)

9.2.5.2 Load triaxiality effects

When load condition changes, both Rubber model and Onion model behaviour change significantly. Under the triaxial tensile stress status the parameter R_{tri} is defined as the factor of stress triaxiality (Chen and Mai 1998b), it is expressed as follows:

$$R_{tri} = \frac{\sigma_m}{\sigma_s} \qquad \textbf{(9- 1)}$$

Where σ_m is the average stress which is equal to $\frac{1}{3}(\sigma_1 + \sigma_2 + \sigma_3)$, σ_s is Von Mises

equivalent stress which is equal to $\sqrt{\frac{(\sigma_1-\sigma_2)^2+(\sigma_2-\sigma_3)^2+(\sigma_1-\sigma_3)^2}{2}}$. It is noted that σ_1, σ_2 and σ_3 represent three stresses which are applied at front, top and left surfaces of Rubber model, Void model and Onion models.

Stress status in micro models is affected by triaxial parameter R_{tri}, thus different load conditions are used to investigate the effects of load triaxiality to the models. In order to use various load triaxiality, the maximum load in Y-direction is fixed but two other loadings are reduced to 60% of original values. The model morphology and load conditions with associated R_{tri} value are listed in Table 9. 6.

Table 9. 6 Different triaxial load conditions for Rubber and Onion models

Name	Geometry	Load (MPa)	Direction	R_{tri}
Rubber model	a=10,b=4	68.41	Y	1.37
Void model	a=10,c=4	34.23	X	
Onion models	a=10,c=4,b-c=2,0.5,0.25,0.15	35.08	Z	
Rubber model*	a=10,b=4	68.41	Y	0.77
Void model*	a=10,c=4	20.54	X	
Onion models*	a=10,c=4,b-c=2,0.5,0.25,0.15	21.05	Z	

* means models are subjected to the same maximum tensile load in Y-direction but subjected to 60% loadings of original values at X-direction and Z-direction.

The curves of maximum PEEQ vs. shell thickness are shown in Figure 9. 11. It is noted that Rubber model is considered as a special Onion model. It is found that Onion models and Rubber model under low triaxial load state produce higher yielding strain in matrix. In addition, Onion models increase PEEQ values quicker with decreasing shell thickness under low triaxial load than high triaxial load.

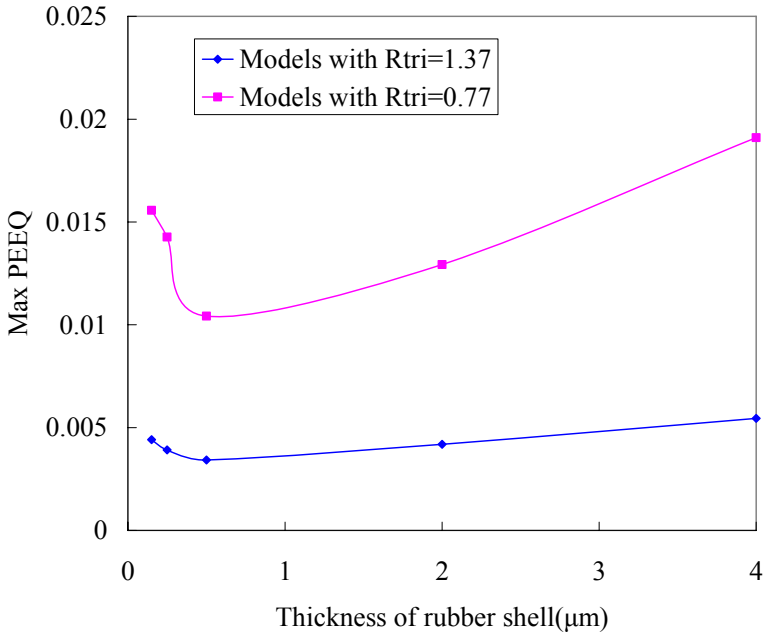

Figure 9. 11 Maximum PEEQ of Rubber and Onion models with different triaxial load conditions

It is also found that shear yielding occurs at the epoxy core in Onion model-3 and -4 as shown in Figure 9. 12, but no yielding strain was found in other Onion models and Rubber models. The magnitude and size of plastic zone in epoxy core increases with the decreasing of shell thickness. It is also found that the plastic zone extends from epoxy matrix to epoxy core when rubber shell diminishes, thus the epoxy core plays role under low triaxial load system.

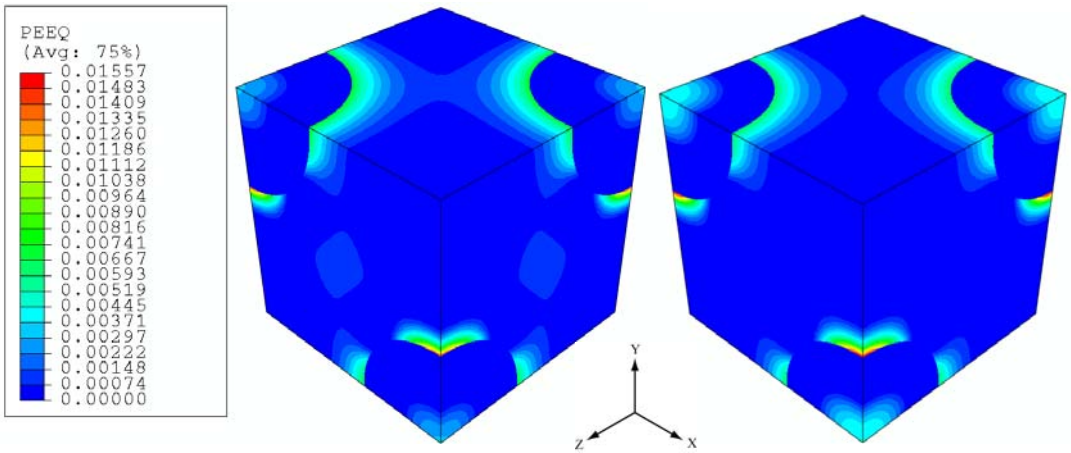

Figure 9. 12 Plastic deformation in Onion model under low triaxial load state (Left: Onion model-3; Right: Onion model-4)

Load conditions also affect the stress distributions of maximum principal stress, Mises

stress and hydrostatic stress in models. The stress status of matrix and rubber is listed in Table 9. 7.

Table 9. 7 Stress status in matrix and rubber particle affected by triaxiality R_{tri}

Component	Rubber model	Rubber model*	Onion model	Onion model*
Rtri	1.37	0.77	1.37	0.77
Shell thickness	0	0	0.25	0.25
Max principal in matrix(MPa)	100.9	108.1	89.39	92.79
Max Mises in matrix(MPa)	67.24	86.47	61.60	81.59
Max Pressure in rubber(MPa)	42.67	35.15	76.04	80.91
Max PEEQ in matrix	0.0055	0.019	0.0039	0.014

*model subjected to low triaxial load.

It is found from that, for Rubber model and Onion models, maximum principal stress, maximum Von Mises stress and maximum PEEQ value in matrix increase with decreased load triaxiality. However, Rubber model has different trend of hydrostatic tension stress's change in rubber part from Onion model. When lateral tensile load decrease (R_{tri} decrease), Rubber model shows hydrostatic tensile stress in rubber part decrease as well which means higher triaxial load condition is helpful for rubber cavitation, but higher triaxial load condition postpones the plastic deformation in matrix in both Rubber model and Onion models. These predictive results agree with previous research from other workers (Guild and Kinloch 1995; Chen and Mai 1998b). However Onion model has reverse trend in that hydrostatic tensile stress in rubber part increases with the decreasing of triaxiality. Thus, at a lower triaxial load state, Rubber model shows that matrix plastic deformation or shear banding may be the major toughening mechanism. Figure 9. 13 demonstrates that lower triaxial load promotes much more plastic deformation in matrix and produces higher max equivalent plastic strain.

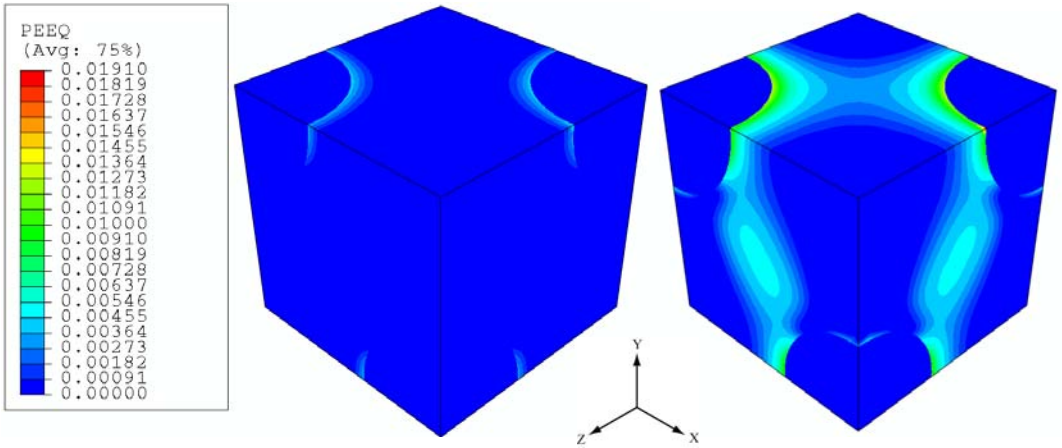

Figure 9. 13 Plastic deformation in Rubber model (Left: higher triaxial load. Right: lower triaxial load)

Secondly, at lower triaxial load state, Onion model has more plastic deformation in matrix as shown in Figure 9. 14. It is obvious that there is plastic deformation occurring at epoxy core which is helpful for toughening purpose.

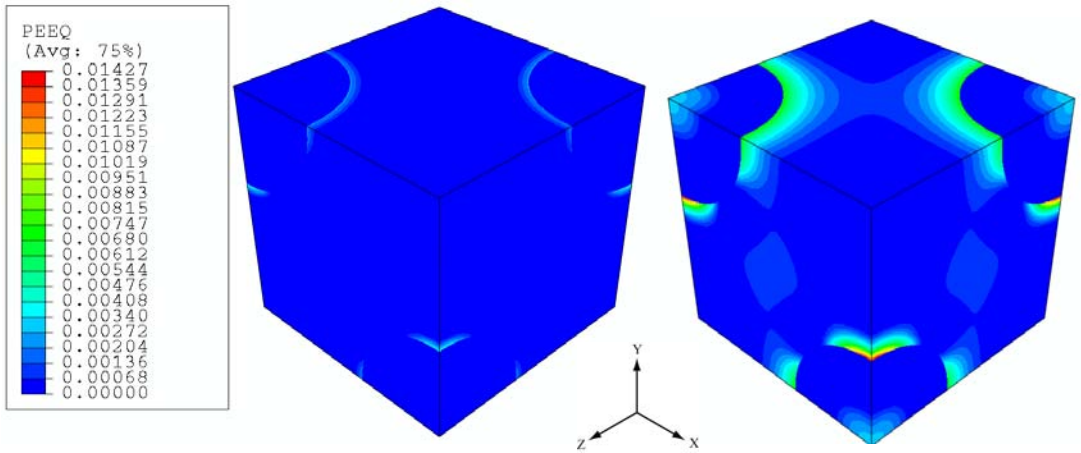

Figure 9. 14 Plastic deformation in Onion model-3 (Left: higher triaxial load. Right: lower triaxial load)

Onion models illustrate that the epoxy core reaches yield under given conditions. When models suffer from low triaxial load and the thickness of rubber shell reduce to a certain value, the plastic zone appears in the epoxy core of Onion models. The PEEQ distribution along the path of AF when under low triaxial load is shown in Figure 9. 15. Onion model-1 and -2 don't have any plastic yielding in epoxy core, whereas Onion model-3 and -4 display various yielding in epoxy core due to different rubber shell thickness. The size and magnitude of plastic zone of epoxy core depends on the rubber shell thickness, the thinner the thickness of rubber shell is, the bigger the plastic zone of epoxy core.

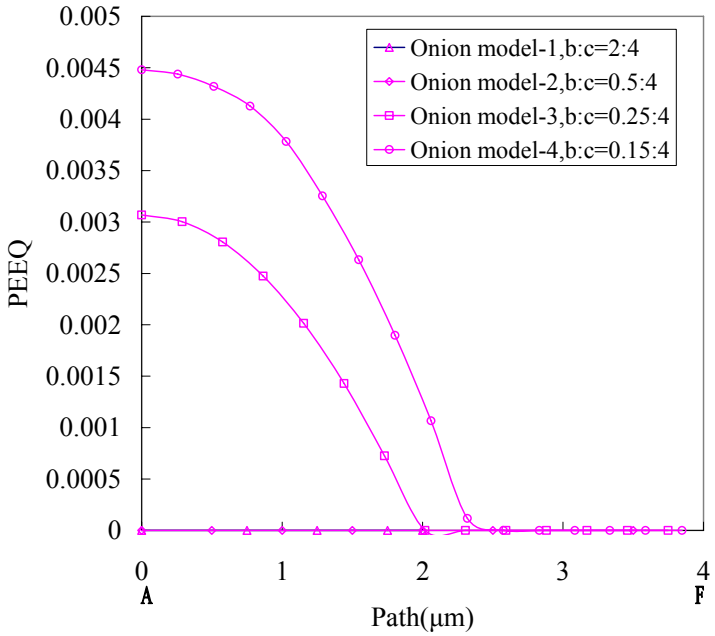

Figure 9. 15 PEEQ distribution in epoxy core along the path A-F (see Figure 9. 1)

The distribution of maximum principal stress in epoxy core is listed in Table 9. 8. It is noted that the distribution of maximum principal stress is constant in Onion model which has thick rubber shell, and the magnitude of maximum principal stress increases with the decreasing of rubber shell. Compared with Onion models, Rubber model shows the maximum principal stress is constant in rubber core at the value around 35MPa which is the same value in the epoxy core of Onion model-1.

Table 9. 8 The distribution of maximum principal stress in epoxy core

Name	Shell thickness(μm)	Largest maximum principal stress (MPa)	Distribution (MPa)
Onion model-1	2.00	35.25	constant
Onion model-2	0.50	56.06	33.40-56.06
Onion model-3	0.25	80.00	25.68-80.00
Onion model-4	0.15	87.95	22.13-87.95

The comparisons of stress states and plastic deformation of Void model under different load triaxiality are plotted in Figure 9. 16. It is found that Void model has similar distribution and magnitude of Von Mises stress under high and low load triaxiality, but the location of minimum Von Mises stress is a little different. The distribution and largest maximum principal stress under both load conditions is similar as well, but Void model under high load triaxiality has 20.71MPa of smallest maximum principal stress while the Void model under lower load triaxiality has only 1.39MPa. The biggest

difference between two load conditions focuses on the pressure state; the pressure stress in the Void model under high load triaxiality shows negative whose magnitude ranges from -46.92MPa to -13.88MPa which implies that this Void model tends to dilation in every place. The Void model under low load triaxiality shows that positive pressure stress up to 5.19MPa in polar position which means compression occurs and dilation occurs in the rest of the model. As expected, the Void model under low load triaxiality always has more plastic deformation than model under high load triaxiality and the plastic zones are linked together on transverse surfaces.

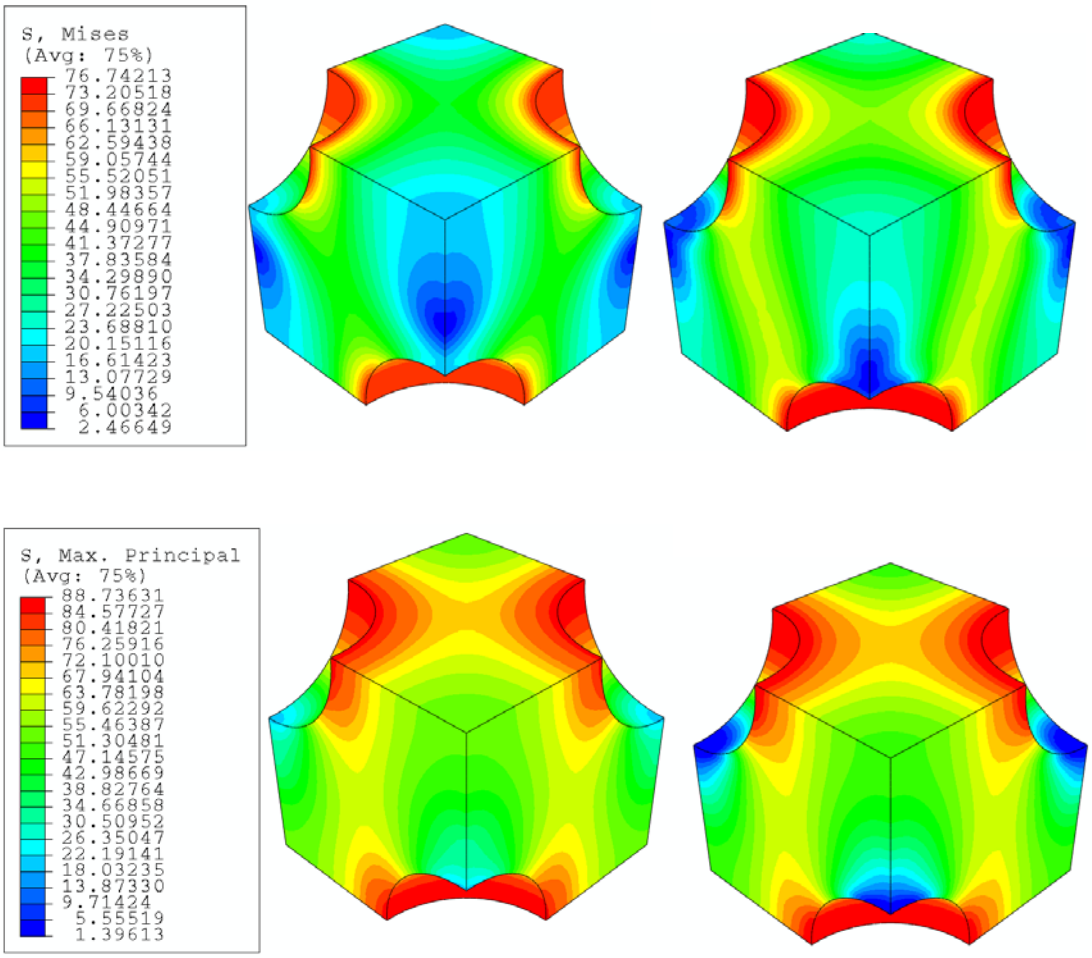

Figure continued

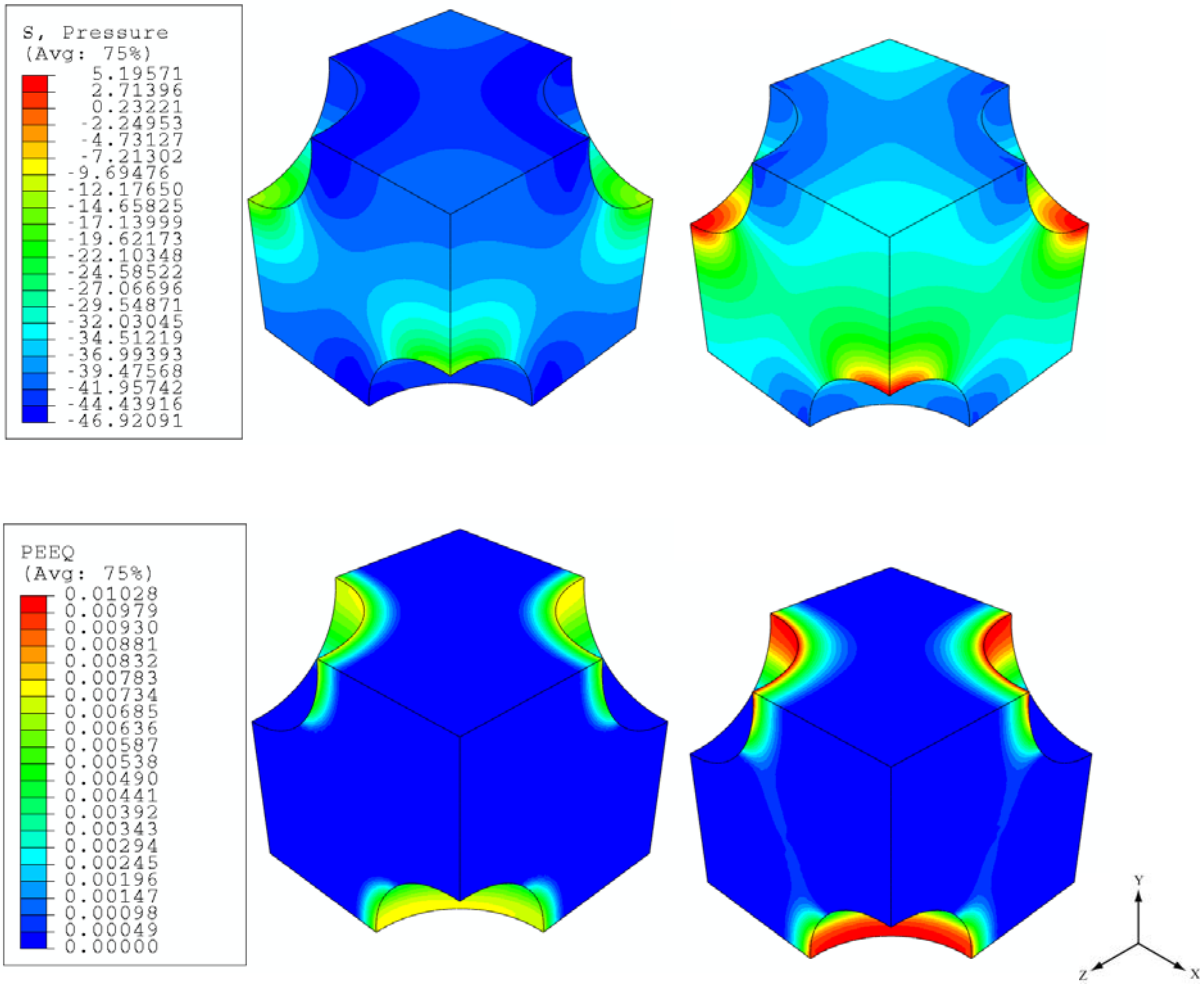

Figure 9. 16 Stress fields and plastic deformation of Void model under various load triaxiality (Left: higher triaxial load. Right: lower triaxial load)

9.3 FEA analysis of micro models in the Double Lap Joint

The stress conditions in real adhesive joints are different from those loaded in an infinite plane with a short crack in the centre. Thus it is worth investigating how the micro structures behave ahead of the crack tip in that real joint geometry. The stress distributions ahead of crack tip were presented by 2D global models and associated submodels. Those models have been discussed in Chapter 7 and principal stresses ahead of crack tip are used as the load conditions for micromodels.

9.3.1 Model geometry, element, material property and boundary conditions

Void model with 13.4% volume fraction was chosen to investigate the deformation behaviour of micro structure because Void model has common character of Rubber model and Onion models after particle cavitation. The geometry and material

properties of Void model used in this section is the same as the Void model which is studied in the previous Section 9.2. Furthermore, this Void model used same element and boundary condition but changed the load conditions.

9.3.2 Load conditions

Two typical DLJs modelling 0.2mm and 0.5mm thickness adhesive have been studied in Chapter 7. In previous modelling work, crack in adhesive is set at the middle position or close to the interface. It is noted that these principal stress conditions were obtained from submodels with 0.1mm crack length; the load used for submodels is 600N which represents a reasonable failure load. The extracted principal stresses from ahead of crack tip are used as the load conditions of Void model as shown in Figure 9. 17. It should be noted that the 'interface crack' in Figure 9. 17 only means the crack is close to interface and this definition is still valid in the following discussion unless otherwise stated.

It is noted that the effect of thickness on principal stresses are different for 0.2mm thickness adhesive and 0.5mm thickness adhesive. Regarding the simulation of 0.2mm adhesive thickness, the stress distribution of middle crack and interface crack is only distinct in the vicinity of crack tip and then all curves become similar when far away crack tip. Regarding the simulation of 0.5mm adhesive thickness, the stress distribution of middle crack and interface crack is distinct from the beginning to far distance ahead of crack tip because thick adhesive gives rise to complex constraints upon adhesive.

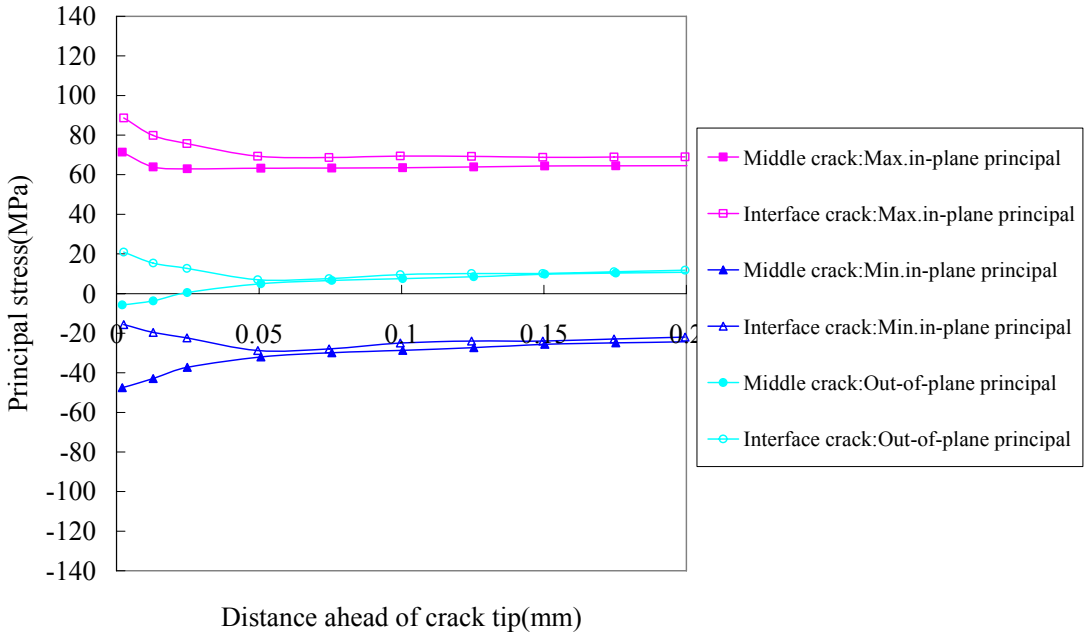

(a) 0.2mm adhesive thickness

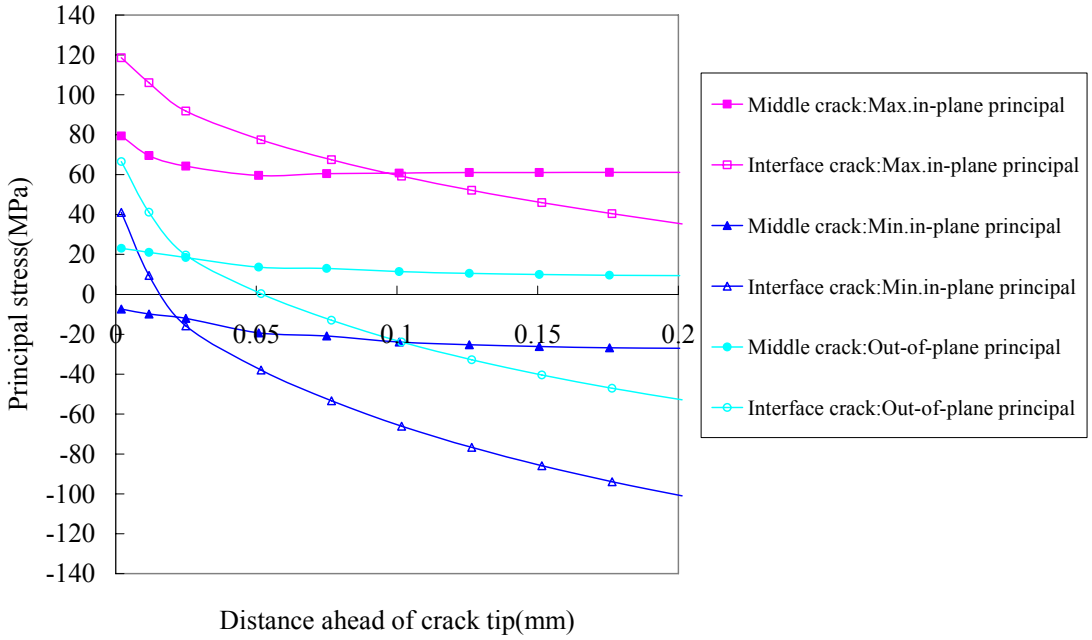

(b) 0.5mm adhesive thickness

Figure 9. 17 Extracted principal stress distributions ahead of crack tip (Top: 0.2mm adhesive thickness; Bottom: 0.5mm adhesive thickness)

Like the boundary conditions and load conditions of micro models discussed in Section 9.2, max principal stress, min principal stress and out-of-plane principal stress from submodels were applied at the top surface(X-direction), front surface (Y-direction) and left surface (Z-direction), respectively (see Figure 9. 1). All top,

front and left surfaces were constrained to move together, respectively; and the other three surfaces (bottom, back and right) were complied with symmetrical boundary conditions. Here a Void model is defined as Middle Void Model (MVM) when the load conditions are derived from submodel which has a crack in the middle of adhesive, and a Void model is defined as Interface Void Model (IVM) when the load conditions are derived from submodel which has a crack close to interface. Likewise, hexahedral elements with structural technology were used for all MVM and IVM. Stress distributions and energy statuses of those micro models were investigated.

9.3.3 FEA results

9.3.3.1 The maximum stress distributions and energy dissipation of Void model in 0.2mm thickness adhesive case

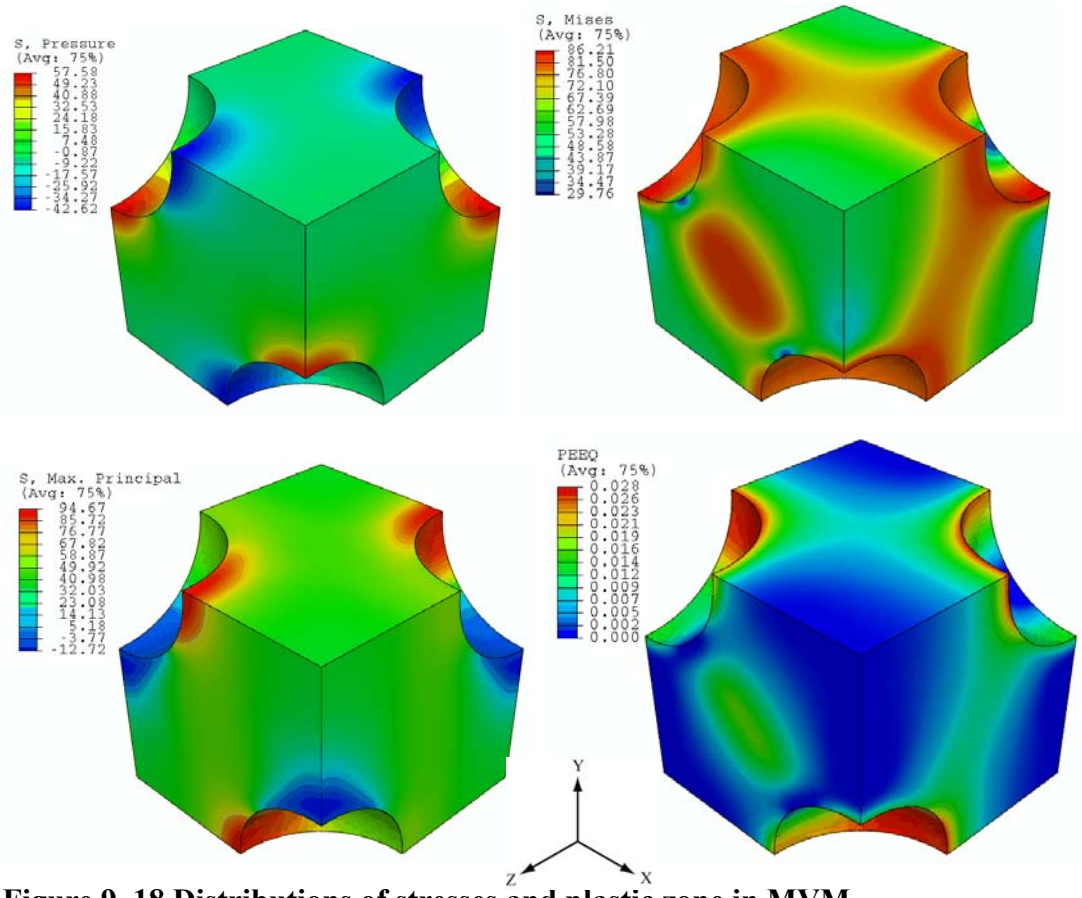

Figure 9. 18 Distributions of stresses and plastic zone in MVM

The distribution of stresses and plastic zone in MVM are shown in Figure 9. 18. It is noted that load conditions are chosen from the first points in Figure 9. 17. It is found that the magnitude order and direction of load play important role upon the Void model.

In the MVM, the left surface suffers from the lowest load, and the top surface suffers from the highest load, thus the minimum Von Mises stress occurs at the left surface and maximum Von Mises stress occurs at the top surface. In addition, the shear yielding band is continuous on the top surface and front surface, but it concentrates at the centre of the left surface.

Furthermore, Von Mises stress has higher value on the left surface than the other two surfaces from the beginning to the end of load. Hydrostatic tensile stress always occurs at the polar position and hydrostatic compression stress occurs at the equator area in the initial load and then diffuses to the surround areas at the end of load. Maximum principal stress has reverse distribution of maximum stress and minimum stress but has the same stress development as hydrostatic stress.

Since the maximum load was applied on the top surface, MVM was elongated along with the direction of this load; therefore maximum plastic deformation is focussed on the void surface which is close to the back or front surface. In addition, the shear yielding bands elsewhere have small magnitude compared with those void surfaces. All three surfaces have shear yielding band, the magnitude of these bands is influenced by the load conditions but the band shape is decided by the magnitude and direction of maximum load. This means shear yielding bands do not change their shapes when the loadings at the top and front surfaces decease by absolute value or the load at the left surface even changes its direction.

When the load conditions are chosen far from the crack tip (see Figure 9. 17), it was found all MVMs have similar stress distribution at the beginning of load, but at the end of load, top surface suffers from higher Von Mises stress than other two surfaces. This is because out-of plane load changes from negative to positive and then remains constant, and both magnitudes of maximum in-plane load and minimum in-plane load decreases and then remains constant. It is also found that the plastic deformation changes distribution. The maximum plastic deformation is focussed on the left surface instead of internal void surface, but all shear yielding band remain the shape.

The IVM has very similar stress distribution as MVM. The differences in stresses are shown in Figure 9. 19.

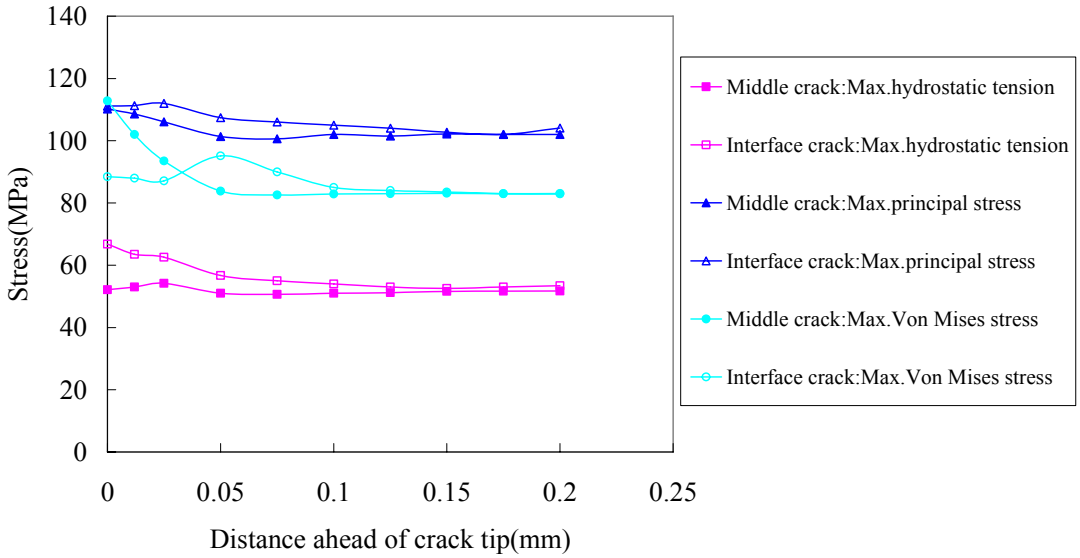

Figure 9. 19 Stress distributions in MVM and IVM along the distance ahead of crack tip

It is noted that both MVM and IVM have similar results with respect to maximum principal stress; MVM has higher Von Mises stress and lower hydrostatic tension stress than IVM in the close field of crack tip; both models have very similar stress conditions in the far field of crack tip because they are subjected to similar load there. It should be noted that IVM has highest Von Mises stress at the distance of 0.5mm away from crack tip; this is attributed to the fact that IVM is subjected to the maximum compressive load on one surface and two tensile load on other two surfaces at this point. Thus higher Von Mises stress in IVM is developed when compressive load increases (see Figure 9. 17, top) which results in a peak value of Von Mises stress. For MVM, the compressive load always decreases, moreover main tensile load decreases as well (see Figure 9. 17, top), thus the Von Mises stress in MVM decreases quickly then remains constant.

Furthermore, IVM has the plastic deformation concentrating at the void surface like MVM, but the maximum value is close to left or right surface since out-of plane principal stress applied on IVM is tensile load and much bigger than that applied on MVM. This change definitely influences the position of maximum plastic deformation in Void models as shown in Figure 9. 20. It is noted that load conditions are chosen from the first points in Figure 9. 17.

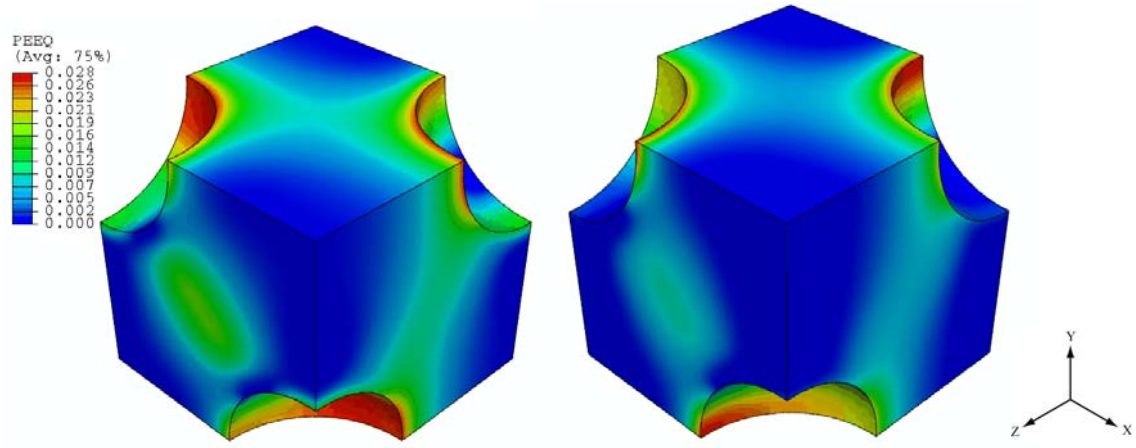

Figure 9. 20 Distribution of plastic deformation in Void models (Left contour: MVM; Right contour: IVM)

According to energy balance theory, external work done to micro model is equal to the sum of internal energy. For Void model, the internal energy is divided into two parts: one is energy dissipation caused by plastic deformation and this energy is irreversible, and another part is the stored energy due to elastic deformation and this energy is reversible. It is very clear from Figure 9. 21 that both external work of MVM and IVM are larger than counterpart plastic dissipation energy, thus the difference of external work and plastic dissipation at each point is the elastic stored energy in matrix.

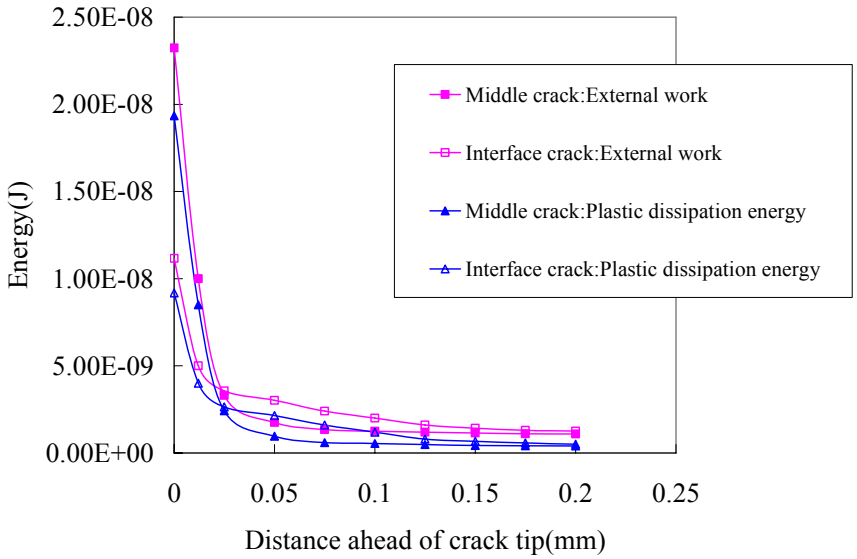

Figure 9. 21 Energy dissipations in MVM and IVM along the distance ahead of crack tip

It is clear that both external work and plastic dissipation energy of MVM is higher than those of IVM in the very vicinity of crack tip, then those energies tend to be similar far from crack tip. This implies that crack in DLJ goes through the interface more easily

than the middle of adhesive.

It is known that Von Mises stress is the general measurement of shear yielding under multiaxial load. Compared with IVM, MVM has higher Von Mises stress in the very vicinity of crack tip then lower Von Mises stress after approximately 0.035mm away from crack tip. However, it is found that the highest Von Mises stress of IVM is 0.5mm distant from the crack tip, but the energy is not the maximum at this point, thus the hydrostatic tension stress has to be taken into account in order to explain this phenomenon reasonably. For most polymers, plastic yielding is affected by the hydrostatic tension, thus the Von Mises yielding criterion for micro model can be modified to the following equation which combines Von Mises and hydrostatic stress:

$$\sigma_e + p\sigma_m \geq \sigma_c \qquad \textbf{(9- 2)}$$

Where σ_m is hydrostatic stress or mean stress which is equal to $\frac{\sigma_1 + \sigma_2 + \sigma_3}{3}$. The value p is constant parameter which depends on material. For IVM, it has lower Von Mises stress and higher hydrostatic stress in the vicinity of crack tip, this leads to higher modified Von Mises stress and higher plastic dissipation energy.

9.3.3.2 The maximum stress distributions and energy dissipation of Void model in 0.5mm thickness adhesive case

The stress distribution is much more complicated in the thick adhesive joints than in the thin adhesive joints, especially in the interface area. This is because thick adhesive between adherends has more mobility and deforms more freely. Thus the load applied at micro models is complex. The stress tendency of MVM and IVM under the triaxial load is shown in Figure 9. 22. It is noted that the load conditions are chosen from DLJ submodel (see Figure 9. 17, 0.5mm adhesive thickness)

It is clear that IVM has higher maximum principal and hydrostatic tensile stresses than MVM thanks to higher load at the beginning and subsequently has similar value of those stresses because of decreasing of main load on the top surface (see Figure 9. 17). Both MVM and IVM have similar Von Mises stress ahead of crack tip, although IVM is subjected to higher main load but all its three loadings are tensile load and MVM is subject to two tensile loadings and one compressive load. In result, both IVM and

MVM has similar Von Mises stress distribution ahead of crack tip, again this is contributed to the fact that compressive load leads to the development of the Von Mises stress.

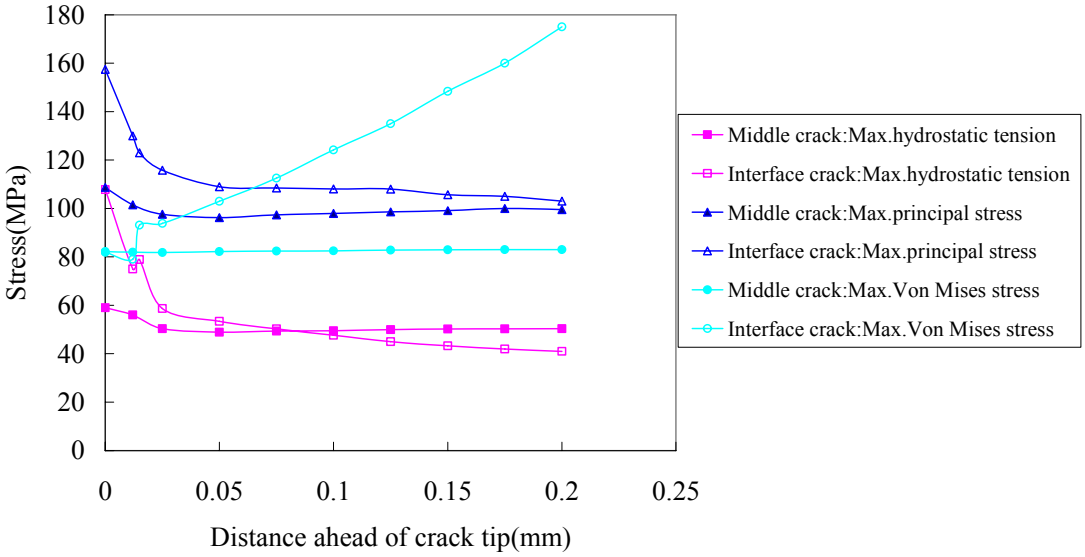

Figure 9. 22 Stress distributions in MVM and IVM along the distance ahead of crack tip

The MVM has almost constant Von Mises stress ahead of crack tip and far away from the crack tip; this is because all three loadings tend to be constant: even at the beginning there is high tensile load but the compressive load is low (see Figure 9. 17, 0.5mm thickness adhesive). In addition, tensile load is low and compressive load is high at the field far away from crack tip, thus the total effect of those loadings means that the MVM has similar Von Mises stress. Other two stresses including hydrostatic tension stress and Maximum principal stress do not change significantly in MVM.

For IVM, the load condition changes significantly (see Figure 9. 17, 0.5mm thickness adhesive) which definitely results in quick changes of stress status in IVM. It is noted that all three loadings are positive at the beginning which means IVM is subjected to triaxial tensile load. However at the point of 0.015mm away from crack tip, the minimum in-plane principal stress decreases to negative which implies IVM start to suffer from compressive load on one surface, thus the compressive load makes a contribution to the Von Mises stress in IVM (see Figure 9. 22). After this, compressive load continues increasing which results in increasing Von Mises stress even the main load decreases, after the point of 0.5mm away from crack tip, another load change

from tensile load to compressive load which gives rise to the Von Mises stress in IVM even the main load continue decreasing (see Figure 9. 17).

The energy trends of IVM and MVM are shown in Figure 9. 23. IVM has slightly higher external work and plastic dissipation energy than MVM in the vicinity of the crack tip, but the difference in these energies increases ahead of the crack tip because IVM has much higher Von Mises stress than MVM. Both external work and plastic dissipation energy of MVM decreases a little ahead of crack tip due to little change in Von Mises stress. Furthermore, the scatter between external work and plastic dissipation energy increases so that more elastic energy is stored in micro structure. For IVM, energies go down first and then increase very quickly which agrees with the change in Von Mises stress.

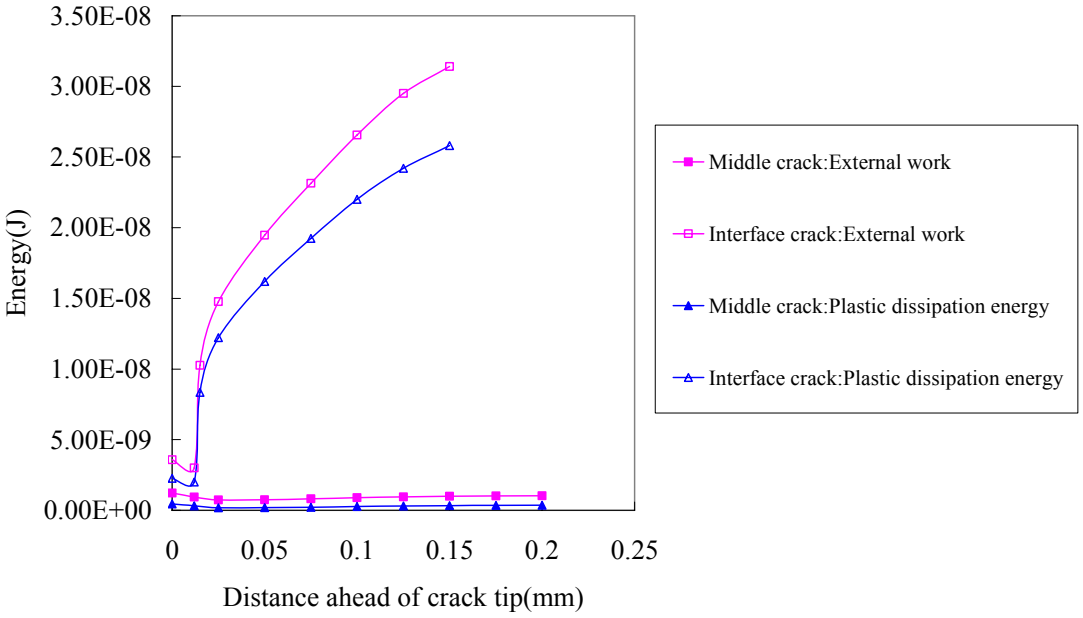

Figure 9. 23 Energy dissipations in MVM and IVM along the distance ahead of crack tip

9.4 Conclusions

First, Rubber model, Void model and four Onion models have been studied under the load derived from infinite centre crack panel. The local stress and strain fields clearly display the morphological effects and triaxial factors to these micro models, thus the following conclusions can be obtained.

The stress fields and associated plastic zone depends on the load triaxiality

significantly. The Rubber model always has higher Von Mises stress and maximum principal stress and much more plastic deformation under low load triaxiality than the Rubber model under high load triaxiality, but the pressure stress in Rubber model decreases with the decreasing of the load triaxiality. Thus high triaxial load promotes rubber particle's cavitation, and this is more distinct ahead of crack tip because of very high stress triaxial condition there. After rubber cavitation, more plastic deformation is produced under high triaxial load because Void model has higher PEEQ value than Rubber model. Thus, rubber cavitation is an essential toughness process in high triaxial load system. In contrast, under lower triaxial load, Rubber model has higher PEEQ value than Void model, thus rubber cavitation does not help to yield more plastic deformation in this condition. However, low triaxial load condition promotes the development of plastic deformation in epoxy matrix of Rubber model.

Void model has similar Von Mises stress and maximum principal stress under various load conditions, however Void model produce more plastic yielding zone under lower load triaxiality. Furthermore, polar position of Void model suffers from compression and other positions are in dilation.

The cavitation and shear deformation in Onion models depend on the thickness of rubber shell; Onion model-1 with thick rubber shell has the same stress condition as Rubber model. This is reasonable since the thick rubber shell is able to absorb all force and energy from epoxy matrix in all load conditions and triaxiality. The epoxy core plus rubber shell of Onion model-1 acts similarly to the rubber particle in the Rubber model. The magnitude and size of plastic deformation in Onion model increase with the decreasing thickness of rubber shell. Moreover, under low triaxial load, there is plastic deformation in epoxy core when rubber shell decreases to a specific value. This does not occur in high triaxial load. Like Rubber model, Onion model under low triaxial load promotes plastic deformation in the matrix but has similar ability of rubber cavitation as under high triaxial load when the rubber shell decreases like Onion model-3. Moreover, Onion model under low triaxial load has more capability of cavitation as the rubber shell decreases further like Onion model-4. Thus the Onion model has a significant advantage which allows to cavitation easily under various load condition. It is also found the thinner rubber shell the Onion model has, the more rubber cavitation and plastic deformation occur, especially plastic deformation appears

in the epoxy core in Onion model with very thin rubber shell.

For all models, the Von Mises stress inside the rubber particle or rubber shell tends to zero or very small value because rubber has very low modulus and incompressible behaviour. But the three principal stresses and pressure stress show a very high value and increase with the decreasing of rubber shell (Rubber model is considered as a special Onion model here).

Secondly, the stress condition derived from Double Lap Joint was introduced as the load conditions of Void model. The real stress conditions ahead of crack tip are very complicated and these conditions affect the micro models significantly. Two load conditions derived from middle crack and bottom crack in different adhesive thicknesses (0.2mm and 0.5mm adhesive thickness) were considered.

The modelling results show that the magnitude of load plays an important role upon the Void model. Maximum Von Mises stress occurs at the surface where maximum load is imposed and continuous yielding shear band is produced there. Hydrostatic tensile stress always occurs at the polar position and hydrostatic compression stress occurs at the equator area. Maximum principal stress has reverse distribution of maximum stress and minimum stress but has the same stress developing process as hydrostatic stress when load further from the crack tip.

For the case of Void model in 0.2mm adhesive thickness, it is noted that maximum principal stress is not so useful to explain the plastic deformation since this stress has very similar distribution and magnitude in IVM and MVM. Generally Von Mises stress is the measurement of plastic deformation for IVM and MVM, and the hydrostatic tensile stress plays a very important contribution to the development of plastic yielding. Therefore the plastic yielding criterion must combine Von Mises stress and hydrostatic stresses in order to give reasonable explain of Void models. When the Void models are subjected to the load derived from the 0.2mm adhesive thickness, it is found that the external work and plastic dissipation energy decrease with the increasing distance ahead of crack tip mainly because the absolute value of all three loads decrease along the crack tip. Furthermore, the energy stored in Void model in the form of elasticity is quite small.

For the case of Void model with 0.5mm adhesive thickness, MVM and IVM have very similar principal stress distributions to the 0.2mm adhesive thickness. However the Von Mises stress in IVM is different because the crack in the bottom position with 0.5mm thickness adhesive endures significantly higher deformation. Negative principal stresses exist in this case which implies that IVM is subjected to very high compression and results in severe plastic yielding. It is found that compressive load is important in developing Von Mises stress which gives rise to plastic dissipation. Thus, the direction of load has important effect to the micro model. Furthermore, more elastic energy has been stored in IVM than MVM.

Chapter-10 Overall conclusions and future work

10.1 Overall conclusions

10.1.1 Conclusions on experimental tests

There are two chapters presenting experiments in this work. Chapter 4 describes the manufacture and tensile test of Double Lap Joints (DLJs). It is noted that the results of Chapter 4 were compared with FEA simulation of Chapter 7. Chapter-5 describes the failure tests of adhesive bonded joints, and the results in this chapter were used to determine the parameters of cohesive zone model (CZM). Then, the CZM was applied to simulate DLJ model in Chapter 7 and Mixed Mode Bending (MMB) model in Chapter 8.

Double lap joints (DLJs) tests

The failure locus and joint strength of DLJs were studied by changing the adhesive thickness. The adhesive thickness was chosen as 0.2mm, 0.3mm and 0.5mm respectively. It is found that most specimens show an adhesive failure, but there is a very thin adhesive layer remaining at adherends. The specimens using 0.2mm and 0.3mm adhesive thickness have similar joint strength and scatter, but specimens using 0.5mm adhesive thickness obviously have lower joint strength and bigger scatter than other specimens.

There are two manufacture methods used to make DLJs, one is vacuum bag and another is direct weight. It is found that the outer adherends in overlap area is slightly deformed which is caused by the pressure from vacuum bag method. The deformed adherends cause internal stress in joints which final leads to premature failure. This means that an even pressure applied at specimens is not optimum in manufacture process. Thus the pressure applied to the specimens by direct weight was introduced to avoid the above problem.

It is found that several factors affect the joint strength via various ways. The surface

treatment is the most important step in whole manufacture process. Grit blasting must be used otherwise the joint is extremely weak. It is known that AV119 adhesive is paste adhesive which consists of a number of air voids, and air voids is a main cause of pre-mature failure in adhesive layer under load, thus the air removal before bonding is extremely important. Furthermore, adhesive degassing affects the failure surface. It is found that insufficient void removal results in discontinuous and coarse failure surface because voids enlarge and escape from adhesive during curing. The curing temperature of AV119 was chosen at 120°C. This is because low temperature cannot give adequate curing and high temperature will increase internal stress. Worse of all high curing temperature will cause decomposition. Attention has to be paid to the process of joint assembly in jig; this is because bad parallel condition of adherends results in low load capability.

It is found that most specimens have adhesive failure. But there is a very thin layer remained at adherends under optical microscope, and the average thickness of this thin layer is 10μm approximately. Thus the failure of adhesive joints can be considered as cohesive failure in a sense.

Joints failure mode tests

In this work, three failure tests were accomplished. These tests include fixed arm test (mode-I), 4 point End Notched Flexure test (mode-II) and Mixed Mode Bending test (mode-I/II). The purpose of these three tests is to determine the parameters in cohesive zone model (CZM) applications.

In the Fixed Arm Peel test, it is found that adhesive thickness affects mode-I fracture energy slightly. This is because specimens using thick adhesive thickness tend to rapid crack tip opening and unstable fracture propagation under load. Thus specimens using 0.5mm adhesive thickness have slightly lower fracture energy than specimens using 0.2mm adhesive thickness. The maximum normal stress ($\sigma_{n,0}$) and fracture energy (G_{IC}) were determined from this test.

In the 4 point End Notched Flexure tests (ENF), it is found that specimens using both 0.2mm and 0.5mm adhesive thickness yield very similar results. This is because the

crack propagation in 4 point ENF test is more stable that 3 point ENF test, thus adhesive thickness does not affect fracture energy significantly in a specific thickness range. Large plastic zones (or shear zone) were found at the vicinity of crack front in all specimens, and the length of this plastic zone increases with the increasing of adhesive thickness. The maximum shear stress ($\tau_{s,0}$) and fracture energy (G_{IIC}) were determined from this test.

Mixed mode bending (MMB) tests were produced to study the joint failure under various mixed mode ratio. It is noted that the mixed mode ratio is defined as the mode-II fracture energy to the total fracture energy (G_{IIC}/G_T). In this work, the mixed mode ratio at 0.3, 0.6, and 0.8 were chosen to determine the parameter of BK criterion in CZM application.

Other tests include the tensile test of gauge steel and hardened steel. The obtained material properties are used to calculate the mode-I toughness in fixed arm tests and simulate the adherends in FEA modelling.

10.1.2 Conclusions on macro models

The macro models in this works include the modelling of Double Lap Joint (DLJ) and mixed model bending (MMB). Global 2D and 3D models were accomplished to study DLJ; submodel is also produced as the compliment of global DLJ models. MMB was studied only using 3D model. Adhesive is represented by the Drucker-Prager model since polymer always demonstrates hydrostatic stress dependent behaviour, thus the friction angle and dilation angle were determined from basic stress-strain curves. Furthermore, hardening data was fitted to avoid numerical problems in FEA simulation but without losing accuracy. Adherend is represented using simple elastic-plastic behaviour since hardened steel was used for adherends.

DLJ modelling

The CZM was used in all 3D DLJ simulations and DLJ-B model (crack close to the interface) is chosen as the main FEA model. The parameters were determined by experimental tests. It is found that the results from DLJ-B model are in good

agreement with the results from experimental tests when using various adhesive thicknesses. Both results have matched joint stiffness, failure load and failure displacement. These agreements also demonstrate that the determination of CZM parameters is correct and thus these parameters can be extended to other simulations.

It is noted that the parameters of CZM play a very important role in 3D DLJ simulations. The influence of CZM parameters to modelling results includes the initiation criteria, propagation criteria and mixed mode criteria, and the position of cohesive zone. It is unveiled that the initiation criterion using quadratic nominal stress (Quads) is better than the criterion using maximum nominal stress (Maxs). The FEA results show that the form of damage softening in propagation criterion is less relevant. 3D simulation using mixed mode criteria has better results than simulation using mode independent criterion. The adhesive constitutive law was also studied. Three adhesive material models were used including simple elastic-plastic model, linear Drucker-Prager model and exponent Drucker-Prager model. The modelling results show that both linear Drucker-Prager and exponent Drucker-Prager have more accurate prediction than linear elastic-plastic model, however the linear Drucker-Prager model predicted a lower failure displacement than exponent Drucker-Prager model.

The effects of cohesive zone in 3D models were studied via changing the number of cohesive layers and the position of cohesive layer. It is found that modelling using multi cohesive layers does not affect the simulation results. This implies that cohesive zone can be used at different position without losing modelling accuracy if the crack position is unknown. It is also found that cohesive layer, which is at the interface or close to the interface, produced very similar results. This implies the slight change of cohesive layer position does not affect the modelling results once the parameters of CZM are correct.

More details are unveiled via 2D DLJ models and submodels. J-integral was used to study the effects of modelling geometry on the fracture energy. These geometry effects include crack position, adhesive thickness and crack length. The R-curves are found from 2D modelling because the adhesive layer is strongly constrained by adherends, thus the plastic zone develops with the increasing of crack length, but the fracture energy become stable when crack reaches a specific length due to the complete

development of plastic zone. It is also found that 2D model using 0.5mm adhesive thickness has a final J-integral value which is similar to the value from Fixed Arm Peel test. This implies that joints using thick adhesive layer tend to be pure mode-I opening failure under tensile load. Because the stress singularity always exists around the crack tip and stress status of this area is strongly dependent on element size, submodel is used to alleviate the singularity problem. The principal stresses ahead of crack tip were obtained and then used as the load condition as the micro Void models.

MMB modelling

3D MMB models were accomplished with cohesive zone application. All parameters were determined from experiments and numerical analysis since the parameters were proved correct in previous 3D DLJ simulation. Furthermore, in order to simulate MMB in line with real test conditions, this work employed multi parts which consist of rigid bodies and deformed bodies. This modelling consists of three different mixed mode ratios which are 0.3, 0.6, and 0.8, and the models with and without adhesive layer were also performed.

The results of FEA agree with the experimental results well. It is found that this model is better to simulate the low mixed mode ratio than high mixed mode ratio because the failure at high mixed mode ratio (i.e. mode-II dominant) tends to be unstable. It is found that plastic zone exists ahead of crack front in the models with adhesive layer, and this plastic zone is mostly caused by shear stress and its maximum values are found on the free edge of MMB specimen where plastic zone is free to develop. The plastic dissipation increased quickly with the increasing of mode-II component, but the plastic dissipation becomes stable in the high mode-II range. In addition, VCCT technique was used to monitor the mode-III fracture energy ahead of crack front. It is found that the mode-III fracture energy ahead of crack front is very small compared to the other two mode fracture energies. VCCT also shows that the mode-I and mode-II fracture energy are distributed uniformly ahead of crack front but localize at both free edges.

10.1.3 Conclusions on micro models

The study of micro models mostly focuses on the morphologic effects and load conditions on particle toughening. Three micro models including Rubber model, Void model and Onion (multilayer) model are created and studied. It is noted that Onion models can be modified by change the ratio of core radius to the shell thickness. The load conditions are derived from infinite plane with centred crack and DLJ models. The rubber particle in micro model is represented by hyperelastic behaviour using polynomial model (n=2). The epoxy matrix used exponent Drucker-Prager model.

It is found that the load triaxiality significantly affects the stress status and plastic zone. In Rubber models, low triaxiality load promotes high Von Mises stress and maximum principle stress thus leads to more plastic dissipation. However, high triaxiality load promotes cavitation of rubber particles. After rubber cavitation, Rubber model is changed to Void model and more plastic dissipation is produced under high triaxiality load. Thus the rubber cavitation process is very important to enhance the toughness when system is under high triaxiality load. Low triaxiality load is not helpful to promote rubber cavitation but promotes shear yielding in epoxy matrix. In Void models, it is found that Void models produce more plastic yielding zone under low triaxiality load.

Onion models show that their cavitation and shear yielding behaviour strongly depends on the model morphology. The Onion model using thick rubber shell and small epoxy core can be considered as Rubber model since modelling results show that these two models have very similar stress distribution under various load condition. The magnitude and size of plastic yielding zone in Onion models increase with the decreasing of rubber shell. In addition, Onion model using thin rubber shell has plastic zone in epoxy core under low triaxiality load. It is also found that the decreasing of rubber shell thickness is helpful for rubber cavitation and shear yielding under various triaxiality loadings. Thus the Onion model with thin rubber shell is the most desirable morphology to enhance toughness.

Void model is studied further since the Void model is a structure after the cavitation of Rubber model and Onion model. The load conditions for Void models were derived

from 2D DLJ submodel; and Middle Void Model (MVM) implies that load condition is from the crack which is in the middle of adhesive layer and Interface Void Model (IVM) implies that the load condition is from the crack which is close to the interface. The plastic yielding criteria applied the combination of the Von Mises stress and hydrostatic stress since hydrostatic stress is helpful for developing the plastic yielding. For the case of 0.2mm adhesive thickness, both MVM and IVM has a similar stress distribution. The external work and plastic dissipation decrease with the increasing distance ahead of crack tip and the elastic energy stored in Void models can be ignored. For the case of 0.5mm adhesive thickness, the Von Mises stress in IVM is higher than MVM. It is found that the direction of load plays important role which means compressive load is helpful to develop plastic yielding. Furthermore, more elastic energy was stored in IVM and MVM.

10.1.4 Contributions to the current work

This work aims at the multiscale analysis of adhesive-bonded structure. This multiscale analysis is not only fundamental study and also an immediate practical interest. The cohesive zone model (CZM) is the prerequisite of successful simulation, thus a systematic and precise method is established for the first time to determine and calculate all CZM parameters. These parameters were validated by comparing DLJ simulation and experiments. Furthermore, the effects of constitutive law and traction-separation law to modelling results were also unveiled.

A novel MMB modelling was created on the basis of real testing conditions. Because multi bodies were applied and MMB specimen was loaded via connector elements, the simulation is possible to take into account the change of load direction of mode-I and the change of load position of mode-II in real test. Furthermore, a limited adhesive layer was considered in MMB modelling since researchers working on the same field always ignore the effect of adhesive layer to modelling. It is first time to unveil the plastic zone distribution and magnitude ahead of crack front in this work.

The novel methodology of this work combines macro models and micro models. The results of 3D DLJ model are used for 2D DLJ models and submodels, and then the stress distribution ahead of crack tip in submodels is used as the load condition of

micro models. The results of micro models show that multilayer (onion) model with thin rubber shell is the best morphology to develop the fracture toughness; also this find can be used as the instruction of future material design.

Experiments were used to validate and support the modelling. DLJ with different adhesive thickness were studied. The manufacture method was paid a lot of attention and it is found that the vacuum bag to manufacture DLJ has its disadvantage although this method is most popular one currently. A Fixed arm peel test was used instead of Double Cantilever Beam (DCB) to determine mode-I behaviour. This test has the advantage of obtaining the maximum normal stress ($\sigma_{n,0}$) of CZM conveniently. MMB test is mostly used for unidirectional composites test and few researchers used it to study the adhesive application. This work showed that the MMB test is suitable for testing adhesive fracture toughness under different mixed mode ratio and is able to produce the mixed mode parameter for BK criterion.

10.2 Future work

The current work has proven the successful combination of experiments and FEA simulation in adhesive research. The work also bridged the adhesive joints and micro model via a series of analysis and modelling. Since adhesive application is so broad and in practice people will encounter many new conditions and requirements for adhesive during their exploitation, further study and research in this field is endless and diverse. Based on the current study, possible future research can be focussed on the following topics:

1) Recently, more and more attention has been paid to the environmental degradation and long-term performance of adhesively bonded joints. In general, adhesive strength is significantly affected by moisture absorption and its mechanical properties decrease sharply when moisture uptake increases. Future work can focus on these areas using the current technology. Furthermore, the successful model used in this work can be extended to the study of more general adhesive joints when the known materials properties are provided.

2) The shape of Traction-Separation law in cohesive zone model can be defined as

various forms. Many researchers think the shape of law is less relevant, thus the triangular cohesive zone model are used widely. However, when more ductile materials are used, a trapezoidal cohesive zone model may give better results because it takes account of more plasticity. Regarding the load and unloading stage in T-S law, the penalty stiffness is always considered constant and unloading stage (i.e. softening stage) is generally assumed as linear or exponential behaviour since the T-S shape does not change the modelling results significantly but affects the convergent situation or computation time in FEA. It is still unclear whether the shape of T-S law affects the accuracy of modelling when the joints suffer from more complicated load such as combined mechanical load and thermal load. Moreover, penalty stiffness may change slightly when the plastic zone in the vicinity of the crack tip develops. Thus dynamic penalty stiffness should be considered.

3) DLJ tests in this work were subjected to in-plane deformation. In practice lots of out-plane deformation such as bending and torsion of adhesively bonded joints exist; therefore joints under more complex load should be investigated.

4) The shear yielding is very important as a toughening mechanism. It is known that the shear yielding is usually rate dependent phenomena, thus the rate process could be taken into account in future work.

5) Resulting from the fast development of FEA technology, people are able to apply the state of art technology to study engineering and materials problems. Lately new FEA features such as Extended Finite Element Method (XFEM) are available. XFEM is powerful to predict crack growth along arbitrary paths which do not correspond to element boundaries. Also this technology can be combined with other FEA methods such as Interface Cohesive Zone (similar to CZM) to simulate the durability and damage of adhesive joints.

References

[1]ABAQUS Analysis User's Manual (2007a). "17.5.1 Hyperelastic behaviour of rubber like materials." **6.7-1**.

[2]ABAQUS Analysis User's Manual (2007b). "18.3.1 Extended Drucker-Prager models." **6.7-1**.

[3]ABAQUS Analysis User's Manual (2007c). "25 Connector Elements." **6.7-1**.

[4]ABAQUS Analysis User's Manual (2007d). "26.5.6 Defining the constitutive response of cohesive elements using a traction-separation description." **6.7-1**.

[5]ABAQUS Analysis User's Manual (2009). "34.1.2 Common difficulties associated with contact modeling in Abaqus/Standard." **6.9-2**.

[6]ABAQUS Theory Manual (2009a). "3.2.3 Hybrid incompressible solid element formulation." **6.9-2**.

[7]ABAQUS Theory Manual (2009b). "4.6.1 Hyperelastic material behavior." **6.9-2**.

[8]Abdel Wahab, M.M., Ashcroft, I.A., Crocombe, A.D. and Simth, P.A. (2002). "Numerical prediction of fatigue crack propagation lifetime in adhesively bonded structures." International journal of fatigue **24**: 705-709.

[9]Adams, R.D., Comyn, J. and Wake, W.C. (1997). structural adhesive joints in engineering, Chapmen &Hall.

[10]Alfredsson, K.S. (2004). "On the instantaneous energy release rate of the end-notched flexure adhesive joint specimen." International journal for solids and structures **41**: 4787-4807.

[11]Andersen, T. and Stigh, U. (2004). "The stress-elongation relation for an adhesive layer loaded in peel using equilibrium of energetic forces." International journal for solids and structures **41**: 413-434.

[12]Bagheri, R. and Pearson, R.A. (1996). "Role of particle cavitation in rubber-toughened epoxies: 1. Microvoid toughening." Polymer **37**: 4529-4538.

[13]Baik, J.M. and Thompson, R.B. (1984). "Ultrasonic scattering from imperfect interfaces: A quasi-static model." Journal of nondestructive evaluation **4**: 177-195.

[14]Barenblatt, G.I. (1959). "The formation of equilibrium cracks during brittle fracture." Journal of applied mathematics and mechanics **23**: 434-444.

[15]Barthelemy, B.M., Kamat, M.P. and Brinson, H.F. (1984). Finite element analysis

of bonded joints, Office of naval research.

[16]Bascom, W.D., Cottington, R.L., Jones, R.L. and Peyser, P. (1974). "Fracture of epoxy and elastomer-epoxy polymers in bulk and as adhesives." American chemical society **34**: 300-308.

[17]Benzeggagh, M.L. and Kenane, M. (1996). "Measurement of mixed-mode delamination fracture toughness of unidirectional glass/epoxy composites with mixed-mode bending apparatus." Composite science and technology **56**: 439-449.

[18]Blackman, B.R.K., Hadavinia, H., Kinloch, A.J. and Williams, J.G. (2003). "The use of a cohesive zone model to study the fracture of fibre composites and adhesively-bonded joints." International journal of fracture **119**: 25-46.

[19]Broek, D. (1986). Elementary engineering fracture mechanics, Kluwer academic publishers, Inc.

[20]Camanho, P.P. and Davila, C.G. (2002). Mixed-mode decohesion finite elements for the simulation of delamination in composite materials. Report NASA/TM-2002-211737.

[21]Camanho, P.P., Davila, C.G. and Ambur, D.R. (2001). Numerical simulation of delamination growth in composite materials. NASA-TP-211041.

[22]Carlsson, L.A., Gillespie, J.W. and Pipes, B. (1986). "On the analysis and design of the end notched flexure (ENF) specimen for mode-II testing." Journal of composite materials **20**: 594-604.

[23]Cavalli, M.S. and Thouless, M.D. (2001). "The effect of damage evolution on adhesive joint toughness." Journal of adhesives **76**: 75-92.

[24]Chen, D. and Cheng, S. (1983). "An analysis of adhesive-bonded single-lap joints." Journal of applied mechanics **50**: 109-115.

[25]Chen, W.F. and Han, D.J. (2007a). Plasticity for structural engineers, J.Ross publishing.

[26]Chen, W.F. and Han, D.J. (2007b). Plasticity for structural engineers, J.Ross publishing**:** 257.

[27]Chen, W.F. and Han, D.J. (2007c). Plasticity for structural engineers, J.Ross publishing**:** 250.

[28]Chen, W.F. and Han, D.J. (2007d). Plasticity for structural engineers, J.Ross publishing**:** 258.

[29]Chen, W.F. and Zhang, H. (1991). Structural plasticity:theory, problems, and CAE software. New York, Springer-verlag.

[30]Chen, X.H. and Mai, Y.W. (1998a). "Micromechanical modelling of deformation mechanisms for rubber-toughened polymers." Key Engineering Materials **145-149**: 233-242.

[31]Chen, X.H. and Mai, Y.W. (1998b). "Micromechanics of rubber-toughened polymers." Journal of materials science **33**: 3529-3539.

[32]Crocombe, A.D., Hua, Y.X., Loh, W.K., Wahab, M.A. and Ashcroft, I.A. (2006). "Predicting the residual strength for environmentally degraded adhesive lap joints." International journal of adhesion & adhesives **26**: 325-336.

[33]Curley, A.J., Hadavinia, H., Kinloch, A.J. and Taylor, A.C. (2000). "Predicting the service-life of adhesively-bonded joints." International journal of fracture **103**: 41-69.

[34]Dattaguru, B., Venkatesha, K.S. and Ramamurthy, T.S. (1994). "Finite element estimates of strain energy release rate components at the tip of an interface crack under mode-I loading." Engineering fracture mechanics **49**: 451-463.

[35]Davila, C.G., Camanho, P.P. and de Moura, M.F. (2001). Mixed-mode decohesion elements for analyses of progressive delamination. The 42nd AIAA/ASME/ASCE/AHS/ASC structures, structural dynamics and materials conference, Seattle, Washington.

[36]Davy, P.J. and Guild, F.J. (1988). "The distribution of interparticle distance and its application in finite-element modelling of composite materials." Proceedings of the Royal Society **418**: 95-112.

[37]Day, R.J., Lovell, P.A. and Wazzan, A.A. (2001). "Toughened carbon/epoxy composites made by using core/shell particles." Composite science and technology **61**: 41-56.

[38]Dean, G.D. and Crocker, L. (2001). The use of finite element methods for design with adhesives, Materials centre of national physical laboratory.

[39]Dean, G.D. and Duncan, B.C. (1995). Tensile behaviour of bulk specimens of adhesives. DMM(B)448. Teddington, National Physical Laboratory.

[40]Dean, G.D., Duncan, B.C., Adams, R., Thomas, R. and Vaughn, L. (1996a). Basic mechanical properties for design. CMMT(B)51. Teddington, National Physical Laboratory.

[41]Dean, G.D., Duncan, B.C., Adams, R., Thomas, R. and Vaughn, L. (1996b). Comparison of bulk and joint specimen tests for determining the shear properties of adhesive. CMMT(B)51. Teddington, National Physical Laboratory.

[42]Dean, G.D. and Read, B.E. (2001). "Modelling the behaviour of plastics for design

under impact." Polymer Testing **20**: 677-683.

[43]Delides, C.G., Hayward, D., Pethrick, R.A. and Vatalis, A.S. (2003). "Dielectric and morphological investigations of phase separation and cure in rubber-modified epoxy resins: Comparison between teta- and DDM-based systems." Journal of applied polymer science **47**: 2037-2051.

[44]Diehl, T. (2008). "On using a penalty-based cohesive-zone finite element approach, Part I: Elastic solution benchmarks." International journal of adhesion & adhesives **28**: 237-255.

[45]Dillard, D.A. and Pocius, A.V. (2002). The mechanics of adhesion, Elsevier science B.V.

[46]Duncan, B.C. (1999). Preparation of bulk adhesive test specimens. CMMT(MN)057. Teddington, National Physical Laboratory.

[47]Duncan, B.C. and Dean, G.D. (1996). Test methods for determining shear property data for adhesive suitable for design. CMMT(B)55. Teddington, National Physical Laboratory.

[48]Duncan, B.C., Girardi, M.A. and Read, B.E. (1994a). Basic mechanical properties for design. DMM(B)339. Teddington, National Physical Laboratory.

[49]Duncan, B.C., Girardi, M.A. and Read, B.E. (1994b). The preparation of bulk adhesive samples for mechanical testing. DMM(B)339. Teddington, National Physical Laboratory.

[50]Erlicher, S., Bursi, O.S. and ASCE, A.M. (2008). "Bouc-Wen-type models with stiffness degradation:thermodynamic analysis and applications." Journal of engineering mechanics **134**: 843-855.

[51]Evans, A.G., Ahmad, Z.B., Gibert, D.G. and Beaumont, P.W.R. (1986). "Mechanisms of toughening in rubber toughened polymer." Acta metallurgica **34**: 79-87.

[52]Eyring, H. (1936). "Viscosity, plasticity, and diffusion as example of absolute reaction rates." Journal of chemical physics **4**: 283-291.

[53]Felippa, C.A. (1986). Introduction to finite element methods (Course materials). University of Colorado at Boulder.

[54]Fond, C. (2001). "Cavitation criterion for rubber materials: a review of void-growth models." Journal of polymer science **39**: 2081-2096.

[55]Gali, S., Dolev, G. and Shai, O. (1981). "An effective stress/strain concept in the mechanical characterization of structural adhesive bonding." International Journal of

Adhesion and Adhesives **1**: 135-140.

[56]Giunta, R.K. and Kander, R.G. (2002). "Accelerated aging of polyimide/titanium adhesive bonds using the notched coating adhesion test." Polymer Engineering and Science **42**: 1789-1797.

[57]Goland, M. and Reissner, E. (1944). "The stresses in cemented joints." Journal of applied mechanics **11**: 17-27.

[58]Guild, F. (2004). Toughening mechanisms in rubber modified thermosets. The 27th annual meeting of adhesive society.

[59]Guild, F.J. and Kinloch, A.J. (1995). "Modelling the properties of rubber-modified epoxy polymer." Journal of materials science **30**: 1689-1697.

[60]Guild, F.J. and Young, R.J. (1989). "A predictive model for particulate filled composite materials." Journal of materials science **24**: 2454-2460.

[61]Harris, J.A. and Adams, R.D. (1984). "Strength prediction of bonded single lap joints by non-linear finite element methods." International journal of adhesion & adhesives **4**: 65-78.

[62]Hart-Smith, L.J. (1973). Adhesive-bonded single-lap joints. NASA report.

[63]Hashemi, S., Kinloch, A.J. and Williams, J.G. (1990). "The analysis of interlaminar fracture in uniaxial fibre-polymer composites." Proceedings of the royal society of london. Series A, mathematical and physical sciences **427**: 173-199.

[64]Huang, Y. and Kinloch, A.J. (1990). "Modelling of toughened mechanisms." Polymeric materials **63**: 564-567.

[65]HUNTSMAN (2004). "Publication No.A 314f GB."

[66]ICpeel (2006). "http://www3.imperial.ac.uk/meadhesion/testprotocols/peel."

[67]Irwin, G.R. (1964). "Structural aspects of brittle fracture." Applied materials research **3**: 65-81.

[68]Janssen, M., Zuidema, J. and Wanhil, R.J.H. (2002a). Fracture mechanics, DUP blue print**:** 150.

[69]Janssen, M., Zuidema, J. and Wanhil, R.J.H. (2002b). Fracture mechanics, DUP blue print**:** 136.

[70]Janssen, M., Zuidema, J. and Wanhil, R.J.H. (2002c). Fracture mechanics, DUP blue print**:** 151.

[71]Janssen, M., Zuidema, J. and Wanhil, R.J.H. (2002d). Fracture mechanics, DUP blue print**:** 133-154.

[72]Jasiuk, I., Sheng, P.Y. and Tsuchida, E. (1997). "A spherical inclusion in an elastic

half-space under shear." Journal of Applied Mechanics **64**: 471-479.

[73]Jeong, H.Y. and Pan, J. (1995). "Macroscopic constitutive law for porous solids with pressure-sensitive matrices and its implications to plastic flow localization." International journal of solids and structures **32**: 3669-3691.

[74]Kawashita, L.F., Moore, D.R. and Williams, J.G. (2005). "Analysis of peel arm curvature for the determination of fracture toughness in metal-polymer laminates." Journal of materials science **40**: 4541-4548.

[75]Kinloch, A.J. (1987a). Adhesion and adhesives: Science and technology, Chapman and hall Ltd**:** 267.

[76]Kinloch, A.J. (1987b). Adhesion and adhesives: Science and technology, Chapman and hall Ltd**:** 281.

[77]Kinloch, A.J. (1987c). Adhesion and adhesives: Science and technology, Chapman and hall Ltd**:** 282.

[78]Kinloch, A.J. (1989). Rubber-toughened plastics. Washington DC, American chemical society.

[79]Kinloch, A.J. (1997). "Adhesives in engineering." Processing of the institution of mechanical engineers Part G-Journal of aerospace engineering **211**: 307-335.

[80]Kinloch, A.J. and Guild, F. (1996a). Predictive modelling of the properties and toughness of rubber-toughened epoxies. Toughened plastics II:Novel applications in science and engineering. C. K. Riew and A. J. Kinloch, The american chemical society.

[81]Kinloch, A.J. and Guild, F.J. (1996b). Predictive modeling of the properties and toughness of rubber-toughened epoxy, American Chemical Society.

[82]Kinloch, A.J., Shaw, S.J. and Huntston, D.L. (1983). "Deformation and fracture behaviour of a rubber-toughened epoxy: 2. Failure criteria." Polymer **24**: 1355-1363.

[83]Kinloch, A.J., Wang, Y. and Williams, J.G. (1993). "Mixed-mode delamination of fibre composite materials." Composites science and technology **47**: 225-237.

[84]Kinloch, A.J. and Williams, J.G. (2002). Chapter 8 The mechanics of peel tests. The mechanics of adhesion. D. A. Dillard and A. V. Pocius. Amsterdam, Elsevier science B.V. **1:** 273-301.

[85]Knox, E.M. and Cowling, M.J. (2000). "Durability aspects of adhesively bonded thick adherend lap shear joint." International journal of adhesion & adhesives **20**: 323-331.

[86]Kunz, S.C. and Beaumont, P.W.R. (1981). "Low-temperature behaviour of epoxy-rubber particulate composite." Journal of materials science **16**: 3141-3152.

[87]Lavrentyev, A.I. and Rokhlin, S.I. (1994). "Model for ultrasonic characterization of environmental degradation of interfaces in adhesive joints." Journal of applied physics **76**: 4643-4650.

[88]Lee, S.J. and Lee, G.L. (1992). "Development of a failure model for the adhesively bonded tubular single lap joint." Journal of adhesives **40**: 1-14.

[89]Lee, S.M. (1993). "An edge crack torsion method for mode-III delamination fracture testing." Journal of composite technology and research **15**: 193-201.

[90]Lee, S.Y., Rus, G. and Park, T. (2007). "Detection of stiffness degradation in laminated composite plates by filtered noisy impact testing." Computational Mechanics **41**: 1-15.

[91]Li, G. (1999). "Nonlinear finite element analysis of the stress and stain distributions across the adhesive thickness in composite single-lap joints." Composite structure **46**: 395-403.

[92]Li, S., Thouless, M.D., Waas, A.M., Schroeder, J.A. and Zavattieri, P.D. (2006). "Mixed-mode cohesive-zone models for fracture of an adhesively bonded polymer-matrix composites." Engineering fracture mechanics **73**: 64-78.

[93]Liljedahl, C.D.M., Crocombe, A.D., Wahab, M.A. and Ashcroft, I.A. (2006). "Damage modelling of adhesively bonded joints." International journal of fracture **141**: 147-161.

[94]Lim, W.W., Hatano, Y. and Mizumachi, H. (1994). "Fracture toughness of adhesive joints I: Relation between strain energy release rates in three different fracture modes and adhesive strength." Journal of applied polymer science **52**: 967-973.

[95]Loh, W.K. and Crocombe, A.D. (2002). "Environmental degradation of the interfacial fracture energy in an adhesively bonded joint." Engineering fracture mechanics **69**: 2113-2128.

[96]Lu, F., Cantwell, W.J. and Kausch, H.H. (1997). "The role of cavitation and debonding in the toughening of core-shell rubber modified epoxy systems." The journal of materials science **32**: 3055-3059.

[97]Mafi, E.R. and Ebrahimi, M. (2008). "Role of core-shell rubber particle cavitation resistance on toughenability of epoxy resins." Polymer Engineering and Science **48**: 1376-1380.

[98]Malm, R. (2009). Predicting shear type crack initiation and growth in concrete with non-linear finite element method. Department of civil and architectural engineering, Royal institute of technology (KTH).

[99]Margetan, F.J., Thompson, R.B. and Gray, T.A. (1988). "Interfacial spring model for ultrasonic interactions with imperfect interfaces: Theory of oblique incidence and application to diffusion-bonded butt joints." Journal of nondestructive evaluation **7**: 131-152.

[100]Oliveira, J.M.Q., de Moura, M.F.S.F., Silva, M.A.L. and Morais, J.J.L. (2007). "Numerical analysis of the MMB test for mixed-mod I/II wood fracture." Composite science and technology **67**: 1764-1771.

[101]Oplinger, D.W. (1991). "Effects of adherend deflections in single-lap joints." Internatioal Journal of solid structures **31**: 2565-2587.

[102]Ozel, A. and Kadioglu, F. (2002). Non-linear analysis of adhesively bonded single lap joint in bending load. The tenth international conference on machine design and production, Cappadocia, Turkey.

[103]Poon, Y.M., Luk, W.L. and Shin, F.G. (2002). "Statistical spherical cell model for the elastic properties of particulate-filled composite materials." Journal of Materials Science **37**: 5095-5099.

[104]Raju, I.S., Crews, J.H. and Aminpour, M.A. (1988). "Convergence of strain energy release rate components for edge-delaminated composite laminates." Engineering fracture mechanics **30**: 383-396.

[105]Reeder, J.R. (1992). An evaluation of mixed-mode delamination failure criterion. NASA-TM 104210.

[106]Reeder, J.R. (2003). "Refinements to the mixed-mode bending test for delamination toughness." Journal of composites technology and research **25**: 191-195.

[107]Reeder, J.R. and Crews, J.H. (1992). "Redesign of the mixed-mode bending delamination test to reduce nonlinear effects." Journal of composite technology and research **14**: 12-19.

[108]Reeder, J.R. and Crews, J.R. (1990). "Mixed-mode bending method for delamination testing." American institute of aeronautics and astronautics **28**: 1270-1276.

[109]Rice, J.R. (1968). Mathematical analysis in the mechanics of fracture. Fracture, Academic press**:** 192-311.

[110]Riew, C.K. and Kinloch, A.J. (1996). Toughened plastics II:Novel approaches in science and engineering. Washington DC, The american chemical society.

[111]Runesson, K. (2005). "Implicit integration of elastoplastic relations with reference to soils." International journal for numerical and analytical methods in

geomechanics **11**: 315-321.

[112]Sawa, T. and Suga, H. (1996). "Finite-element stress analysis of double-lap adheisve joints." Journal of adhesive science and technology **10**: 1255-1271.

[113]Schellekens, J.C.J. and de Borst, R. (1993). "A nonlinear finite-element approach for the analysis of model-I free edge delamination in composites." International journal for solids and structures **30**: 1239-1253.

[114]Schuecker, C. and Davidson, B.D. (2000). "Evaluation of the accuracy of the four point bend end-notched flexure test for mode-II delamination toughness determination." Composite science and technology **60**: 2137-2146.

[115]Steenbrink, A.C. and Van der Giessen, E. (1997). "A numerical study of cavitation and yield in amorphous polymer-rubber blends." Journal of engineering materials and technology **119**: 256-261.

[116]Sultan, J.N. and McGarry, F.J. (1973). "Effect of rubber particle size on deformation mechanisms in glassy epoxy." Journal of polymer science **13**: 29-35.

[117]Tracey, D.M. (1976). "Finite element solutions for crack tip behaviour in small scale yielding." Journal of engineering materials and technology **98**: 146-151.

[118]Turon, A., Davila, C.G., Camanho, P.P. and Costa, J. (2005). An engineering solution for using coarse meshes in the simulation of delamination with cohesive zone models. Report NASA/TM-2005-213547.

[119]Tvergaard, V. and Hutchinson, J.W. (1993). "Influence of plasticity on mixed mode interface toughness." Journal of the mechanics and physics of solids **41**: 1119-1135.

[120]Wake, W.C. (1982). Adhesion and the formulation of adhesive, Applied science Pub, London, p.54.

[121]Wang, M.C. (2003). Finite element method. Beijing, Tsinghua university press.

[122]Wang, Q.Z. and Lee, D.J. (1999). "Predictive modelling for rubber-toughened polymers." Mechanics of materials **31**: 705-716.

[123]Wang, Y. and Williams, J.G. (1992). "Corrections for Mode II fracture toughness specimens of composites materials." Composite science and technology **43**: 251-256.

[124]Wells, A.A. (1963). Application of fracture mechanics at and beyond general yielding. British welding research association report.

[125]Wise, C.W., Cook, W.D. and Goodwin, A.A. (2000). "CTBN rubber phase precipitation in model epoxy resins." Polymer **41**: 4625-4633.

[126]Wu, E.M. and Jr. Reuter, R.C. (1965). Crack extension in fiberglass reinforced

plastics. TAM Report No.275, University of Illinois.

[127]Wu, G.F. and Crocombe, A.D. (1994). "Simplified finite element modelling of structural adhesive joints." Computers and structures **61**: 385-391.

[128]Xiao, X.R., Foss, P.H. and Schroeder, J.A. (2004). "Stiffness prediction of the double lap shear joint. Part1: Analytical solution." International Journal of Adhesion and Adhesives **24**: 229-237.

[129]Yang, Q.D. and Thouless, M.D. (2001). "Mixed-mode fracture analysis of plastically-deforming adhesive joints." International journal of fracture **110**: 175-187.

[130]Yang, Q.D., Thouless, M.D. and Ward, S.M. (2001). "Elastic-plastic mode-II fracture of adhesive joints." International journal for solids and structures **38**: 3251-3262.

[131]Yee, A.F. and Pearson, R.A. (1986a). "Toughening mechanisms in elastomer-modified epoxies. Part 1:mechanical studies." Journal of materials science **21**: 2462-2474.

[132]Yee, A.F. and Pearson, R.A. (1986b). "Toughening mechanisms in elastomer-modified epoxies. Part 2: microscopy studies." Journal of materials science **21**: 2475-2488.

[133]Yen, H.Y. (2000). New analysis and design procedures for ensuring gas turbine blades and adhesive bonded joints structural integrity and durability, The Ohio state university.

[134]Yorkgitis, F.M., Tran, C., Eiss, N.S., Hu, T.Y., Yilgor, I., Wilkes, G.L. and McGrath, J.E. (1984). "Siloxane modifiers for epoxy resins." Advances in Chemistry Series: 137-161.

[135]Zou, Z., Reid, S.R., Li, S. and Soden, P.D. (2002). "Modelling interlaminar and intralaminar damage in filament wound pipes under quasi-static indentation." Journal of composite materials **36**: 477-499.